THERMAL MANAGEMENT OF CASTING MOULDS USING HEAT PIPES

By

Abraham Groenewald

Thesis presented in partial fulfillment of the requirements for the degree
Master of Science in Engineering at the University of Stellenbosch

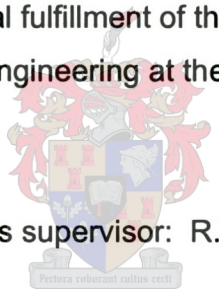

Thesis supervisor: R.T Dobson

January 2001

DEPARTMENT OF MECHANICAL ENGINEERING
UNIVERSITY OF STELLENBOSCH

DECLARATION

I, Abraham Groenewald, the undersigned, hereby declare that the work contained in this thesis is my own original work and has not previously, in its entirety or in part, been submitted at any university for a degree.

SUMMARY

The use of cylindrical heat pipes for the thermal control and management of casting moulds have been investigated. Heat pipes are tubes that possess a high capability to transfer heat, up to a thousand times or more than an equivalent solid copper rod. The heat pipes used in this thesis are copper tubed, use water as working fluid and have (phosphor-bronze) screen mesh wicks. Experiments relating to practical casting situations in industry were designed and performed, using pure tin as the casting metal. Three cases pertaining to the requirements of an industrial casting mould were considered. The first case considered heating of a mould through heat pipes, in order to keep it at a specific temperature. The second case relates to the situation where metal is cast around a core, and the core is cooled by a heat pipe connected to a heat sink. The heat sink in this case was an air cooled fin. The third case is representative of the situation where molten metal is cast into an external mould and the mould heats up due to the energy flowing in from the casting. In order to cool the mould, heat pipes are used to transport the heat to a water cooled heat sink.

These three cases were modeled theoretically, which included using a standard finite element method (FEM) computer package, NASTRAN 2.0 for Windows. For the FEM simulations, the heat pipes are modeled using an equivalent conductivity approach. Theoretical and experimental results are to within $\pm$ 30% of each other, but better results could possibly be achieved using a better finite element model for the heat pipes.

A simulation case was performed to compare the use of an un-cooled mould with a heat pipe cooled mould, and a two and a half time improvement of production rate was achieved.

In support of the above mentioned casting related experiments, experiments have also been performed on a specially designed cylindrical heat pipe to determine the evaporator and condenser heat transfer coefficients. It was found that the heat pipe can transfer more than 500 W for vertical operation and around 160 W for horizontal operation. The heat transfer coefficients of the condenser and evaporator ends are in the order of 1800 to 2000 W/m^{2}K.

Experiments were also performed on the fins used as the heat sink in the experiment where core cooling is investigated, to compare the experimentally determined fin heat transfer coefficient with the theoretically predicted coefficient.

A theoretical study was also performed for an inclined ammonia thermosyphon in order to compare the theory to a set of previously determined experimental results. The theory produced accurate results for vertical operation, but it is clearly limited for inclined operation, and can lead to inaccurate results.

A special correlation factor, the *splashing factor*, was defined to analyse the deviation between the theoretical and experimental results. The splashing factor can be used in two ways. Firstly, it can be used as a design correction factor and secondly, it can be processed to indicate which operational variables have the highest impact on the discrepancy between the theory and the experimental data.

It is recommended that further research into the use of heat pipes for the thermal control of moulds be considered, based on the results achieved in this thesis. Furthermore, a finite element model for a heat pipe can also be considered. It is also recommended that the use of the splashing factor be considered for the analysis of thermosyphons.

OPSOMMING

Die moontlikheid om hittepype te gebruik in die termiese beheer van gietvorms is ondersoek. Hittepype is buise wat oor 'n baie goeie warmte-oordragsvermoë beskik, 'n duisend maal of beter as 'n ekwivalente soliede koper staaf. Die hittepype wat gebruik is in die tesis is gesëelde koperbuise, wat water gebruik as werksvloeier en ook 'n (fosfor-brons) sifdraad pitmateriaal bevat. Eksperimente wat verband hou met industriële gietprosesse is ontwerp en uitgevoer. Suiwer tin is gebruik as die gietmateriaal. Drie giet gevalle is ondersoek. Die eerste geval het die verhitting van 'n gietvorm met hittepype behels. Die tweede geval hou verband met die situasie waar metaal om 'n kern gegiet word en die kern word afgekoel deur middle van 'n hittepyp wat gekoppel is aan 'n hitteput, wat in die geval 'n lugverkoelde fin is. Die derde geval hou verband met die situasie waar gesmelte metal gegiet word in 'n eksterne gietvorm en die gietvorm verhit as gevolg van die energie wat vanaf die gietstuk invloei.

Hierdie drie gevalle is teoreties gemodelleer, wat die gebruik van 'n eindige element analise (EEA) rekenaarpakket insluit (NASTRAN 2.0 for Windows). Tydens die EEA simulasies is die hittepype gemodelleer met behulp van die ekwivalente geleidingskoëffisiënt metode. Teoretiese en eksperimentele resultate is binne $\pm$ 30% van mekaar. Beter resultate kan moontlik verkry word as 'n verbeterde eindige element model vir die hittepype ontwikkel kan word.

'n Simulasie geval is uitgevoer om die produksietempo van 'n onverkoelde gietvorm te vergelyk met 'n hittepyp-verkoelde gietvorm, en 'n verbetering van twee en 'n half maal is gevind vir die verkoelde gietvorm.

Ter ondersteuning van die bogenoemde gietverwante eksperimente en teoretiese modelle, is eksperimente ook op 'n spesiaal ontwerpte silindriese hittepyp uitgevoer om die kondeser en verdamper hitte-oordragskoëffisiënte te bepaal. Daar is bevind dat die hittepyp meer as 500 W kan oordra tydens vertikale gebruik en ongeveer 160 W tydens horisontale gebruik. Die

hitte-oordragskoëffisiënte vir die kondenser en verdamper is in die orde van 1800 tot 2000 W/m^2K. Eksperimente is ook uitgevoer op die finne wat gebruik is as die hitteput in die geval waar die kern verkoeling ondersoek is, om die eksperimenteel bepaalde fin hitte-oordragskoëffisiënte te vergelyk met die teoretiese koëffisiënt.

'n Teoretiese studie is ook uitgevoer vir 'n skuins termoheuwel sodat die teorie vergelyk kan word met 'n stel bestaande resultate. Die teorie gee akkurate voorspellings vir vertikale gebruik, maar is duidelik beperk en kan lei tot onakkurate resultate vir skuins gebruik.

'n Spesiale faktor (*splashing factor*) is gedefiniëer om die verskil tussen die teoretiese en eksperimentele resultate mee te analiseer. Hierdie factor kan op twee maniere gebruik word. Eerstens kan dit gebruik word as 'n korreksiefaktor en tweedens kan dit geprosesseer word om aan te dui watter veranderlikes die hoogste impak het op die verskil in eksperimentele en teoretiese resultate.

Dit word aanbeveel dat verdere navorsing gedoen word op die gebruik van hittepype vir die termiese beheer van gietvorms, gebasseer op die resultate wat verkry is uit die tesis. Verder kan 'n eindige element model vir 'n hittepyp ontwikkel word. Dit word ook aanbeveel dat die "splashing factor" oorweeg word in die analise van termohewels.

TABLE OF CONTENTS

LIST OF FIGURES

LIST OF TABLES

NOMENCLATURE

a_o	splashing factor constant
A	area (m^2)
C_1	pool boiling constant
C_2	film nucleate boiling constant
C_f	friction coefficient
C_p	specific heat capacity (J/kg K)
d	diameter (m)
D	diameter (m)
D_h	hydraulic diameter (m)
$D_{h(r)}$	$\frac{4A_r}{\wp_r}$ (m)
E	energy (J), error
f	friction factor
f_ϕ	condenser inclination factor
g	gravitational constant (=9.81m/s^2)
h	heat transfer coefficient (W/m^2 K)
h_{fg}	latent heat of evaporation (J/kg)
k	thermal conductivity (W/m K)
K_p	$P_i L_m / \sigma$
L	length (m)
L_m	$\left(\sigma / g(\rho_l - \rho_g)\right)^{0.5}$
m	mass (kg)
$\dot{m}$	mass flow rate (kg/s)
n	number
n_i	splashing factor exponent
N	number
Nu	Nusselt number

$N_{\mu f}$	$\mu_l \Big/ \left(\sigma g \left(\frac{\sigma}{g(\rho_l - \rho_g)} \right)^{0.5} \right)^{0.5}$
Nu_{ef}	$h_{ef} L_m / k_l$
Nu_g	$h_g d_i / k_g$
Nu_{lf}	$4 h_{lf} \delta_{lf} / k_l$
Nu_p	$h_p d_i / k_l$
Nu_r	$h_r D_{h(r)} / k_l$
p	perimeter (m)
P	pressure (bar or Pascal), power (W)
P_c	critical pressure
Pr	Prandtl number = $\mu C_p / k$
$\dot{q}$	heat transfer rate (W)
$\dot{q}''$	heat flux (W/m^2)
$\dot{Q}$	heat transfer rate (W)
r	radius, radial co-ordinate
r^2	standard deviation
Ra	Raleigh number = $\frac{\beta g d_i^4 \dot{q}''_{ewi} C_{pl} \rho_l^2}{\mu_l k_l^2}$
Re	Reynolds number
$\mathrm{Re_c}$	$\frac{\dot{q}_c}{\pi d_i \mu_l h_{\mathrm{lg}}}$
$\mathrm{Re_{cond}}$	$\frac{\rho_g u_c d_i}{\mu_g}$, where u_c is the radial velocity of the condensing gas
$\mathrm{Re_{evap}}$	$\frac{\rho_g u_e d_i}{\mu_g}$, where u_e is the radial velocity of the evaporating gas
$\mathrm{Re_{fa}}$	$4 \dot{q}''_{ewi} L_f / \mu_l h_{\mathrm{lg}}$
$\mathrm{Re_g}$	$\frac{\rho_g V_g d_i}{\mu_g}$
$\mathrm{Re_r}$	$\frac{\rho_l V_r D_{h(r)}}{\mu_l}$

$\mathrm{Re_v}$	$\frac{\dot{q}''_{ewi} L_m}{\rho_v h_{lg} \nu_l}$
$\mathrm{Re_x}$	$\frac{4\dot{q}''_{ewi}(L_e - x^*)}{h_{lg}\mu_l}$
S	splashing factor
t	thickness (m)
T	temperature (°C)
V	velocity (m/s)
x	longitudinal direction variable (m)
x^*	distance from start of evaporator (m)
X	pool boiling regime variable
y	circumferential direction variable (m)
z	transformation variable for fin analysis, axial co-ordinate (m)

Subscripts and superscripts

a	average, ambient, atmosphere, adiabatic
al	aluminium
b	base
c	condenser, cold, convection
cv	control volume
$CCNB$	combined natural convection and nucleate boiling
$cond$	condensation
e	evaporator
env	environment
$evap$	evaporation
f	film, fluid, fin
g	gas
h	hot, hydraulic
hp	heat pipe
i	internal, interfacial, in
int	internal, interfacial
KU	Kutataledze
l	liquid
m	melt
n	number
NB	nucleate boiling
NC	natural convection

o	outside, out
p	pool
r	rivulet
rw	resistance wire
s	surface, solder, solid
w	wick, water or wall

Greek symbols

β	coefficient of thermal expansion (K^{-1}), fin radius transformation variable (i.e $z = \beta r$)
δ	film thickness (m)
ε	radiative emissivity, voidage fraction
ϕ	angle of inclination (°)
γ	blowing / suction shear correction factor
η	film boiling regime variable
η_f	fin efficiency
φ	blowing or suction factor, wick porosity
κ	wick permeability
λ	latent energy of fusion (J/kg)
μ	dynamic viscosity ($N.s/m^2$)
ν	kinematic viscosity = μ/ρ (m^2/s)
Π	potential energy function for the finite element method
θ	angle of rotation (°)
ρ	density (kg/m^3)
σ	surface tension (N/m), Stefan-Boltzman constant (W/m^2K^4)
τ	shear stress (N/m^2)
ψ	$\left(\frac{\rho_v}{\rho_l}\right)^{0.4}\left(\frac{P_i \nu_l}{\sigma}\left(\frac{\rho_l^2}{\sigma g(\rho_l-\rho_v)}\right)^{0.25}\right)^{0.25}$
$\wp$	perimeter (m)

Abbreviations

FEM	Finite element method
FDM	Finite difference method
BEM	Boundary element method
FVM	Finite volume method

CHAPTER 1 - Introduction

Since the patent of the 'heat pipe' in 1963 by Grover, on behalf of the US Atomic Energy Commission (following earlier patents of Perkins and Gaugler), heat pipes and thermosyphons have been the subjects of intensive research. Many applications have grown from the original idea so that today they are playing an important role in the global industry. Although before the 1960's, thermosyphons were used in gas fired baking ovens and proposed for use in heat exchangers (Dunn & Reay, 1994), the coming of the space age and the rapid growth of the computer, electronics and information revolutions have placed the demand for high heat transfer capabilities and sparked the research and development of new types of heat pipes for many applications. The space and electronics industries (which are high technology industries) have probably created the critical mass for heat pipe developments, but the advantages of heat pipes from a heat transfer and energy efficient point of view are obvious, and there are many applications where older technologies and fixed practices can be radically improved by using heat pipes. The use of the heat pipes is thus not necessarily limited to the developed countries, but can also be effectively applied in the developing countries. The philosophy behind this thesis is to do research on heat pipes, but to keep the South African industry in mind, and focus on possible areas of heat pipe application locally. The SA casting industry is geared for future growth, especially the manufacturing of engine components seems to be a future market. This situation has led to the decision that the thermal management and control of casting moulds should be investigated, using heat pipes as the enhanced heat transfer devices.

For a casting operation, three potential benefits of using heat pipes are proposed:

- Higher production rate of castings (by faster heat transfer in the moulds)
- Better quality of castings (by more accurate thermal control of casting moulds)
- Savings in amount of energy used to produce castings

The work done towards this thesis can be grouped into parts as follows:

1. The performance of theoretical and experimental heat transfer studies of castings and moulds, using heat pipes
2. The performance of theoretical and experimental studies on the heat transfer devices such as the heat pipes and heat sinks used for the thermal control of the castings
3. An analysis on an inclined ammonia thermosyphon, which is not related to castings, but provides a platform from which the internal thermo-fluid behaviour of a thermosyphon (or heat pipe) can be modelled

Parts 1 and 2 are contained within the body of the thesis. Part 3 is located in appendix D.

The objectives of the thesis are the following:

- To experimentally evaluate the heat transfer characteristics of the heat pipes in terms of heat transfer coefficients and maximum heat transfer rate, and compare with theoretical models
- To experimentally evaluate the heat transfer characteristics of an air cooled fin's heat transfer coefficient and compare the results with theoretical models
- To create a simple, yet representative finite element model for a heat pipe that can readily be used in a standard finite elements computer program
- To design and perform experiments regarding the heating of a casting mould using heat pipes, and to compare results with those obtained using a theoretical model
- To design and perform experiments regarding the cooling of a core using a heat pipe and air cooled fin, and to compare results with those obtained using a theoretical model
- To design and perform experiments regarding the cooling of an external mould using heat pipes and a water cooled heat sink, and to compare results with those obtained using a theoretical model
- To asses whether it is advantageous to use heat pipes in casting moulds for thermal control and quantify, and establish and quantify the benefits if possible
- To perform an analysis on the internal thermo-fluid behaviour of a simple heat pipe (thus the inclined thermosyphon, appendix D) and to compare the accuracy and relevancy of the theoretical model used. To find which operating variables have the most significant impact on the prediction inaccuracies

The thesis has been organised in the following fashion: The total literature study regarding heat pipes and castings is located in chapter 2. All the theory used in the thesis is located in chapter 3. The experimental procedures regarding the heat pipe, the air cooled fins and the three casting related experiments are described in chapter 4. The thermal models of the experiments performed in chapter 4 are developed in chapter 5, and the theoretical and experimental results thereof are presented in chapter 6. Chapter 7 presents a chosen simulation case, so as to compare the production rate of a casting with and without the use of heat pipes in the mould. The discussion, conclusions and recommendations are located in chapters 8 and 9.

CHAPTER 2 - Literature Study

This literature study consists of two sections. Section 2.1 relates to heat pipes and thermosyphons and section 2.2 relates to casting.

2.1 HEAT PIPES AND THERMOSYPHONS

Very little published literature relating to the use of heat pipes in the thermal management of castings and casting moulds could be found. Therefore, parts of section 2.1 is rather general and does not necessarily pertain to the use of heat pipes in casting moulds, or to the thermosyphon analysis in appendix D of this thesis. For this section, where a reference is not given, the information is based on three heat pipe textbooks (Faghri, 1995; Dunn and Reay, 1994; Peterson, 1994).

2.1.1 TYPES OF HEAT PIPES

A few types of available heat pipes will now be discussed.

2.1.1.a Thermosyphon

A thermosyphon is also described as a 'wick-less heat pipe', since it has no capillary wick for the purpose of liquid return to the evaporator. It consists of a (cylindrical) container that is partially filled with a working fluid. Heat is absorbed through evaporation of the liquid to gas (through the latent heat of evaporation) and it is rejected through condensation of the gas to liquid. This has the advantage that heat transfer can take place over the heat pipe length, while the internal vapour and liquid stays at a constant temperature, with the benefit that the thermal resistances are low.

A thermosyphon can only operate in 'bottom heating mode', which means that in a gravity field, the heat source must be below the heat sink. The reason for this is that gravity causes the condensate that forms inside the condenser wall to flow downwards towards the pool – therefore the pool is fed naturally and the liquid needed for evaporation is maintained. If the heat source is placed above the heat sink, there is no mechanism that will cause liquid return to the evaporator.

Condensation heat transfer

The forces that act on the condensate liquid are due to gravity, buoyancy and viscous shear between the counter current gas-liquid flow. (Gas moves towards the condenser section and liquid flows towards the evaporator section) The film thickness and flow speeds can be determined by solving the continuity, momentum and energy equations for a liquid film

control volume and the solution (for vertical laminar flow) is standard in most heat transfer textbooks.

A widely used correlation is presented by Gross (1992) for reflux condensation heat transfer inside a closed thermosyphon. He made use of 2889 data points from 18 research works to find a general correlation. His working parameters included 10 working fluids (water, Dowtherm A, acetone, methanol, ethanol, R11, R113, R22, R115 and R13B1), internal temperatures varied between 14°C and 340°C, the pressure varied between 0.04 bar and 39.5 bar, the condenser length varied between 102 mm and 2450 mm, and the inclination angle varied between 0° and 85°. The heat transfer coefficient can fall into one of three ranges, namely the laminar range, the wavy-laminar range and the turbulent range, and correlations are given for each range. Gross could not comment on the accuracy of measurements taken as details of the measuring techniques are missing in most of the experimental publications he used. Different fluids also show different behaviour. The deviation of experimental data outside of the correlations is found to be about $\pm$ 30%. Three main reasons are proposed why deviations may occur:

- The effect of shear stress at the liquid-film interface
- The effect of non-condensable gases inside the thermosyphon
- Flooding of the condenser zone due to liquid, transported from out of the evaporator, that deposits on the inside of the condenser walls. (Such as the "geysering" of a liquid slug along the axial length of the thermosyphon)

Dobson and Kröger (2000) present a correlation for the condensation heat transfer coefficient of an ammonia filled (long) thermosyphon, as a function of the heat transfer rate, internal temperature (therefore pressure), the ratio of the liquid fill height over the evaporator length and the inclination angle.

Bontemps et al. (1989) investigated the heat transfer performance of a toluene-loaded thermosyphon. They compared their theoretical results to existing correlations and have taken into account the effects of inclination with an empirical formula.

Evaporation heat transfer

In thermosyphons, a falling film of liquid is established in the condenser section that persists into the evaporator section. The liquid that is leaving the condenser section is subcooled. As it descends into the evaporator section it reaches saturation temperature and later becomes superheated, and nucleation boiling may take place in the film. Evaporation and nucleate boiling will exist in the pool section as well.

Boiling is usually classified into three types, namely nucleate boiling, convective boiling and film boiling (Whalley, 1987). The type of boiling expected to occur in a thermosyphon is usually nucleate boiling, where vapour bubbles start to grow from nucleation sites. Two types of nucleation exist, namely homogeneous or heterogeneous nucleation. Heterogeneous nucleation typically starts at a wall, which has cracks and crevices in it on microscopic scale, wherein gas becomes entrapped. Vapour bubbles originate at several places on the surface and form the 'boiling bubbles' that flows through the liquid during boiling. Homogeneous nucleation happens in extreme cases, where there are no nucleation sites on the vessel walls. Mercury in a rotating dish will form a convex meniscus due to the centrifugal forces involved. If water is heated inside this mercury 'bowl' (which is very smooth so that no nucleation sites exist), the temperature of the water can be raised high above 100°C (at 1 bar) before boiling starts. At 1 bar and around 321°C the total amount of water will change phase, all at once, with explosive results.

The calculation of a heat transfer coefficient for boiling (heterogeneous type) as well as tools such as the pool boiling curve are presented (Whalley, 1987) that can be used as an estimate of evaporative heat transfer that takes place in the pool of a thermosyphon. There are two differences in a thermosyphon:

- Usually the pool is confined to a relatively small volume, but has a large area through which heat enters, as opposed to boiling in a kettle where a relatively small element heats a large volume of liquid
- Two phase flow phenomena can result in the periodic displacement of liquid and gas from out of the pool

Two-phase flow phenomena include different flow patterns, for instance bubbly flow, plug flow, stratified flow, wavy flow, slug flow or annular flow (Whalley, 1987), which complicate analyses.

Shiraishi et al. (1981) present experimentally determined correlations for the pool and film in the evaporator section of a thermosyphon. They used water, ethanol and Freon 113 as the working fluids, but only considered vertical operation.

El-Genk and Saber (1997 and 1998) present correlations for the heat transfer coefficients in the pool and film regions inside the evaporator. The pool heat transfer is relevant for small cylindrical enclosures with uniform wall heating. They used 731 data points for liquid pools of water, ethanol, methanol, Dowtherm-A, R-11 and R-113. Their correlations span over three regimes, which are natural convection, combined convection and nucleate boiling heat transfer. Their correlations are within $\pm$15% of the experimental data. For the liquid film

region, they derived their correlations from 305 data points using ethanol, acetone, R-11 and R-113 as the working fluids. The same three heat transfer regimes are identified, namely laminar convection, combined convection and nucleate boiling. Once again results are expected to be ±15% accurate.

Stephan and Abdelsalam (1980) present a pool boiling correlation as a constant multiplied with a power of the heat flux, where the constant is a function of the internal pressure. This correlation is probably better suited for use with ammonia as the working fluid.

Dobson and Kröger (2000) present a correlation for the evaporator heat transfer coefficient of a thermosyphon, using ammonia as the working fluid, as a function of the heat transfer rate, internal temperature (therefore pressure), the ratio of the liquid fill height to the evaporator length and the inclination angle.

Groenewald (2000) presents an investigation of an inclined ammonia filled thermosyphon, and introduces a 'splashing factor', which compares the experimental heat transfer coefficient in the evaporator with that of a 'limited' theoretical model. The splashing factor is assumed to be a function of five variables, namely the heat transfer rate, the internal temperature, the difference between the hot and cold water temperatures, the pool height to evaporator length ratio and the angle of inclination. This factor can be manipulated statistcally to help show which variables have the largest influence on the deviation between theory and reality.

Kang (2000) has investigated the effect of tube inclination on pool boiling heat transfer. He found that the heat transfer coefficient is influenced by the inclination angle, especially inside a smooth tube. He compared results for three different inclination angles, 0°, 45° and 90° and found that the inclined (45°) operation leads to the highest heat transfer coefficient. As only water was considered, this is not necessarily true for other working fluids.

Limitations

Some of the limitations associated with thermosyphon will now be discussed.

The flooding and entrainment limits

As the relative velocity between the liquid and vapour at the liquid-vapour interface increases (because of a higher heat transfer rate), the shear stress on the liquid film increases, which retards the flow of the liquid back to the evaporator section. The limit is reached when an increase in temperature difference between the evaporator and condenser wall temperatures will not result in a higher heat transfer rate through the thermosyphon. The most common concern for long thermosyphons with large liquid fill ratios, large axial heat fluxes and small

radial heat fluxes, is the flooding limit. There are two major fundamental semi-empirical correlations for prediction of the flooding limit of open two-phase systems, which are the Wallis correlation and the Kutateladze stability criteria.

Zuo and Gunnerson (1994a) have performed a numerical study on the flooding limit of a vertical thermosyphon. They calculated the flooding limit (or the point where flow reversal takes place) as a function of the operating temperature for a 2.5 m long (evaporator length = condenser length = 1 m) water filled thermosyphon with a diameter of 17 mm. The results agreed well with the data collected by Nguyen-Chi.

The dry-out limitation

The dry-out limitation is usually associated with thermosyphons with very small working fluid fill ratios and also where the radial evaporator heat flux is relatively small. This means that the higher the heat flux into the evaporator, the more liquid needs to evaporate. Since there is no pool as a 'back-up' source of liquid, there will be a heat flux at which the thickness of the falling film (coming from the condenser into the evaporator) will approach zero at the bottom of the evaporator wall. A higher heat flux will cause the film to start drying out from the bottom upwards – effectively shortening the evaporation area. The evaporator wall temperature will increase but the heat transfer rate will not.

The boiling limitation

This limitation is usually associated with thermosyphons with large fill volumes and high radial heat fluxes in the evaporator section. As the heat flux is increased, nucleate boiling occurs in the evaporator section. At the critical heat flux (CHF), the gas bubbles coalesce near the pipe wall, which blocks the liquid working fluid from touching the wall. Since the gas usually has a much lower thermal conductivity, the thermal resistance for heat flow into the liquid increases substantially. The evaporator wall temperature therefore has to increase to maintain the same heat flux.

Minimum liquid fill requirement

The literature gives equations to determine the minimum amount of working fluid, as a function of the thermosyphon geometry, working fluid properties and heat transfer rate.

Zuo and Gunnerson (1994b) undertook a numerical study on the effect of the working fluid inventory on thermosyphon performance. A minimum working fluid inventory required for stable thermosyphon performance was established. Less working fluid inventory can induce dry-out, cause evaporator wall temperature excursions and dramatically decrease the heat transfer capability. The minimum working fluid inventory increases with the input heat flux but

decreases with the internal temperature due to larger liquid viscosity at low temperatures. They found that generally, the minimum liquid fill increases with larger ratios of total length over diameter and condenser length over evaporator length. Optimum working fluid inventory that will lead to the highest heat transfer capacity is also investigated.

Other literature regarding thermosyphons

Shiraishi et al. (1995) have performed a visual study on flow behaviour in an inclined thermosyphon. They used a 13-mm-I.D. glass tube, 930 mm long thermosyphon with Freon 113 as the working fluid. Inclination angles varied between 5° and 90°. This is one of the very few studies of this type done, as the heat transfer is flow pattern dependant. This is especially true when operating at inclination angles, for instance to explain why the critical heat flux for a thermosyphon is a maximum at around 45° – 60°. They used a video camera and a still camera to take pictures of typical flow patterns. They found that annular flow is observed for vertical or near vertical operation, while stratified flow occurs at inclined angles. In the case of stratified flow, the upper part of the evaporator wall inside can be wetted by lapping of large waves and impingement of liquid droplets. For stratified flow, the dry-out condition is caused by liquid waves that retard the returning condensate.

Zuo and Gunnerson (1994.c) have numerically modelled a vertical thermosyphon, using water as a working fluid. Their theoretical and experimental results were in good agreement. They have also (1995.a) performed an analysis on an inclined two-phase thermosyphon. Good agreement between the theoretical and experimental values for the mean heat transfer coefficients was obtained.

Zuo and Gunnerson (1995.b) also investigated the effect of size reduction on thermosyphon performance, using numerical simulations. They included effects of the liquid film thickness, liquid pressure and normal stress which start to play a role when the thermosyphon becomes small. It was found that critical heat flux limits the heat transfer capacity of larger thermosyphons, but flooding appears to limit the heat transfer in smaller thermosyphons. For smaller inside diameters, the advantage of high effective axial conductivity of the thermosyphon becomes less. Therefore, for smaller scale heat transport from say a microelectronic circuit, the cylindrical type thermosyphon may not be the best.

2.1.1.b Cylindrical heat pipe with wick

This is the type of heat pipe used in the casting experiments of this thesis. It is essentially the same as the thermosyphon, with the difference that it has an internal wick, specifically with the objective to return liquid to the evaporator end either against gravity or in a no-gravity environment. Figure 2.1 shows some typical commercially available cylindrical heat pipes.

Limitations

Except for the limitations mentioned in section 2.1.1.a, the wick structure imposes further limits. Two of these limits are:

The capillary limit

This is a very common limitation encountered in the operation heat pipes, especially where liquid viscosity is high. This limit is associated with the ability of a wick structure to 'pump' liquid back to the evaporator through capillary action. It depends on the working fluid properties and the wick structure.

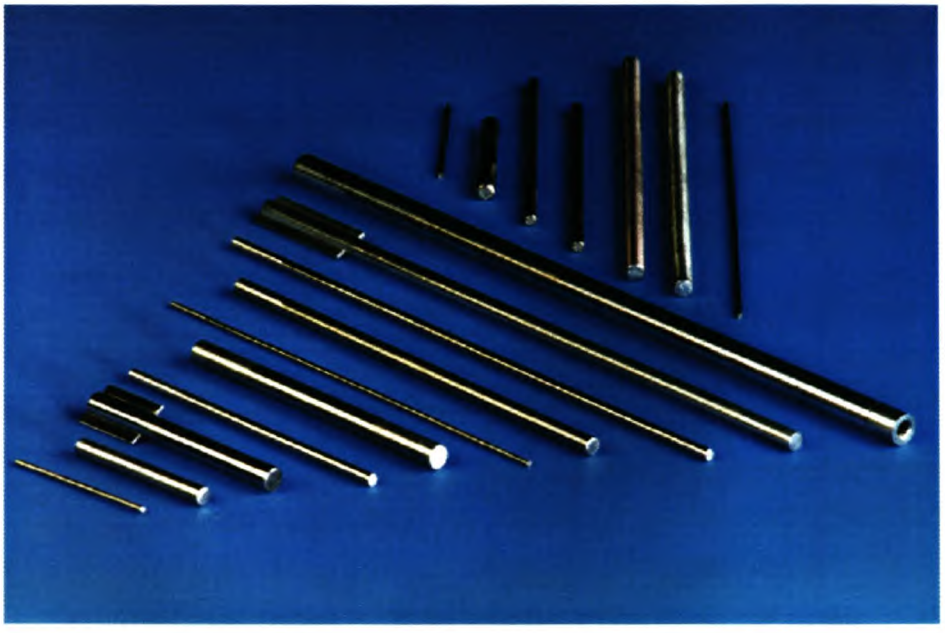

Figure 2.1 Commercially available cylindrical heat pipes

The frozen start-up limit

This limitation is associated with a frozen working fluid, during the start-up process, typically as is the case when metal is used as the working fluid. Normal operation can only take place when the heat pipe as a whole has heated up enough to melt the metal.

Wick structures

Three types of homogeneous wick structures will now be discussed.

The wrapped screen wick

This is the wick type used in the heat pipes used in this thesis. It is a relatively common wick type, and consists of multiple wraps of wire screen mesh, lined against the inside of the container wall. Its capillary pumping ability is high, the thermal conductivity is low and the permeability is low-to-average.

The sintered metal wick

This type of wick consists of packed spherical particles, felt metal fibres or powder lined against the inside of the container wall. The capillary pumping ability is high, the thermal conductivity is average and the permeability is low-to-average.

The axially grooved wick

In this case, rectangular, circular, triangular or trapezoidal grooves are cut into the inside part of the container wall. The capillary pumping capability is low, the thermal conductivity high and the permeability average-to-high.

The wick structure influences the condensation and evaporation processes. Demidov and Yatsenko (1994) performed an analysis on the heat and mass transfer in the evaporation zone of a heat pipe using the 'inverted meniscus' approach. They performed mathematical analyses to observe the evaporation process, the growth of vapour zones (bubbles) and to plot the corresponding patterns of isotherms and mass flux lines within the capillary structure. They found that a thermally stable area exists when the interface boundary enters inside the capillary structure. The bubbles start growing from the places where direct contact exists between the wick and the bulges of the heating wall. As the heat load is increased, the bubbles extend into the wick.

Other literature regarding the cylindrical heat pipe with wick

The behaviour of the vapour phase was studied by Issacci (1991). The use of spectral methods for heat pipe analysis was proposed. According to the author the finite difference method, which is popular for the modelling of vapour flow, is costly in terms of the computational effort needed to solve the equations. Furthermore, at least a two dimensional model is needed to effectively model mass and heat transfer. Spectral methods involves Fourier analysis and an eigenvalue problem, where the approximated answer is assumed to be the sum of N terms as a function of x and y (the heat pipe co-ordinates). By choosing an appropriate series representation that will satisfy the boundary conditions and substituting it into the continuity, momentum and energy equations, the needed coefficients can be determined, using orthogonality properties. It is found that using five terms or less did not result in very accurate answers, more than ten terms gave 'acceptable' answers and twenty terms or more gave very accurate answers, as compared to results found with the finite difference method. Their conclusion is therefore that good results can be obtained with much less computational effort by using this method. No experimental work was done.

The modelling of heat transfer into a heat pipe for a localised heat input zone was considered by Rosenfeld (1987). For the cooling of wing leading edges on hypersonic aircraft, high heat fluxes on a surface such as from a laser beam, the cooling of microelectronic components and spacecraft thermal management, a non-uniform or localised heat input is common. A one dimensional heat conduction model was developed, and solutions were obtained for two separate boundary conditions – one was solved analytically and the other was solved numerically. Experimental results correlated well with the theoretically modelled results. Cao and Faghri (1989) did the same type of analysis, but argued that an overall energy balance rather than an input condition should determine the operating temperature of the heat pipe. For this case radial and axial conduction plays an important role. Their results compared well with the experimental data of Rosenfeld.

2.1.1.c Pulsating heat pipe

A pulsating heat pipe consists of a long meandering tube filled with a working fluid. The size of the internal diameter of the tube is in the region of the "capillary length", allowing discrete liquid plugs and vapour bubbles to co-exist. In the heated section evaporation takes place causing the pressure in the vapour bubbles to increase. This increase in pressure in the vapour bubbles causes pressure differentials across some of the liquid plugs. Due to these pressure differentials some of the liquid plugs will move. In the cooled section condensation takes place causing the pressure to decrease in the vapour bubbles. This decrease in pressure also causes pressure differentials across some of the liquid plugs causing those plugs to move as well. Due to the fact that all the liquid plugs and vapour bubbles are interconnected by a single tube the movement of any plug will cause neighbouring liquid plugs to move as well, causing all the liquid plugs to oscillate in an irregular aperiodic manner. The liquid plugs do not move as discrete entities all the time and some of the liquid plugs can coalesce to create a single plug or some split up to form two separate liquid plugs. This is a relatively new type of heat pipe (patented during the early 1990's by Akachi) and the modelling of the inside dynamics still proves to be problematic. This type of heat pipe seems to have a promising future though, since it is relatively simple to manufacture, uses no wick structure, has good thermal characteristics and it's design lends itself to favourable and functional shapes, such as flat plates for the mounting of electronic components or the manufacture of high performance fins.

2.1.1.d Capillary pumped loop (CPL) heat pipe

A capillary pumped loop heat pipe is in the form of a closed loop, as is shown in figure 2.2. The difference between this type of heat pipe and a cylindrical heat pipe is the fact that the two phases, liquid and vapour, do not flow in counter current to each other but seperately in different sections of the looped pipe. In the condenser where gas condenses to liquid the two

phases exist together in the form of gas bubbles and liquid slugs. The CPL is an attractive option in the thermal management of spacecraft.

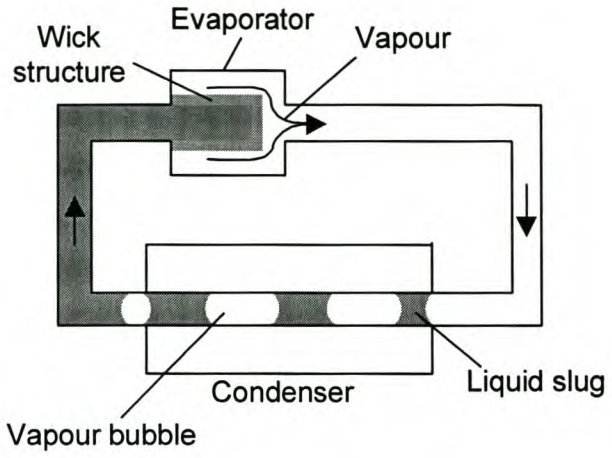

Figure 2.2 Capillary pumped loop heat pipe (CPL)

There are other types of heat pipes available as well, such as the variable conductance, flat plate, flexible and micro heat pipes.

2.1.2 APPLICATIONS OF HEAT PIPES

There are several applications in which heat pipes are used.

Die casting and injection moulding

Most modern dies are at least water cooled, but it can be difficult to take water cooling channels to inaccessible parts of the die. It is also often inconvenient to take water cooling to movable or removable nozzles, sprue pins and cores. Thermal shock, which exists because of the temperature difference between the molten metal and the cooling water, is also experienced. In some dies it may be required to constantly heat parts of the die so as to keep the metal molten as it flows towards more remote parts; but once the mould is filled with metal, the requirement changes from heating to cooling for rapid solidification to take place.

By inserting heat pipes into a mould, temperature gradients across the mould can be evened out, without connecting it to the water cooling circuits. Another use of heat pipes is to help transfer heat away from areas in the mould where hot spots occur in the casting. This helps to improve the production rate and the quality of the castings involved. Heat pipe core pins have been used in plastic injection moulding in cores where high heat loads need to be transferred away from the molten plastic. Heat pipes using sodium as a working fluid have been used to aid in the cooling of steel castings such as gear wheels. Faster cooling was

achieved using a heat pipe located in a copper chill which was inserted into the hub of the wheel.

Cooling of electronic components

This is one of the most important fields where heat pipes are currently used. The largest number of heat pipes is manufactured to cool electronic components. Usually the objective for the thermal control of an electronic component is to keep it below a manufacturer's maximum specified service temperature. Investigations have shown that overheating of 10°C can reduce the reliability of some systems by about 50%. Components such as thyristors, high voltage transistors, integrated circuits (ic's or 'micro chips') other high voltage components and microelectronics components may be connected to heat pipes, which will then transfer the heat to a suitable heat sink at a remote location.

Energy conservation

Industrial processes often create hot flue gases that are rejected into the atmosphere without recovering heat energy. Energy recovery can be achieved using heat pipe heat exchangers. Two types of heat pipe heat exchangers are normally used in industrial processes, namely the gas-gas heat exchanger and the gas-liquid heat exchanger. Flue gas from a process flows over the one side of the finned heat pipe array and the heat is transported over a low thermal resistance to other gas, or liquid.

The uses of heated gas, from the gas-gas heat exchanger, can be grouped into three categories

- Heat recovery in air conditioning systems
- Recovery of heat from a process exhaust stream to preheat air for space heating
- The recovery of heat for reuse in the process, such as preheating of combustion air

The flue gases from a bakery are used for waste heat recovery, using a loop thermosyphon heat exchanger (Dube et al., 2000). By installing the system, the heat recovered from the flue gas can be used to heat up the proofing oven. This cut out the gas previously needed for the heating of the proofing oven. The savings in running cost would result in a payback period (of the initial capital cost) of about one and a half years.

Space applications

Satellites commonly use heat pipes for thermal management, since the capillary wick structure provides the liquid return in the very low-gravity environment. A satellite with one surface facing the sun and another facing deep space will naturally be hot on the sunny side

and cold on the other. Using heat pipes can help to establish temperature flattening over the satellite.

Solar heating systems

Solar energy can be absorbed through a solar collector and thermosyphons or heat pipes can be used to transport the heat to the water tank or geyser where heating of the water can take place. Another use is to install a bank of solar collector/thermosyphons at a residence to heat the interior air in winter via solar irradiation. During the night, the thermosyphons will act as thermal diodes since the heat can now only be transported from the inside to the outside through conduction over the axial length.

The use of capillary pumped heat pipes integrated to flat solar collectors have been proposed and evaluated (Bazzo et al., 2000). This design consists of an aluminium tube with fine circumferential grooves machined on its inner surface to provide the capillary action. There is also an insert in the tube to direct the fluid towards the inside of the aluminium tube and hence the grooves. This capillary pump is connected to a solar collector, which is a copper plate with a glass panel above it. The heat that collects in the copper plate is conducted towards the heat pipe evaporator, where the working fluid (acetone) is heated. The condenser zone is located in the water tank where water is to be heated.

Ovens and furnaces

One of the first applications of thermosyphons was in baking ovens (1867). Normal flame-heated baking ovens warmed the firebrick in the firebox, through which heat was conducted into the baking chamber, to prevent contamination of the food with the combustion products. Using the thermosyphons, energy saving of 25% or more was realised and the chamber had a more uniform temperature.

The use of heat pipes for the cooling of arc furnace electrodes have also been proposed (Bullerschen, 1991). Water cooled metal shanks have been introduced for the reduction of graphite consumption in electric arc furnaces. The forced water flow through the shank creates a safety risk, as it induces extra stress on the electrodes and a burst or water leak can be potentially disastrous since a vapour explosion can take place if water flows into the molten metal region. By using a heat pipe the risk of a failure in the first instance is reduced and secondly, should a failure occur, an explosion is highly unlikely to result. Two alternatives were investigated. A copper-water heat pipe in the shank was modelled

numerically and gave the best results from a heat transfer point of view, while sodium filled steel would be a safer option, although more expensive and less effective.

2.2 CASTING

The literature study relating to casting is presented in two categories. Firstly there is a section that considers the modelling of the casting process (inside the mould cavity), phenomena such as the flow of molten metal into the mould cavity, solidification and internal heat transfer through convection and conduction in the casting. Secondly, the heat transfer between the casting and mould surfaces needs consideration, since the heat transferred from the casting to the mould will determine the mould temperature.

2.2.1 MODELING OF THE CASTING PROCESS (INSIDE MOULD CAVITY)

There are essentially two types of models associated with the casting process of metal, namely micro- and macro models. Micro models take into account metallurgical effects, such as prediction of crystallic formations, macrosegregation and material structures, caused by flow and heat transfer. Macro models consider continuum type control volumes and the conventional energy, momentum and continuity equations. Stefanescu et al (1990) suggested that a combination of both macroscopic and microscopic models is needed to accurately describe the solidification kinetics of castings.

When a molten metal is cast into a (cooler) mould, heat transfer takes place from the hot metal outwards to the mould and a temperature gradient exists. The metal will start to solidify at its outer regions where the temperature is the coolest. An inwardly moving solidification front is created. The difference between the solidification of a pure metal and an alloy, is the fact that a two-phase (solid-liquid) or 'mushy' zone exists in a solidifying alloy. The reason for the mushy zone is that depending on the chemical composition, there is a temperature range (between the solidus and liquidus temperatures) in which solid dendrites and interdendritic liquid co-exist. A common way to treat the mushy zone is as a porous solid structure that is saturated with liquid. Two aspects that seem common to all alloys are:

- The existence of a finite freezing range
- The formation of a mushy zone during solidification

Prescott and Incropera (1996) analysed the convection heat and mass transfer in alloy solidification, dislocations and non-uniform distributions of chemical composition and the formation of porosities and hot tears. The temperature gradient that exists during metal solidification causes density changes, and therefore buoyancy forces exists which can create fluid motion and convection. In a side chilled casting, the thermally induced density gradient is perpendicular to the gravitational body force and hence convection occurs. Except for the

thermally driven buoyancy forces, there are also ***solutal*** buoyancy forces. Solutal buoyancy forces only exist in the mushy zone, where a mixture of solid and liquid is present. Usually, the density of the solid is somewhat higher than that of the liquid at the same temperature (with ice being an exception), so that depending on the solid liquid ratio at a specific position in the mushy zone, pressure gradients exist. Depending on the alloy constituents and their density properties in the liquid and solid form, the buoyancy driven forces will either augment or oppose the thermally driven buoyancy forces. For an Al-4.5%wt Cu alloy, these forces will augment one another. For a Pb-19%wt Sn alloy, the forces will however oppose one another. Although the solutal buoyancy forces originates in the mushy zone, the effect of their eddies will be transported into the pure liquid zone. Since visualisation of flow patterns in solidifying metal is difficult to achieve, they have experimented with transparent analog alloys, such as salt – water solutions. The solidification of an H_2O-2%wt was for instance studied. They constructed a mathematical model, using continuity, momentum energy and species equations in the three zones of interest. Their theoretical results showed good qualitative agreement with the experimental results, but good accuracy was still illusive due to the complexity of the problem. It is noted that the incorporation of microscopic phenomena into the macroscopic convection models needs to be addressed in an effort to improve results.

According to Stefanescu et al. (1990), the microscopic approach should for instance be able to predict metallurgical properties such as bainitic, pearlitic or martensitic structures (for iron – carbon alloys). One of the main problems to couple the micro and macro models is because of the latent heat during solidification. The calculation of the 'evolution of fraction of solid' needs to be considered. They developed a latent heat method of solving the heat source term in the conduction equation and compared it to other methods. This method apparently had a more accurate prediction of the enthalpy evolution throughout the castng. It is suggested that the fraction of solid is dependant on the specific alloy used and the conditions that the mould is filled at and therefore each foundry should use its own measured data to get the most accurate results.

Two popular numerical methods to model the process of filling the mould with metal and the associated heat transfer during casting are the finite difference method (FDM) and the finite element method (FEM). Lally et al. (1990) investigated a number of solution strategies, using finite difference techniques, for heat flow models of continuous casting processes which were compared for interfacing with optimisation algorithms.

Usmani et al. (1992) used a finite element method for mould filling and heat transfer in metal castings. The Taylor-Galerkin method has been used to model the heat transfer during filling (because of its advection dominated nature). They focus on the fact that the way in which a

mould is filled has important consequences on the quality of the finished casting. The primary benefit of a mould filling simulation is that it will provide a more realistic, non uniform temperature distribution when the casting mould is filled so that better initial values can be used to model the rest of the solidification process, once the mould is filled. They ignored turbulence though, arguing that the low Prandtl numbers of liquid metals causes low turbulence effects. In this type of analysis, where liquid metal is pumped into a cavity and the volume increases with time until it is filled, the relevant nodes have to be 'connected' at the right times. This is called fluid front tracking. A 'pseudo-concentration' function was used to track the fluid surface. Von Karman's law of the wall is used to obtain the flow boundary conditions near the walls of the mould. The theoretical model was tested by comparing heat transfer and the fluid flow front between two parallel plates for experimental and theoretical cases. They found reasonable and stable results, and extended the model for the filling of general shapes.

Gethin *et al.* (1992) also considered a finite element model for pressurised solidification in the squeeze casting process. The effect of pressure on the solidus and liquidus temperatures were included in the model, but it only had a marginal effect on the solidification process.

H[tu and Ilinca (1999) have also performed a relatively in depth FEM casting simulation. Their model differed from that of Usmani et al. since it used a transition zone for the front tracking (including a mushy zone) and not just a step function approach. Wall boundary conditions are determined by the Chezy law. They modelled three cases:

- The collapse of a water column into a horizontal space – this was compared (visually) to an experiment and very good comparison was achieved
- The filling and solidification of a square plate (100 x 200 x 5 mm) – temperatures in the mould were measured and compared to theoretical temperatures and good agreement was obtained
- The filling and solidification of an engine piston was modelled. Realistic theoretical results were obtained but no experimental verification was done

The incorporation of turbulent fluid flow and heat transfer into finite element models of castings has been investigated (Thomas and Najjar, 1991). Steady state fluid flow within the liquid pool region in a continuous steel-slab casting is associated with a high Reynolds number and turbulence plays an important role. The incorporation of turbulence into a finite element model often leads to instabilities. By investigating various solution strategies, relaxation factors and meshes, guidelines were developed in order to achieve convergence for these types of problems. Reasonable agreement between theory and experiments were achieved.

Another numerical study of coupled turbulent flow and solidification was performed by Aboutalebi and Guthrie (1995). A two dimensional model was developed to account for coupled turbulent flow and heat transfer with solidification in the mould and sub-mould region of a steel slab caster. The k-ε model is used to model turbulence and the mushy zone is modelled with a modification of the standard enthalpy-porosity technique. The equations were solved numerically by using Patankar's SIMPLER control volume algorithm. The model was able to predict the experimental shell thickness with reasonable accuracy.

A relatively new method employed to model castings is by using boundary element methods (BEM). Rosindale and Davey (1998) have used BEM to create a transient model for the hot chamber injection system in the pressure die casting process. At this stage, it is not clear how well the boundary element method compares with the finite element method and where it may be advantageous to use.

2.2.2 HEAT TRANSFER ACROSS THE CASTING-MOULD INTERFACE

In order to model the heat transfer over the interface of two materials that are in perfect contact with one another, an equivalent interface thermal conductivity can be used (Poulikakos, 1994). For actual casting-mould interfaces though, the interfacial contact resistance is more complex. Thermal expansion and contraction often form gaps between the boundaries of the casting and the mould. These gaps are filled with air and other gases, and acts as thermal insulation, which has a significant impact on the heattransfer coefficient over the interface.

Loulou et al. (1998) have done research on the thermal contact resistance during the first stages of metal solidification. (They mention that a fast cooling rate promotes a fine grained structure and improves mechanical properties). On microscopic scale, a mould surface is not completely smooth and small asperities exist on the profile. When liquid metal is poured onto the mould surface, solidification starts from nucleation sites, which are the points where the peaks of the asperities are in contact with the liquid metal. (The valleys are not wetted due to surface tension) A solid film or shell develops therefore relatively quickly next to the mould boundary. As further solidification takes place the air gap starts to be formed as the casting is 'pulled' away from the mould surface. In order to determine the thermal resistance as a function of time, metal is cast into a mould and temperatures are measured, to determine the heat flow. The experimental data would be used to determine the thermal resistance, by using the 'residual functional minimisation' technique.

Griffiths (2000) modelled the interfacial heat transfer coefficient during unidirectional solidification of an aluminium alloy. A finite element model was used to predict the size of the gap with respect to time, and the effect of conduction over the air layer as well as radiation is included in the model. He compared theoretical and experimental results. The experiment consists of a cylindrical refractory fire tube mounted on a water cooled copper base, into which molten aluminium alloy is poured. The tube is heated to 900°C and left to cool to 780°C, to try and remove all trapped gasses. An Al-7%wt Si alloy, also at 780°C, is cast into the cavity. Heat is thus forced to flow only in the axial direction towards the copper chill (hence the term unidirectional solidification). The air gap and heat transfer coefficient between the casting and chill was modelled and compared to experimental results. The deviation between experimental and theoretical results is in the order of 50%.

Trovant and Argyropoulos (2000) performed an experimental study to determine the heat transfer coefficient between the casting and mould as a function of time. They cast aluminium and tin alloys in different types of moulds, such as copper, sand and graphite. The thermal resistance at the interface changes during four stages:

- Directly after the metal is poured into the mould
- A thin shell of solid metal exists next to the mould wall. Theheat is mainly transferred by conduction through intermittent contact at the asperities. (Also to a lesser extent by conduction and radiation through the 'gas valleys')
- Where the casting first pulls away from the mould. The metal and mould is not in direct contact anymore, but the asperities still dictate the heat transfer path from the metal to the mould
- When the gap reaches a size where the surface roughness doesn't play a significant heat transfer role anymore

They were able to relate the heat transfer coefficient to:

- The air gap size
- Roughness of the mould surface
- The conductivity of gas in the gap
- The thermo-physical properties of the metal and mould

CHAPTER 3 - Theory

This chapter will mainly discuss the theory and present applicable equations and correlations in support of the thesis.

3.1 THERMOSYPHON THEORY

For a thermosyphon, heat is transferred over the evaporator wall, through the evaporator internal section, the condenser internal section and the condenser walls.

3.1.1 HEAT TRANSFER OVER THE EVAPORATOR AND CONDENSER WALLS

Fourier's law of conduction through a cylindrical shell can be used to calculate the wall thermal resistances. For a shell with length L, inside diameter d_i, outside diameter d_o and conductivity k, the thermal resistance is:

$$R = \frac{\ln(d_o / d_i)}{2\pi kL} \tag{3.1}$$

3.1.2 CONDENSER INTERNAL HEAT TRANSFER

The simplest analysis to determine the internal heat transfer coefficient in the condenser section is to consider laminar film condensation on a vertical wall, as shown in figure 3.1.

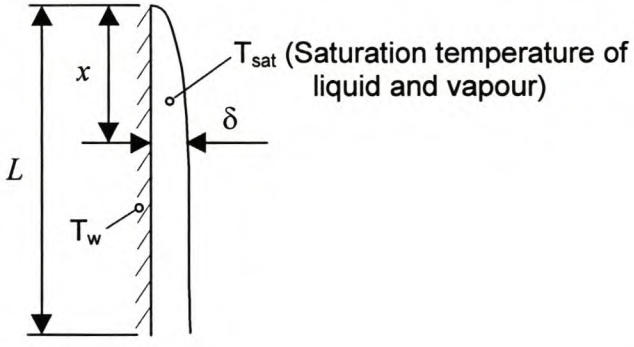

Figure 3.1 Laminar film condensation on a vertical wall

The film thickness for condensation on a vertical plate is given as (Mills, 1992):

$$\delta(x) = \left[\frac{4xk_l(T_{sat} - T_w)\nu_l}{h_{fg}g(\rho_l - \rho_v)} \right]^{1/4} \tag{3.2}$$

For laminar liquid flow, the heat transfer coefficient h is simply $h = \frac{k_l}{\delta}$ and substituting equation 3.2 into it yields:

$$h(x) = \left[\frac{h_{fg} g(\rho_l - \rho_v) k_l^3}{4x(T_{sat} - T_w)\nu_l} \right]^{1/4} \tag{3.3}$$

The average heat transfer coefficient over the total length L of the wall is:

$$\bar{h} = \frac{1}{L} \int_0^L h(x)dx = 0.943 \left[\frac{h_{fg} g(\rho_l - \rho_v) k_l^3}{L(T_{sat} - T_w)\nu_l} \right]^{1/4} \tag{3.4}$$

The thermal resistance for the film on the plate with area A is:

$$R = \frac{1}{\bar{h}A} \tag{3.5}$$

Equation 3.5 is limited by the fact that the film flow can become wavy laminar or turbulent relatively soon and the laminar assumption is no longer valid. In order to handle the transitions between these flow regimes, it is helpful to re-organise the equations into forms containing representative dimensionless numbers, where especially the Nusselt, Reynolds and Prandtl numbers play a significant role.

The Reynolds number (based on a hydraulic diameter) is defined as $\mathrm{Re} = \frac{\rho V d_h}{\mu}$, and the hydraulic diameter for a liquid film of thickness δ and width W is determined as:

$$d_h = \frac{4A_{cross\,section}}{\wp_{wetted}} = \frac{4\delta W}{W} = 4\delta \tag{3.6}$$

For a mass flow rate $\dot{m}$ for the liquid film, the Reynolds number simplifies to:

$$\mathrm{Re} = \frac{4\dot{m}}{\mu_l W} \tag{3.7}$$

In order to determine a relevant Nusselt number for condensation, it is found that the grouping of $\left(\frac{\nu_l^2}{g} \right)^{1/3}$ have the units of length, and the Nusselt number is defined as:

$$Nu = \frac{h(\nu_l^2 / g)^{1/3}}{k_l} \tag{3.8}$$

Instead of using equation 3.3, an analogous equation for laminar flow is found as:

$$Nu = \left(\frac{3}{4}\mathrm{Re}\right)^{-1/3} \tag{3.9}$$

Equation 3.9 is expected to hold for $Re < 30$

Using the same definitions, experimentally determined heat transfer correlations for the other two flow regimes (for water) are given by (Mills, 1992):

$$Nu = 0.822\,\mathrm{Re}^{-0.22};\quad for\quad 30 < \mathrm{Re} < 5800\,\mathrm{Pr}_l^{-1.06} \quad \text{(wavy laminar)} \tag{3.10}$$

$$Nu = 3.8\times10^{-3}\,\mathrm{Re}^{0.4}\,\mathrm{Pr}_l^{0.65};\quad for\quad 5800\,\mathrm{Pr}_l^{-1.06} < \mathrm{Re} \text{ (turbulent)} \tag{3.11}$$

There are other correlations as well available in the literature that are based on experimental results. One such a set of correlations for the condensation heat transfer coefficient in reflux condenser tubes, considering ten different working fluids, has been determined by Gross (1992) and is now presented:

For $\mathrm{Re}_c f_\phi < 2$:

$$h_c = 0.925(\mathrm{Re}_c\, f_\phi)^{-1/3}\frac{k_l}{\left(\dfrac{\mu_l^2}{\rho_l g(\rho_l-\rho_g)}\right)^{1/3}} \tag{3.12}$$

For $2 \le \mathrm{Re}_c\, f_\phi \le 1333\,\mathrm{Pr}_l^{-0.96}$:

$$h_c = 0.884(\mathrm{Re}_c\, f_\phi)^{-1/4}\frac{k_l}{\left(\dfrac{\mu_l^2}{\rho_l g(\rho_l-\rho_g)}\right)^{1/3}} \tag{3.13}$$

For $1333\,\mathrm{Pr}_l^{-0.96} < \mathrm{Re}_c\, f_\phi$:

$$h_c = 0.044\,\mathrm{Pr}_l^{0.4}(\mathrm{Re}_c\, f_\phi)^{1/6}\frac{k_l}{\left(\dfrac{\mu_l^2}{\rho_l g(\rho_l-\rho_g)}\right)^{1/3}} \tag{3.14}$$

where;

$$\mathrm{Re}_c = \frac{\dot{Q}}{\pi d_i \mu_l h_{fg}} \tag{3.15}$$

and

$$f_\phi = 1 \quad (vertical\ operation); \qquad f_\phi = \frac{2.87}{\cos\phi}\left(\frac{d_i}{L_c}\right) \quad (inclined\ operation) \tag{3.16}$$

ϕ is the inclination angle, where $\phi = 0°$ implies horizontal, and $\phi = 90°$ vertical operation.

For the theoretical analysis of condensation in an *inclined* thermosyphon (in other words going through a similar process that is used to derive equation 3.3), the film flow problem becomes two dimensional and has to be solved numerically. Such a two dimensional analysis on an inclined thermosyphon is performed in appendix D.

3.1.3 EVAPORATOR INTERNAL HEAT TRANSFER

Heat transfer in the evaporator section can basically take place through four mechanisms:

i) Film evaporation
ii) Film nucleate boiling
iii) Pool evaporation
iv) Pool boiling

Two-phase flow phenomena such as plug flow, stratified flow, wavy flow, slug flow or annular flow can cause complications to a lesser or greater extent (depending on the working fluid properties). But due to the complexities of this type of flow it is not attempted to theoretically model the process.

Film evaporation and pool evaporation usually only occurs at low heat fluxes. An exception is when subcooled liquid enters the evaporator from the falling liquid film that forms in the condenser. The liquid may have to travel through a short distance before it becomes superheated and boiling starts to occur. For film evaporation, equation 3.9 to 3.11 can be used to determine the heat transfer coefficient.

Pool boiling

The boiling process is complex and difficult to model theoretically. Pool boiling heat transfer coefficients are therefore mostly given by experimentally determined correlations. The pool boiling is influenced by surface effects, the pool geometry, the heat flux and the fluid properties. It is difficult to find a general correlation that will be a good fit for all boiling pools. One attempt to produce a general pool boiling heat transfer coefficient, is reported by Whalley (1987) as:

$$h = 0.106 p_c^{0.69} \dot{q}''^{0.7} (1.8 p_R^{0.17} + 4 p_R^{1.2} + 10 p_R^{10}) \tag{3.17}$$

where p_c is the critical pressure in bar, $p_R = \frac{p}{p_c}$ and $\dot{q}''$ is the heat flux (W/m^2).

Equation 3.17 is reasonably well suited for large diameter pools but is not necessarily suited for thermosyphon pools which are smaller.

A relatively well known correlation, specifically developed for a two-phase thermosyphon (using water, ethanol and Freon 113 as working fluids) is presented by Shiraishi (1981) as:

$$h = 0.32 \frac{\rho_l^{0.65} k_l^{0.3} C_{pl}^{0.7} g^{0.2}}{\rho_v^{0.25} h_{fg}^{0.4} \mu_l^{0.1}} (P_i / P_a)^{0.23} (\dot{q}'')^{0.4} \tag{3.18}$$

where P_i is the internal thermosyphon pressure and P_a is the atmospheric pressure.

Stephan and Abdelsalam (1980) have presented a simpler correlation:

$$h = C_1 (\dot{q}'')^{0.745} \tag{3.19}$$

where the constant C_1 needs to be found for a specific working fluid. For ammonia it is given by:

$$C_1 = 0.3063 + 0.1214 P_i - 0.002336 P_i^2 \tag{3.20}$$

where P_i is the internal pressure measured in bar.

El-Genk and Saber (1997) proposes correlations for pool boiling, and divide the pool into three zones, namely natural convection, nucleate boiling and combined natural convection and nucleate boiling. For the pool region, a dimensionless parameter is defined as:

$$X = \psi Ra^{0.35} \mathrm{Pr}_l^{0.35} K_p^{0.7} \mathrm{Re}_v^{0.7} \tag{3.21}$$

where;

$$= \left(\frac{\rho_v}{\rho_l} \right)^{0.4} \left(\frac{P_i \nu_l}{\sigma} \left(\frac{\rho_l^2}{\sigma g (\rho_l - \rho_v)} \right)^{0.25} \right)^{0.25} \tag{3.22}$$

$$Ra = \frac{\beta g d_i^4 \dot{q}''_{ewi} C_{pl} \rho_l^2}{\mu_l k_l^2} \tag{3.23}$$

$$K_p = P L_m / \sigma \tag{3.24}$$

$$L_m = \left(\sigma \Big/ g(\rho_l - \rho_g) \right)^{0.5} \tag{3.25}$$

$$\mathrm{Re}_v = \frac{\dot{q}''_{ewi} L_m}{\rho_v h_{\mathrm{lg}} \nu_l} \tag{3.26}$$

If $X < 10^6$ (natural convection):

$$Nu_{(NC)} = 0.475 Ra^{0.35} (L_m / d_i)^{0.58} \tag{3.27}$$

where the Nusselt number is simply defined as $\frac{h d_i}{k_l}$

If $X > 2.1\times10^{7}$ (nucleate boiling):

$$Nu_{(NB)} = (1 + 4.95\psi)Nu_{KU}(L_m/d_i)^{-1} \tag{3.28}$$

where;

$$Nu_{KU} = 6.95\times10^{-4}\,\mathrm{Pr}_l^{0.35}\,\mathrm{Re}_v^{0.7}\,K_p^{0.7} \tag{3.29}$$

and if $10^{6} \le X \le 2.1\times10^{7}$ (combined natural convection and nucleate boiling):

$$Nu_{(CCNB)} = (Nu_{p(NC)}^{4} + Nu_{p(NB)}^{4})^{0.25} \tag{3.30}$$

Film boiling

Jialun et al. (1992) have proposed a correlation for film-averaged nucleate boiling, based solely on their own data, as:

$$h_{lf} = 0.0062C_2^{-1.2}\,\mathrm{Re}_{fa}^{0.4}\,\mathrm{Pr}_l^{1.25}\,k_l(\nu_l^2/g)^{-1/3} \tag{3.31}$$

where the film averaged Reynolds number is given as:

$$\mathrm{Re}_{fa} = 4\dot{q}''_{ewi}L_f/\mu_l h_{fg} \tag{3.32}$$

and

$$C_2 = \frac{1.5\left(1-\left(\frac{L_p}{L_e}\right)^{2/3}\right)}{\left(1-\frac{L_p}{L_e}\right)^{2/3}} \tag{3.33}$$

L_f is the length of the film subject to boiling.

El-Genk and Saber (1998) have also proposed correlations for the film region inside the evaporator, much in the same way as they did for the pool. Firstly, a dimensionless parameter is defined as:

$$\eta = \mathrm{Re}_x\,K_p^2\,\mathrm{Re}_v^2/\mathrm{Pr}_l \tag{3.34}$$

where

$$\mathrm{Re}_x = \frac{4\dot{q}''_{ewi}(L_e - x)}{h_{fg}\mu_l} \tag{3.35}$$

and x is the position on the film starting from the top of the evaporator.

If $\eta < 10^{9}$ (natural convection):

$$Nu_{(NC)} = (4/3)^{1/3}\,\mathrm{Re}_x^{-1/3} \tag{3.36}$$

If $\eta > 2.7\times10^{10}$ (nucleate boiling):

$$Nu_{(NB)} = 1.115\times10^{-3} N_{\mu f}^{0.33} \mathrm{Pr}_l^{0.35} K_p^{0.7} \mathrm{Re}_v^{0.7} \tag{3.37}$$

and if $10^9 \le \eta \le 2.7\times10^{10}$ (combined natural convection and nucleate boiling):

$$Nu_{(CCNB)} = (Nu_{ef(NC)}^3 + Nu_{ef(NB)}^3)^{1/3} \tag{3.38}$$

where in this case, the Nusselt number is defined as $\frac{h_{ef} L_m}{k_l}$.

The heat transfer correlations given by El-Genk for both the liquid pool and film regions in the evaporator, was determined for vertical operation only. Therefore, the overall heat transfer coefficient determined by these correlations can be modified for inclined cases by an equation of Pioro (1985):

$$h_{inclined} = 0.61e^{0.5(\sin\phi)^4} \times h_{vertical} \tag{3.39}$$

Minimum liquid fill requirement

Faghri (1995) presents a simplified analysis to determine the minimum liquid film volume. If the assumption is made that the minimum fill volume is only that required to maintain the liquid film on the walls of the (vertical) thermosyphon, the minimum volume can be calculated as (where L_a is the length of the adiabatic section of the thermosyphon):

$$V_{\min} = \left[\frac{4}{5}(L_c + L_e) + L_a\right]\left[\frac{3\dot{Q}\mu_l(\pi d_i)^2}{\rho_l^2 g h_{fg}}\right]^{1/3} \tag{3.40}$$

3.2 HEAT PIPE THEORY

The cylindrical heat pipe differs from the thermosyphon because of the capillary wick structure that is included for liquid return to the evaporator. One of the features of the heat pipe is that it can function in a gravity free environment, horizontally or against gravity. Since the amount of heat transfer is directly related to the amount of liquid that evaporates and condenses, it is necessary to analyse the capillary pumping capability of the wick, and not just the heat transfer that takes place.

3.2.1 HEAT TRANSFER IN HEAT PIPES

Condenser internal heat transfer

The condenser heat transfer analysis is different from that of the thermosyphon, since instead of having a falling liquid film that grows thicker as it runs downwards there is a liquid filled wick of uniform width over the total condenser length. Different types of wick structures requires different analysis. For screen mesh wicks, there are two ways to determine the effective thermal conductivity.

Defining the voidage fraction as (Dunn and Reay, 1994):

$$\varepsilon = \frac{Volume\ of\ working\ fluid\ in\ wick}{Total\ volume\ of\ wick} \tag{3.41}$$

and assuming that the wick and working fluid are effectively in parallel, the effective thermal conductivity of the wick can be written as a combination of the solid (mesh) and liquid (working fluid) conductivities:

$$k_w = (1-\varepsilon)k_s + \varepsilon k_l \tag{3.42}$$

The second method is to assume that the fluid and the solid are effectively in series, with

$$k_w = \frac{1}{\frac{1-\varepsilon}{k_s} + \frac{\varepsilon}{k_l}} \tag{3.43}$$

The second method is expected to be more appropriate for two or more mesh layers next to one another.

Faghri (1995) gives an equation for the effective thermal conductivity of a sintered metal powder wick, as:

$$k_w = \left(\frac{2 + k_l/k_s - 2\varphi(1-k_l/k_s)}{2 + k_l/k_s + \varphi(1-k_l/k_s)} \right) \tag{3.44}$$

where φ is the wick porosity.

Evaporator internal heat transfer

Heat pipes are usually designed to have very little excess working fluid during operation, so that pool boiling does not really play a role. Because of the wick structure, there is also no liquid film in the evaporator as is the case with the thermosyphon, but a liquid filled wick, just as is the case in the condenser. Nucleate boiling does seem to play a role, but no general correlations could be found to include the boiling heat transfer equations into the heat

transfer analysis as well. It was decided for this thesis to also use the effective thermal conductivity of the wick structure, as was done for the condenser end.

3.2.2 LIQUID TRANSPORT IN THE WICK

When a tube of radius r is inserted into liquid and there is a gas, such as ambient air, surrounding the liquid, there will be a density gradient between the high density liquid and the low density gas. This will create a force per unit length of $F' = \sigma \cos\theta$ all around the internal diameter where the liquid, wall and gas come together, so that a capillary force F_{cap} exists, pulling the liquid into the tube:

$$F_{cap} = \sigma \cos\theta (2\pi r) \tag{3.45}$$

For a vertical tube in a gravity field, liquid will be pulled up to a height h. The mass of this liquid plug will be $\pi r^2 h \rho_l$ and therefore the force exerted by the gravity will be:

$$F_{grav} = \pi r^2 h \rho_l g \tag{3.46}$$

For equilibrium the capillary force and the gravity force must be equal, so that the capillary height is found to be:

$$h = \frac{2\sigma \cos\theta}{r \rho_l g} \tag{3.47}$$

It is common to express the effect of capillary force as a pressure difference over the liquid plug. Noticing that the pressure difference over this column of liquid is given by $\Delta P = \rho_l g h$ equation 3.47 can be re-written as:

$$\Delta P = \frac{2\sigma \cos\theta}{r} \tag{3.48}$$

The capillary pressure difference supplies the driving force to return the liquid to the evaporator section. For a general heat pipe operating at an angle ϕ (measured from the horizontal plane) in a gravity field, there are three pressure heads that will have to be overcomed by the capillary pressure head, namely the gravity pressure head, the flow resistance pressure head of the liquid and the frictional pressure head for the vapour flow resistance.

The capillary pressure head (ΔP_c)

This is similar to equation 3.48, where r_{eff} depends on the wick structure used.

$$\Delta P_c = \frac{2\sigma \cos\theta}{r_{eff}} \tag{3.49}$$

The gravity pressure head (ΔP_g)

This is simply given as:

$$\Delta P_g = \rho_l g L_{eff} \sin\phi \tag{3.50}$$

where L_{eff} is the effective length over which the fluid has to be transported.

The liquid flow resistance pressure head (ΔP_l)

This pressure head is associated with moving the fluid through the pores and channels of the wick. It can be expected that the higher the mass flow rate, the higher the pressure drop would be. According to Darcy's law (Dunn and Reay, 1994):

$$\Delta P_l = \frac{\mu_l L_{eff} \dot{m}}{\rho_l \kappa A_{wick}} \tag{3.51}$$

where κ is the wick permeability and A_{wick} is the wick cross sectional area.

The vapour frictional pressure head (ΔP_v)

This pressure head is due to the frictional force that exists on the interface between the (counter current flowing) liquid and vapour. This is given as:

$$\Delta P_v = 4C_f \frac{L_{eff}}{d_v} \frac{\dot{m}^2}{\rho_v A_v^2} \tag{3.52}$$

where d_v and A_v are the diameter and area of the flow passage for the vapour and C_f is the coefficient of friction.

Liquid flow can take place if $\Delta P_c \geq \Delta P_g + \Delta P_l + \Delta P_v$, i.e. if:

$$\frac{2\sigma \cos\theta}{r_{eff}} \geq \rho_l g L_{eff} \sin\phi + \frac{\mu_l L_{eff} \dot{m}}{\rho_l \kappa A_{wick}} + 4C_f \frac{L_{eff}}{d_v} \frac{\dot{m}^2}{\rho_v A_v^2} \tag{3.53}$$

For a specific wick structure, working fluid, operating temperature and inclination angle, the only variable in equation 3.51 is the mass flow rate, $\dot{m}$. Equation 3.51 is a quadratic equation and there will thus be a maximum mass flow rate that the wick will be able to return to the condenser. The amount of heat transfer through the heat pipe is essentially given by:

$$\dot{Q} = \dot{m} h_{fg} \tag{3.54}$$

therefore, a maximum return mass flow rate directly translates to a maximum possible heat transfer rate. This is known as the capillary limit, which is usually the most important limiting factor for a heat pipe.

The theory of the other limits as shown in figure 3.2 is not discussed.

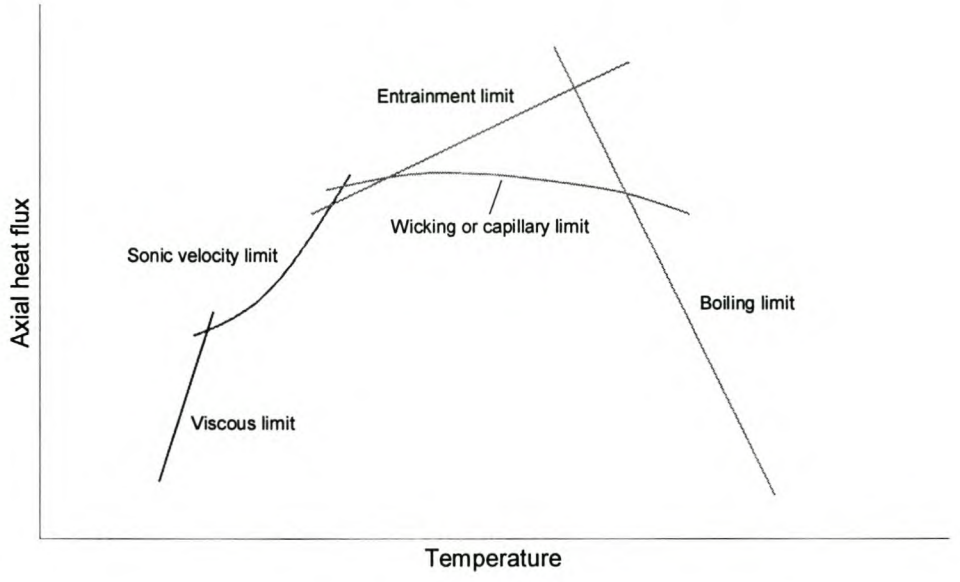

Figure 3.2 Limitations to heat transport in the heat pipe

3.3 CASTING THEORY

As noted in the literature study, the casting theories can be regarded as being for the casting process of inside the mould and the heat transfer over the casting-mould interface.

3.3.1 MODELING OF THE CASTING PROCESS (INSIDE MOULD CAVITY)

The internal dynamics for casting can be regarded as consisting of two stages, namely the filling of the mould and the solidification kinetics after the mould is filled. The basic principle to model both processes is to use the continuity, momentum and energy equations over discretised control volumes. For solidification of alloys the species or chemical composition equations need to be considered in the mushy zone. For filling, the amount filled has to be tracked with time, and relevant nodes have to be connected as the mould fills. Various methods can be used to model the casting dynamics such as finite difference methods (FDM), finite element methods (FEM), finite volume methods (FVM) and boundary element methods (BEM). The modelling and discretisation depends on the casting geometry, is laborious and tedious to do by hand and can be done using commercial computer simulation packages.

3.3.2 HEAT TRANSFER ACROSS THE CASTING-MOULD INTERFACE

Consider the case where two different materials are in perfect contact over the boundary as shown in figure 3.3. The equivalent interfacial conductivity associated with the distance Δx between the two nodes can be found as (Poulikakos, 1994):

$$k_{int} = \frac{\Delta x}{\frac{\Delta x_1}{k_1} + \frac{\Delta x_2}{k_2}} \tag{3.55}$$

which means that the approximate interfacial heat flux over the interface (taking the direction from node 1 to 2 as positive) is given by:

$$\dot{q}'' = \frac{k_{int}(T_1 - T_2)}{\Delta x} = \frac{(T_1 - T_2)}{\left(\frac{\Delta x_1}{k_1} + \frac{\Delta x_2}{k_2}\right)} \tag{3.56}$$

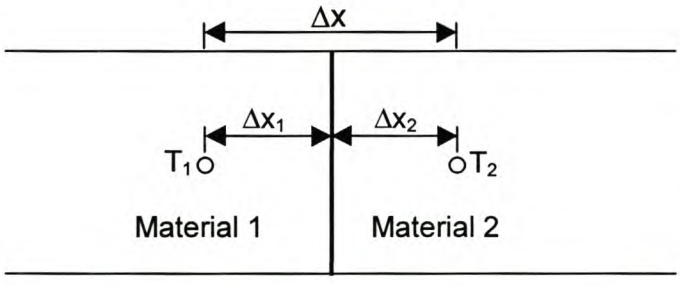

Figure 3.3 Two materials in perfect contact at their boundaries

During the filling of a casting, the movement of the melt over the casting surface can induce forced convection over the boundary. After filling, during casting solidification, there are 4 stages associated with the heat transfer over the boundary:

Stage 1

This stage is directly after the molten metal is positioned next to the mould wall. For this stage perfect contact between the casting and mould is assumed and equation 3.56 would be appropriate.

Stage 2

This stage is characterised by the solidification of a thin shell of metal next to the mould wall. At both the mould and metal surfaces at the interface there will now be asperities and there is thus intermittent contact between the peaks, through which heat is conducted. Conduction and radiation will also take place over the small air gaps between points of contact. This is also known as interfacial contact resistance, and is a function of the interfacial conductivity,

the contact pressure, the hardness and the roughness of the surfaces. The contact resistance should usually be determined experimentally.

Stage 3

This occurs when the casting first pulls away from the mould surface. There is no more contact between the casting and mould so that heat transfer only takes place through conduction and radiation across the air gap. What is important though is that during this stage the distance between the peaks of the mould and casting is of the same order as the amplitude of the surface roughness, so that the asperities will still dictate the *path* of heat flow from the metal to the mould.

Stage 4

This is the stage where the gap grows to a size where the asperities or surface roughness can effectively be neglected. If the thermal expansion is taken into account for a discretised model, the resistance between the casting and mould can be modelled relatively well as a function of the gap between the interfacial surfaces.

3.4 APPLICABLE SUPPORTING THEORY

This is theory used in the thesis that is not thermosyphon, heat pipe or casting theory, such as convection, radiation, finite elements and finite differences theory.

3.4.1 APPLICABLE CONVECTION THEORY

For the casting experiments in the thesis, parts of the moulds were exposed to the atmosphere, which implies that one of the mechanisms of heat transfer from the moulds to the atmosphere would be through natural convection. For other experimental work, heat transfer by forced convection to a fluid such as air or water had to be considered. This section will therefore discuss natural and forced convection theory.

Natural convection

Natural convection flow is a buoyancy-induced motion resulting from body forces acting on density gradients which arises from temperature gradients in the fluid. The theoretical approach usually starts by invoking the *Boussinesq* approximation for the continuity, momentum and energy equations and solving using similarity or numerical solutions.

For a horizontal plate (top face heated, bottom insulated), the following correlation (Kays & Crawford, 1993) can be used to determine natural convection coefficient:

$$Nu_L = 0.54(Gr_L \Pr)^{1/4} \quad for \quad 10^5 < Gr_L \Pr < 2\times10^7 \quad (laminar) \tag{3.57}$$

or

$$Nu_L = 0.14(Gr_L \Pr)^{1/3} \quad for \quad 2\times10^7 < Gr_L \Pr < 3\times10^{10} \quad (turbulent) \tag{3.58}$$

where Gr_L is the Grashof number (L is the shortest length of the plate), and is given by:

$$Gr_L = \frac{g\beta L^3 (T_{surface} - T_a)}{\nu^2} \tag{3.59}$$

where $\beta = \frac{1}{T_R}$ and $T_R = 0.5(T_{surface} + T_a)$ and the Nusselt number is based on the length of the plate, L.

For a heated rectangular horizontal plate facing downwards, with shorter side L and longer side W, (Mills 1992):

$$Nu_L = 6.5\left[1 + 0.38\frac{L}{W}\right]\left[(1+X)^{0.39} - X^{0.39}\right]Ra_L^{0.13} \tag{3.60}$$

where: $$X = 13.5Ra_L^{-0.16} \tag{3.61}$$

and Ra_L is the Rayleigh number based on L, with definition:

$$Ra_L = Gr_L \Pr \tag{3.62}$$

For a vertical plate with height L, the average Nusselt number for laminar and turbulent flows respectively is given as (Mills, 1992):

$$Nu_L = 0.68 + 0.67(Ra_L\Psi)^{1/4} \quad for \quad Ra_L \le 10^9 \tag{3.63}$$

$$Nu_L = 0.68 + 0.67(Ra_L\Psi)^{1/4}(1 + 1.6\times10^{-8}Ra_L\Psi)^{1/12} \quad for\ 10^9 \le Ra_L \le 10^{12} \tag{3.64}$$

with: $$\Psi = \left[1 + \left(\frac{0.492}{\Pr}\right)^{9/16}\right]^{-16/9} \tag{3.65}$$

or it can be expressed as a function of the position x along the wall (Kays & Crawford, 1993):

$$Nu_x = 0.508\left(\frac{\Pr^2}{0.952 + \Pr}\right)^{1/4} Gr_x^{1/4} \quad for \quad laminar \quad flow \tag{3.66}$$

$$Nu_x = 0.0295\left[\frac{\Pr^7}{(1 + 0.494\Pr^{2/3})^6}\right]^{1/15} Gr_x^{2/5} \quad for \quad turbulent \quad flow \tag{3.67}$$

The properties in the above equations are dependant on the temperature of the air. When calculating properties, the average of the surface temperature and the ambient temperature is used.

Forced convection

Two equations often used are the Gnielinski equation and the Dittus-Boelter equation.

The Dittus-Boelter equation is given as:

$$Nu = 0.023\,\mathrm{Re}^{0.8}\,\mathrm{Pr}^{0.4} \tag{3.68}$$

The Gnielinski equation is:

$$Nu = \frac{(f/8)(\mathrm{Re}-1000)\,\mathrm{Pr}}{1+12.7(f/8)^{1/2}(\mathrm{Pr}^{2/3}-1)} \tag{3.69}$$

where the friction factor f is given as:

$$f = \left(0.79\ln(\mathrm{Re}) - 1.64\right)^{-2} \tag{3.70}$$

The Nusselt and Reynolds numbers are based on the hydraulic diameter of the duct through which the convective fluid flows. The Gnielinski equation is expected to be more accurate in general, since it also includes the friction factor.

3.4.2 APPLICABLE RADIATION THEORY

Radiation had to be considered for the heat transfer from the surfaces of the moulds exposed to the environment. All surfaces are assumed to be grey and diffuse. The most general equation between a number of N grey and diffuse surfaces, is given as (Modest, 1993):

$$\frac{\dot{q}_i''}{\varepsilon_i} - \sum_{j=1}^{N}\left(\frac{1}{\varepsilon_j}-1\right)F_{i-j}\dot{q}_j'' + H_{oi} = \sum_{j=1}^{N}F_{i-j}(E_{bi}-E_{bj}) \quad (\text{for } i = 1, 2, \ldots, \mathrm{N}) \tag{3.71}$$

where ε is the surface emissivity, F_{i-j} is the view factor between surfaces i and j, H_o denotes external radiation and E_b is the blackbody emissive power (heat flux emitted from a blackbody, in W/m^{2}K) at the temperature of the surface, given by (Modest, 1993):

$$E_b(T) = n^2\sigma T^4 \tag{3.72}$$

The temperature T is in Kelvin and usually $n = 1$ for ambient air. σ is the Stefan-Boltzman constant and has a value of 5.67×10^{-8} W/m^{2}K^4.

3.4.3 APPLICABLE FINITE DIFFERENCE THEORY

The modelling of the conduction heat transfer in the moulds used for the core cooling case (see sections 4.4, 5.4 and appendix C), is done using the finite difference method. This is a well known method and is regularly used to solve conduction heat transfer problems numerically. A plane or volume to be solved is discretised into a grid of nodes. The basis of this method is that it utilizes truncated Taylor terms – created by the conduction differential equation, to express the unknown temperature of a node on the grid at a certain time and

position as a linear function of the surrounding node temperatures. These surrounding node temperatures can either be from the previous time step, (explicit method), or from the current time step (implicit method). When using the explicit method, the surrounding temperatures from the previous time step are already known. The implicit method implies that these temperatures are not known and therefore a set of equations have to be solved simultaneously. It is thus easier to get answers using the explicit method, but it becomes unstable for larger time steps. The implicit method is more involved but is unconditionally stable and much larger time steps can be used, which may save processing time. The Crank-Nicholson scheme combines the explicit and implicit methods. Only the case of conduction in cylindrical co-ordinates is considered in this thesis. The general conduction equation (with no source term) in cylindrical co-ordinates is (Poulikakos, 1994):

$$\rho c \frac{\partial T}{\partial t} = k\left[\frac{1}{r}\frac{\partial}{\partial r}\left(r\frac{\partial T}{\partial r}\right)+\frac{1}{r^2}\frac{\partial^2 T}{\partial \theta^2}+\frac{\partial^2 T}{\partial z^2}\right] \tag{3.73}$$

where r denotes the radial axis, z the axial axis and θ the angle of rotation. When the heat load is symmetrical though, equation 3.73 doesn't have to be a function of the angle θ, and reduces to:

$$\rho c \frac{\partial T}{\partial t} = k\left[\frac{1}{r}\frac{\partial}{\partial r}\left(r\frac{\partial T}{\partial r}\right)+\frac{\partial^2 T}{\partial z^2}\right] \tag{3.74}$$

On performing the full differentiation and providing for possible anisotropic material properties, equation 3.74 becomes:

$$\rho c \frac{\partial T}{\partial t} = \frac{k_r}{r}\frac{\partial T}{\partial r}+k_r\frac{\partial^2 T}{\partial r^2}+k_z\frac{\partial^2 T}{\partial z^2} \tag{3.75}$$

For a rectangular, equally spaced grid where j is a number between 1 and J associated with the position of a node along the radial axis r, and i is a number between 1 and I that denotes the position of a node along the axial direction z, the finite difference discretisation of equation 3.75 becomes:

$$\frac{\rho c}{\Delta t}\left(T_{i,j}^{P+1}-T_{i,j}^{P}\right)=\left[-\frac{k_r}{r\Delta r}-\frac{2k_r}{\Delta r^2}-\frac{2k_z}{\Delta z^2}\right]T_{i,j}^{\beta}+\left[\frac{k_r}{\Delta r^2}\right]T_{i,j-1}^{\beta}+\left[\frac{k_z}{\Delta z^2}\right]T_{i+1,j}^{\beta}$$
$$+\left[\frac{k_r}{r\Delta r}+\frac{k_r}{\Delta r^2}\right]T_{i,j+1}^{\beta}+\left[\frac{k_z}{\Delta z^2}\right]T_{i-1,j}^{\beta} \tag{3.76}$$

For the explicit method $\beta = P$, and for the implicit method $\beta = P + 1$, where P is the number that counts the time step. Δr, Δz and Δt are the size of discretisations for the radial direction, axial direction and time, respectively.

Equation 3.76 presents a problem at $r = 0$, since r is a denominator in the equation. To overcome this problem, it is known from Taylor's theorem that:

$$\frac{\partial T}{\partial r}(r,t) = \frac{\partial T}{\partial r}(0,t) + r\frac{\partial^2 T}{\partial r^2}(0,t) + Error(r^2) \tag{3.77}$$

and since the solution will be symmetric, $\frac{\partial T}{\partial r}(0,t) = 0$, so that in the case where $r \to 0$ and neglecting the error term, equation 3.77 becomes:

$$\frac{1}{r}\frac{\partial T}{\partial r}(r,t) = \frac{\partial^2 T}{\partial r^2}(r,t) \qquad \text{(for } r = 0 \text{ only)} \tag{3.78}$$

Substituting equation 3.78 into equation 3.74 yields:

$$\rho c\frac{\partial T}{\partial t} = 2k_r\frac{\partial^2 T}{\partial r^2} + k_z\frac{\partial^2 T}{\partial z^2} \quad \text{(for } r = 0 \text{ only)} \tag{3.79}$$

Therefore, if $r = 0$, the finite difference equation becomes:

$$\frac{\rho c}{\Delta t}\left(T_{i,j}^{P+1} - T_{i,j}^{P}\right) = \left[-\frac{4k_r}{\Delta r^2} - \frac{2k_z}{\Delta z^2}\right]T_{i,j}^{\beta} + \left[\frac{k_z}{\Delta z^2}\right]T_{i+1,j}^{\beta} + \left[\frac{4k_r}{\Delta r^2}\right]T_{i,j+1}^{\beta} + \left[\frac{k_z}{\Delta z^2}\right]T_{i-1,j}^{\beta} \tag{3.80}$$

which does not include the value of r at all.

The development and solution of equations including boundary conditions is done for the Core Cooling experimental case (see sections 4.4 and 5.4) in appendix C.

3.4.4 APPLICABLE FINITE ELEMENT THEORY

Finite element methods originated as a method of stress analysis, but can be utilised to solve problems in heat transfer, fluid flow, lubrication, electric and magnetic fields and others. In general, the finite element method models a structure as an assemblage of small parts (elements). Each element is of simple geometry and therefore easier to analyse than the actual structure. Thus a complicated solution is approximated by a model that consists of piecewise–continuous simple solutions. Usually, the smaller the element size, the better the approximation, but it also depends on the choice of elements used in the model, as well as the size of time steps used for transient models. There are a number of element types that can be used, such as 1 dimensional (rod element), 2 dimensional (plate, axial-symmetrical element), 3 dimensional (solid element) and so on. For conduction heat transfer, the objective is to find a set of equations of the form [C]{T} = {P}, where [C] is the conductivity matrix, {T} is the unknown node temperature vector and {P} is the thermal load vector.

There are three methods that can be used to find the contents of the matrix [C] and the vector {P}, namely:

- The direct method
- The variational method
- Weighed residual methods

Simple examples of using the direct method and variational method will be presented.

The direct method

Consider the simple uniform bar shown in figure 3.4. Let q be the heat flux per unit area, k the thermal conductivity, T the temperature, A the cross-sectional area and let the nodal heat flux be considered positive when directed into the bar at either end.

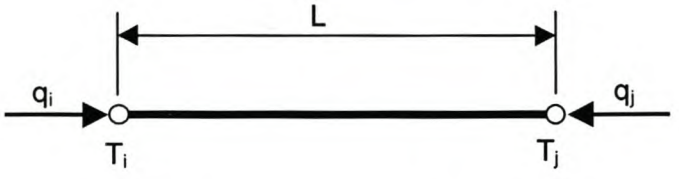

Figure 3.4 One dimensional bar with heat loads

Using Fourier's heat conduction equation, $q = -k\frac{dT}{ds}$, the heat flux into the bar at node i is (for steady state conditions):

$$q_i = \frac{k}{L}(T_i - T_j) \tag{3.81}$$

and the heat flux into the bar at node j is:

$$q_j = \frac{k}{L}(-T_i + T_j) \tag{3.82}$$

Rewriting these two equations in matrix form gives:

$$\frac{k}{L}\begin{bmatrix} 1 & -1 \\ -1 & 1 \end{bmatrix}\begin{bmatrix} T_i \\ T_j \end{bmatrix} = \begin{bmatrix} q_i \\ q_j \end{bmatrix} \tag{3.83}$$

which is of the form [C]{T} = {P}. For a discretised structure with N nodes, a number of N two-by-two matrices will result, which can then be joined together in an NxN matrix. Standard mathematical techniques such as Gauss-elimination (for linear systems) can be used to solve for the unknown temperature.

The direct method is easy to understand but becomes limited when complex structures need to be analysed. A more general approach is to make use of the variational method.

The variational method

The modern form of the Raleigh-Ritz approximation technique is the finite element method. Expressions for potential energy (known as functionals) are minimised so as to find the equilibrium configuration of a system.

As an example, consider the bar shown in figure 3.5:

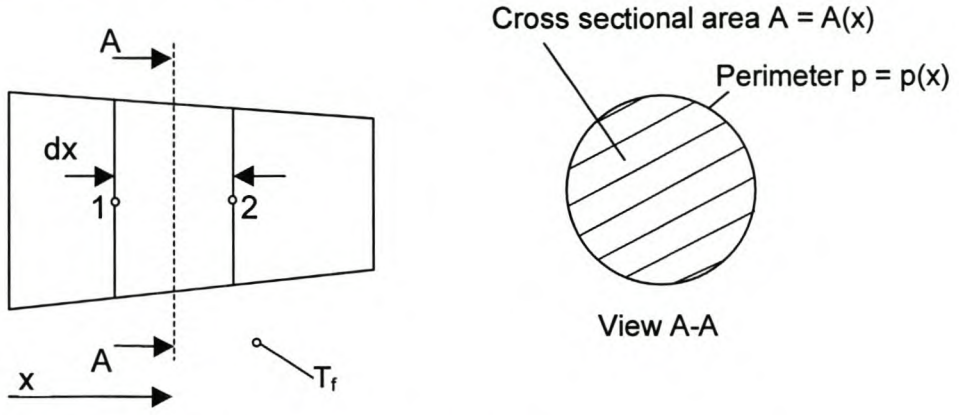

Figure 3.5 Bar with heat loads and convection boundary conditions

T_f is the temperature of the fluid surrounding the bar, and h is the heat transfer coefficient between the fluid and the bar surface. Assume that heat is internally generated at rate Q per unit volume. Performing a steady state energy balance over the control volume dx, yields the governing differential equation:

$$\frac{d}{dx}(Ak\frac{\partial T}{\partial x}) + QA + h(T_f - T)p = 0 \tag{3.84}$$

A finite element formulation can be developed from the following functional:

$$\Pi = \int\left[\frac{1}{2}Ak\left(\frac{\partial T}{\partial x}\right)^2 + \frac{1}{2}hpT^2 - (QA + hpT_f)T\right]dx \tag{3.85}$$

The above equation assumes that T is a continuous function. For the finite element discretisation over each element, T has to be expressed in matrix form, namely

$$T = [\mathbf{N}]\{\mathbf{T}_e\} \tag{3.86}$$

where $[\mathbf{N}]$ is generally known as the shape function matrix. The shape function matrix is necessary to interpolate the temperature between nodal temperatures, so that temperatures are piecewise continuous over the domain of each element.

For the two-node element in figure 3.4,

$$\{\mathbf{T}_e\} = \begin{bmatrix} T_1 \\ T_2 \end{bmatrix} \quad and \quad [\mathbf{N}] = \begin{bmatrix} (L-x)/L \\ x/L \end{bmatrix} \tag{3.87}$$

Substituting into equation 3.85, the functional for a single element becomes:

$$\Pi_e = \frac{1}{2}\{\mathbf{T}_e\}^T \int_0^L [\mathbf{N}_{,x}]^T Ak[\mathbf{N}_{,x}]dx\{\mathbf{T}_e\} + \frac{1}{2}\{\mathbf{T}_e\}^T \int_0^L [\mathbf{N}]^T hp[\mathbf{N}]dx\{\mathbf{T}_e\} - \{\mathbf{T}_e\}^T \int_0^L [\mathbf{N}]^T QAdx$$
$$- \{\mathbf{T}_e\}^T \int_0^L [\mathbf{N}]^T hpT_f dx \tag{3.88}$$

Furthermore,

$$\left\{\frac{\partial \Pi}{\partial \mathbf{T}_e}\right\} = \{\mathbf{0}\} \quad yields \quad ([\mathbf{k}] + [\mathbf{h}_{ls}])\{\mathbf{T}_e\} = \{\mathbf{r}_Q\} + \{\mathbf{r}_{ls}\} \tag{3.89}$$

where;

$$[\mathbf{k}] = \int_0^L [\mathbf{N}_{,x}]^T Ak[\mathbf{N}_{,x}]dx; \qquad [\mathbf{h}_{ls}] = \int_0^L [\mathbf{N}]^T hp[\mathbf{N}]dx \tag{3.90}$$

$$\{\mathbf{r}_Q\} = \int_0^L [\mathbf{N}]^T QAdx; \qquad \{\mathbf{r}_{ls}\} = \int_0^L [\mathbf{N}]^T hpT_f dx \tag{3.91}$$

For a structure consisting of numerous elements, the matrices for each element can be assembled, and a complete set of equations is then available, in the form of:

$$([\mathbf{K}] + [\mathbf{H}_{ls}])\{\mathbf{T}\} = \{\mathbf{R}\}; \tag{3.92}$$

where $[\mathbf{K}] = \sum[\mathbf{k}]$; $[\mathbf{H}_{ls}] = \sum[\mathbf{h}_{ls}]$; $\{\mathbf{T}\} = \sum\{\mathbf{T}_e\}$ and $\{\mathbf{R}\} = \sum\{\mathbf{r}_Q\} + \sum\{\mathbf{r}_{ls}\}$

CHAPTER 4 - Experimental Work

The experimental planning, procedures and equipment used are discussed in this chapter. (Experimental results are not discussed here but in Chapter 6). The experimental work is grouped into five sections:

- Determination of the heat pipe thermal characteristics (§4.1)
- Determination of the fin thermal characteristics (§4.2)
- Preheating of a die using external heating elements and heat pipes (henceforth referred to as the *Mould Heating Case*) (§4.3)
- Cooling of a core using a heat pipe and fins (henceforth referred to as the *Core Cooling Case*) (§4.4)
- Cooling of a casting mould using heat pipes and a water cooled heat sink (henceforth referred to as the *Mould Cooling Case*) (§4.5)

4.1 DETERMINATION OF HEAT PIPE THERMAL CHARACTERISTICS

4.1.1 HEAT PIPE DESCRIPTION AND SPECIFICATIONS

Two types of cylindrical heat pipes were utilised for the (casting) experimental work. They are supplied by a company specialising in the manufacturing of heat pipes, namely Thermacore International, and are of the following dimensions:

- Heat pipe with a 1/2" diameter and 12" length (Part number: IMC-E16012HT)
- Heat pipe with a 3/8" diameter and 8" length (Part number: IMC-E12008HT)

The heat pipes are manufactured from pure copper tubes, with a thickness of 0.46mm. The insides of these specific heat pipes are filled with a small amount of water at a low pressure, which acts as the working fluid. Inside the tube a double layer of phosphor bronze screen mesh is lined against the wall, and acts as the wick structure that transports liquid through capillary action. The thickness of one layer of screen mesh is 0.16mm, so that the total wick thickness is 0.32mm. The void volume of the mesh is 60%. (Thus the volume of the metal is only 40% of the total screen mesh volume – 60% will therefore be filled with water) The ends

of the heat pipe are sealed with a solder with a melting temperature of 296°C. Although this is the maximum allowable internal temperature, the manufacturers suggested that the temperature should not exceed 250°C, since the latent heat of evaporation of the water reduces significantly from this point onwards. These heat pipes are plated with a tin based material for cosmetic purposes, but in this case they are not plated, to prevent any possible effect that the plating may have on the thermal contact between the heat pipes and their surroundings.

Special heat pipe

The objective of this experiment is to determine the evaporator and co.ndenser heat transfer coefficients of the heat pipe, for different operating conditions. In order to do this, the heat transfer rate through the heat pipe as well as the internal temperatures (at the condenser and evaporator ends) need to be known. Because the standard heat pipes that were bought are closed off at the ends, it is not possible to measure their internal temperatures. Therefore a specially designed and manufactured heat pipe is required. This heat pipe is designed with "thermocouple wells", which are cylindrical inserts into which thermocouples can be placed to measure the internal temperature. Figures 4.1 and 4.2 show a diagram and photographs of the special heat pipe.

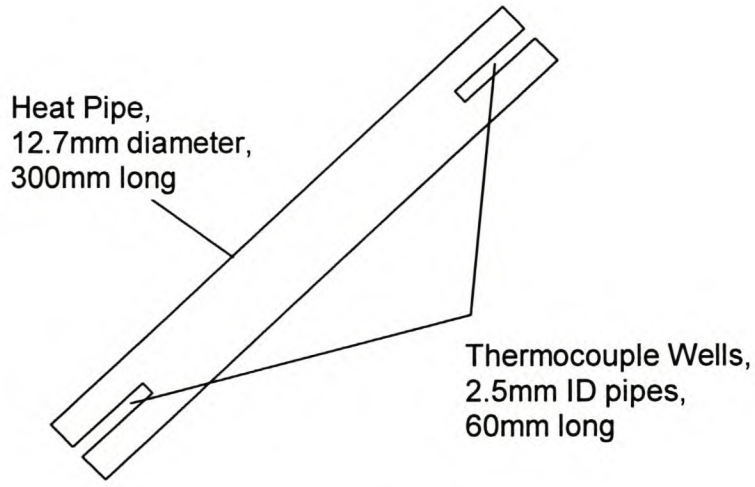

Figure 4.1 Schematic of special heat pipe

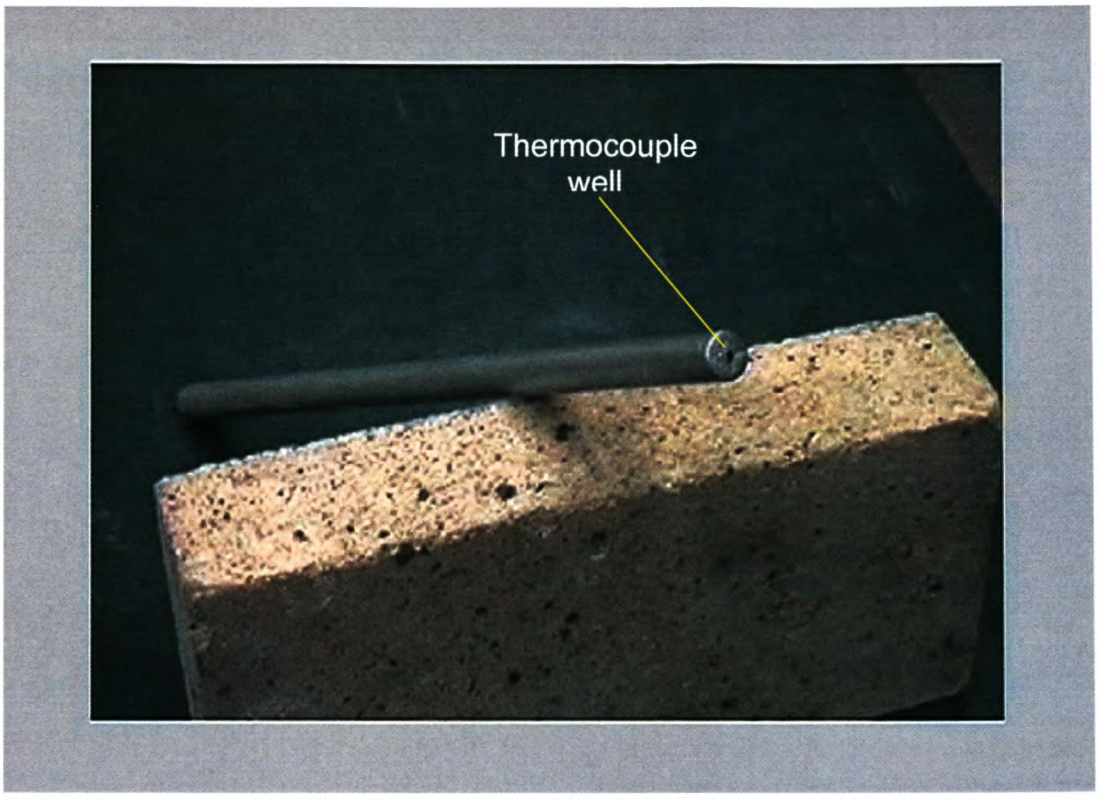

Figure 4.2.a The special heat pipe, with the thermocouple well opening shown

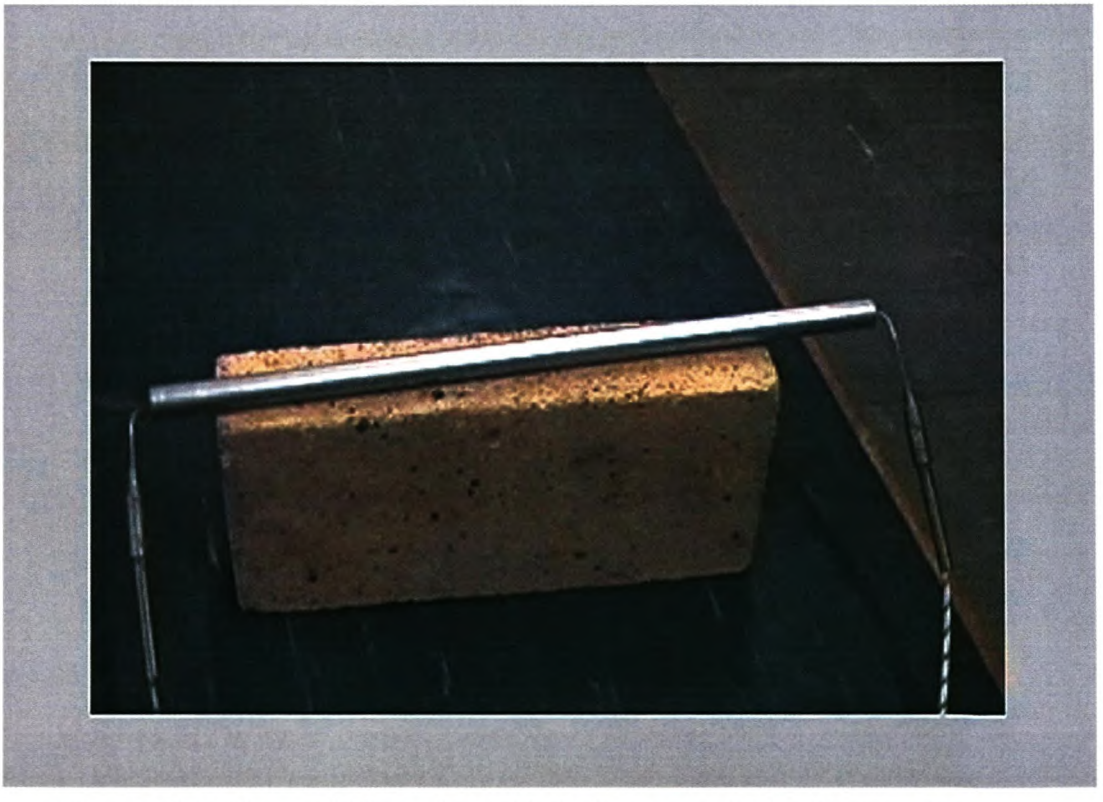

Figure 4.2.b The special heat pipe, with the thermocouples inside the wells

4.1.2 EXPERIMENTAL DESIGN AND SET-UP

In order to determine the heat transfer characteristics of the heat pipes the following requirements are considered:

- A suitable heat source and sink such that the heat transfer rate through the heat pipe can be accurately determined
- The internal temperature of the heat pipe must be measured during operation at both the evaporator and condensor ends
- The set-up must be able to function properly in vertical (bottom heating mode) operation as well as horizontal operation

Three ways of heating the evaporator end were considered. Firstly, heating by means of hot water or steam was considered. The problem with hot water is that the maximum temperature is limited to 100°C at standard atmospheric pressure. Since the temperatures of the experimental moulds were expected to be much higher than this (the melting temperature of tin is 232°C), higher heating temperatures are needed. Steam can be superheated to 250°C or more, but will be at a high pressure. This would necessitate high pressure equipment and invoke an unnecessary safety risk and high costs.

Secondly, it was considered to put the heat pipe in molten tin. The very high heat transfer coefficient between the molten metal and the heat pipe has the effect that the temperature on the evaporator wall will be very close to the temperature of the melt. The problem with this method is that it would be difficult to keep the tin molten and also to measure the heat loss from the melt and then there are also safety risks involved.

The third and chosen heating method considered was to make use of a cylindrical aluminium heating block. The block is heated by means of resistance wire that is wound around the circumference at equally spaced intervals. There is a 13.5 mm diameter hole in the centre, just a bit larger than the outside diameter of the heat pipe (12.7 mm). The heat pipe can then be placed inside the hole, and the gap is filled up with solder. It is known that good cohesion

(wetting) between solder and aluminium is not easily established, but in this case the only function of the solder is to fill the air gap and ensure good thermal contact. The heating block is shown schematically in figure 4.3.

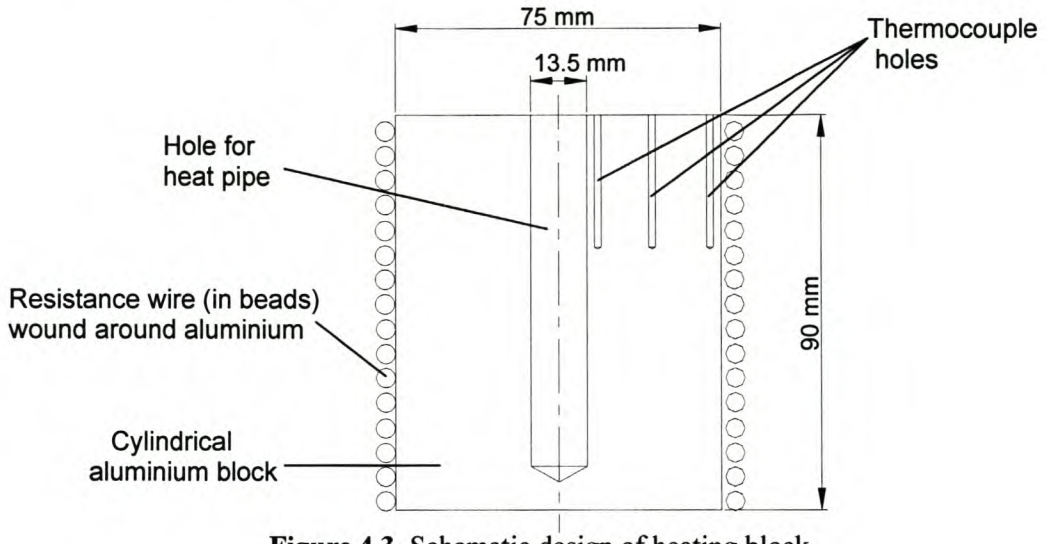

Figure 4.3 Schematic design of heating block

Three holes of 1.6 mm diameter are drilled into the block at diameters of 18 mm, 44 mm and 62 mm, so that the temperatures can be measured by thermocouples. The heat transfer rate into the heat pipe can be calculated using Fourier's law of conduction, if the thermal conductivity and the radial temperatures are known.

Two options were considered for the heat sink to cool the condenser end. The first option could be to use a cooling block, similar to the heating block at the evaporator end. The only drawback of this method is that it is difficult to get effective uniform cooling of the block, unlike is the case with heating. Furthermore, it is considered better if another type of cooling can be used, as diversity in measurement methods regarding the heat transfer rate should help to eliminate consistent error by using only one method. The second and chosen option is to make use of direct water cooling - typically water flowing through a cooling jacket over the heat pipe. It is relatively easy to provide uniform cooling with this method.

Two ways were considered to determine the heat transfer rate. One way would be to measure the temperature difference between the inlet and outlet water. Since the mass flow

rate of the cooling water has to be relatively high to increase the heat transfer coefficient between the heat pipe wall and the water, this temperature difference will not be very high (maximum about 0.5 °C). An 0.1 °C temperature measurement error will therefore result in a consistent error of 20% in the calculated heat transfer rate.

The second (and chosen) way is to pump a known mass of water in a closed loop through the cooling jacket. The temperature increase of the mass of water over time can then be used to calculate the heat transfer rate. If the heat losses to the atmosphere and the heat gain from the pump can be adjusted for accurately, the average heat transfer rate calculated by this method should be accurate. (Although more fluctuation is expected because of periodic temperature fluctuations in the mass of water, due to convection streams)

The way that the water enters the cooling jacket is important. As is seen from figure 4.4, a good way to design a jacket is to align the inlet flow direction along the axial direction of the heat pipe, so as to get an even distribution of cooling water around the heat pipe.

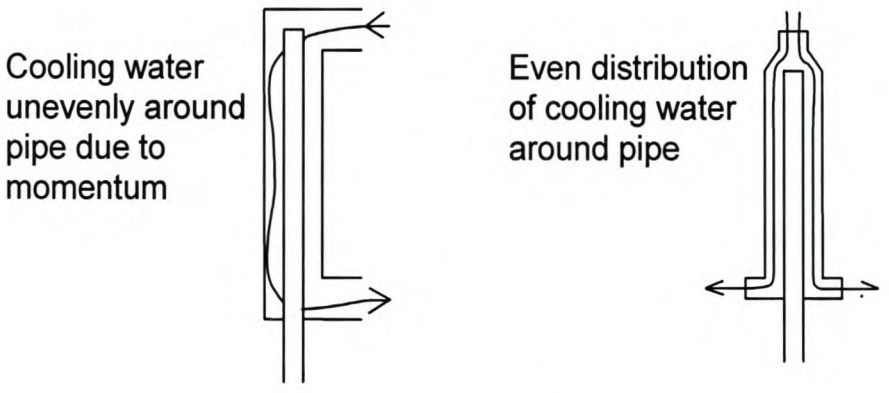

Figure 4.4 Conceptual designs of cooling jacket

The design of the cooling jacket is shown in figure 4.5

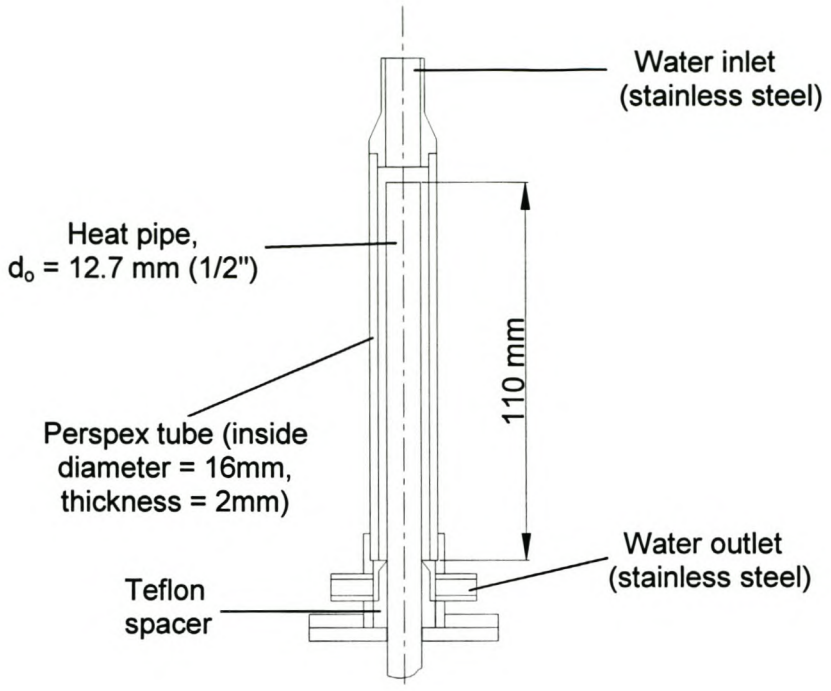

Figure 4.5 Schematic design of cooling jacket

The schematic lay-out of the experimental set-up is given in figure 4.6. Photographs of the experiments are shown in figure 4.7.

The measurements taken (as shown in figure 4.6) are:

T_1 Temperature of bulk water in tank (Thermocouple, type T)

T_2 Outside radial temperature of heating block at r = 31 mm (Thermocouple, type J)

T_3 Middle radial temperature of heating block at r = 22 mm (Thermocouple, type J)

T_4 Inner radial temperature of heating block at r = 9 mm (Thermocouple, type J)

T_5 Evaporator internal temperature of heat pipe (Thermocouple, type K)

T_6 Condenser internal temperature of heat pipe (Thermocouple, type K)

T_7 Ambient temperature (Thermocouple, type T)

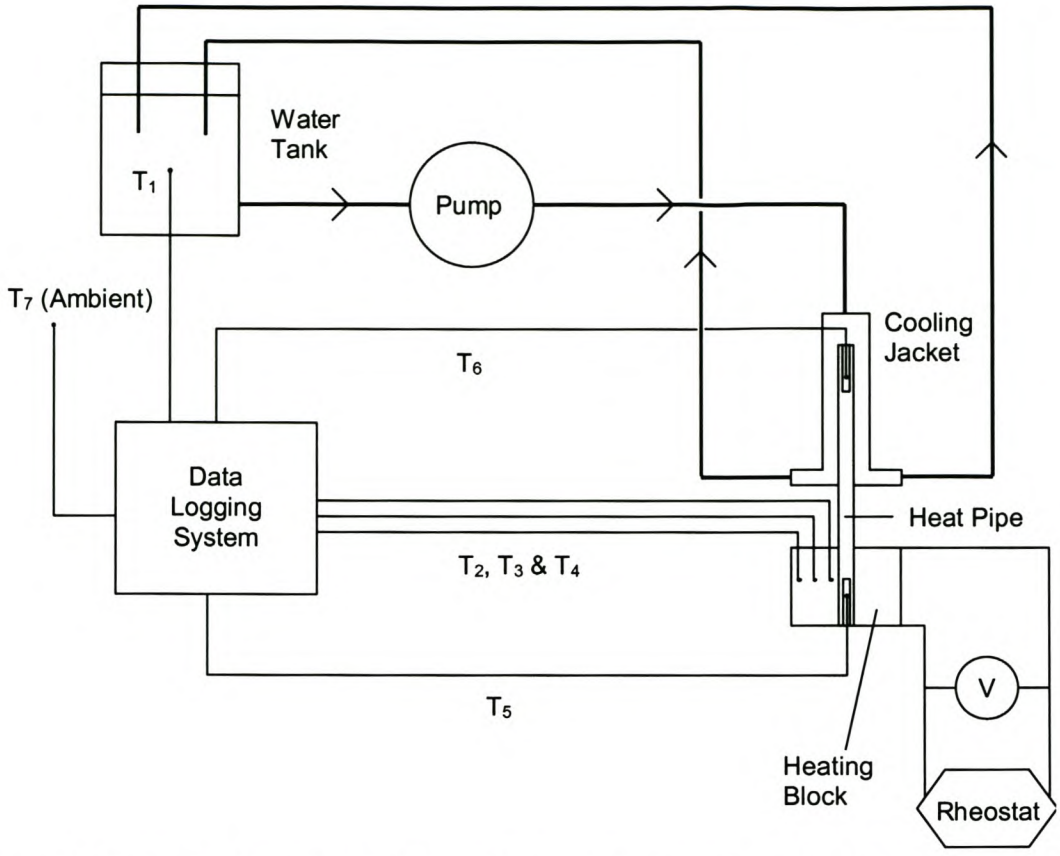

Figure 4.6 Schematic of experimental set-up for determination of heat pipe thermal characteristics

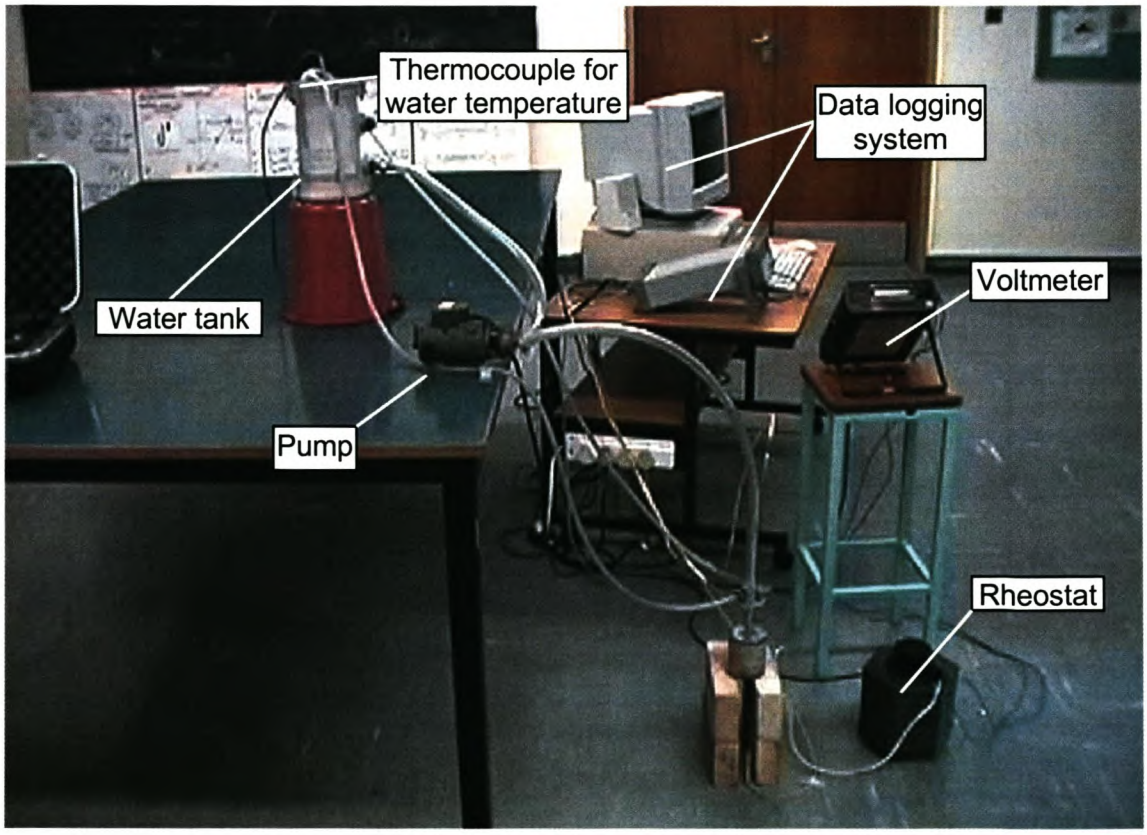

Figure 4.7.a Experimental set-up

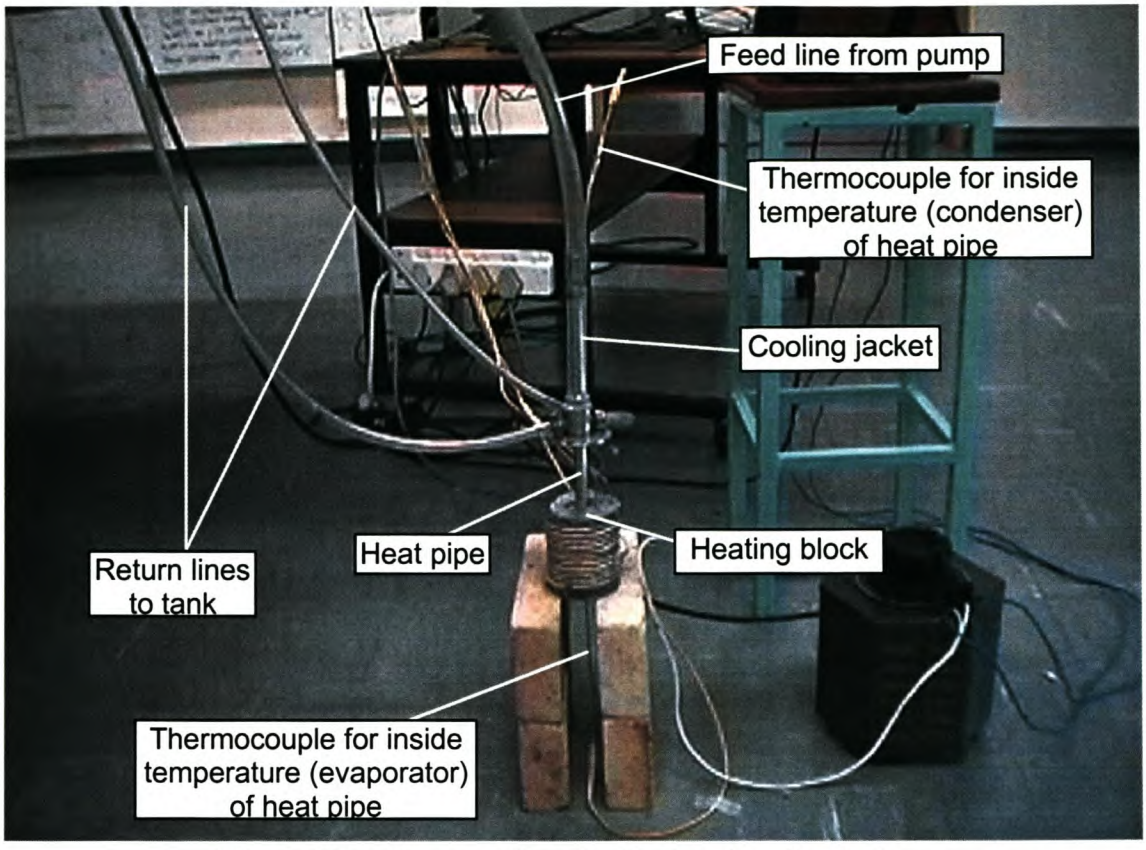

Figure 4.7.b Close up of heating block and cooling jacket

4.1.3 EXPERIMENTS PERFORMED

Mass flow rate of water through cooling jacket

To estimate the heat transfer coefficient between the heat pipe and the cooling water flowing through the jacket, the mass flow rate of the water is needed. An experiment was performed to determine the mass flow rate of the water for different temperatures. To measure the mass flow rates, water was pumped through the system, into a bucket. When the bucket is close to being filled, it is removed from underneath the water outlet. This process was timed with a stop watch. The mass of water in the bucket is weighed and the mass flow rate is calculated. This was done for 3 temperatures of water, at 58°C, 40°C and 22°C. The mass flow rates as a function of water temperature are shown in figure 4.8.

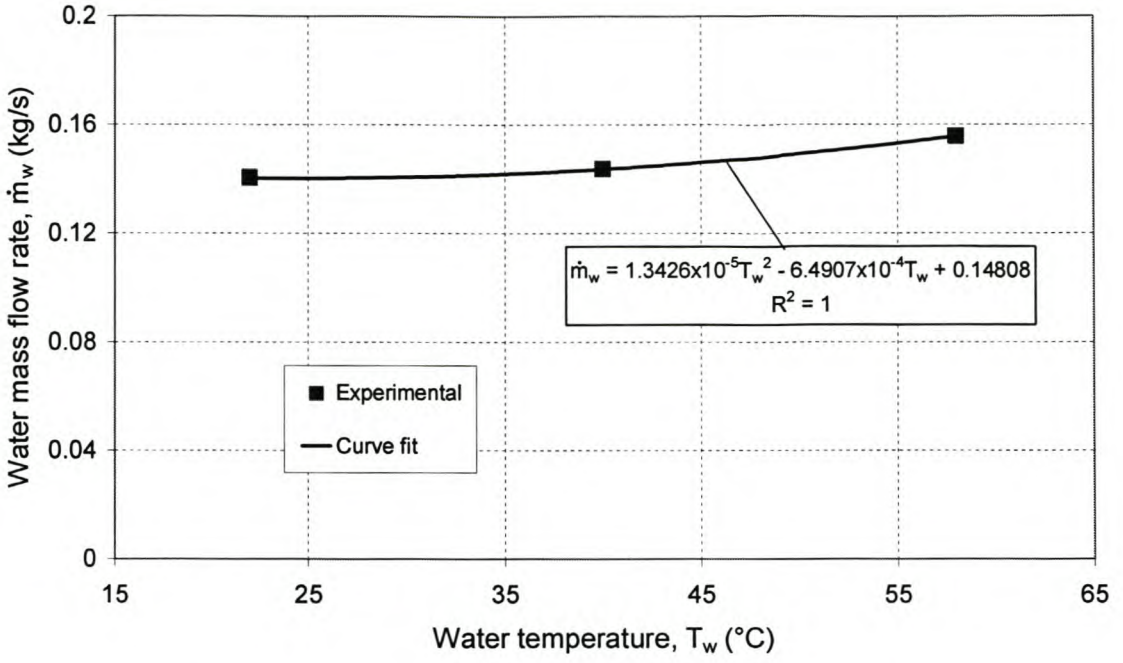

Figure 4.8 Mass flow rate of water as a function of temperature

Heat loss to the environment and heat gain from the pump

The tank and pipes through which the water is pumped, is not insulated and therefore heat losses to the environment would occur. Also, since the water is pumped in a closed cycle, the energy given to the water by the pump, ultimately has to be converted into heat – thus causing a temperature rise of the pumped water. An experiment was performed to determine the heat loss to the environment and heat gain from the pump, as a function of the difference between the water temperature and the ambient temperature. This was done by pumping water through the system with the evaporator end of the heat pipe covered with insulation material. In one case, water that is hotter than ambient was pumped until it reached a steady temperature. This was also done with water that is cooler than ambient. Figure 4.9 shows the temperatures as a function for these two cases. It can be derived that the heat gain from the pump to the water must be the same as the total heat loss to the environment from the water with a difference of about 8.5 °C between the water and ambient temperatures. Along each curve in figure 4.9 the rate of change of the temperature difference versus time, $\frac{d(T_{water} - T_{ambient})}{dt}$, can be found by considering the gradient of the curve. The gradient can

therefore be expressed as a function of the temperature difference. Since the ambient temperature can be considered relatively constant,

$$\frac{d(T_{water} - T_{ambient})}{dt} \approx \frac{d(T_{water})}{dt} \qquad (4.1)$$

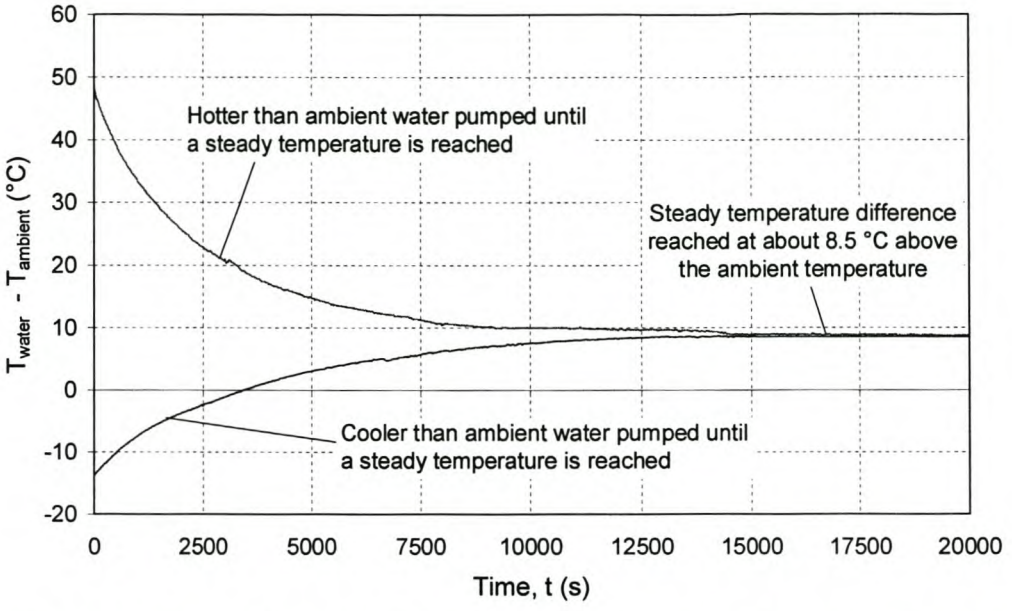

Figure 4.9 Temperatures of hotter and cooler than ambient pumped water as a function of time

The gradients on discretised sections of the curves in figure 4.9 were determined and are plotted versus the temperature difference in figure 4.10.

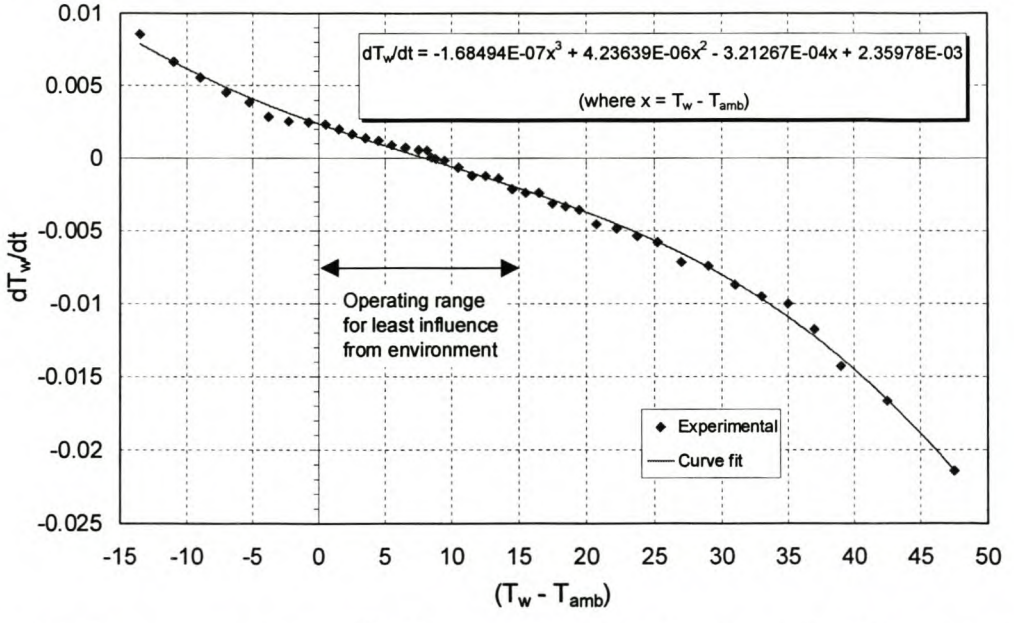

Figure 4.10 Temperature gradient $\frac{dT_w}{dt}$ for water plotted as a function of the difference between water and ambient temperatures

A curve fit is placed through the data points and it gives an equation for the (time based) temperature gradient as a function of the temperature difference between the water and ambient. The heat loss from or heat gain to the water can now be determined as:

$$\dot{Q}_{env} = m_w C_{p(water)} \frac{dT_w}{dt} \qquad (4.2)$$

The mass of the pumped water in the system is $m_w = 2.5\ kg$.

Heat pipe thermal characteristics

In order to determine the heat transfer coefficients at the evaporator and condensor ends of the heat pipe, the temperatures on the outside walls of the condensor and evaporator, as well as the internal temperatures are needed. Only the special heat pipe with the thermocouple wells can be used for the measurement of internal temperatures. Although the diameter of the heat pipe is expected to have an influence on the heat transfer coefficient, this effect is expected to be small for a reduction from 1/2" diameter (the special heat pipe's size) to 3/8" diameter (the untested heat pipes' size). Thus the smaller heat pipes' heat transfer coefficients are assumed to be the same as the larger ones. As a check, the heat transfer capabilities of the normal 1/2"x12" heat pipe would also be tested and compared to the special heat pipe, to see whether the inserts of the wells makes any significant difference to the overall thermal resistance. (The results of this check are located in Chapter 6, figures 6.11 and 6.12)

The heat transfer rate through the heat pipe is controlled by adjusting the voltage over the resistance wire around the heating block. The resistance of the heating wire is $9.6\ \Sigma$ (at room temperature) and is assumed to be constant. The circulating cooling water was generally heated from ambient to about 15°C above ambient, as this is the region where heat transfer between the water and surroundings is the least. (See figure 4.10). Tests were performed for vertical and horizontal positions of the special and standard (1/2"x12") heat pipes. The experimental inputs are shown in tables 4.1 and 4.2:

Table 4.1 Voltage over resistance wire of heating block for experiments performed on the special heat pipe (1/2" diameter x 12" length, including thermocouple wells)

Vertical operation			**Horizontal operation**	
Experiment number	Resistance wire voltage and power		Experiment number	Resistance wire voltage and power
1.1	40 V (= 167 W)		1.7	30 V (= 94 W)
1.2	51 V (= 271 W)		1.8	40 V (= 167 W)
1.3	60 V = (375 W)		1.9	50 V (= 260 W)
1.4	70 V = (510 W)		1.10	75 V (= 586 W)
1.5	80 V = (667 W)			
1.6	90 V = (844 W)			

Table 4.2 Voltage over resistance wire of heating block for experiments performed on the standard heat pipe (1/2" diameter x 12" length)

Vertical operation			**Horizontal operation**	
Experiment number	Resistance wire voltage		Experiment number	Resistance wire voltage
1.11	40 V		1.16	40 V
1.12	50 V		1.17	60 V
1.13	60 V		1.18	75 V
1.14	70 V			
1.15	85 V			

(The maximum heat transfer rate was reached earlier for the horizontal cases than for the vertical cases, therefore less experiments were needed for the horizontal cases). The thermal modelling regarding this section is discussed in section 5.1. The processed results are located in section 6.1, with a sample calculation on how to determine the heat transfer coefficients from the experimental data located in appendix B (section B.1).

4.2 DETERMINATION OF THE FIN THERMAL CHARACTERISTICS

For the core cooling experimental case, an air cooled fin is used as the heat sink. It was decided to design a fin and manufacture it, and also determine its heat transfer characteristics experimentally.

4.2.1 DESIGN AND MANUFACTURE OF FIN

The objective was not to design and manufacture the most effective fin possible, but rather to manufacture a simple fin that can be analysed theoretically. The core that needs cooling (for the core cooling case of section 4.4) has a length of 90 mm, and the heat pipe would be embedded 80mm deep inside the core. Since the heat pipe used for the core cooling case (1/2" diameter x 12" length) is just over 300 mm long, it was decided that 150 mm would be an appropriate length for the fin.

The design of the fin was limited by the manufacturing tools available in the workshop. The best way to manufacture the fin appeared to be to cut the needed grooves into a solid round aluminium bar, on a lathe with a parting tool. Parting tools of 2 mm and 3 mm thickness were available. After experimenting, it was established that 2 mm spaces could be cut, provided that the fin thickness is not less than 1.5 mm. 1.5 mm is relatively thick for a fin, but it does not present any particular problem.

It is important to measure the base temperature of the fin. In order to do this, 1.6 mm diameter holes (30 mm deep) were drilled laterally into the cylindrical fin core, close to the base where the fins are rooted. The material selected for the fin is a 75 mm solid aluminium round bar of type 6082 T6 – as to combine strength and machinability with a good thermal conductivity ($k = 204$ W/mK). Figures 4.11(a & b) show the fin, where the laterally drilled hole and thermocouples can be seen.

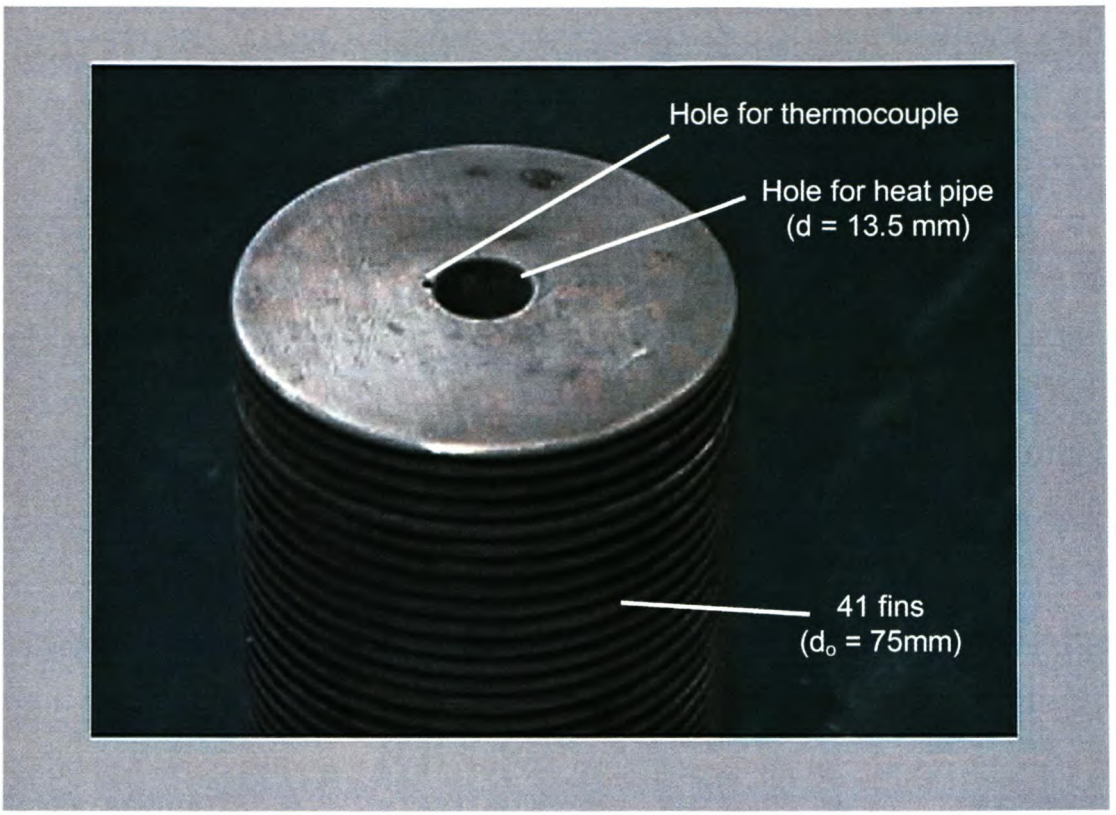

Figure 4.11.a Aluminium fin, showing the lateral hole in base for the thermocouple

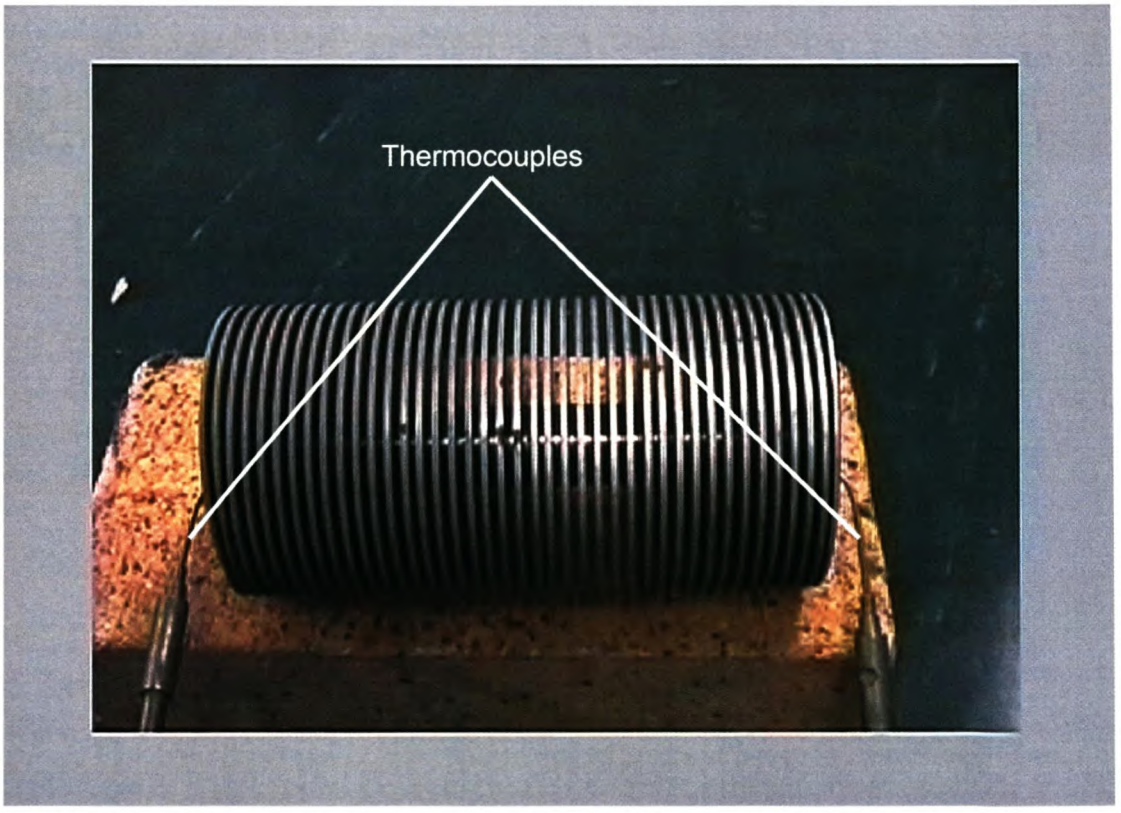

Figure 4.11.b Thermocouples inserted into the lateral holes to measure base temperature

4.2.2 EXPERIMENTAL DESIGN AND SET-UP

The objective is to experimentally determine the forced convection coefficient between the fins and cooling air. The aluminium heating block described in section 4.1 will be used as the heat source. This time the heat pipe is soldered into the (air cooled) fin, which is the heat sink. The fin needs to be cooled by air flowing over it, typically inside a duct (refer to figure 4.12). The heat transfer rate from the fins to the air can be calculated if the mass flow rate of the air and the difference between the inlet and outlet air temperatures are known. By measuring the radial temperatures on the heating block, the heat transfer rate into the evaporator can also be calculated, as an energy balance check. The effect of the mass of the fins will also be considered for transient heat transfer. (Refer to section 5.2 for the modelling of the fin's approximated thermal capacity and the heat transfer coefficient for duct flow for the air flowing in between two fins)

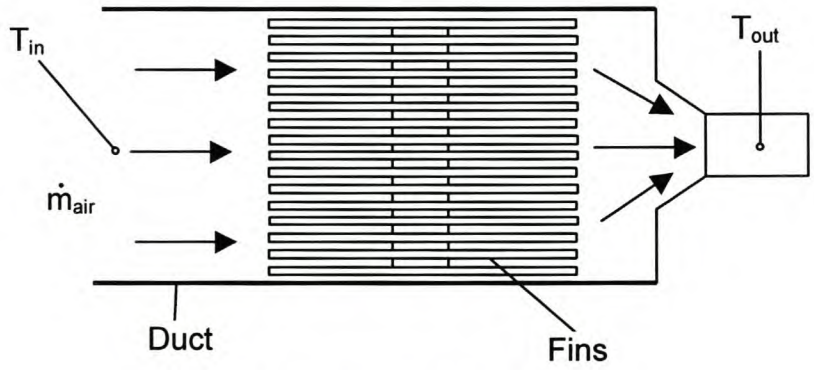

Figure 4.12 Schematic of fin in duct

Consider figure 4.13. The cooling air is supplied by a high pressure line (also for the core cooling case, section 4.4). A valve is fitted just after the feeding point. This is used to lower the pressure of the air and control the air flow. The air then flows through a pipe in which an orifice plate is located. The pressure drop of the air over the orifice plate is used to measure the mass flow rate of the air. The pipe leads to a settling chamber where the air flow is spread evenly and the velocity is reduced, before it flows through the insulated duct in which the fins are located. The orifice is designed according to the British Standard 1042 Sections 1.1 – 1.4. A sample calculation to determine the mass flow rate of the air using these is given in appendix B (section B.2)

An air flow distributor was designed to ensure uniform flow over the fins. If the air were just left to flow directly out of the pipe, stratified flow could result over the fin. The distributor is a T-piece, made from stainless steel pipes, which is fitted to the pipe entering the settling chamber. Equally spaced holes are drilled into both sides of the vertical pipe. This causes the air to blow out sideways at more or less the same velocity. In this way, pressure is built up in the chamber and a uniform outflow of air towards the fins is achieved. An outlet nozzle with mixing baffles was also designed as to ensured well mixed air where the outlet temperatures are measured. The experimental set-up is shown schematically in figure 4.13.

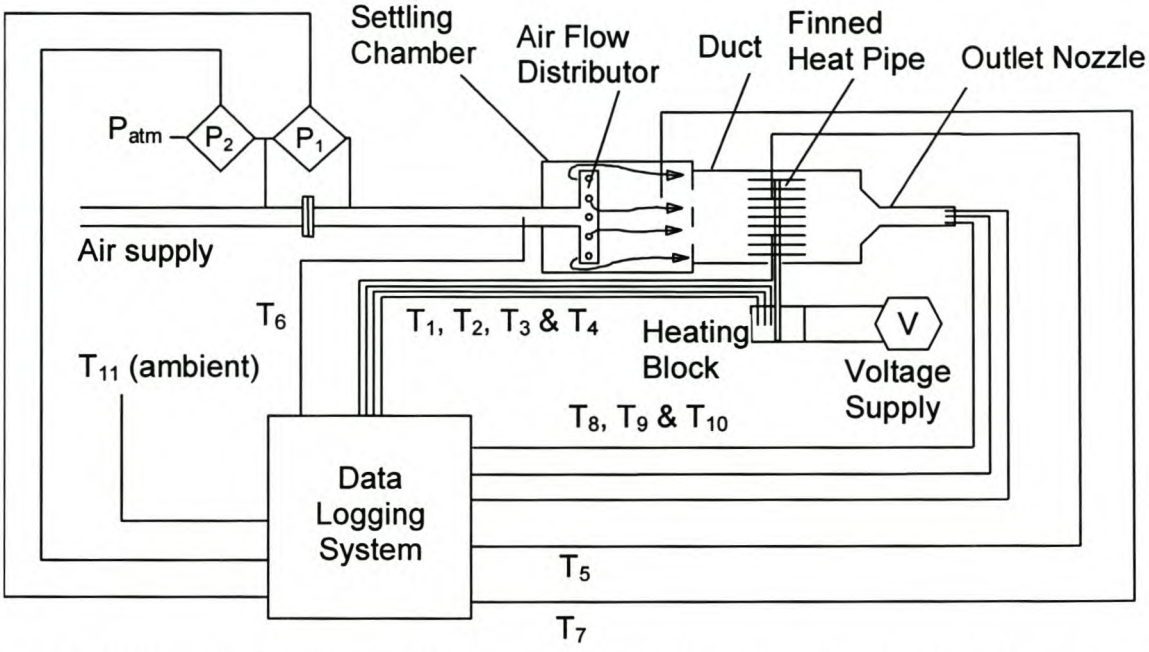

Figure 4.13 Schematic of experimental set-up to determine the fin's heat transfer characteristics

The measurements taken (figure 4.13) are the following:

T_1 Outside radial temperature of heating block at d = 62 mm (Thermocouple, type J)

T_2 Middle radial temperature of heating block at d = 44 mm (Thermocouple, type J)

T_3 Inner radial temperature of heating block at d = 18 mm (Thermocouple, type J)

T_4 Fin base temperature (bottom) (Thermocouple, type J)

T_5 Fin base temperature (top) (Thermocouple, type J)

T_6 Inlet air temperature in pipe (Thermocouple, type T)

T_7 Inlet air temperature in settling chamber (Thermocouple, type T)

T_8 Outlet air temperature (Thermocouple, type T)

T_9 Outlet air temperature (Thermocouple, type T)

T_{10} Outlet air temperature (Thermocouple, type T)

T_{11} Ambient air temperature (Thermocouple, type T)

P_1 Pressure difference over orifice plate (Pressure transducer)

P_2 Pressure difference between ambient and orifice inlet (Pressure transducer)

The equipment and calibrations are discussed in section 4.7

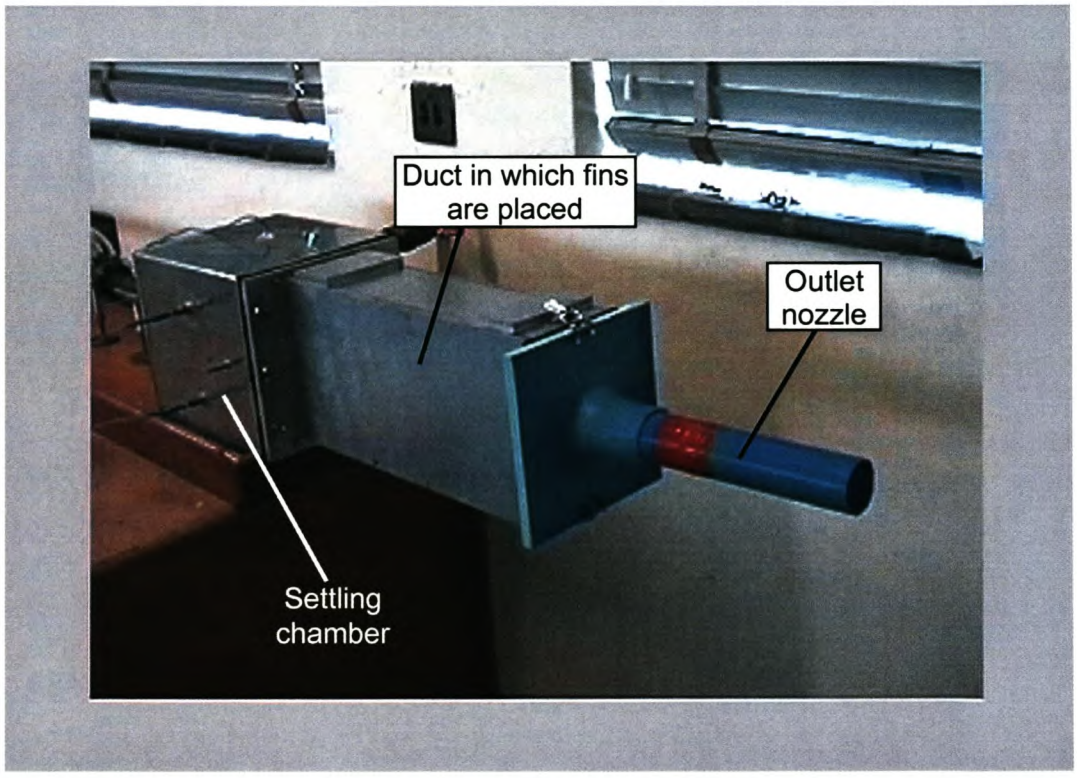

Figure 4.14.a Duct and air outlet

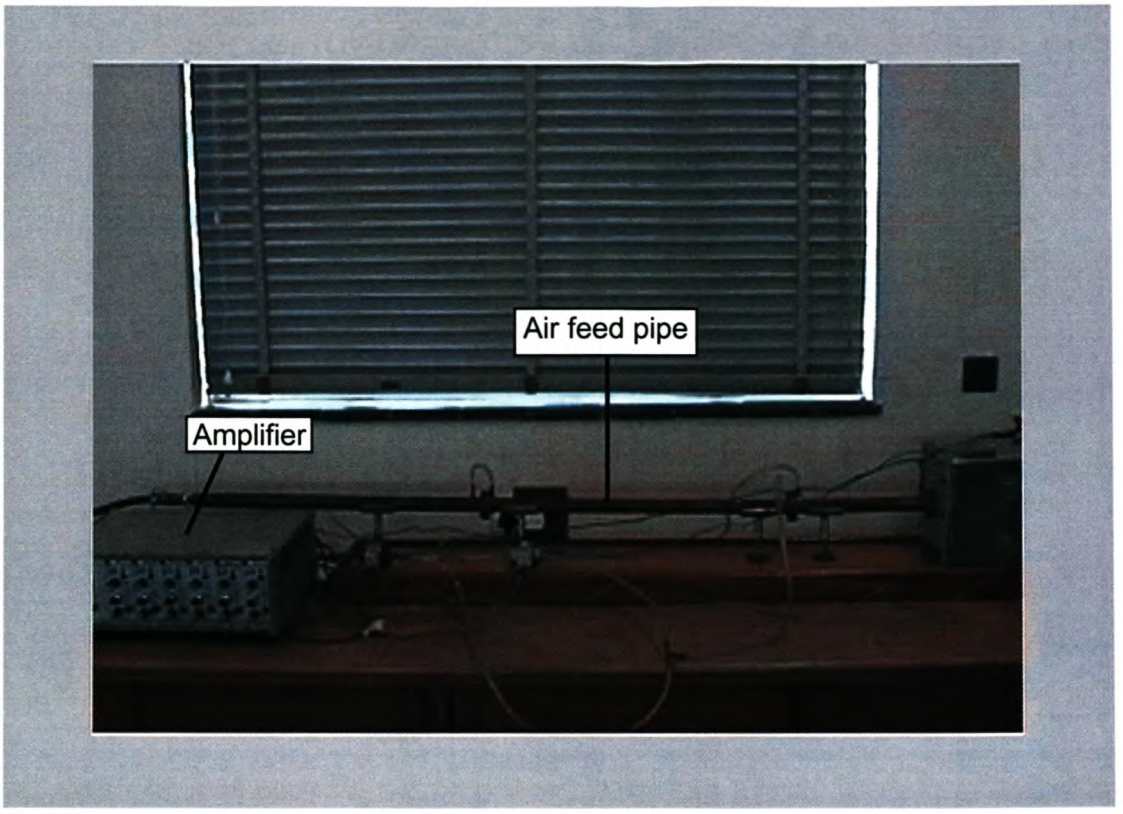

Figure 4.14.b Air feed pipe and amplifier

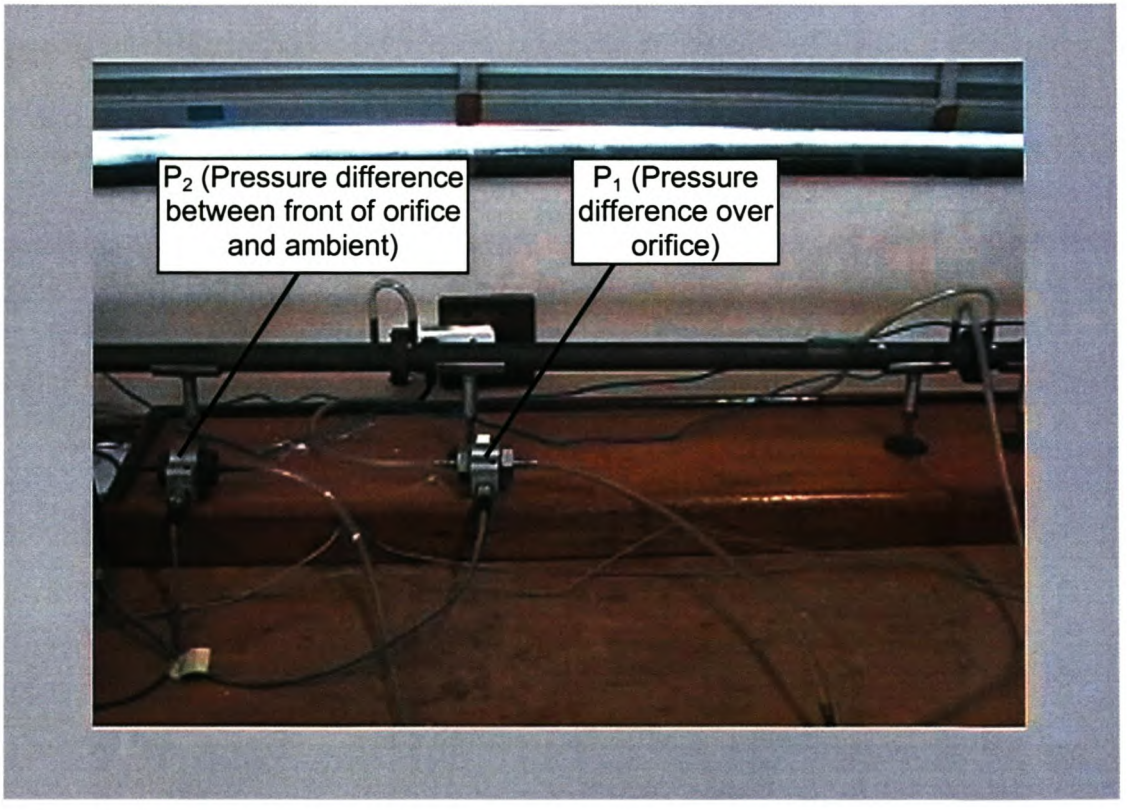

Figure 4.14.c Pressure difference meters (transducers)

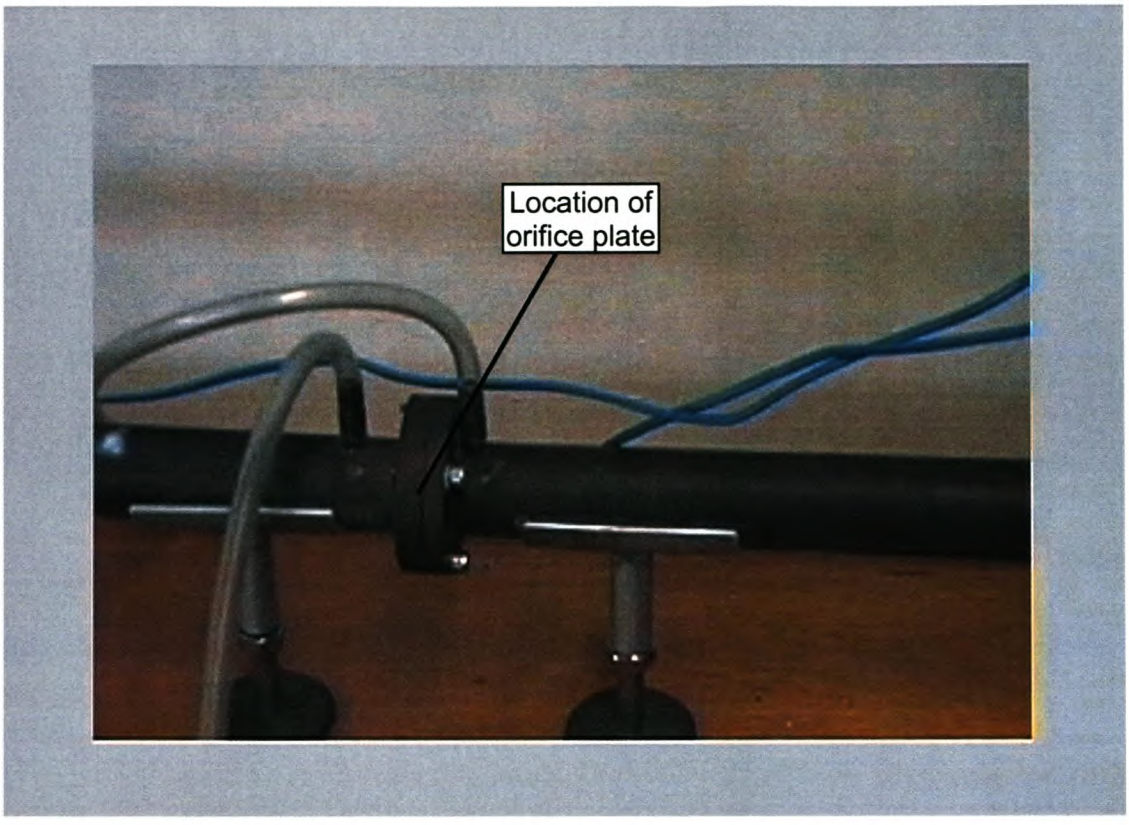

Figure 4.14.d Orifice pressure difference measurement

4.2.3 EXPERIMENTS PERFORMED

The voltage over the resistance wire of the heating block is changed to control the heat input into the evaporator of the heat pipe. The mass flow rate of the air is changed to obtain different fin cooling rates. The experimental inputs are shown in table 4.3:

Table 4.3 Voltage over resistance wire of heating block and air mass flow rates for experiments performed to determine fin heat transfer characteristics

Mass flow rate of air ≈ 12.5 g/s			**Mass flow rate of air ≈ 21.5 g/s**	
Experiment number	Voltage		Experiment number	Voltage
2.1	50 V (= 260 W)		2.3	60 V (= 375 W)
2.2	70 V (= 510W)		2.4	80 V (= 667 W)
			2.5	100 V (= 1042 W)

Mass flow rate of air ≈ 24 g/s			**Mass flow rate of air ≈ 30.5 g/s**	
Experiment number	Voltage		Experiment number	Voltage
2.6	65 V (= 440 W)		2.9	70 V (= 510 W)
2.7	85 V (= 753 W)		2.10	90 V (= 844 W)
2.8	105 V (= 1148 W)		2.11	110 V (= 1260 W)

The thermal modelling regarding the fin is located in section 5.2. Results are located in section 6.2 and sample calculations regarding the fin are located in appendix B (sections B.2 and B.3).

4.3 THE MOULD HEATING CASE

This is the first experimental case that represent a practical casting mould set-up. (Cases 4.1 and 4.2 are done in support of the casting related experiments) Some industrial casting moulds need to be pre-heated or continuously heated. To heat the moulds, it is common practice to make use of open gas flames. This process has the disadvantages that high heat losses are experienced, it is difficult to control and keep the mould at a specified temperature, and also that surface cracking and carbonising of the mould take place.

Currently, as an alternative to direct gas-flame heating of the mould, electrical heating elements can be used. There are basically three configurations in which electrical elements can be used to heat a mould. One configuration is to heat by means of radiation/convection by placing elements on the outside, some distance away from the mould, comparable to heating an object in an oven. A second option is to place heating elements into metal pads, that can be fixed directly on the side of a mould. The third configuration is to place heating elements into the mould itself. This experimental case suggests another alternative to heat a mould - by penetrating the mould with heat pipes that are connected to an external heat source.

4.3.1 EXPERIMENTAL DESIGN AND SET-UP

This experiment should be designed such that the following requirements are met:

- the experimental set-up is simple enough to model theoretically
- maintainability and replacement of components in an industrial mould are kept in mind
- the amount of heat input to the heat source can be measured

Heat source and sink

In order to meet the design requirement that the mould should be simple enough to model theoretically, both the heat sink and source are mild steel blocks. Two heat pipes (3/8" diameter x 8" length) are used to perform the heat transfer between them. The heat source block is heated by two round cartridge heating elements. The fitting of the heat pipes into these blocks differed from that of the other experiments (in sections 4.4 and 4.5) in two ways. Firstly, the blocks were split in the middle, so that they can be clamped onto the heat pipes and heating elements. Secondly, no solder was used between the heat pipe and mild steel surfaces. These two steps were included to facilitate replacement of components, and also to see whether there would be any significant contact thermal resistance between the heat pipes and the steel block if no solder is used. The holes were reamed to ensure good thermal contact between the heat pipes and heating elements and their surroundings. It was debatable whether the experiment had to be insulated or not. Although good insulation would lead to more accurate theoretical results compared to experimental results, it would also be the least realistic as far as real castings are concerned. Industrial moulds have surfaces that are open to the atmosphere. Furthermore the surface emissivity can change with temperature and oxidation layers, and usually the natural convection coefficient is uncertain. It was thus decided not to insulate the surfaces, so that a sensitivity analysis on the changing effects can be performed.

Figures 4.15 (a & b) show the experimental set-up for this experiment. The thermal modelling is discussed in section 5.3 and the results are located in section 6.3.

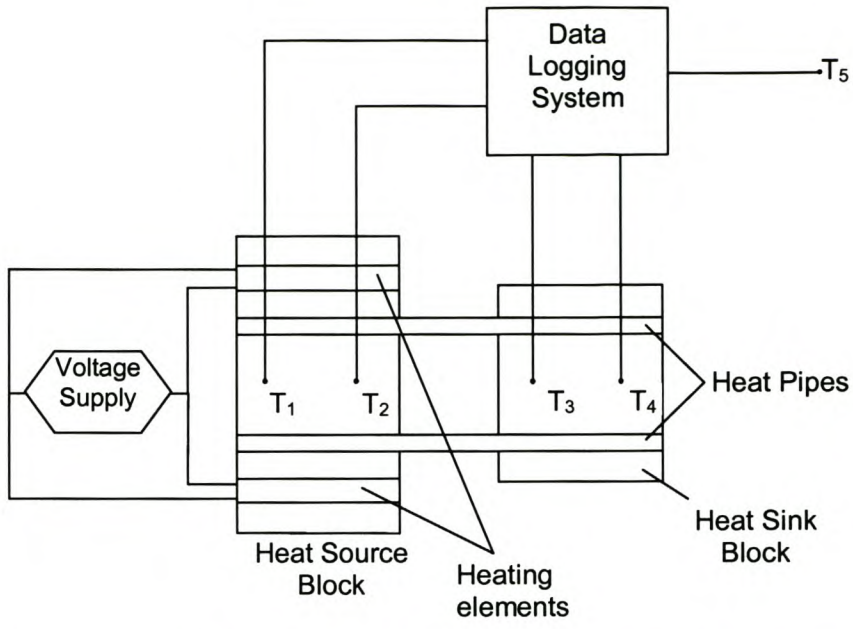

Figure 4.15.a Schematic experimental lay-out of the mould heating experiment. The heat source block has dimensions of 30x80x130 mm, and the heat sink block 30x80x100mm

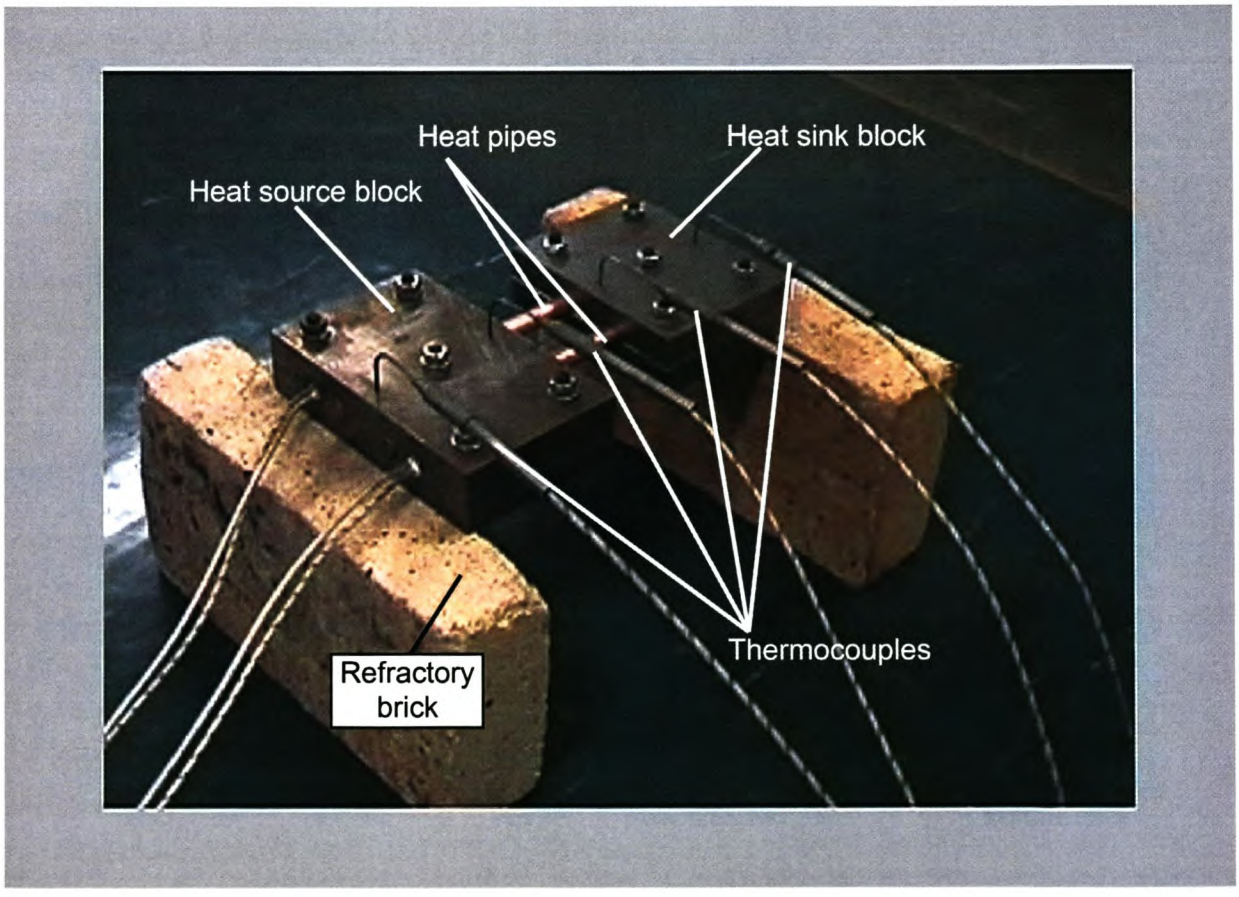

Figure 4.15.b The mould heating experiment

4.3.2 EXPERIMENTS PERFORMED

Measurements on heat source block alone

For the modelling of these experiments, certain material properties are needed, such as the conductivity and specific heat capacity of the steel, as well as the properties of the heating elements. Since the experiment were to be done un-insulated, radiation and convection heat transfer coefficients are needed. Although these values can be read of tables, calculated or estimated, there is still uncertainty about the correctness of the chosen values, since they were not directly experimentally determined for this specific case. To assist in the judgement of whether the chosen properties are accurate, an experiment was performed where the heating elements heats the heating block alone. After a while, the elements are switched off and the block is left to cool down. By comparison of experimental and modelled temperature results, the accuracy of the model (and thus the chosen values for properties and coefficients) can be assessed. The elements were heated with a 250W heat output from both the heating elements.

Heat transfer from source to sink with the heat pipes

Three experiments were performed with the source block connected to the sink block by means of the heat pipes. The voltage over the heating elements were adjusted so as to generate different heat outputs, shown in table 4.4. The elements are switched on for some time before they are switched off and cooling is allowed to take place.

Table 4.4 Power input to (each) heating element for the mould heating experiments

Experiment number	Power input to heating elements	Experimental description
3.1	250 W	Only heat source block is heated and temperatures are taken
3.2	250 W	The heat source block is connected to the heat sink block with the heat pipes. Temperatures of both blocks are taken
3.3	200 W	Same as experiment 3.2
3.4	100 W	Same as experiment 3.2

4.4 THE CORE COOLING CASE

Many industrial castings have holes or passages that necessitate the use of a core during the casting process. The core is often a difficult component to cool because of it's geometry and placement. During manufacture, an un-cooled core often becomes hotter than the specified temperature. This leads to production losses, since the core has to be removed and cooled externally. A heat pipe can be inserted into the core to cool it. In this case the core need not be removed to cool it externally and can be cooled in situ thus saving mould down time.

4.3.1 EXPERIMENTAL DESIGN AND SET-UP

The following are the important design requirements:

- Air cooled fins are to be used at the condenser end of the heat pipe to cool the core
- The casting should be easy to produce and remove from the mould
- Simple to model, yet representative of an industrial case

To place the largest direct heat load on the heat pipe, it was decided that the core should be thin. But since the temperature of the core had to be measured by insertion of a thermocouple, it had to be thick enough to allow for that. The heat pipe used in this experiment has a diameter of 12.7 mm (1/2"). The thermocouple for the temperature measurement has a 1.6 mm diameter. The core is designed to be 90 mm long, with a 30 mm diameter on top and a 25 mm diameter at the bottom. The heat pipe is inserted 80 mm deep into the core. The fin is fixed to the condenser end of the heat pipe, the same way as is described in section 4.2.

The casting itself has a top external diameter of 45 mm and a bottom external diameter of 40 mm. The external mould thus has the same internal diameters. The casting and mould are tapered for ease of removal of the casting. Refer to figure 4.16. The schematic of the experimental set-up is shown in figure 4.17.

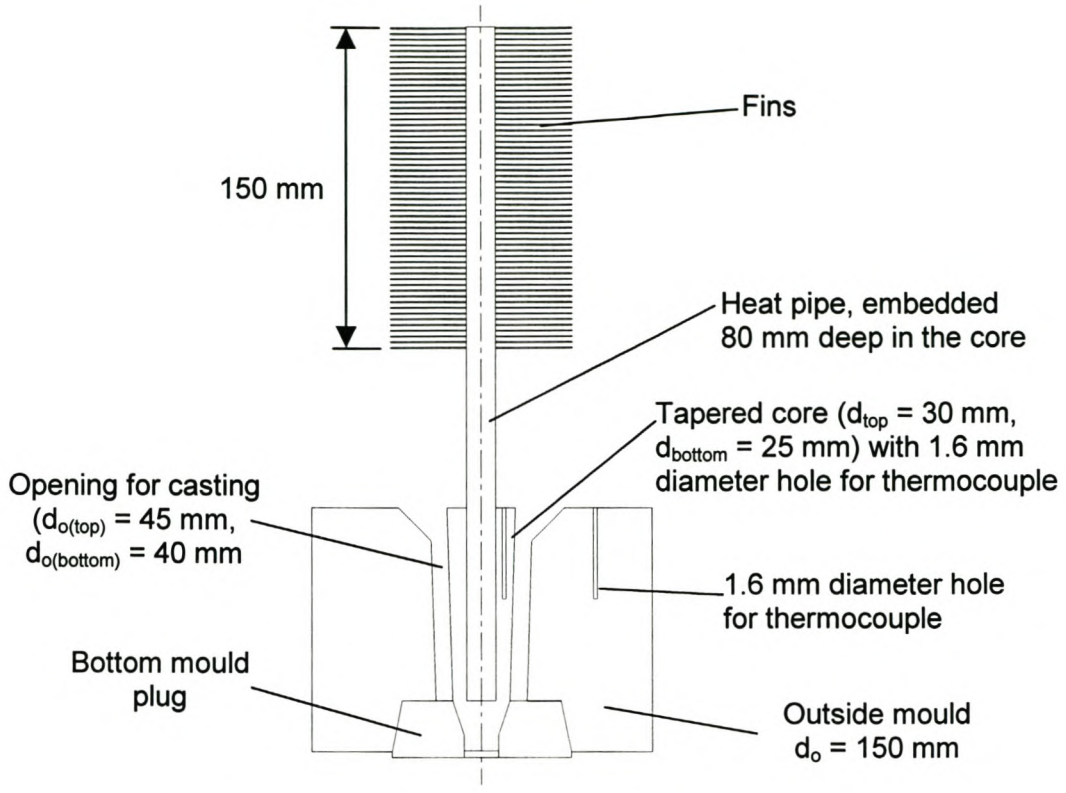

Figure 4.16 Design of mould and core for the core cooling case

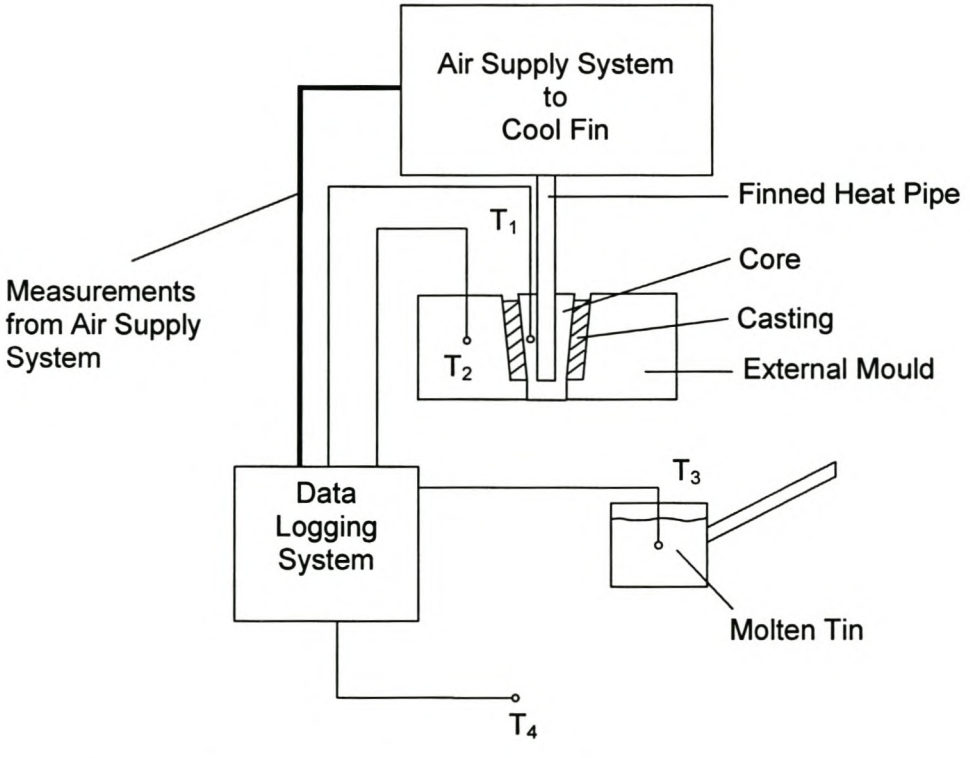

Figure 4.17 Schematic lay-out of the core cooling experiment

The measurements taken (figure 4.17) are the following:

T_1 Temperature of the core (Thermocouple, type J)

T_2 Temperature of the external mould (Thermocouple, type J)

T_3 Temperature of the molten tin, just before casting (Thermocouple, type J)

T_4 Ambient temperature (Thermocouple, type T)

Referring to figure 4.17, the air supply system to cool the fin is the same system described in figure 4.13. The measurements from the air supply system, are therefore temperatures T_4 to T_{10} and pressures P_1 and P_2 shown in figure 4.13.

4.4.2 EXPERIMENTS PERFORMED

The casting experiments are grouped into three cases, as is shown in table 4.5.

Table 4.5 Experiments performed for the core cooling case

Experiment number	Description of experiment
4.1 to 4.4	The casting is made without the heat pipe-and-fin combination to cool the core. The casting and core is left inside the internal mould to cool
4.5 to 4.8	The casting is made without the heat pipe-and-fin combination to cool the core. The casting and core is removed from the internal mould to cool through natural convection
4.9 to 4.13	The heat pipe-and-fin combination is inserted in the core. The casting and core is removed from the internal mould and is cooled through forced air convection over the fin

The thermal modelling is discussed in section 5.4 and the results are located in section 6.4.

Figures 4.18 (a to d) show photographs of the experiment.

Figure 4.18.a Core, heat pipe and fin for the core cooling case

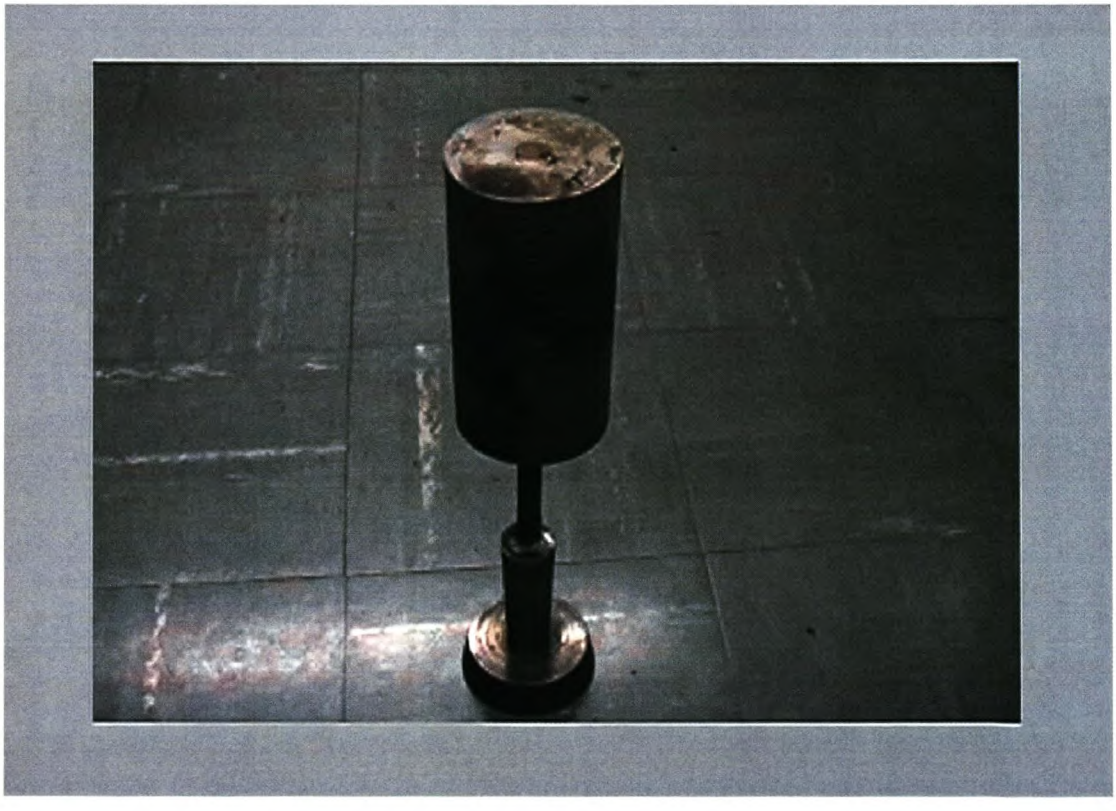

Figure 4.18.b Core, heat pipe and fin standing in bottom mould plug

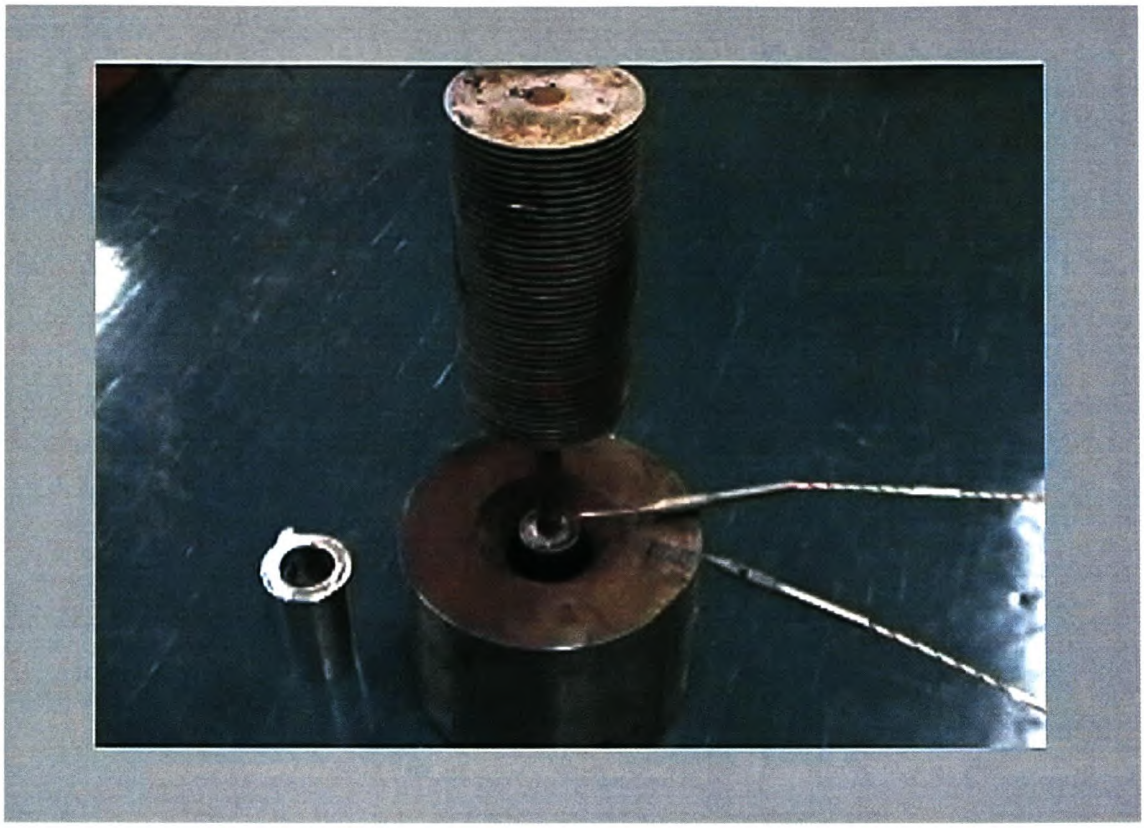

Figure 4.18.c Core, heat pipe and fin combination in outer mould, showing thermocouples and a casting

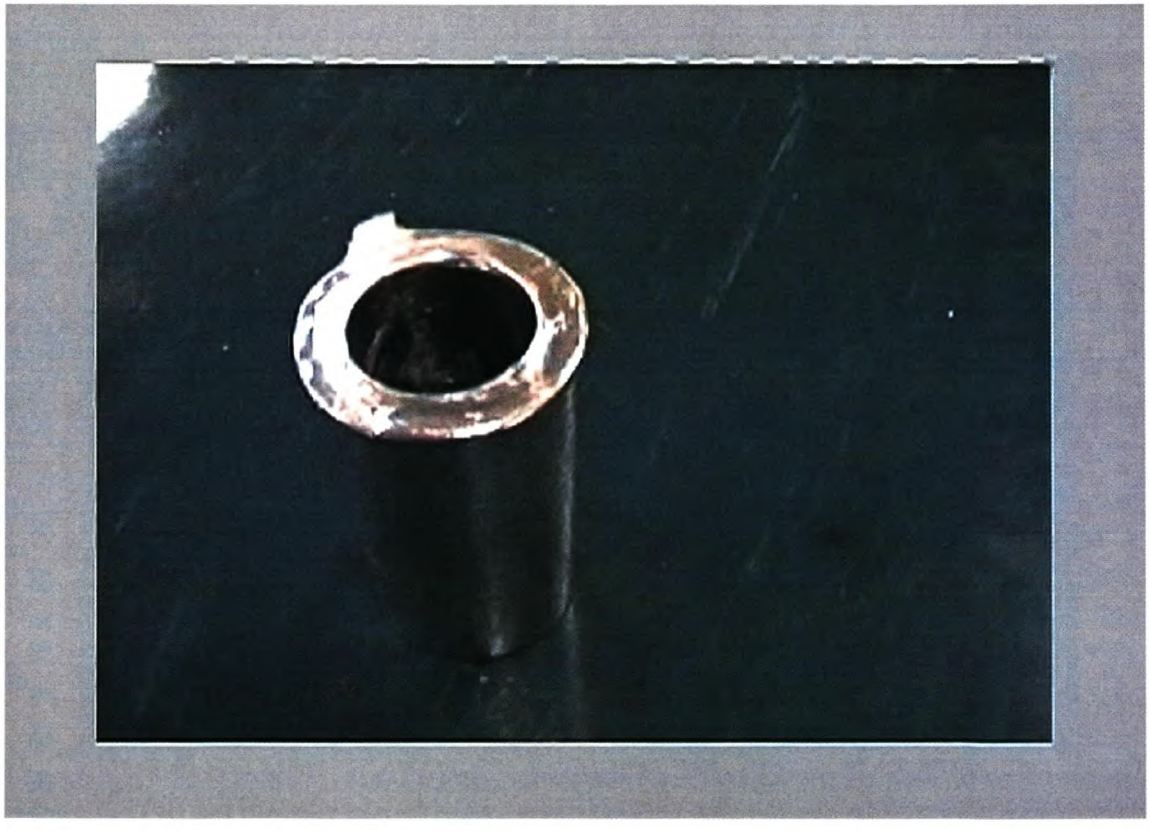

Figure 4.18.d A typical solidified tin casting

4.5 THE MOULD COOLING CASE

This experiment is designed to be representative of the case where an external mould is heated from the inside by means of a volume of molten metal that is cast into it. Usually industrial moulds of this type are cooled by means of water channels. This experiment suggests the use of heat pipes connected to a heat sink, instead of water, to cool the mould.

4.5.1 EXPERIMENTAL DESIGN AND SET-UP

The following requirements were considered:

- Design an experimental casting mould that is representative of an industrial casting, yet simple enough to model theoretically
- Use a combination of heat pipes and a water cooled steel heat sink to cool the mould
- The casting must be easy to produce and remove from the mould

The design of the mould is shown in figure 4.19. It consists of a cylindricalwall, with tapered side walls, which is necessary to ensure that the casting can be removed after solidification. It is important that the walls taper outwards towards the bottom of the mould and that the mould bottom is removable, so that the casting can be removed if the heat sink is fixed above it. Four holes are drilled into the side mould to fit heat pipes in. The 3/8"x8" heat pipes are utilised in this case. The heat sink is basically a round mild steel block with a hole through the centre through which the molten tin can be cast. The sink is cooled by means of water flowing through channels, parallel to the heat pipes. The heat sink and casting mould is separated by a tufnol disk-shaped insulation spacer. The reason for this is to make sure that heat cannot be transferred from the mould through conduction, radiation or convection, but only by means of the heat pipes. Temperatures of the mould are measured by drilling 1.6 mm holes for thermocouples in the middle of the mould wall. These thermocouple holes are also drilled into the heat sink. The schematic layout of the experiment is shown in figure 4.20. Figure 4.21 shows a photograph of the experimental mould and casting.

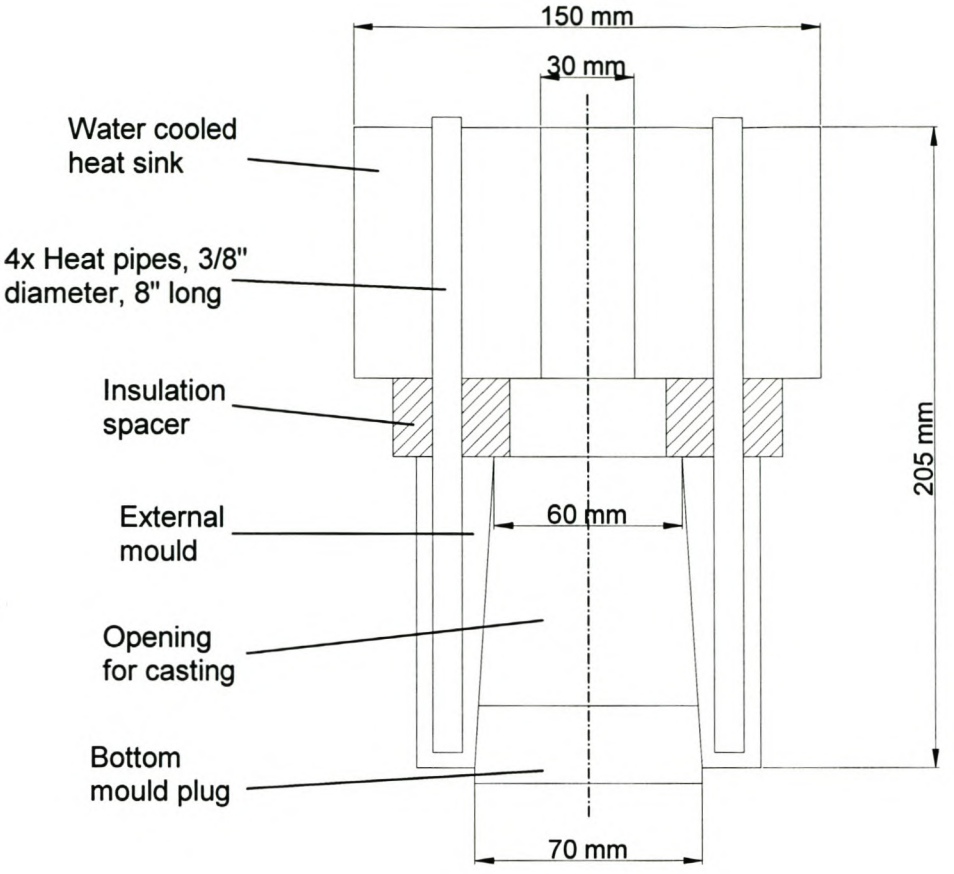

Figure 4.19 Schematic design of mould and heat sink for the mould cooling case

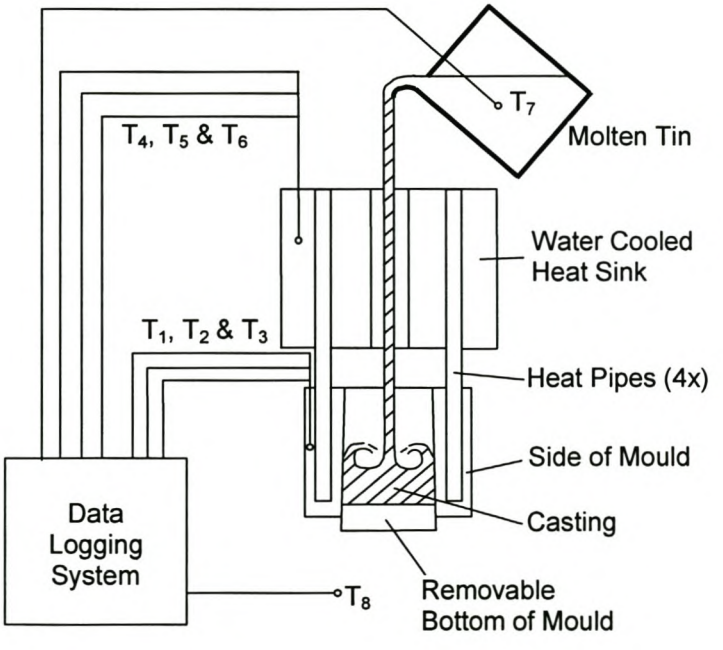

Figure 4.20 Schematic lay-out of mould cooling experiment

The measurements taken (figure 4.20) are the following:

T_1 Mould temperature (Thermocouple, type J)

T_2 Mould temperature (Thermocouple, type J)

T_3 Mould temperature (Thermocouple, type J)

T_4 Heat sink temperature (Thermocouple, type J)

T_5 Heat sink temperature (Thermocouple, type J)

T_6 Heat sink temperature (Thermocouple, type J)

T_7 Temperature of molten tin, just before casting (Thermocouple, type J)

T_8 Ambient temperature (Thermocouple, type T)

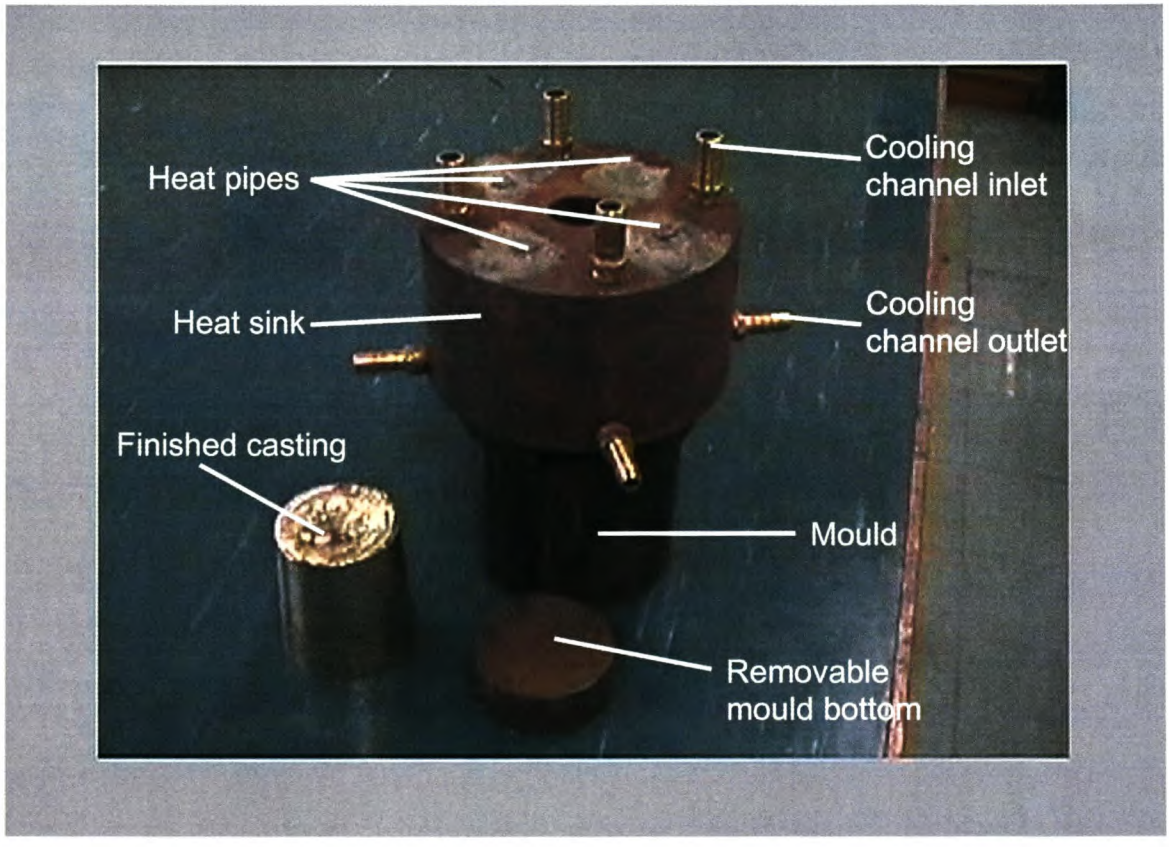

Figure 4.21 Mould (with removable bottom), water cooled heat sink and tin casting for the mould cooling experiments

4.5.2 EXPERIMENTS PERFORMED

Table 4.6 describes the experiments.

Table 4.6 Experiments performed for the mould cooling case

Experiment number	Description of experiment
5.1	The casting is made into the mould, with no heat pipes inserted. The casting is left inside the mould to cool
5.2	The casting is made into the mould, with no heat pipes inserted. The casting is removed from the mould after solidification
5.3 (a to d)	The casting is made into the mould, which is connected to the heat sink through heat pipes. The casting is left inside the mould to cool
5.4	The casting is made into the mould, which is connected to the heat sink through heat pipes. The casting is removed from the mould after solidification

4.6 EQUIPMENT AND CALIBRATIONS

4.6.1 EQUIPMENT USED

Data logging system

The data logging system consists of a Hewlett-Packard 34970A data acquisition unit, connected to a personal computer (with the relevant software) through a communications port. The data acquisition unit have the capability to convert the electrical potential (mV) output from the thermocouples to temperatures, for all types of thermocouples (for instance type K, T or J). The pressure difference measurements are kept in Volts and not converted to Pascal, though.

Amplifier

The amplifier is used to amplify the electrical outputs from the pressure transducers, during pressure measurements. It is a Hottinger DA-24 amplifier. The amplified signal is then connected to the data acquisition unit of the data logging system.

Pressure transducers

The transducer used to measure the pressure difference over the orifice plate (P_1 in figure 4.13) is a Hottinger 25022 transducer with a pressure difference capability of 0.1 bar. The other transducer (P_2 in figure 4.13) is a Hottinger 5013 transducer with a pressure difference capability of 1 bar.

Betz micromanometer

This manometer was used for the calibration of the pressure transducers. It is a Betz micromanometer with a pressure range of 5000 Pa, or 500mm water.

Pump

The pump used (as shown in figure 4.6) is made by the Stuart Turner company, with product number 9A0367.

Rheostat

The rheostat has a range of 0 to 220 V.

4.6.2 CALIBRATIONS

The thermocouples were not calibrated since the data logging system is able to automatically convert the electrical measurements into temperature readings. The pressure transducers had to be calibrated though, since only a voltage reading could be measured and logged.

The Betz micromanometer was used to calibrate the pressure transducers. A pressure difference was induced over the transducer, and this difference was measured by the manometer. For each recorded pressure, there is a corresponding electrical potential reading which is also recorded. The pressure difference can then be plotted as a function of the voltage reading. Figures 4.22 and 4.23 show the pressure difference versus voltage readings recorded for the two pressure transducers, P_1 and P_2 (as shown in figure 4.13).

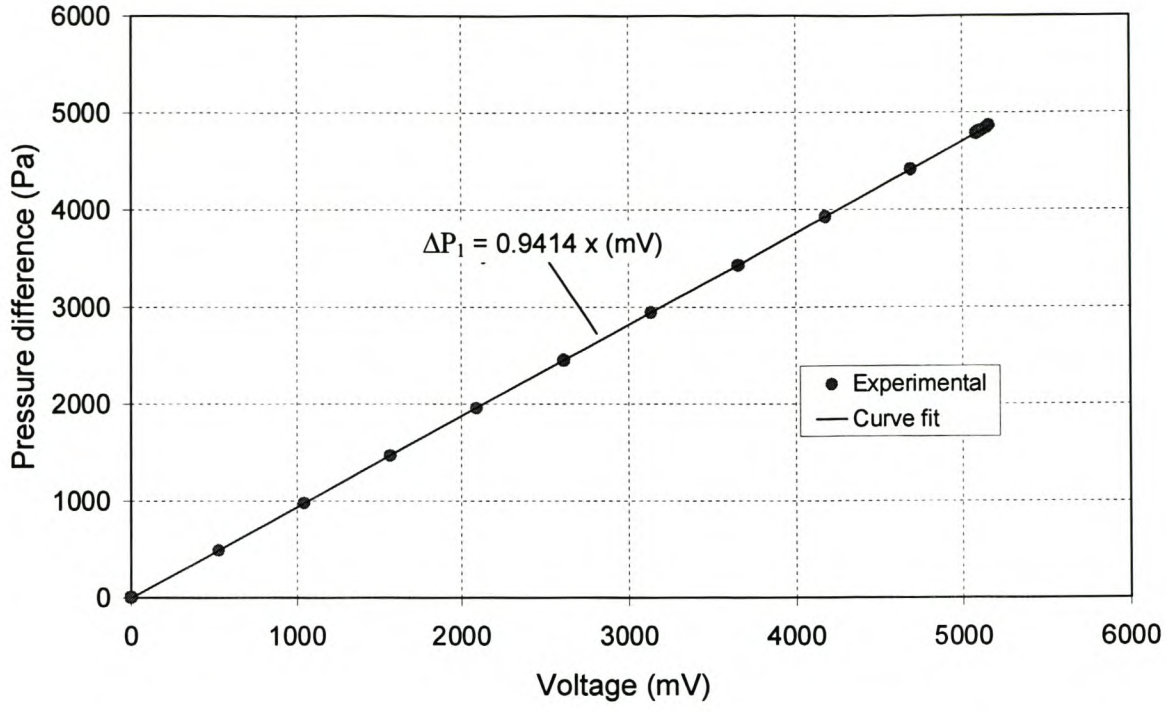

Figure 4.22 Pressure difference over the orifice (ΔP_1) as a function of the amplified voltage output from the pressure transducer

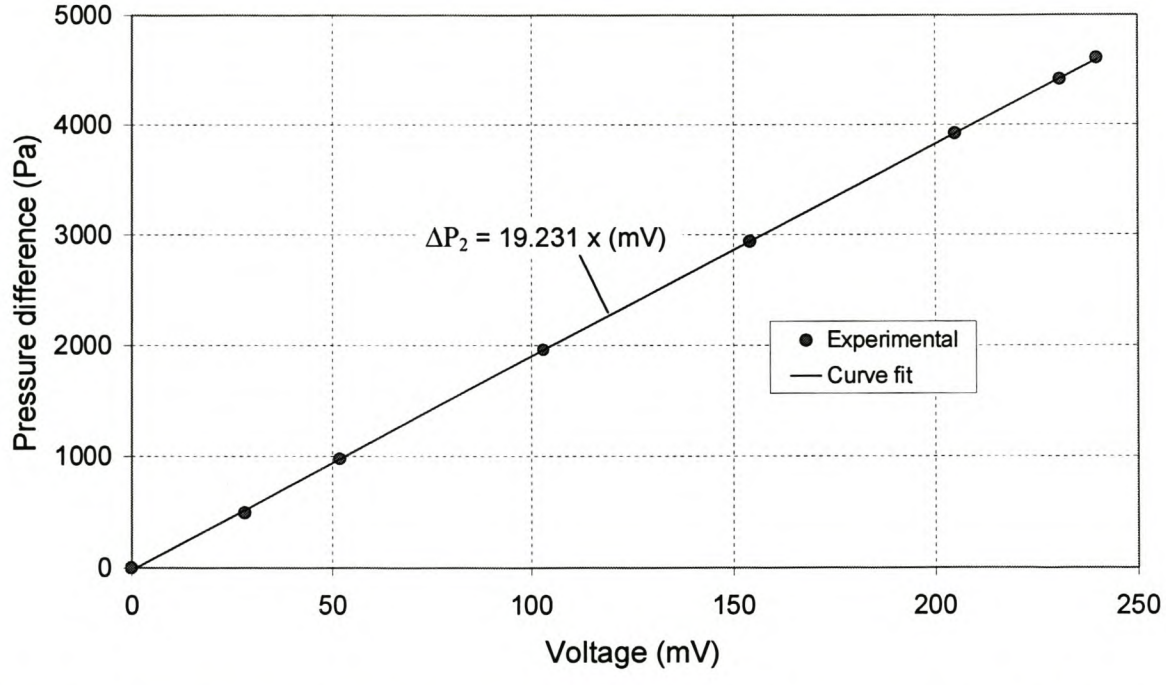

Figure 4.23 Pressure difference between the orifice inlet and atmosphere (ΔP_2) as a function of the amplified voltage output from the pressure transducer

CHAPTER 5 - Thermal Modelling

The theoretical thermal models for the heat pipes, fins and casting experiments are developed in this chapter.

5.1 THERMAL MODELLING OF THE HEAT PIPES

In this section, four methods are used to thermally model the heat pipes:

- Thermal resistance model (§ 5.1.1)
- High conductivity, low thermal capacity solid model (§ 5.1.2)
- Outer shell & super conductive core model (§ 5.1.3)
- Theory for the experimental determination of correlations for the evaporator and condenser heat transfer coefficients of the heat pipe (§ 5.1.4)

5.1.1 THERMAL RESISTANCE MODEL

Figure 5.1 shows the heat pipe and thermal resistance circuit.

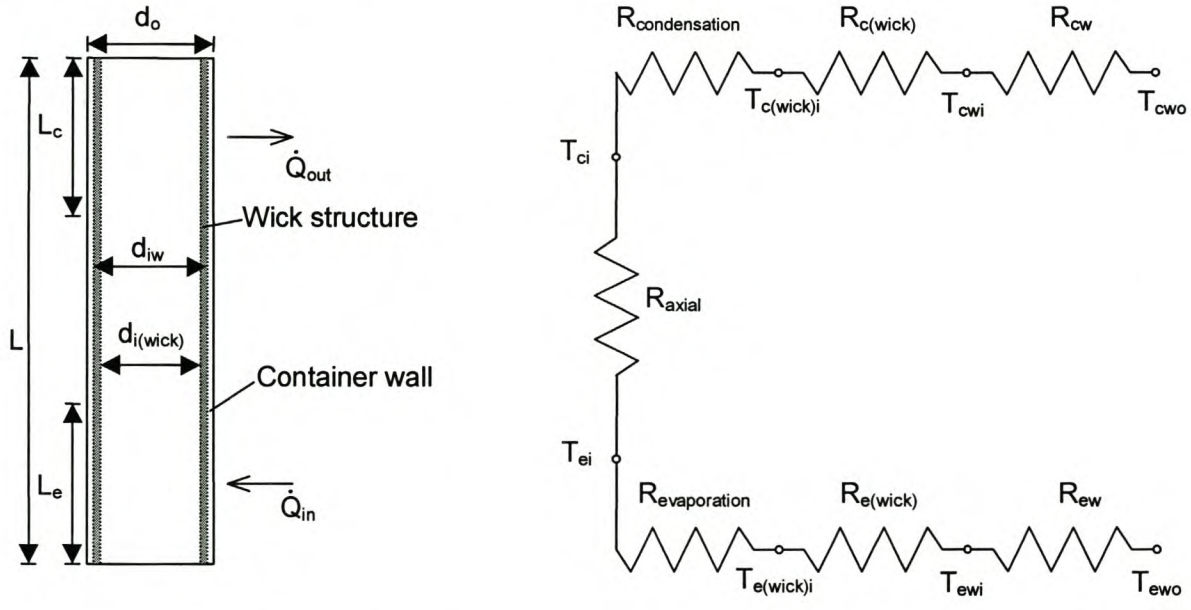

Figure 5.1 Heat pipe with corresponding thermal resistance circuit

Container wall thermal resistances

The thermal resistances for the container walls is the resistance for a cylindrical shell, obtained from Fourier's law of conduction (Mills, 1992):

$$R_{ew} = \frac{\ln(d_o / d_{iw})}{2\pi k_w L_e} \tag{5.1}$$

$$R_{cw} = \frac{\ln(d_o / d_{iw})}{2\pi k_w L_c} \tag{5.2}$$

Wick structure thermal resistances

The same type of equations used for the wall are again applicable, therefore:

$$R_{e(wick)} = \frac{\ln(d_{iw} / d_{i(wick)})}{2\pi k_{wick} L_e} \tag{5.3}$$

$$R_{c(wick)} = \frac{\ln(d_{iw} / d_{i(wick)})}{2\pi k_{wick} L_c} \tag{5.4}$$

A straight forward assumption cannot be made to assign a value for the effective wick conductivity k_{wick}, though. As is explained in chapter 4, a wick consisting of two layers of phosphor bronze (brass) screen mesh is lined against the inside of the container wall. The mesh takes up 40% of the volume, and the remaining 60% consists of water. Three methods are suggested to calculate the effective thermal conductivity of the wick structure.

Method 1: Assume perfect contact and alignment between mesh layers

With the assumption that 40% of the conduction area is brass and 60% is water, the combined conductivity for a single water filled mesh layer can be calculated as:

$$k_{mesh\ layer} = 0.4k_{brass} + 0.6k_{water} \tag{5.5}$$

The conductivity of brass is $k_{brass} = 111$ W/mK, and water has a conductivity of between $k = 0.5$ and 0.7 W/mK, for the temperature range in which the heat pipe performs. As a relatively general case, assume that $k_{water} = 0.6$ W/mK.

Therefore, since it is assumed that the two mesh layers are perfectly in contact and aligned;

$$k_{wick} = 0.4(111) + 0.6(0.6)$$

$$= 44.76\,W/mK \qquad (5.6)$$

The conductivity given in equation 5.6 is probably too high, since the assumptions for its derivation are unrealistic. Small areas of mesh that do not touch against one another will be filled with water and will significantly impact on the value of the effective conductivity.

Method 2: Ignore the conductivity of the brass

This method is conservative, in the sense that the mesh layer is assumed to be only water. This is assumed to be the "worst case scenario" for the conductivity of the wick. Therefore, take

$$k_{wick} = 0.6\,W/mK \qquad (5.7)$$

Method 3: Assume wick and water layers in series

This method is a compromise between methods 1 and 2. It assumes that one mesh layer consists of liquid and brass layers lying directly against one another. The liquid layer has 60% of the thickness and the brass layer has 40% of the thickness, as is shown in figure 5.2.

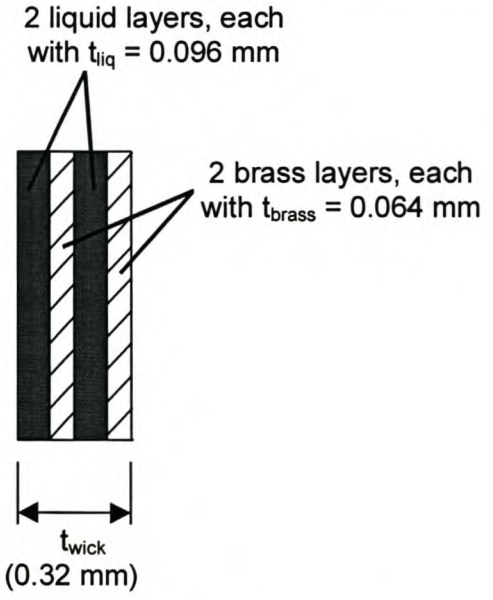

Figure 5.2 Approximation of wick consisting of two mesh layers

Using Fourier's law of conduction over a flat plate, the thermal resistance of the mesh model as shown in figure 5.2 can be expressed as:

$$R_{wick} = \frac{t_{wick}}{k_{wick}A} = \frac{2t_{water}}{k_{water}A} + \frac{2t_{brass}}{k_{brass}A}$$ which reduces to

$$k_{wick} = \frac{t_{wick}}{2(\frac{t_{water}}{k_{water}} + \frac{t_{brass}}{k_{brass}})} = \frac{0.32}{2(\frac{0.096}{0.6} + \frac{0.064}{111})} = 0.996\,W/mK \quad ** \qquad (5.8)$$

**(Although this conductivity value (equation 5.8) is more or less 45 times smaller than the one given in equation 5.6, it corresponds well to the experimentally determined value, therefore suggesting that the water in the wick plays a more significant role than may be expected)

Evaporation and condensation thermal resistances

According to the kinetic theory of phase change, the heat transfer coefficient between the interface of a liquid and gas where evaporation or condensation takes place, is given by (Mills, 1992):

$$h_i = \left(\frac{2}{\pi RT}\right)^{1/2} \frac{\rho_g h_{fg}^2}{T} \qquad (5.9)$$

where T is temperature in Kelvin and R is the gas constant of the substance. (R= 461.9 J/kgK for water). Assuming that the shape of the wick does not influence the kinetic gas theory significantly, the thermal resistances can be expressed as:

$$R_{condensation} = \frac{1}{\left(\pi d_{i(wick)} L_c\right)\left(\frac{2}{\pi RT}\right)^{1/2} \frac{\rho_g h_{fg}^2}{T}} \qquad (5.10)$$

$$R_{evaporation} = \frac{1}{\left(\pi d_{i(wick)} L_e\right)\left(\frac{2}{\pi RT}\right)^{1/2} \frac{\rho_g h_{fg}^2}{T}} \qquad (5.11)$$

Axial thermal resistance

The value for the axial thermal resistance is given as: (Groll, 1992)

$$R_{axial} = \frac{T}{h_{fg}\rho_g}\frac{\Delta P_g}{\dot{Q}} \tag{5.12}$$

The condensation, evaporation and axial thermal resistances are assumed to be very small for the heat pipes used and are therefore neglected in the remainder of the thesis.

5.1.2 HIGH CONDUCTIVITY, LOW THERMAL CAPACITY SOLID MODEL

Since an objective of this thesis is to find a suitable model for a heat pipe that can be used in a standard finite element computer program (NASTRAN), this model is considered. Although the thermal resistance model (section 4.1.1) is more scientifically correct and the experimentally determined correlations (section 4.1.4) should be the most accurate, they cannot be incorporated into a standard finite elements program, without changing the program. Three properties have to be assigned to a solid finite element in order to model heat transfer, namely the density, conductivity and specific heat capacity. Other variables like convection coefficients and surface radiation properties are also needed, but they are modelled as boundary conditions on the relevant elements only. Since a heat pipe is not solid nor homogeneous, a solid finite element (which is homogeneous in the standard program) will not be able to model it completely correctly, but only as an approximation. The finite element models were only used for the experimental cases where the smaller type heat pipe (3/8" diameter x 8" length) was used, therefore the rest of this section will only be concerned with properties and dimensions pertaining to that specific heat pipe type.

The mass of the heat pipe (3/8" diameter x 8" length) is 45 grams, and its volume is $\frac{\pi(0.009525)^2}{4}(0.2032) = 14.48\times10^{-6}\ m^3$, so that the effective solid density is calculated as:

$$\rho_{solid} = \frac{0.045}{14.48\times10^{-6}} = 3107.9\ kg/m^3 \tag{5.13}$$

The copper container wall (and brass wick) is assumed to be the only masses that have heat capacities. The specific heat capacity of copper is given to the solid element, therefore:

$$C_{p(solid)} = 385\,W/mK \tag{5.14}$$

For the calculation of the conductivity, refer to figure 5.3:

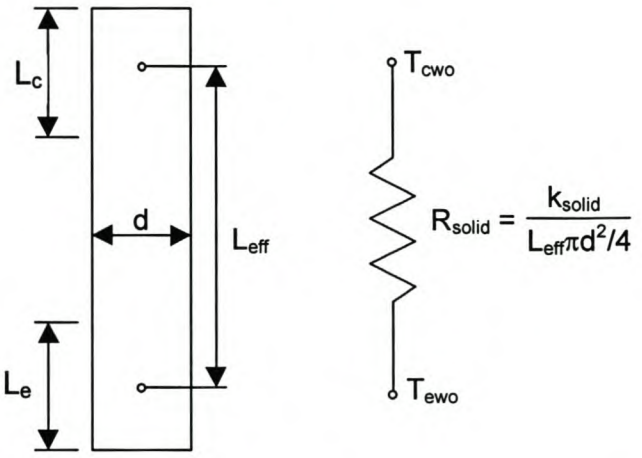

Figure 5.3 Thermal resistance of heat pipe modelled as a solid round bar

The total thermal resistance for the heat pipe (thus all 7 resistances shown in figure 5.1) is represented by a single axial resistance for the solid round bar, R_{solid}. The effective length of the conduction path is given by L_{eff}, which is the distance between the centres of the evaporator and condenser sections.

Based on experimental results (refer to section 6.1), a reasonable average heat transfer coefficient (condenser and evaporator ends) for the heat pipe is $h = 2000$ W/m^{2}K. Consider the mould heating experiment (refer to section 4.3). The condenser and evaporator lengths are 80mm each, and the diameter is 3/8" (= 9.525 mm). The heat pipe is 8" (= 203.2 mm) long and the effective length consequently is 203.2 – 80 = 123.2 mm. The total thermal resistance is:

$$R_{solid} = R_c + R_e = 2\left(\frac{1}{(2000)\pi(0.009525)(0.08)}\right) = 0.41773\,°C/W \tag{5.15}$$

and therefore:

$$k_{solid} = \frac{0.1232}{(0.41773)(\frac{\pi(0.009525)^2}{4})} = 4139\,W/mK \qquad (5.16)$$

Thus, the three properties needed for the finite element model are now calculated.

5.1.3 OUTER SHELL AND SUPER CONDUCTIVE CORE MODEL

This model is suggested as a possible improvement of the thermal resistance model described in section 5.1.2, for use in the standard finite element computer program. The heat pipe is considered as consisting of an annular outer shell and an inner core as shown in figure 5.4. Both the outer shell and inner core are assumed to be made up of solid and homogeneous material, as to comply with the requirements of the FEM program. The thermal properties of the two materials are completely specified by the thermal conductivity, specific heat and density.

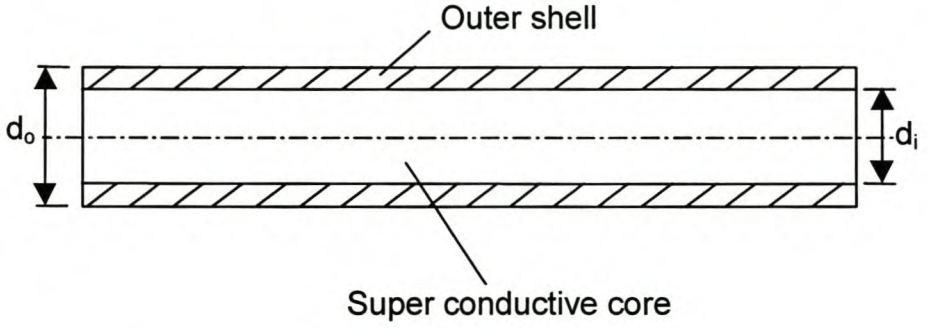

Figure 5.4 Schematic of outer shell and super conductive core model

The following assumptions are made regarding the core and shell:

- The major thermal resistance is caused by the container wall and wick structure (assume 95% of the total resistance), which represents the outer shell. Only 5% of the thermal resistance is therefore caused by the core.

- 95% of the mass of the heat pipe is assumed to be located in the shell, with the specific heat capacity assumed to be that of copper. 5% of the mass is assumed to be located in the core, with the specific heat capacity of the core assumed to be that of water vapour.
- The thickness of the shell is equal to the thickness of the container wall (0.46 mm) and two layers of mesh (0.32 mm) thus $t_{shell} = 0.78$ mm and consequently for the relevant heat pipe (3/8" diameter x 8" length) $d_o = 9.525$ mm (≈ 9.5 mm) and $d_i = 7.965$ mm (≈ 8 mm).

Shell properties

Based on the same assumptions made as in section 5.1.2, the total thermal resistance for the heat pipe is, from equation 5.15, $R_{total} = 0.41773\ °C/W$. Therefore,

$$R_{shell} = 0.95(0.41773) = 0.3968\ K/W \tag{5.17}$$

Since $R = \frac{\ln(d_o/d_i)}{2\pi kL}$, and the lengths of the condenser and evaporator sections on which the thermal resistance of equation 5.15 is based are both 80 mm, the shell conductivity is calculated as:

$$k_{shell} = \frac{0.3968(2)\pi(0.16)}{\ln(9.5/8)} = 1.42\ W/mK \tag{5.18}$$

The volume of the shell is $V_{shell} = \frac{\pi(0.0095^2 - 0.008^2)}{4}(0.2032) = 4.189 \times 10^{-6}\ m^3$, and with 95% of the mass (45 g) assumed to be located in the shell, the density is:

$$\rho_{shell} = \frac{0.95(0.045)}{5.029 \times 10^{-6}} = 10\,204.5\ kg/m^3 \tag{5.19}$$

The specific heat capacity of the shell is assumed the same as that of copper, therefore:

$$C_{p(shell)} = 385\ J/kgK \tag{5.20}$$

Core properties

The axial resistance of the core should only be 5% of the total thermal resistance and therefore:

$$R_{core} = 0.05(0.41773) = 0.02089\ K/W \tag{5.21}$$

Based on an effective length of 123.2 mm (to correspond with the condenser and evaporator lengths of 80 mm each);

$$k_{core} = \frac{L_{ef}}{R_{core} A_{core}} = \frac{0.1232}{0.02089\left(\frac{\pi(0.008)^2}{4}\right)} = 117328.2\ W/mK \tag{5.22}$$

The volume of the core is $V_{core} = \frac{\pi(0.008)^2}{4}(0.2032) = 10.21\times10^{-6}\ m^3$, and 5% of the mass of 45 g is 2.25 g and thus the density is:

$$\rho_{core} = \frac{0.00225}{10.12\times10^{-6}} = 220.4\ kg/m^3 \tag{5.23}$$

Since the core consists of water vapour, the value for the specific heat capacity is based on that of saturated steam, which is C_p = 1850 J/kgK at 0°C and C_p = 2020 J/kgK at 100°C. The average of these two values is assigned to the core, so that:

$$C_{p(core)} = 1935\ J/kgK \tag{5.24}$$

5.1.4 MODEL FOR DETERMINATION OF EXPERIMENTAL CORRELATIONS

The data obtained from performing the experiments described in section 4.1, can be used to calculate heat transfer coefficients for the condenser and evaporator sections of the heat pipe. Figure 5.5 shows the relevant detail of the heat pipe in the experimentalset-up and an accompanying thermal resistance circuit.

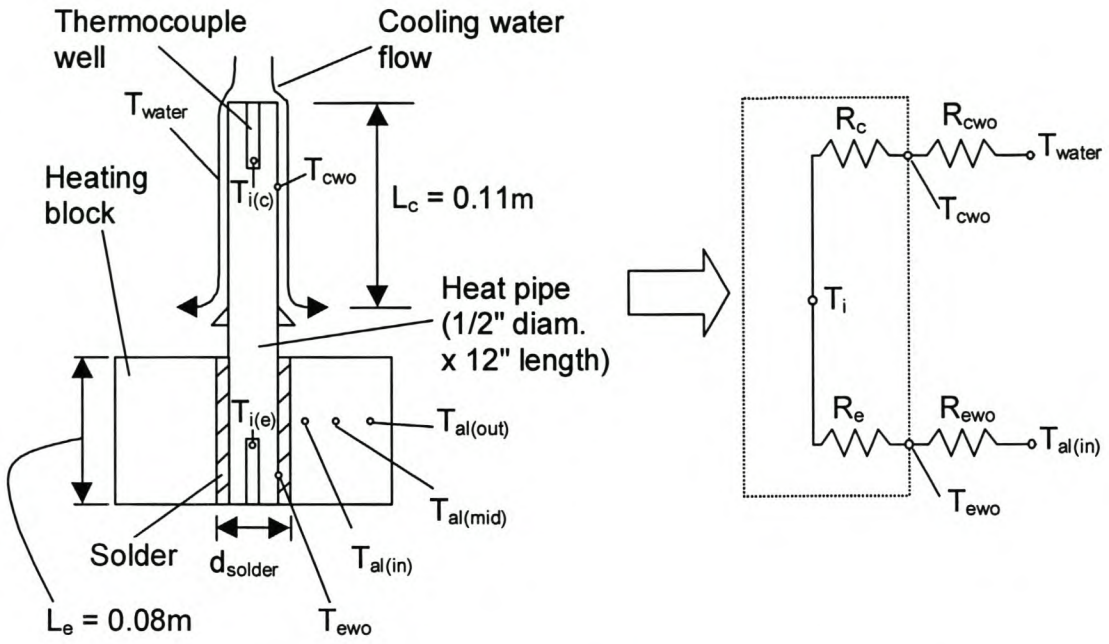

Figure 5.5 Heat pipe in experiment and accompanying thermal circuit

The objective is to determine the two resistances R_e and R_c, from which the wanted heat transfer coefficients, h_e and h_c can be determined. For the configuration in figure 5.5, the evaporator and condenser heat transfer coefficients are given by:

$$h_e = \frac{1}{R_e A_{ewo}} = \frac{1}{R_e \pi (0.0127)(0.08)} = \frac{313.3}{R_e} \tag{5.25}$$

$$h_c = \frac{1}{R_c A_{cwo}} = \frac{1}{R_c \pi (0.0127)(0.11)} = \frac{227.9}{R_c} \tag{5.26}$$

If the evaporator and condenser heat transfer rates and wall temperatures, as well as the internal temperature of the heat pipe are known, the resistances can be expressed as:

$$R_e = \frac{(T_{ewo} - T_i)}{\dot{Q}_e} \quad \text{and} \quad R_c = \frac{(T_i - T_{cwo})}{\dot{Q}_c} \tag{5.27}$$

The value of the internal temperature is taken as the average of the internal condenser and evaporator temperatures:

$$T_i = \frac{T_{i(e)} + T_{i(c)}}{2} \tag{5.28}$$

The wall outside temperatures are expressed as:

$$T_{ewo} = T_{al(in)} - R_{ewo}\dot{Q}_e \tag{5.29}$$

$$T_{cwo} = T_{water} + R_{cwo}\dot{Q}_c \tag{5.30}$$

The resistance R_{ewo} consists of two cylindrical shell thermal resistances – an aluminium shell (with outside diameter 18 mm and inside diameter of 13.5 mm) and a solder shell (with an outside diameter of 13.5mm and inside diameter of 12.7mm). The solder used to fill the gap between the heat pipe and the heating block, is an alloy consisting of 65% lead and 35% tin. The approximated equivalent conductivity for the solder is therefore:

$$k_{solder} = 0.35k_{tin} + 0.65k_{lead} = 0.35(66.6) + 0.65(35.3) = 46.3\,W/mK \tag{5.31}$$

The thermal resistance on the outside of the evaporator wall can therefore be expressed as:

$$R_{ewo} = R_{al} + R_{solder} = \frac{\ln(18/13.5)}{2\pi(204)(0.08)} + \frac{\ln(13.5/12.7)}{2\pi(46.3)(0.08)} = 0.0054303\,K/W \tag{5.32}$$

To determine R_{cwo}, the heat transfer coefficient between the cooling water and outside wall of the heat pipe is needed. If the Reynolds number (based on hydraulic diameter) of the cooling water is known, the Nusselt number can be found, from which the heat transfer coefficient can be determined. For an annulus with outer diameter d_o and inner diameter d_i, the hydraulic diameter is $d_h = d_o - d_i$. Furthermore, the Reynolds number is written as:

$$\mathrm{Re}_{d_h} = \frac{\rho V d_h}{\mu} = \frac{4\dot{m}}{\mu\pi(d_o + d_i)} \tag{5.33}$$

The cooling jacket has an inside diameter of 16mm, so that for equation 5.33, $d_o = 0.016$ m and $d_i = 0.0127$ m. For a measured water temperature, the mass flow rate can be determined from figure 4.7 and the viscosity from standard property tables.

According to the Gnielinski equation,

$$Nu_{d_h} = \frac{(f/8)(\mathrm{Re}_{d_h} - 1000)\,\mathrm{Pr}}{1 + 12.7(f/8)^{0.5}(\mathrm{Pr}^{2/3} - 1)}, \text{ where} \tag{5.34}$$

$$f = \left(0.97\ln\left(\mathrm{Re}_{d_h}\right) - 1.64\right)^{-2} \tag{5.35}$$

Using equation 5.34 the heat transfer coefficient outside of the condenser wall becomes

$$h_{cwo} = \frac{Nu_{d_h} k_{water}}{d_o - d_i} = \frac{Nu_{d_h} k_{water}}{(0.016 - 0.0127)} = 303.03(Nu_{d_h} k_{water}) \tag{5.36}$$

Having determined the value of h_{cwo}, it follows that:

$$R_{cwo} = \frac{1}{h_{cwo} A_{cwo}} = \frac{1}{h_{cwo}\pi(0.0127)(0.11)} = \frac{227.85}{h_{cwo}} \tag{5.37}$$

The heat transfer rates at the evaporator and condenser ends still needs to be determined. The condenser end heat transfer rate is determined in the following way: The mass of the cooling water pumped in the cycle is exactly 2.5 kg. The net rate of heat transfer into the water can be expressed as:

$$\dot{Q}_{water} = mC_p \frac{dT_{water}}{dt} = (2.5)C_p \frac{dT_{water}}{dt} \tag{5.38}$$

The value of $\frac{dT_{water}}{dt}$ is approximated by using the temperature difference of the bulk water for two consecutive time steps, and dividing it through the time increment, so that:

$$\frac{dT_{water}}{dt} \approx \frac{T_{water(\text{current time step})} - T_{water(\text{previous time step})}}{\Delta t} \tag{5.39}$$

There are three components that influence the total amount of heat transferred to the water. They are the heat transferred via the heat pipe, heat gain from the pump and heat losses to the environment. In order to find the heat transferred via the heat pipe, the other two

components need to be filtered out. (This is discussed in chapter 4, section 4.1). The net heat gain from the environment (heat gained from pump minus heat lost to ambient) is therefore:

$$\dot{Q}_{env} = mC_p\left(\frac{dT_w}{dt}\right)_{env} \tag{5.40}$$

where $\left(\frac{dT_w}{dt}\right)_{env}$ can be found from figure 4.10

To find the actual heat transfer rate through the condenser, it follows that:

$$\dot{Q}_c = \dot{Q}_{water} - \dot{Q}_{env} \tag{5.41}$$

To determine the evaporator heat transfer rate, the temperature differences between the temperatures measured at the radial positions of the heating block is used. Consider the control volume shown in figure 5.6, which is the aluminium cylinder between the inner and middle thermocouple holes.

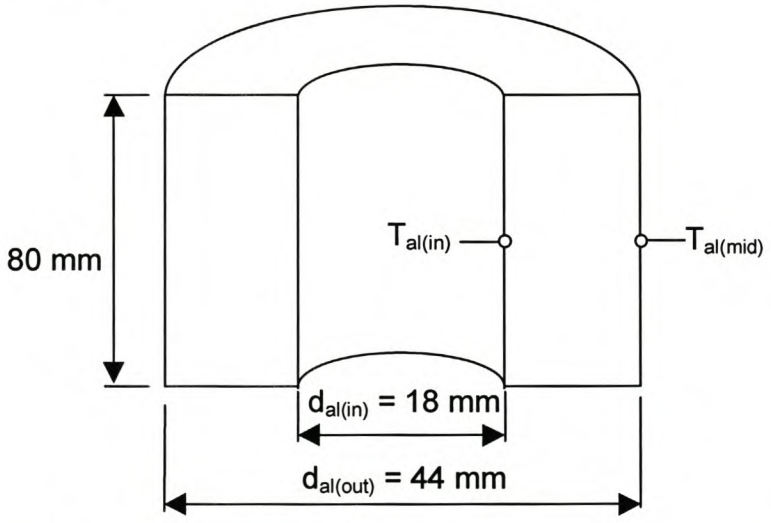

Figure 5.6 Control volume of aluminium shell used to determine the evaporator heat transfer rate

The thermal resistance between the two temperatures in figure 5.6 is

$$R_{al} = \frac{\ln(44/18)}{2\pi(204)(0.08)} = 0.008717\,W/mK \tag{5.42}$$

For steady state conditions, the radial heat transfer rate through the control volume is

$$\dot{Q}_{al} = \frac{\Delta T}{R} = \frac{(T_{al(mid)} - T_{al(in)})}{0.0087166} = 114.72(T_{al(mid)} - T_{al(in)}) \quad (5.43)$$

During the experiments, the temperature of the heating block did not stay constant– the temperatures increased with time, until steady state was achieved. Before steady state is achieved, some of the energy flowing into the control volume is absorbed by the mass and causes a temperature rise. By defining the average temperature ofthe control volume at any time as $T_{cv} = \frac{T_{al(mid)} + T_{al(in)}}{2}$, and calculating the temperature difference for this average control volume temperature over the measured time step as $\Delta T_{cv} = T_{cv\,(current\ time\ step)} - T_{cv\,(previous\ time\ step)}$, the heat transfer rate to heat the control volume is calculated as

$$\dot{Q}_{cv} = \frac{(mC_p)_{al}(\Delta T_{cv})}{\Delta t} = \frac{(2770)(0.08)\frac{\pi}{4}(0.044^2 - 0.018^2)(875)\Delta T_{cv}}{\Delta t} = 245.49\frac{\Delta T_{cv}}{\Delta t} \quad (5.44)$$

The corrected evaporator heat transfer is therefore:

$$\dot{Q}_e = \dot{Q}_{al} - \dot{Q}_{cv} \quad (5.45)$$

Enough information is now available so that the condenser and evaporator heat transfer coefficients (equations 5.25 and 5.26) can be calculated. These heat transfer coefficients are assumed to be functions of certain important variables. It was decided that for this case, these variables should be the heat transfer rate, the difference between the evaporator- and condenser wall outside temperatures and the internal temperature. A function of the following type is assumed to exist:

$$h = a_o(\dot{q}'')^{n_1}(T_{ewo} - T_{cwo})^{n_2}(T_i)^{n_3} \quad (5.46)$$

where $\dot{q}'' = \frac{\dot{Q}}{A_{ewo}}$ for the evaporator and $\dot{q}'' = \frac{\dot{Q}}{A_{cwo}}$ for the condenser heat transfer coefficient. (Other variables such as the liquid fill height to evaporator height and the angle of inclination were not considered for this study). By taking the natural logarithm on both sides of equation 5.47, it becomes:

$$\ln(h) = \ln(a_o) + n_1 \ln(\dot{q}'') + n_2 \ln(T_{ewo} - T_{cwo}) + n_3 \ln(T_i) \qquad (5.47)$$

which is of the form $Y = A + n_1 Y_1 + n_2 Y_2 + n_3 Y_3$ and therefore a multi-linear equation. The values for A (and hence a_o), and the exponents n_i can be found by grouping the relevant data and performing a multi-linear regression. (A standard feature on spreadsheet packages). The results of this analysis are located in section 6.1.

5.2 THERMAL MODELLING OF THE FINS

Fin heat transfer rate

For a fin (see figure 5.7) with isothermal temperature T_f, outside diameter d_o and inside (base) diameter of d_i, over which air flows with temperature T_a such that the convection heat transfer coefficient between the air and fin surface is h_{fc}, the heat transfer rate is simply $\dot{Q} = h_{fc} A(T_f - T_a)$. A real fin is not isothermal though, but has a temperature distribution along it's radius. The fin efficiency, which takes into account this effect, is a function of the fin properties and geometry as well as the convection coefficient between the air and fin surface, have to be included to correct the heat transfer equation.

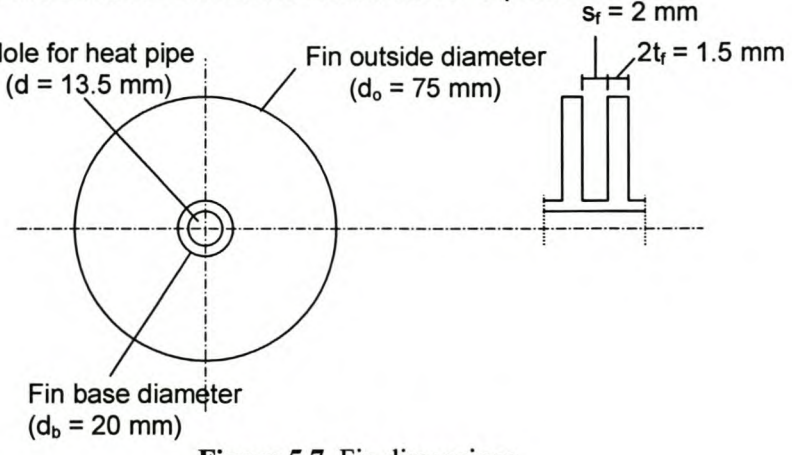

Figure 5.7 Fin dimensions

For the fin shown in figure 5.7, the fin efficiency is (Mills, 1992):

$$\eta_f = \frac{(2r_b/\beta)}{(r_o^2 - r_b^2)} \frac{K_1(\beta r_b)I_1(\beta r_o) - I_1(\beta r_b)K_1(\beta r_o)}{K_o(\beta r_b)I_1(\beta r_o) + I_o(\beta r_b)K_1(\beta r_o)} \tag{5.48}$$

where I_n and K_n are order n modified Bessel functions of the first and second kind respectively, and

$$\beta = \left(\frac{h_{fc}}{t_f k_{fin}}\right)^{1/2} \tag{5.49}$$

The heat transfer rate for a number of N fins (each with 2 surfaces from which heat transfer to the air takes place) with base temperature T_b is thus given by:

$$\dot{Q}_{fins} = 2Nh_{fc}\left(\frac{\pi(d_o^2 - d_b^2)}{4}\right)\eta_f(T_b - T_a) = Nh_{fc}\left(\frac{\pi(d_o^2 - d_b^2)}{2}\right)\eta_f(T_b - T_a) \tag{5.50}$$

Determination of convection coefficient

Except for the convection coefficient h_{fc}, all the other variables in equation 5.51 are known or are readily measured. To determine h_{fc}, the hydraulic diameter approach is used. The passage between two fins through which the air flows can be regarded as a duct. Although the width of this duct changes as the air move onwards through the passage, it makes no difference, since the width cancels out of the hydraulic diameter equation. The hydraulic diameter of a duct with arbitrary width W (such as the space between two fins) reduces to

$$d_h = \frac{4A}{\wp} = \frac{4s_f W}{2W} = 2s_f \tag{5.51}$$

Therefore a constant hydraulic diameter of $2s_f$ can be assumed for the total air flow passage between two fin surfaces. The Reynolds number based on hydraulic diameter is defined as:

$$\mathrm{Re}_{d_h} = \frac{\rho V d_h}{\mu} = \frac{\left(\dot{m}_{air}/A\right)(2s_f)}{\mu} = \frac{\left(\dot{m}_{air}/\left(Ns_f(d_o - d_b)\right)\right)(2s_f)}{\mu} = \frac{2\dot{m}_{air}}{\mu N(d_o - d_b)} \tag{5.52}$$

The Gnielinski equations (eq.'s 5.34 and 5.35) for turbulent flow through a duct can be used to determine the Nusselt number (based on the hydraulic diameter) for flow through the fins, from which the heat transfer can be determined as:

$$h_c = \frac{Nu_{d_h} k_{air}}{d_h} = \frac{Nu_{d_h} k_{air}}{2s_f} \tag{5.53}$$

The air temperature rises as it flows past the fins, because of the heat transferred to it. If there are no losses, the heat transferred from the fins must be equal to the amount transferred to the air. The air temperature T_a is taken as the average of the inlet and outlet air temperatures. This implies iteration since the heat transfer rate from the fins have to be determined using a chosen air temperature first, before the rise in air temperature can be calculated. The rise in cooling air temperature is:

$$\Delta T_{air} = \frac{\dot{Q}}{(\dot{m}C_p)_{air}} \tag{5.54}$$

Fin thermal capacitance

For transient heat transfer from a heat pipe to a fin, heat will not only be transferred from the fin surface to the air, but also will be absorbed by the fins themselves, causing a temperature rise. The fin is divided into five control volume segments, shown in figure 5.8.

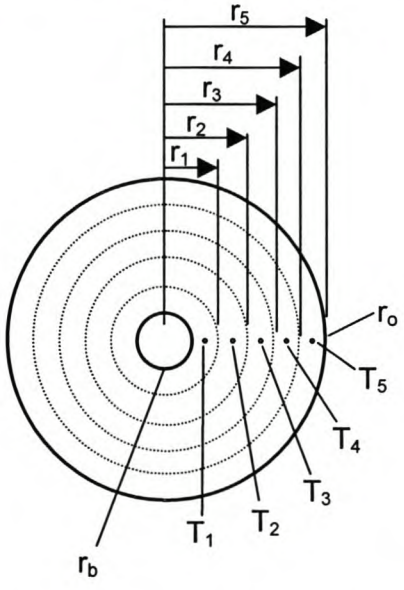

Figure 5.8 Fin control volumes for thermal capacitance

For the fin considered (see section 4.2), the radii are as follows:

r_b = 0.01m r_1 = 0.0155m r_2 = 0.021m

r_3 = 0.0265m r_4 = 0.032m $r_5 = r_o$ =0.0375m

so that

$r(T_1)$ = 0.01275m $r(T_2)$ = 0.01825m $r(T_3)$ = 0.02375m

$r(T_4)$ = 0.01275m $r(T_5)$ = 0.02925m

To find the temperatures T_i as shown in figure 5.8, the temperatures of the fin at the corresponding radii ($r(T_i)$) need to be known. The average temperature of the i^{th} control volume is assumed to be the temperature T_i at position $r(T_i)$. Consider the following variable transformations:

$$\theta = \frac{T(r) - T_a}{T_b - T_a} \quad \text{and} \quad z = \beta r \tag{5.55}$$

so that:

$$z_b = \beta r_b \quad \text{and} \quad z_o = \beta r_o \tag{5.56}$$

The temperature at any radius is given as (Mills, 1992):

$$\theta = C_1 I_o(z) + C_2 K_o(z) \tag{5.57}$$

with:

$$C_1 = \frac{K_1(z_o)}{F} \quad \text{and} \quad C_2 = \frac{I_1(z_o)}{F} \tag{5.58}$$

and:

$$F = I_0(z_b)K_1(z_o) + I_1(z_b)K_0(z_o) \tag{5.59}$$

The mass of control volume i is given by:

$$m_{cv}(i) = \rho_{al}(2t_f)\pi(r_i^2 - r_{i-1}^2) = (2)(2770)(0.00075)\pi(r_i^2 - r_{i-1}^2) = 13.0533(r_i^2 - r_{i-1}^2) \tag{5.60}$$

(where $r_{(0)} = r_b$)

The temperature change of the control volume is defined as:

$\Delta T_{cv(i)} = T_{i(current\ time\ step)} - T_{i(previous\ time\ step)}$, and the heat transfer rate absorbed by a control volume is:

$$\dot{Q}_{cv(i)} = \frac{m_{cv(i)} Cp_{al} \Delta T_{cv(i)}}{\Delta t} \tag{5.61}$$

For a total number of N fins, the heat transfer rate absorbed by the fin mass is therefore:

$$\dot{Q}_{fin\ mass} = N \cdot \sum_{i=1}^{5} \dot{Q}_{cv(i)} \tag{5.62}$$

5.3 THERMAL MODELLING OF THE MOULD HEATING CASE

5.3.1 MODEL STRUCTURE

This model corresponds to the experimental work, described in section 4.3. (Refer to figures 4.14 and 4.15 for more descriptive details) This experiment was modelled using finite element methods (standard FEM program, NASTRAN 2 for Windows), which is a suitable method to model complex geometries with. It can be seen from figure 5.9 that the design is symmetric around both the x-z and the y-z planes. The symmetry implies that the heat flux over these planes must be equal to zero. Effectively, this means that the set-up can be modelled by a quarter of the design "cut out" along the centre-lines, with insulated boundaries on these cut-lines. The surfaces that are open to atmosphere are given radiation and convection boundary conditions. A heating element has a magnesium oxide (MgO_2) core, around which resistance wire is spun. Around this, another thin layer of magnesium oxide is added, so that the wire is electrically insulated. This is surrounded by a thin stainless steel shell. The heating element is modelled in two ways, as shown in figure 5.10 The first model describes the element more or less as it is made, with a MgO_2 core, surrounded by a layer of resistance wire material, and an outer insulation layer made of MgO_2 The heat is generated only by the resistance wire material. The second model assumes a homogeneous heating element material, with yet to be determined properties.

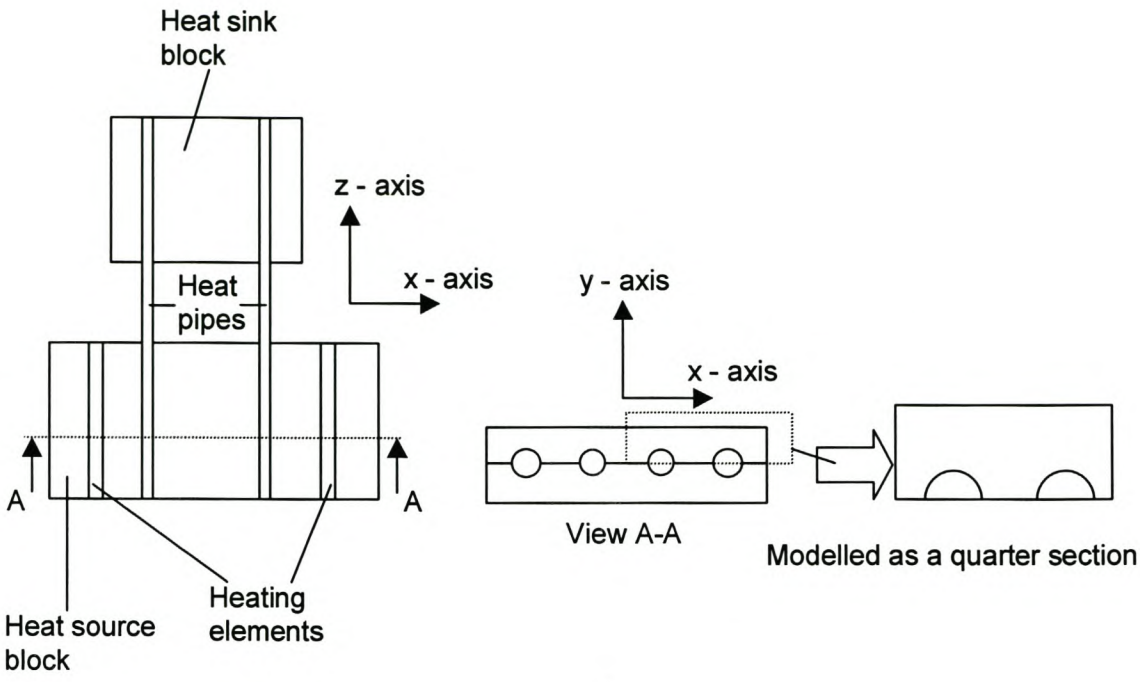

Figure 5.9 Conceptual modelling for the mould heating case

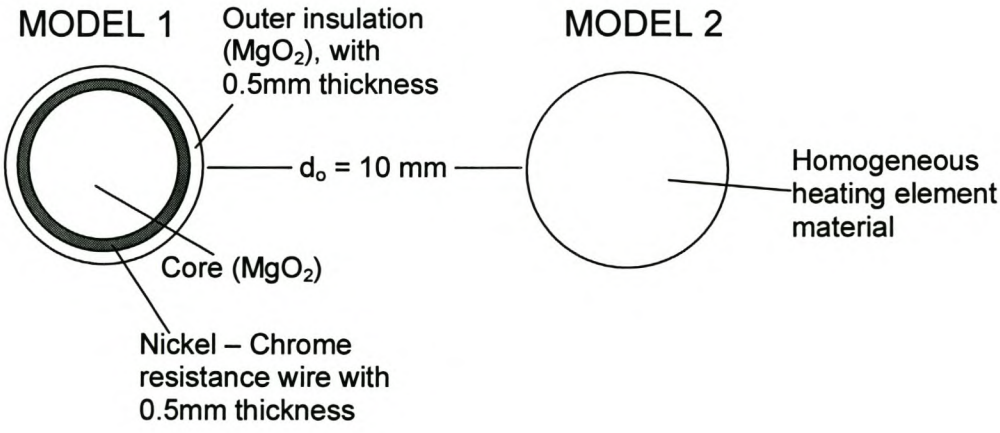

Figure 5.10 Cross sections of the two models used for the heating elements

The model for the mould heating case is discretised into finite elements and the structures are shown in figures 5.11 (a-c). The material properties used for the model are given in appendix A.

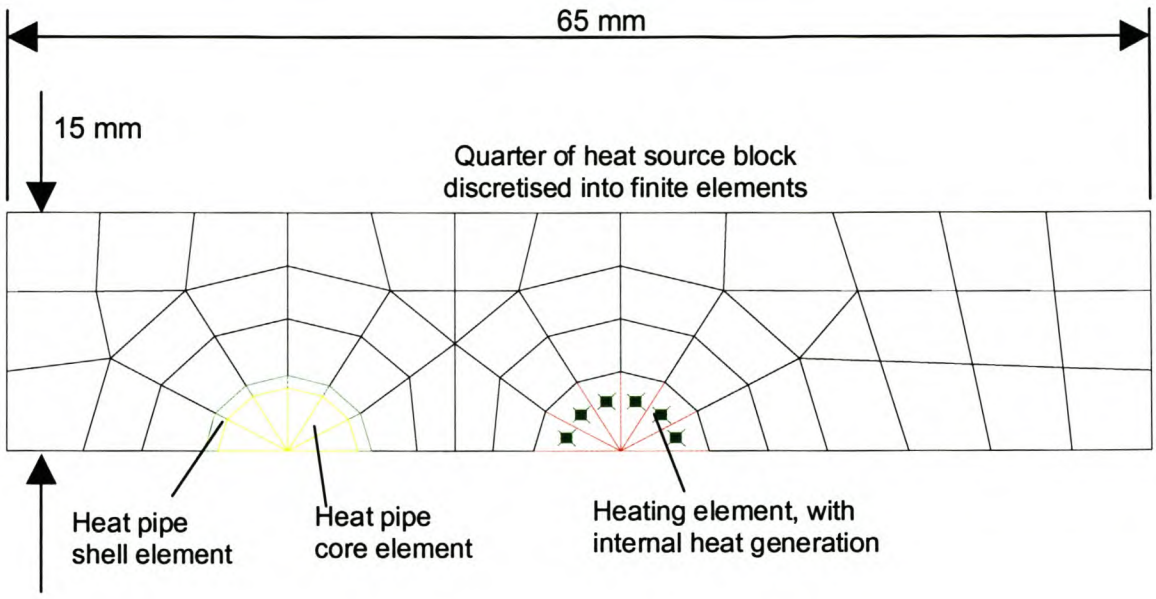

Figure 5.11.a Side view of finite element model for the mould heating case

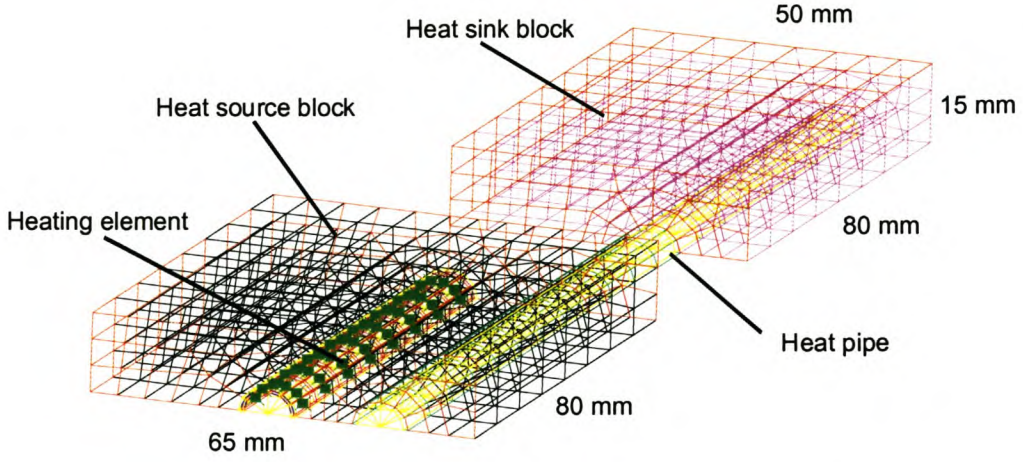

Figure 5.11.b Three dimensional view of finite element model for the mould heating case

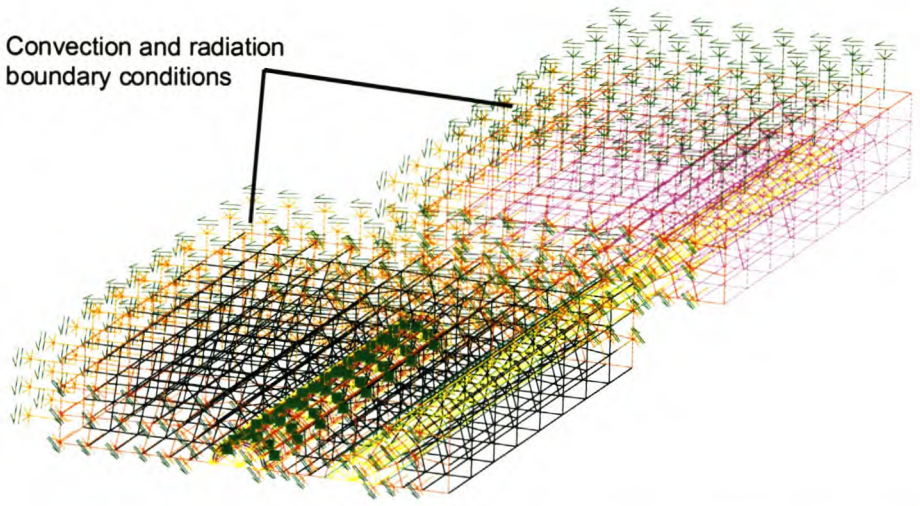

Figure 5.11.c Three dimensional finite element model for the mould heating case, showing convection and radiation boundary conditions on selected surface elements

5.3.2 CONVECTION AND RADIATION BOUNDARY CONDITIONS

The finite element program used assumes an insulated boundary if no boundary conditions are given. (Such as is the case at the symmetry planes). It is necessary to define convection and radiation boundary conditions on the surfaces that are open to the surroundings. Radiation boundary conditions require that the surface emissivity is known. For real life steel surfaces, and therefore casting moulds, this value is hard to determine unambiguously since relatively large changes in the value can occur with different temperatures, surface finish, oxide layers and so on. For instance, polished steel has an emissivity of around $\varepsilon = 0.05$, a clean steel casting has values of around $\varepsilon = 0.52 - 0.56$, and steel oxide has a value of around $\varepsilon = 0.8$ (Modest, 1993) The newly machined mould surfaces were relatively bright, but during the experiments oxide layers formed on the surface because of the high temperatures involved. Since the surface is somewhere in between bright and heavily oxidised, an approximate value for this experiment was chosen as:

$$\varepsilon_{steel} = \frac{0.1 + 0.8}{2} = 0.45 \qquad (5.63)$$

Natural convection is assumed to take place on the open boundary surfaces. The surfaces for the design is assumed to be one of two, either a horizontal, or vertical flat plate type. There are three areas of interest here. The first area is the (vertical) sides of the heat source and heat sink block, with height 30mm. The two other areas are the horizontal surfaces of the heat source block (80x130mm) and the heat sink block (80x100mm). These two surfaces are further classified as being heated and facing upwards or downwards.

Using the equations for natural convection given in section 3.4.1 the heat transfer coefficient can be determined as a function of wall temperature and the results are shown in figure 5.12

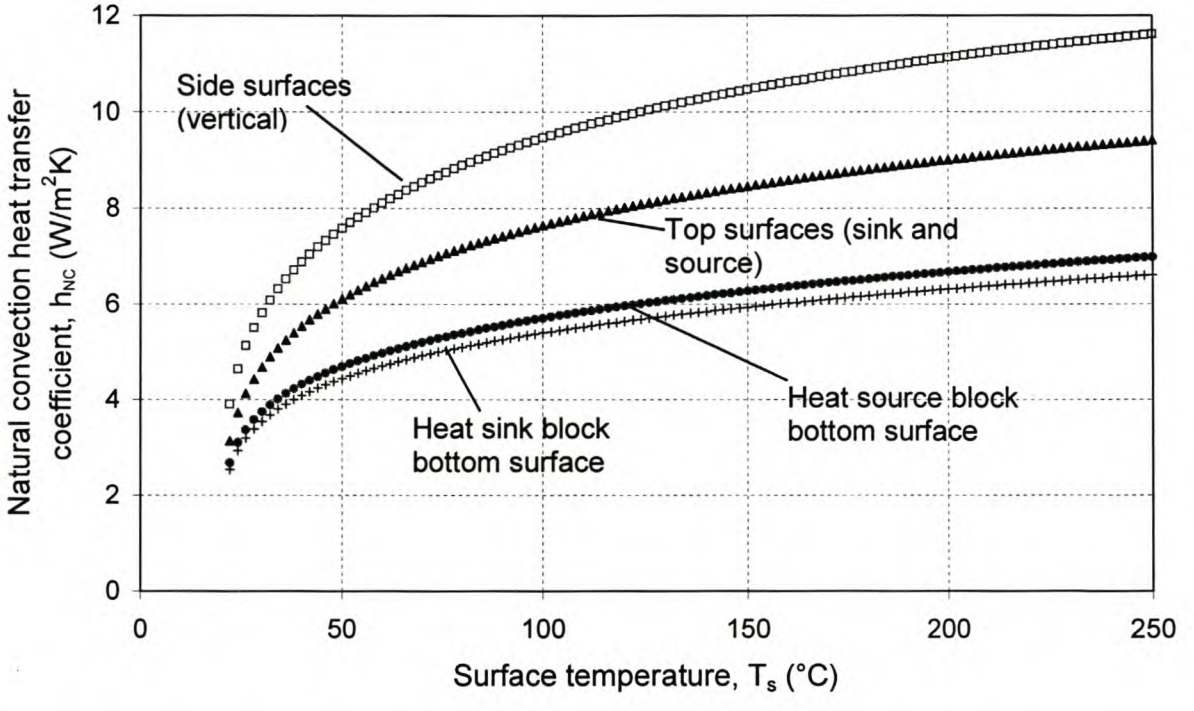

Figure 5.12 Heat transfer coefficients for the mould heating case as a function of surface temperature, assuming an ambient temperature of 20°C

5.3.3 THERMAL LOADS

The thermal load for the mould heating simulation is produced by the internal heat generation through the heating elements. The power input into the heating elements is known. The heat generation is modelled as a power (W) generated per volume (m^3), and assigned to the relevant elements, and coupled to time dependant functions. For a power input P the heat

generation would simply be given as $\dot{Q}''' = \frac{P}{V}$, and for the first model (the resistance wire model) the heat generation in the resistance wire is:

$$\dot{Q}'''_{rw} = \frac{P}{\frac{\pi(0.009^2 - 0.008^2)}{4}(0.08)} = 468102.8(P)\ W/m^3 \qquad (5.64)$$

whereas for the homogeneous heating element it is:

$$\dot{Q}'''_{hom} = \frac{P}{\frac{\pi(0.01)^2}{4}(0.08)} = 159154.9(P)\ W/m^3 \qquad (5.65)$$

5.3.4 NUMERICAL SOLUTION PROCESS

The model is solved by using the NASTRAN FEM program. The results achieved by using this finite element program for the thermal modelling of the mould cooling case can be found in section 6.3.

5.4 THERMAL MODELLING OF THE CORE COOLING CASE

5.4.1 MODEL STRUCTURE

The core cooling case is shown schematically in figure 5.13 and consists of five parts, which are the casting, the core, the external mould, the heat pipe and the fins. The objective is to determine what the influence of the heat pipe and air cooled fin is on the core temperature. The thermal circuit for the core cooling case is shown in figure 5.14.

The casting, core and external mould

The core and the external mould are cylindrical and symmetrical around the axial axis. The core and mould are therefore modelled by using finite difference methods for cylindrical coordinates. The condition of axial symmetry can be used and only a two dimensional grid has to be constructed for the three dimensional model.

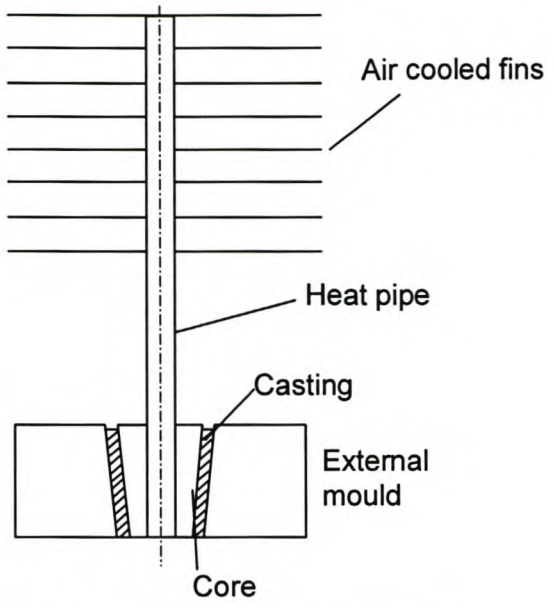

Figure 5.13 Schematic of core cooling model

The numerical modelling of the casting, core and external mould (using finite differences) is described completely in appendix C and will therefore not be discussed any further in this section. There is a slight difference between the finite difference model and the real casting, since the model does not include the slight taper, but assumes straight walls.

The heat pipe

The heat pipe is modelled as two thermal resistances, namely the condenser and evaporator resistances, as illustrated for instance in figures 5.5 and 5.14. The heat transfer coefficients for the evaporator and condenser ends, h_e and h_c, are experimentally determined as functions of the heat flux, the internal temperature and the temperature difference between the evaporator and condenser walls (refer to section 6.1, equations 6.1 to 6.4). If these equations are to be used, the heat transfer coefficient has to be found iteratively and the non-linear functions can lead to instabilities during numerical simulation. Therefore it would be better if constant heat transfer coefficients can be used.

Consider figure 6.11, where the experimentally measured heat transfer rate through the heat pipe is given as a function of the temperature difference, T_{ewo} - T_{cwo}. For the standard heat

pipe, the heat transfer rate is around 250 W for a temperature difference of 75 °C, and therefore the total thermal resistance is:

$$R_{hp} = \frac{\Delta T}{\dot{Q}} = \frac{75}{250} = 0.3\ K/W \tag{5.66}$$

The values in figure 6.11 were calculated from the experimental data obtained by performing experiments 1.1 to 1.6 and experiments 1.11 to 1.15 in table 4.1, regarding the determination of the heat pipe thermal characteristics. For these experiments, the evaporator length $L_e = 80$ mm, the condenser length $L_c = 110$ mm and the diameter $d = 12.7$ mm (1/2"). Thus,

$$R_e + R_c = \frac{1}{h_e \pi (0.0127)(0.08)} + \frac{1}{h_c \pi (0.0127)(0.11)} = \frac{313.30}{h_e} + \frac{227.85}{h_c} = 0.3 \tag{5.67}$$

Assuming that the evaporator and condenser heat transfer coefficients are equal,

$$h_e = h_c = \frac{313.30 + 227.85}{0.3} = 1803.8 \approx 1800\ W/m^2K \tag{5.68}$$

For the core cooling case, the heat pipe is embedded 80 mm deep into the core thus $L_e = 0.08$ m and the fin length is 150 mm, thus $L_c = 0.15$ m. Using the heat transfer coefficient in equation 5.68:

$$R_{e(core\ cooling)} = \frac{1}{h_e A_{ewo}} = \frac{1}{1800\pi(0.0127)(0.08)} = 0.1741\ K/W \tag{5.69}$$

and

$$R_{c(core\ cooling)} = \frac{1}{h_c A_{cwo}} = \frac{1}{1800\pi(0.0127)(0.11)} = 0.1266\ K/W \tag{5.70}$$

The fins

The fins are modelled as described in section 5.2, using the duct (hydraulic diameter based) convection coefficient and includes the lumped thermal capacity of the fin.

The solder resistances

From equation 5.31, k_{solder} = 46.3 W/mK. The diameters of the holes drilled into both the core and the fins, are 13.5 mm, while the outside diameter of the heat pipe is 12.7 mm. The thermal resistances are therefore:

$$R_{se} = \frac{\ln(13.5/12.7)}{2\pi(46.3)(0.08)} = 0.002625\ K/W \tag{5.71}$$

$$R_{sc} = \frac{\ln(13.5/12.7)}{2\pi(46.3)(0.15)} = 0.00134\ K/W \tag{5.72}$$

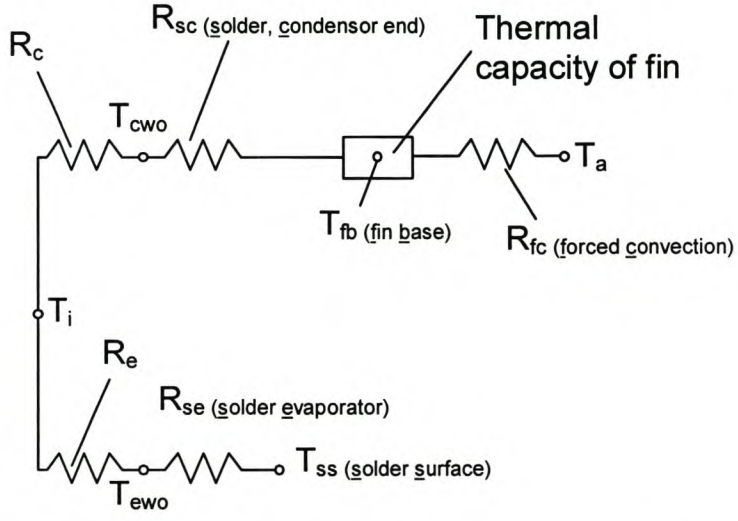

Figure 5.14 Thermal resistances of heat pipe and fins (assuming T_{ss} is calculated by finite differences)

5.4.2 CONVECTION AND RADIATION BOUNDARY CONDITIONS

For the mould surfaces that are open to atmosphere, an emissivity of $\varepsilon = 0.45$ is assigned, as is explained in section 5.3.2. There are two surfaces of importance as far as the convection is concerned. The first is the side of the external mould, modelled as a vertical plate, with height 100mm. The second is the top surface, which is approximated by a rectangular horizontal strip, 52.5mm wide, facing upwards and being heated. Using the convection equations in chapter 3, figure 5.15 shows the relevant boundary conditions as functions of surface temperature.

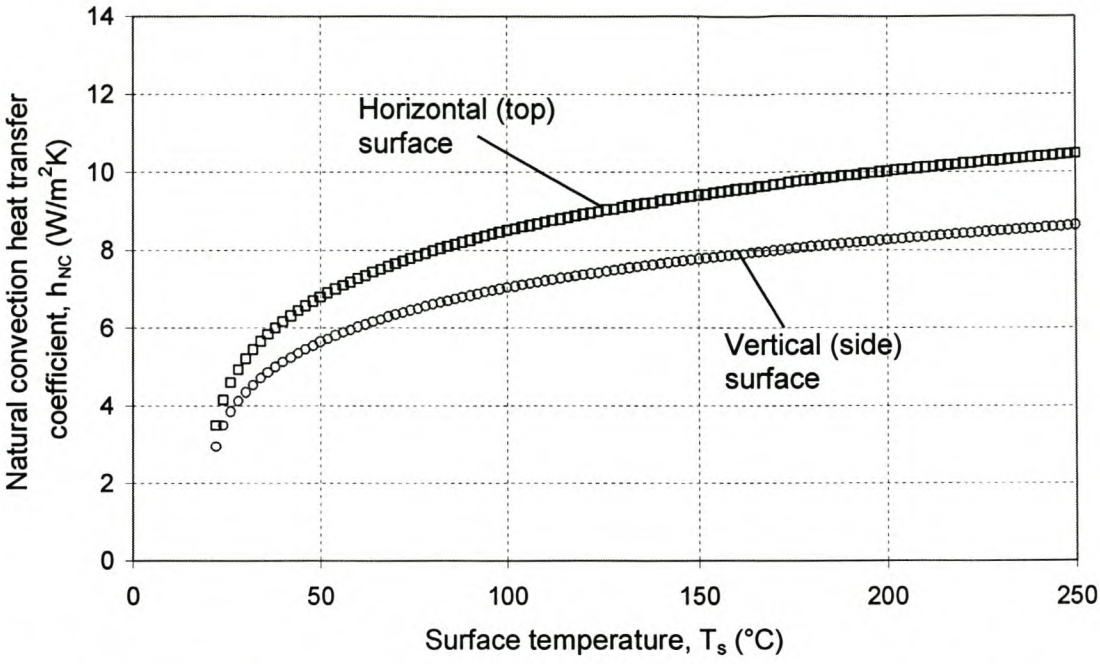

Figure 5.15 Convection heat transfer coefficients for the core cooling case as a function of wall temperature, assuming an ambient temperature of 20°C

5.4.3 THERMAL LOADS

The heat source in this case is the molten tin that is cast in between the core and the external mould. As is described in section 5.4.1, the temperature of the tin and mould can be used to determine the amount of energy that leaves the casting over a period of time. This can be used to determine the new casting temperature.

Tin's melting point is at around 232°C. Thus, when the temperature reaches 232°C, the fusion energy of the tin needs to be considered. The mass of the tin casting is $m = \frac{\pi(0.0425^2 - 0.0225^2)}{4}(0.08)(7310) = 0.597\ kg$, and if it is accepted that when the temperature first reaches 232°C, the casting is still pure liquid, the energy that needs to be rejected by the casting to become 100% solid, is therefore:

$$E = m\lambda_{tin} = (0.597)(15156) = 9048.1\ J \qquad (5.73)$$

For each consecutive time step, the amount of energy lost from the casting is subtracted from this amount of fusion energy. As long as the remaining amount of energy is larger than zero, the temperature is kept at 232°C. As soon as this amount is equal or less than zero, complete solidification is assumed and the temperature difference is once again calculated by using the specific heat capacity of the tin.

5.4.4 NUMERICAL SOLUTION PROCESS

A computer program was written (using MATLAB) to calculate the temperatures and other desired outputs, such as the heat transfer rate through the heat pipe. The flow diagram of the program to show the solution process is presented in figure 5.16.

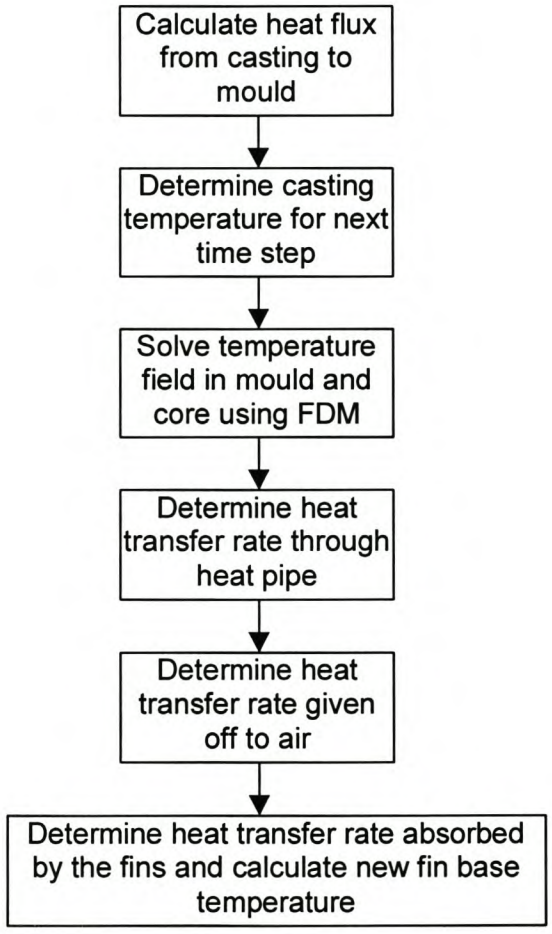

Figure 5.16 Flow diagram of numerical computer program

5.5 THERMAL MODELLING OF THE MOULD COOLING CASE

5.5.1 MODEL STRUCTURE

The mould cooling experiment is described in section 4.5. From figure 5.17 it can be seen that this design is symmetrical around the axes shown, which implies that only a wedge shaped section, one eighth of the total size, needs to be modelled theoretically. In order to cope with the relative complexity of the combination of the heat pipes, mould and heat sink, a FEM computer package (NASTRAN 2 for Windows) is used as the numerical tool. The finite element discretisations are shown in figures 5.18 (a to e).

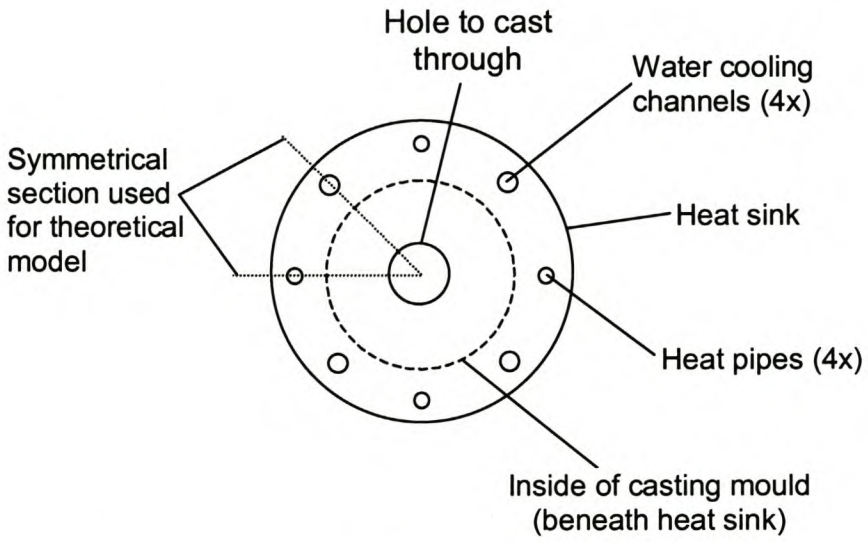

Figure 5.17 Schematic layout (top view) of model for the mould cooling case

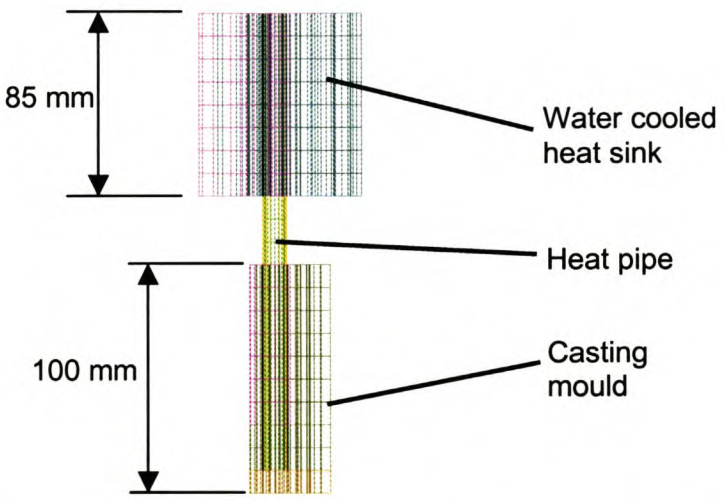

Figure 5.18.a Side view of finite element model for the mould cooling case

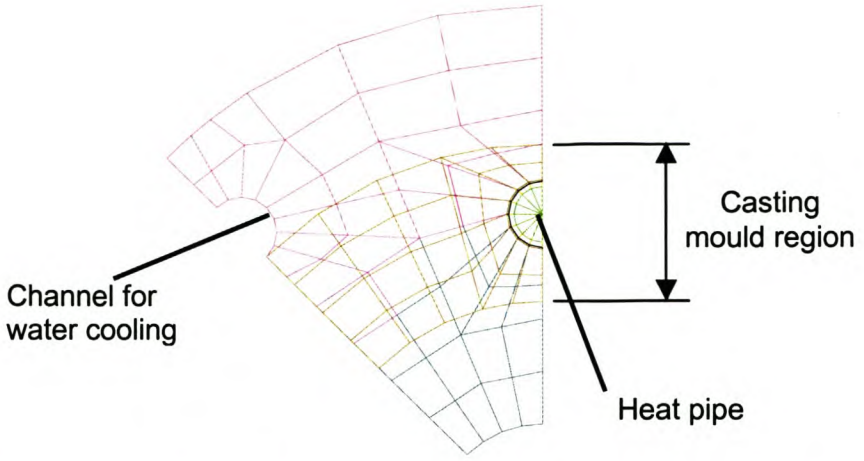

Figure 5.18.b Top view of finite element discretisation for the mould cooling case

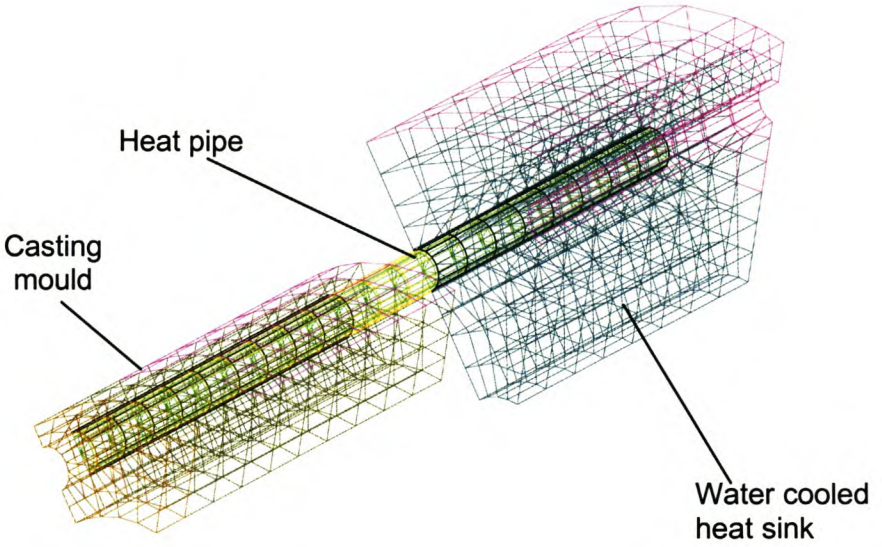

Figure 5.18.c Three dimensional view of finite element model for the mould cooling case

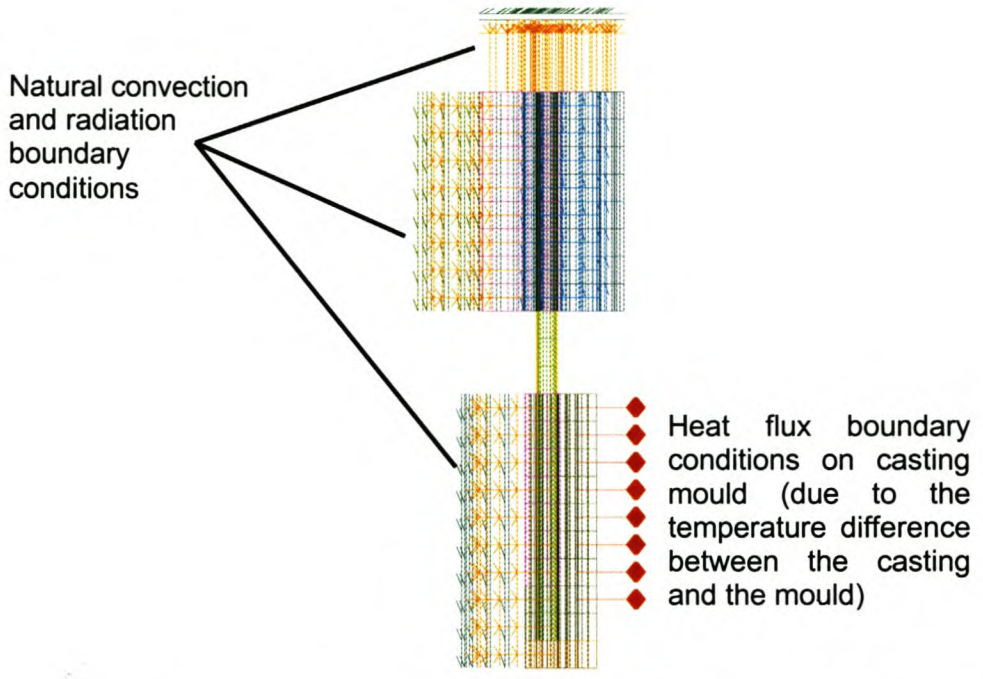

Figure 5.18.d Side view of the model for the mould cooling case, showing boundary conditions

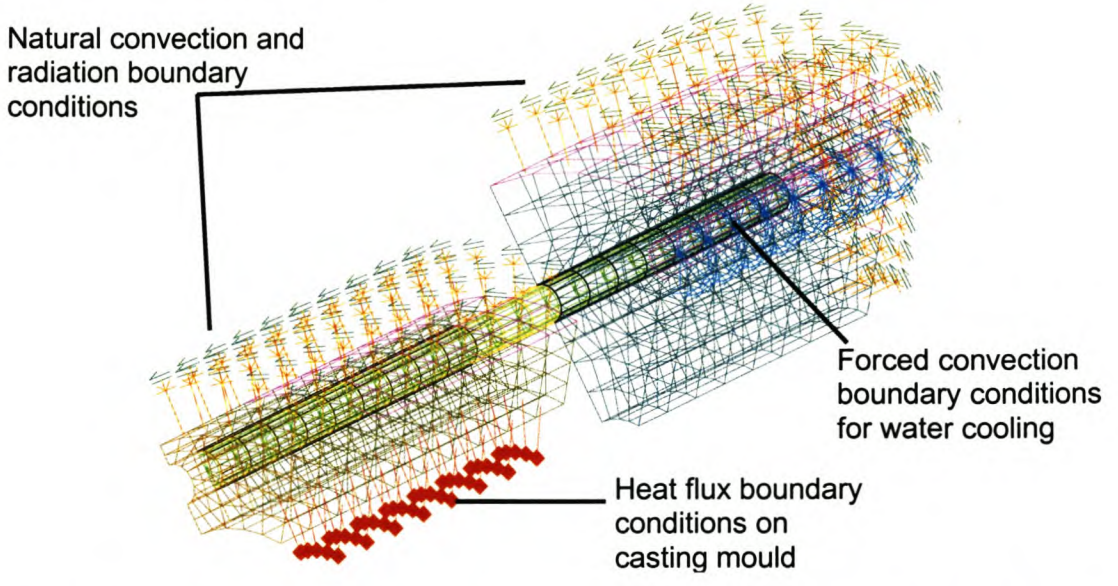

Figure 5.18.e Three dimensional view of finite element model for the mould cooling case, showing boundary conditions

5.5.2 CONVECTION AND RADIATION BOUNDARY CONDITIONS

During the experiments, the prolonged heat load of the casting in the mould and subsequent temperature rise of the mould and heat sink, caused oxidation layers to form on the steel surfaces – more so than was the case for the core cooling and mould heating cases. The emissivity value for radiation should therefore be closer to 0.8, which is the value for steel oxide. An emissivity value of $\varepsilon = 0.6$ is therefore chosen for this case.

The natural convection heat transfer coefficients for the two vertical surfaces (85mm and 100mm heights respectively), as well as the top horizontal surface, (assumed as a flat rectangular plate, with width = 60mm), are found as functions of surface temperature using the natural convection equations of chapter 3. Figure 5.19 shows the heat transfer coefficient for the surfaces.

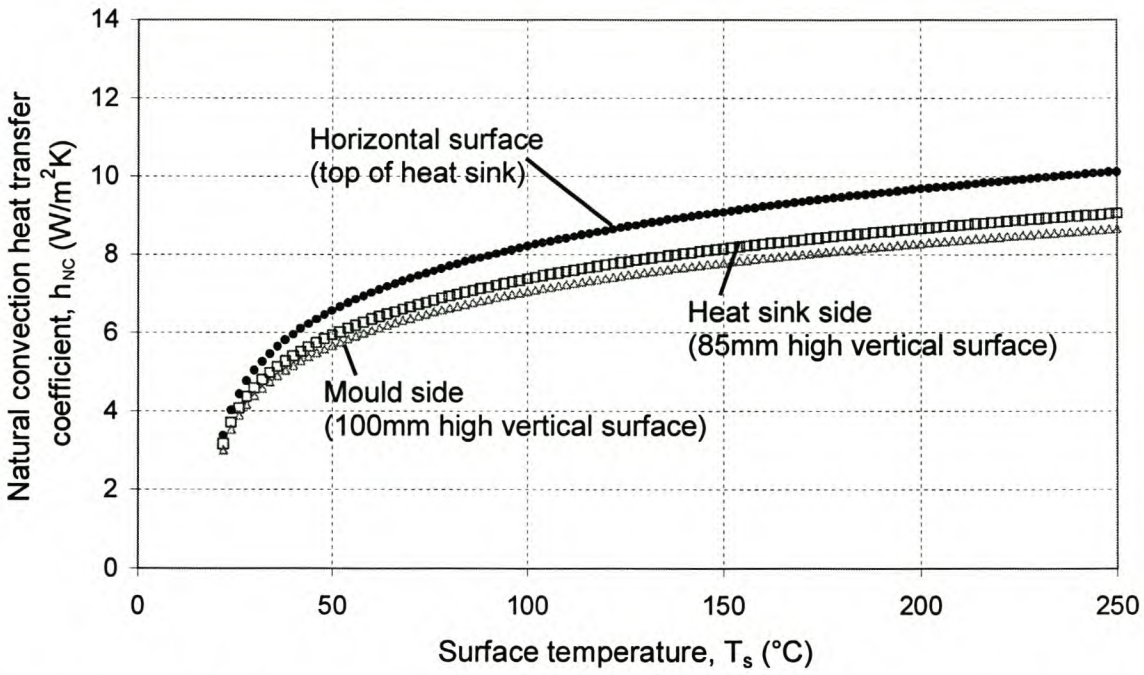

Figure 5.19 Natural convection heat transfer coefficients for the mould cooling model surfaces as a function of surface temperature, assuming an ambient temperature of 20°C

5.5.3 THERMAL LOADS

The thermal loads are caused by the hot casting inside the mould. As the casting cools, its heat is transferred to the surrounding mould (and from there to the heat sink via the heat

pipes). In order to accurately describe the temperature field inside the casting itself, one would need to model it using finite differences or finite elements. The standard FEM (NASTRAN) program does not have the capability to handle the solidification of the casting and furthermore the casting was removed from the mould for some of the experimental runs. Once the casting is modelled inside the mould with the finite elements, it cannot be removed during the numerical solution process. It is possible to create a finite difference model of the casting from which heat fluxes into the mould can be calculated, but the integration of these results with the NASTRAN program would necessitate changes to the NASTRAN program, which is not practical. To cope with this problem, the following approach had to be followed: The casting is modelled as a single control volume with a node at the "mid-area" diameter. The mid-area diameter is the diameter where the area (thus mass) of the part of the casting inside this diameter is equal to the part of the casting outside this diameter, and is calculated as $d_{mid} = \frac{d_{cast}}{\sqrt{2}}$.

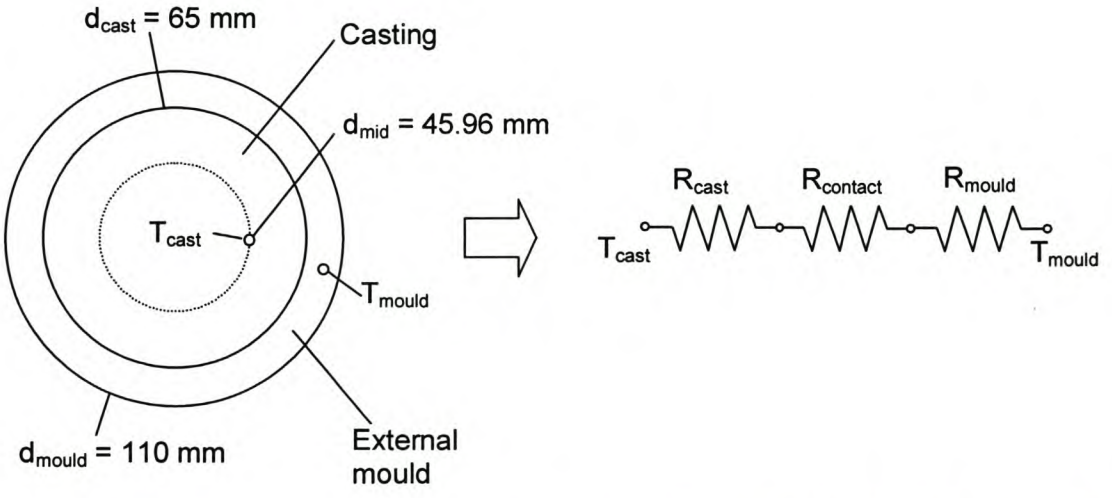

Figure 5.20 The thermal resistance components between casting (lumped mass model) and external mould

The thermal resistances shown in figure 5.20 are:

$$R_{cast} = \frac{\ln\left(\frac{d_{cast}}{d_{mid}}\right)}{2\pi k_{tin} L_{cast}} = \frac{\ln\left(\frac{65}{45.96}\right)}{2\pi(66.6)(0.08)} = 0.010354\ K/W \qquad (5.74)$$

$$R_{mould} = \frac{\ln\left(\frac{(d_{cast} + d_{mould})/2}{d_{cast}}\right)}{2\pi k_{steel} L_{cast}} = \frac{\ln\left(\frac{87.5}{65}\right)}{2\pi(50)(0.08)} = 0.011827\ K/W \tag{5.75}$$

The contact thermal resistance can be written as

$$R_{contact} = \frac{1}{h_{CR} A_{\text{int}}} = \frac{1}{h_{CR}\pi(0.065)(0.08)} = \frac{61.21}{h_{CR}} \tag{5.76}$$

The heat transfer rate per area flowing over the interface between the casting and the mould can therefore be expressed as:

$$\dot{q}'' = \frac{\left(T_{cast} - T_{mould}\right)\Big/\left(R_{cast} + R_{contact} + R_{mould}\right)}{\pi(0.065)(0.08)} = \frac{61.21\left(T_{cast} - T_{mould}\right)}{R_{cast} + R_{contact} + R_{mould}} \tag{5.77}$$

For each time step at which experimental temperatures is logged, the temperature of the mould is known, since it is measured by the thermocouples. Equation 5.77 can be used to estimate the amount of heat flux that left the casting, and hence a new theoretical casting temperature can be calculated for the following time step. The interfacial contact heat transfer coefficient is not known directly, but for the core cooling case (sections 4.4 and 5.4), h_{CR} = 700 W/m^{2}K produced acceptable results (see section 6.4 and appendix C). For the mould cooling case though, a value of h_{CR} = 500 W/m^{2}K produced theoretical results that are closer to the experimental results (refer to section 6.5 and also to chapter 8, where the difference between the contact resistance for the mould cooling and core cooling cases is discussed)

5.5.4 WATER COOLING OF HEAT SINK

To determine the heat transfer coefficient of the cooling water through the heat sink, the Dittus-Boelter equation can be used as:

$$Nu_D = 0.023\,\mathrm{Re}_D^{0.8}\,\mathrm{Pr}^{0.4} \tag{5.78}$$

The mass flow rate of the cooling water was measured to be approximately 0.15 kg/s. The water channels have a diameter of 10 mm. For water at around 17°C (which is close to the average ambient temperature during the experiments), the Reynolds number is:

$$\mathrm{Re}_D = \frac{4\dot{m}_{water}}{\pi\mu D} = \frac{4(0.15)}{\pi(11.0\times10^{-4})(0.01)} = 17362.4 \tag{5.79}$$

and the Prandtl number is $\mathrm{Pr} = 7.8$, so that the Nusselt number is:

$$Nu_D = 0.023(17362.4)^{0.8}(7.8)^{0.4} = 128.9 \tag{5.80}$$

The cooling water heat transfer coefficient is therefore:

$$h_{cw} = \frac{Nu_D k_{water}}{D} = \frac{128.9(0.591)}{0.01} = 7618\,W/m^2K \tag{5.81}$$

5.5.5 NUMERICAL SOLUTION PROCESS

An iterative approach is taken, combining the calculation of a theoretical casting temperature as a function of time (using a spreadsheet) and the determination of the theoretical mould and heat sink temperatures (using NASTRAN). Firstly a value of h_{CR} needs to be chosen. This can be used to find two outputs:

1) The theoretical temperature of the casting, T_{cast} (see figure 5.20) as a function of time

2) The casting-mould interfacial heat flux as a function of time

The interfacial heat flux can now be used as the thermal load input to the NASTRAN program. The theoretical temperatures for the mould and heat sink can be compared with the experimental temperatures. A new value of h_{CR} can now be chosen, guided by the theoretical results obtained. This will cause a new theoretical casting temperature and a new heat flux boundary condition, to be fed into the NASTRAN program. Inspection, rather than a formal convergence criteria is used to decide which value for h_{CR} is the most appropriate. The iteration process is also discussed in more detail in section 6.5, where supporting graphs are available.

CHAPTER 6 - Results

The processed experimental and theoretical results for the heat pipe thermal characteristics, the fins, the mould heating case, the core cooling case and the mould cooling case are presented in this chapter. Where applicable, the theoretical and experimental results are compared, so as to asses the accuracy, relevance and limitations of the theoretical models.

6.1 HEAT PIPE THERMAL CHARACTERISTICS

Results for the special heat pipe (the heat pipe with the thermocouple wells) and the standard 1/2"x12" heat pipe are presented, for both horizontal and vertical operation. The objective is to find the evaporator and condenser heat transfer coefficients. These coefficients are based on the thermal resistances presented by the wall, the wick-and-water structure and the evaporation / condensation, for any evaporator and condenser lengths, L_e and L_c. To find the thermal resistances and thus the heat transfer coefficients, the experimental procedure described in section 4.1 is followed, and the thermal model and equations described in section 5.1.4 are needed (refer to figure 5.5).

Sample calculations to determine the temperatures, heat transfer rates and heat transfer coefficients shown in figures 6.1 to 6.10, are given in Appendix B, where the results shown in figure 6.8 are calculated.

Vertical operation

The following graphs (figures 6.1 to 6.6) shows the processed results for the special heat pipe, for vertical operation, bottom heating mode.

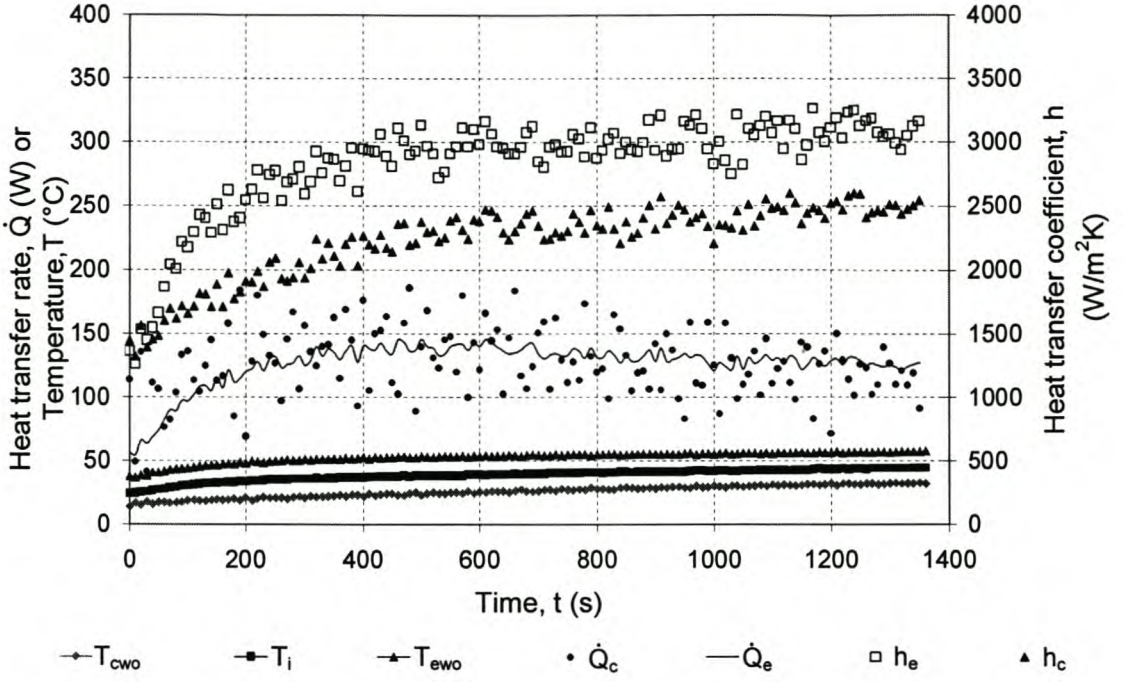

Figure 6.1 Temperatures, heat transfer rates and heat transfer coefficients for the special heat pipe versus time. (Based on experiment 1.1. The resistance wire voltage input = 40 V $\rightarrow \dot{Q}_{rw}$ = 167 W)

Figure 6.1 shows the evaporator and condenser wall temperatures as well as the internal temperature (average of the condenser and evaporator internal temperature) as a function of time. The experimentally determined heat transfer rates are also shown. The corresponding calculated heat transfer coefficients are shown as well. The evaporator heat transfer coefficient is somewhat higher than the condensation coefficient (3000 vs. 2500 W/m^{2}K). A relatively constant heat transfer rate of around 140 W is measured between 400 to 1400 seconds. The resistance of the resistance heating wire is 9.6 Ω, therefore the power input to the resistance wire is calculated as $\dot{Q}_{rw} = \frac{40^2}{9.6} = 167\,W$. This implies that there is a heat loss to the environment of between 25 - 30 W which is about 16% of the heat input. Although the averages of the heat transfer rates at the evaporator and condenser ends are close to one another (thus serving as an energy balance check for the two measurement methods used), the heat transfer rate at the condensor end, as measured by the circulating pumped water, shows much more fluctuation than is the case at the evaporator end. The reason is that the aluminium of the heating block only transfers heat towards the heat pipe through radial

conduction, and very minor temperature fluctuations are expected to take place. The temperature of the bulk mass of water, on the other hand, is subject to convection temperature gradients. An 0.05 °C temperature fluctuation of the water (at T_w = 25 °C), is equivalent to E = 2.5(4180)(0.05) = 523 J. The time interval over which temperatures are measured is 10 seconds, therefore an 0.05°C temperature difference would cause a 523/10 = 52.3 W fluctuation. Usually one would expect the heat transfer rate measured at the condenser end to be closer to the actual heat transfer rate through the heat pipe. In this case, the evaporator heat transfer rate is used instead, because of the fluctuations of the condenser heat transfer rate.

The same basic trends seen in figure 6.1, are present in figures 6.2 to 6.6, for the voltages over the resistance wire of the heating block being 50V, 60V, 70V, 80V and 90V.

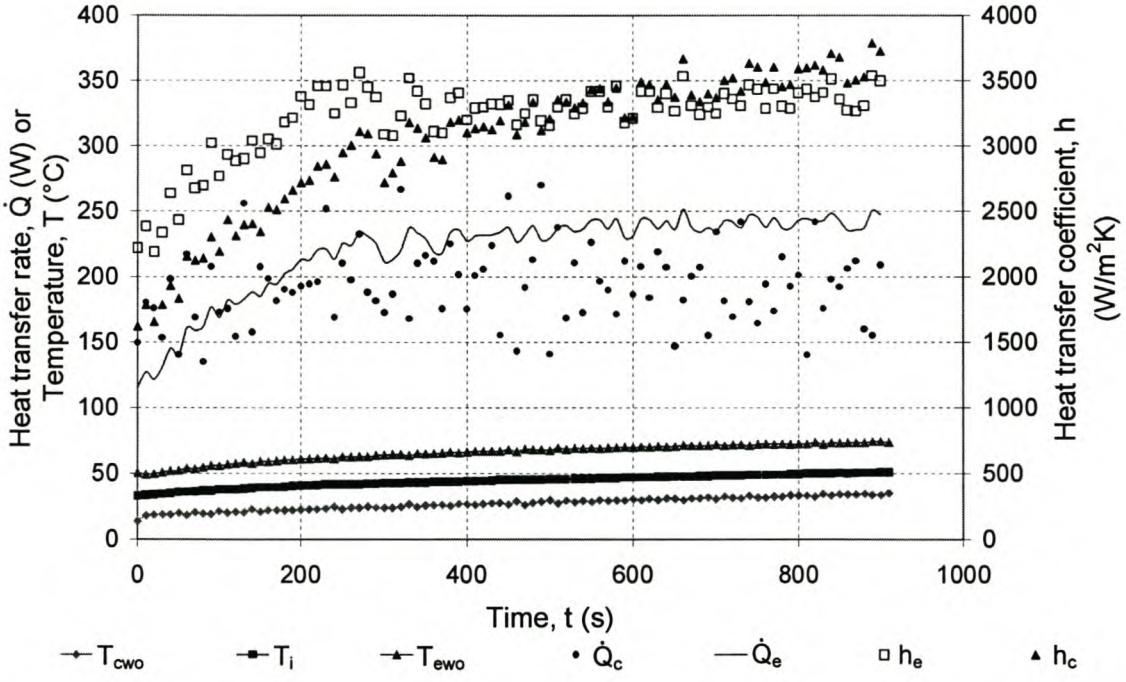

Figure 6.2 Temperatures, heat transfer rate and heat transfer coefficients for the special heat pipe versus time. (Based on experiment 1.2, with the resistance wire voltage input = 51V → $\dot{Q}_{rw}$ = 271 W)

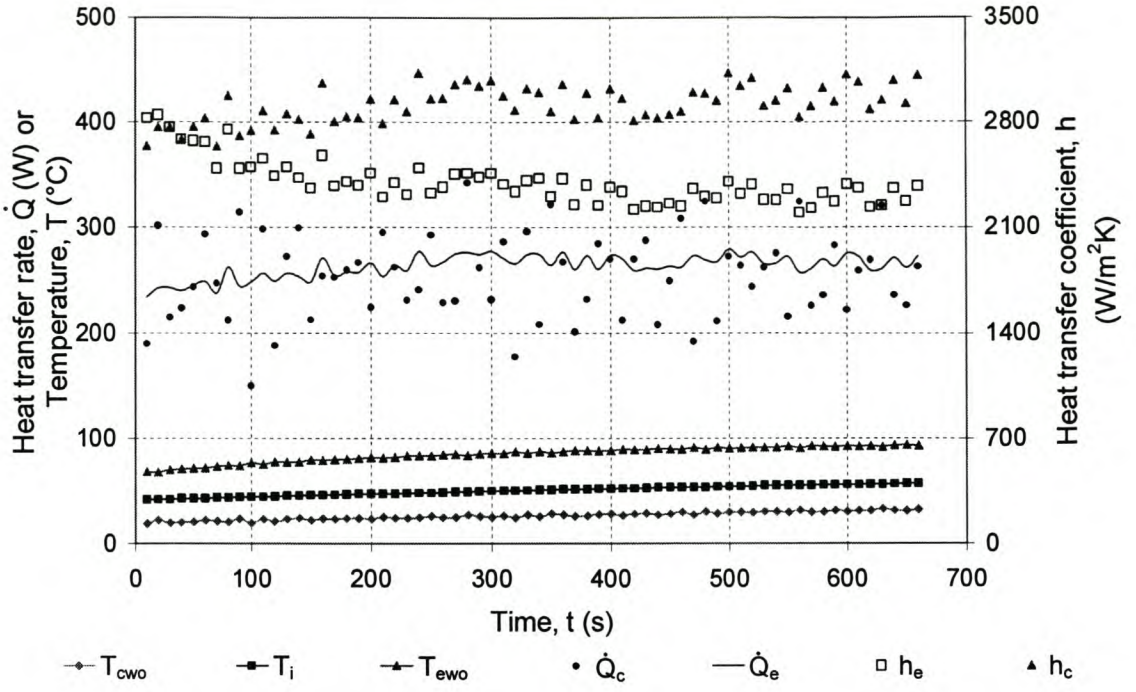

Figure 6.3 Temperatures, heat transfer rate and heat transfer coefficients for the special heat pipe versus time. (Based on experiment 1.3, with the resistance wire voltage input = 60V $\rightarrow \dot{Q}_{rw}$ = 375 W)

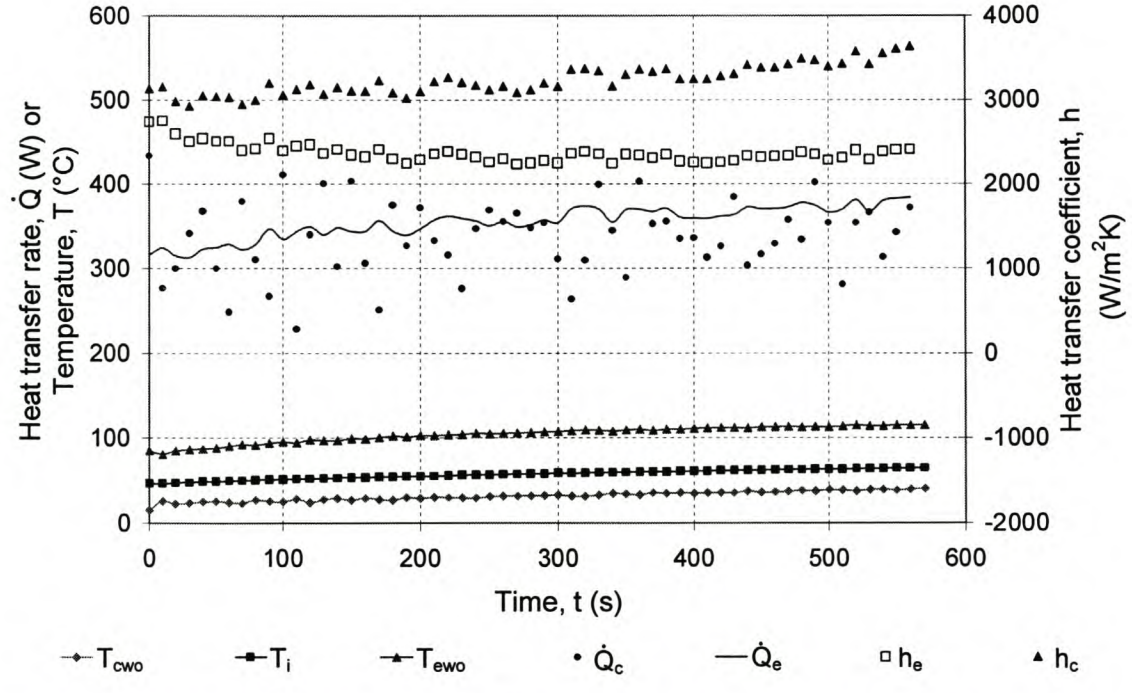

Figure 6.4 Temperatures, heat transfer rate and heat transfer coefficients for the special heat pipe versus time. (Based on experiment 1.4, with the resistance wire voltage input = 70V $\rightarrow \dot{Q}_{rw}$ = 510 W)

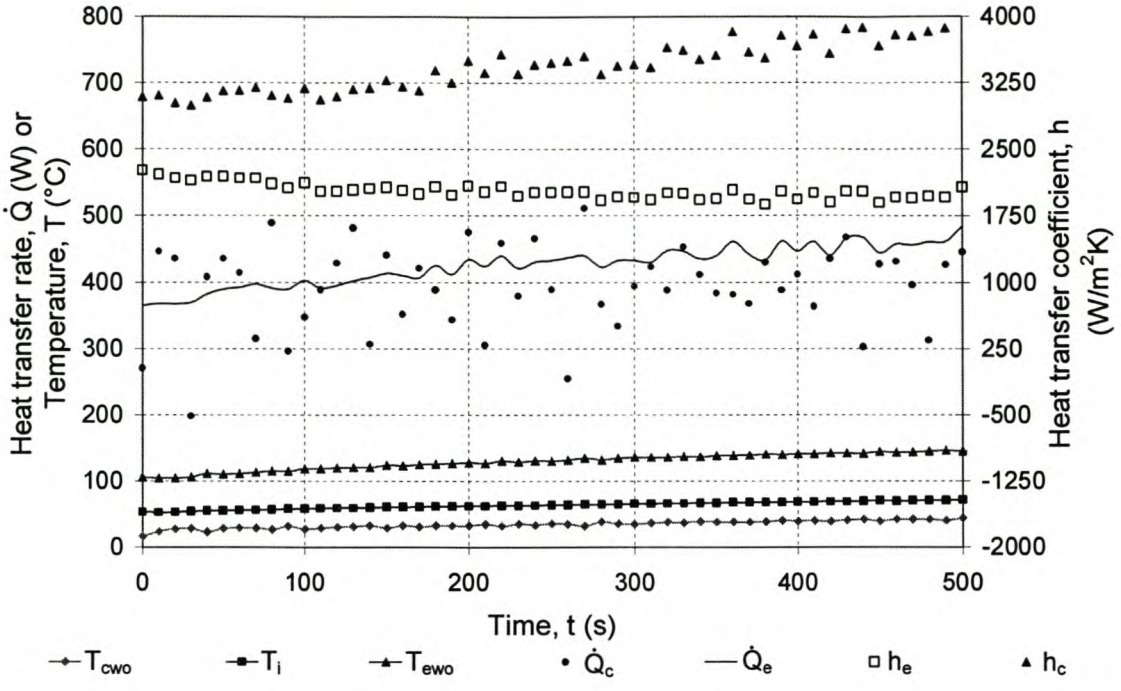

Figure 6.5 Temperatures, heat transfer rate and heat transfer coefficients for the special heat pipe versus time. (Based on experiment 1.5, with the resistance wire voltage input = 80V $\rightarrow \dot{Q}_{rw}$ = 667 W)

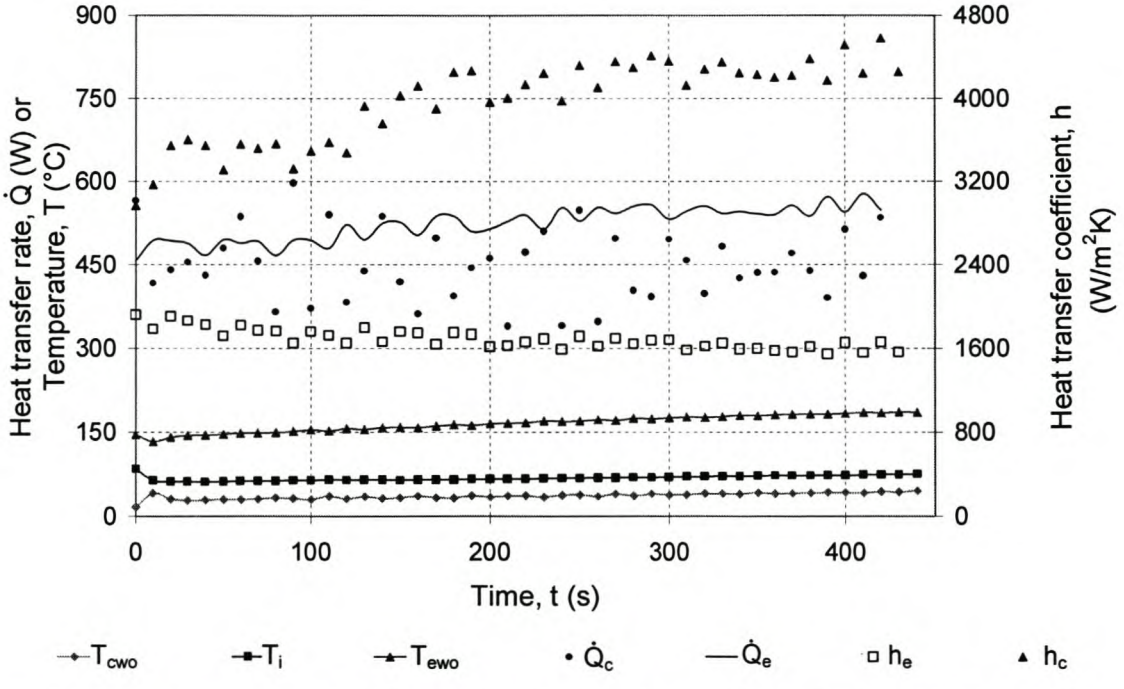

Figure 6.6 Temperatures, heat transfer rate and heat transfer coefficients for the special heat pipe versus time. (Based on experiment 1.6, with the resistance wire voltage input = 90V $\rightarrow \dot{Q}_{rw}$ = 844 W)

Horizontal operation

The graphs for horizontal operation are of the same type as for the vertical case and are shown in figures 6.7 to 6.10. For the vertical case, no clear maximum heat transfer rate could be established. For the horizontal operation, a maximum heat transfer rate of about 160 Watts can be observed (probably due do the capillary limit for horizontal operation). The internal temperature also undergoes a sudden change (jump) after a while, suggesting that a dry-out limit is reached. This is especially evident in figure 6.9 (see T_i).

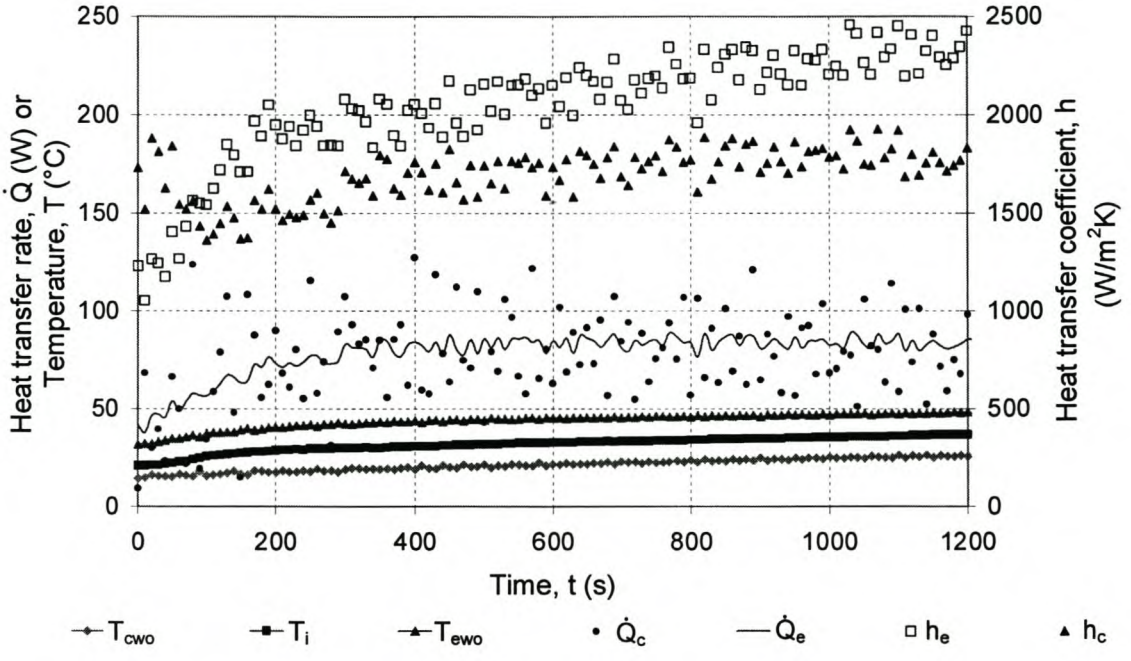

Figure 6.7 Temperatures, heat transfer rates and heat transfer coefficients for the special heat pipe versus time. (Based on experiment 1.7, with the resistance wire voltage input = 30V $\rightarrow \dot{Q}_{rw} = 94$ W)

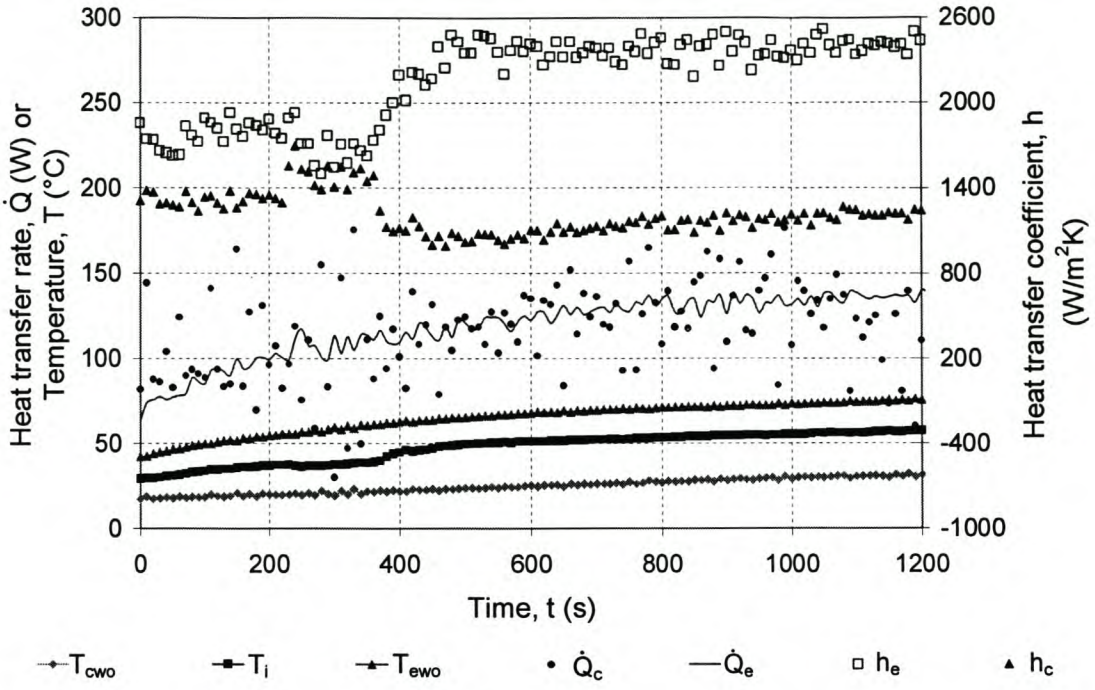

Figure 6.8 Temperatures, heat transfer rate and heat transfer coefficients for the special heat pipe versus time. (Based on experiment 1.8, with the resistance wire voltage input = 40V $\rightarrow \dot{Q}_{rw}$ = 167 W)

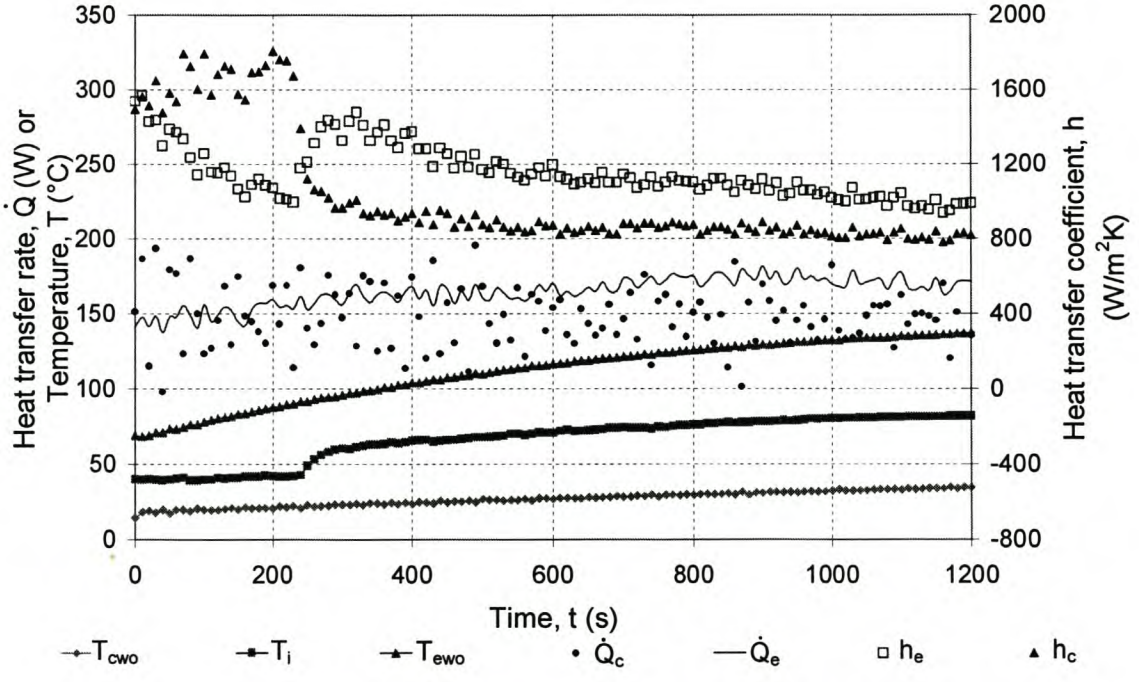

Figure 6.9 Temperatures, heat transfer rate and heat transfer coefficients for the special heat pipe versus time. (Based on experiment 1.9, with the resistance wire voltage input = 50V $\rightarrow \dot{Q}_{rw}$ = 260 W)

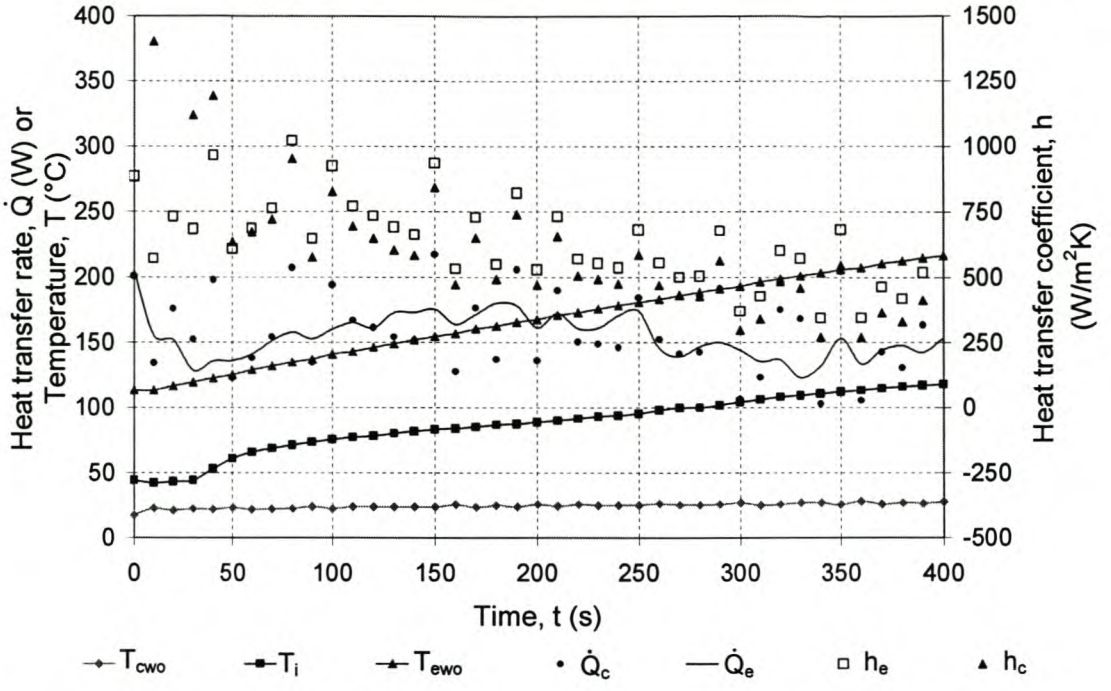

Figure 6.10 Temperatures, heat transfer rate and heat transfer coefficients for the special heat pipe versus time. (Based on experiment 1.10. The resistance wire voltage input = 75V $\rightarrow \dot{Q}_{rw}$ = 586 W)

Comparison between the special and standard heat pipes

The special heat pipe is fitted with thermocouple wells so that the internal temperature can be measured. To see what the effect, if any, of the thermocouple wells are on the performance of the heat pipe, tests were also performed on a standard heat pipe (experiments 1.11 to 1.18). Only the heat transfer rate as well as the condenser and evaporator wall temperatures were known in this case. The heating and cooling areas were the same as for the special heat pipe. The loads in this case were 30 V, 40 V, 60 V, 70 V and 85 V for the vertical case (bottom heating mode) and 40 V, 60 V and 75 V for the horizontal operation. The heat transfer rates versus the temperature difference between the evaporator and condenser wall are shown in figures 6.11 and 6.12.

From figures 6.11 and 6.12 it can be seen that there is probably no significant difference between the overall thermal resistances of the standard and special heat pipes.

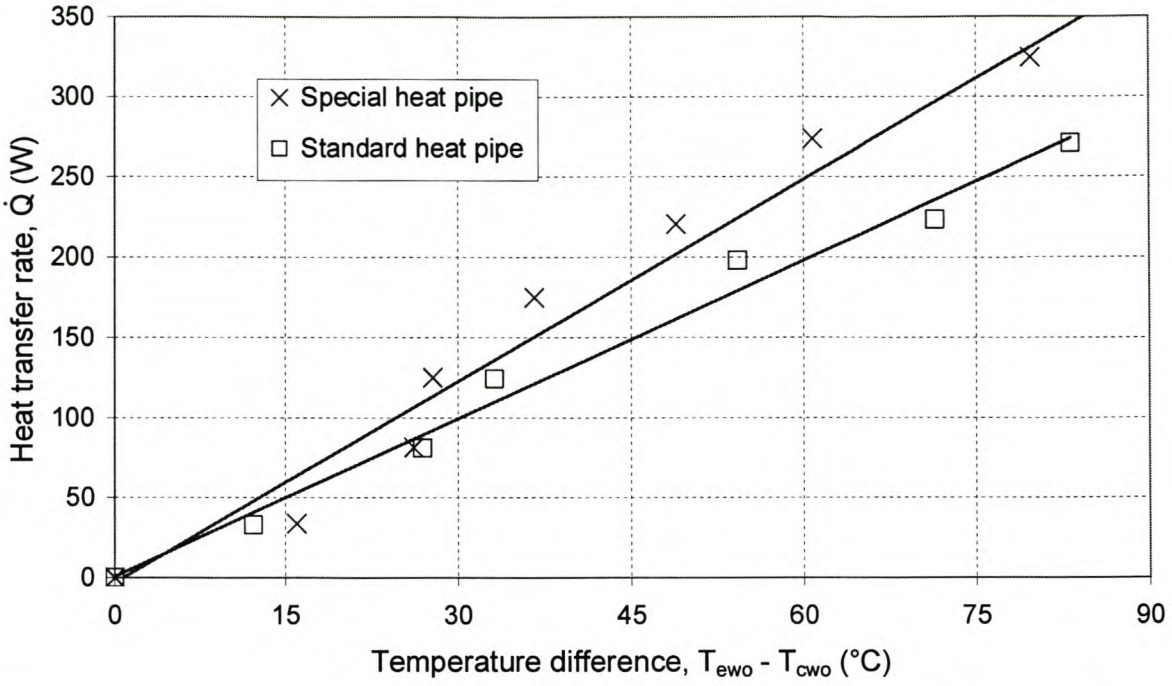

Figure 6.11 Comparison between heat transfer rate versus temperature difference for special and standard heat pipe (Vertical operation, bottom heating mode)

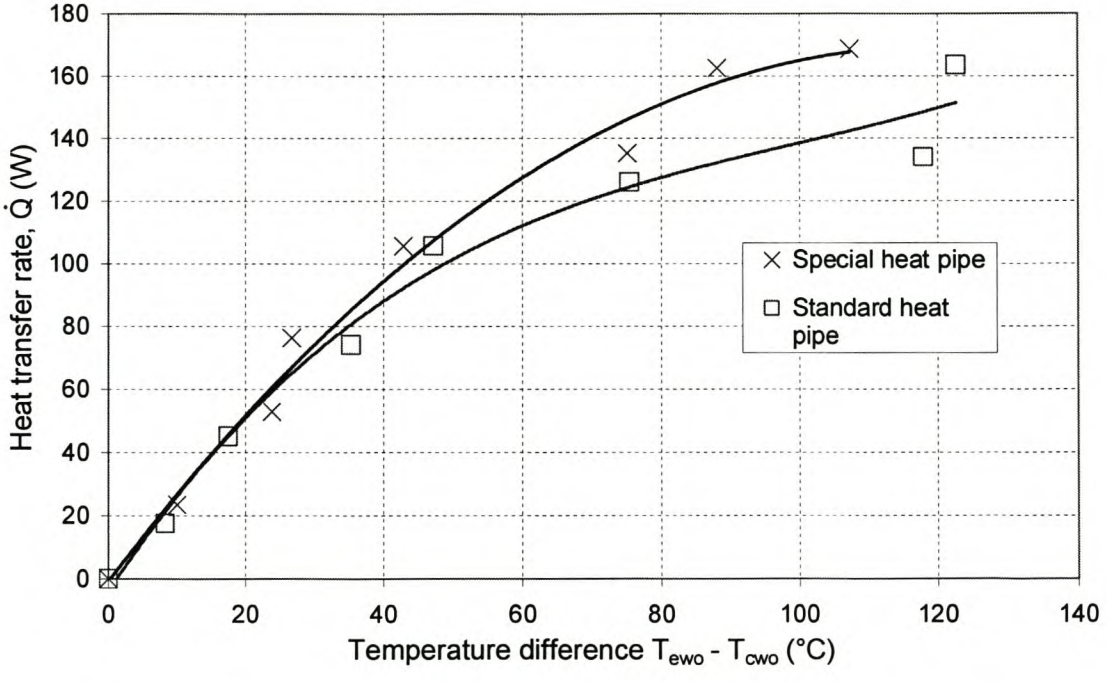

Figure 6.12 Comparison between heat transfer rate versus temperature difference for special and standard heat pipe (Horizontal operation)

As is discussed in section 5.1, the heat transfer coefficients of the heat pipe are expected to be functions of the heat flux, the internal temperature, and the temperature difference between the evaporator and condenser walls of the heat pipe. The graphs in figures 6.1 to 6.10, display the heat transfer coefficients, together with the outside wall temperatures of the condenser and evaporator, the internal temperature and the heat transfer rate, at time intervals of 10 seconds each. This known data can the be used in a multi-linear regression process (refer to equation 5.47, section 5.1), to determine correlations for the heat transfer coefficient as a function of the important variables. The results are given in equations 6.1 to 6.4.

Vertical operation (bottom heating mode)

$$h_{ewo} = 1.3877\left(\frac{\dot{Q}}{A_{ewo}}\right)^{1.152}\left(T_{ewo} - T_{cwo}\right)^{-1.343}\left(T_i\right)^{-0.0412} \tag{6.1}$$

$$h_{cwo} = 33.522\left(\frac{\dot{Q}}{A_{cwo}}\right)^{0.05934}\left(T_{ewo} - T_{cwo}\right)^{-0.10377}\left(T_i\right)^{1.0837} \tag{6.2}$$

Horizontal operation

$$h_{ewo} = 0.1471\left(\frac{\dot{Q}}{A_{ewo}}\right)^{1.16744}\left(T_{ewo} - T_{cwo}\right)^{-1.4992}\left(T_i\right)^{0.7127} \tag{6.3}$$

$$h_{cwo} = 5977.64\left(\frac{\dot{Q}}{A_{cwo}}\right)^{0.18653}\left(T_{ewo} - T_{cwo}\right)^{-0.17452}\left(T_i\right)^{-0.73147} \tag{6.4}$$

To get an idea of the goodness of fit of these correlations as compared to the experimentally determined values, comparisons are made in figures 6.13 to 6.16. From these figures it can be seen that the deviations between the correlations and the experimentally determined heat transfer coefficients for each case (equations 6.1 to 6.4) are between approximately 10% and 25%.

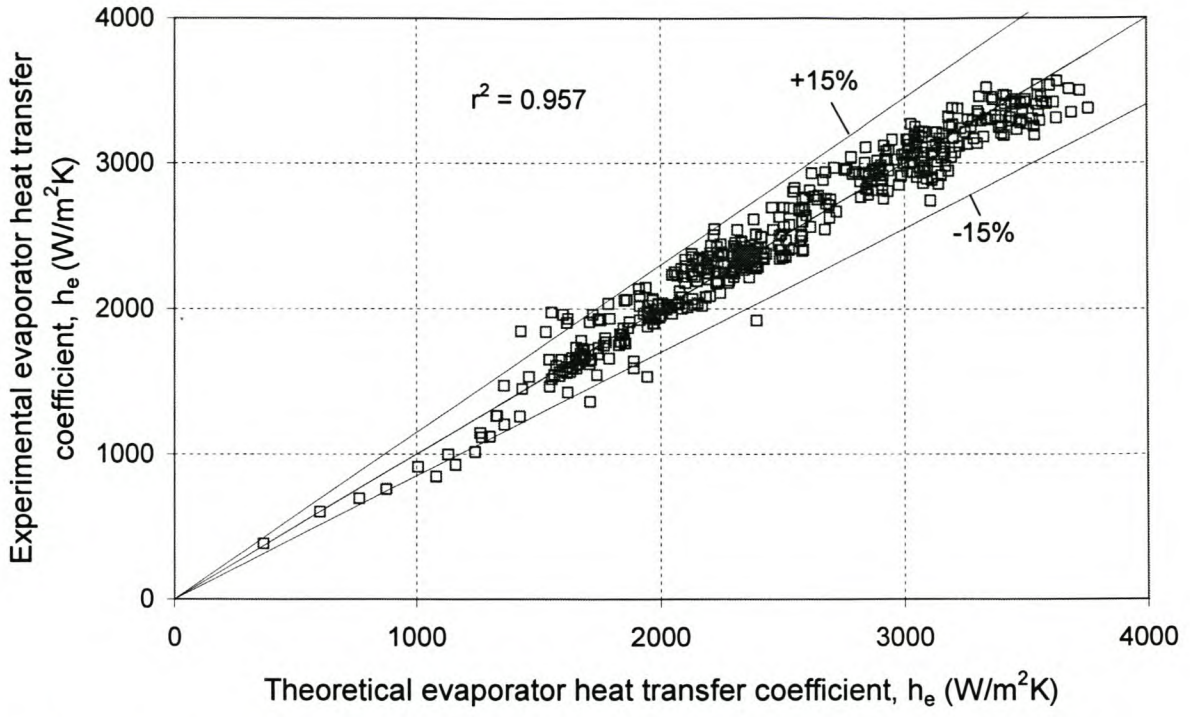

Figure 6.13 Comparison between experimental and theoretical (using equation 6.1) values for the evaporator heat transfer coefficient. Vertical operation. The correlation coefficient is $r^2 = 0.957$

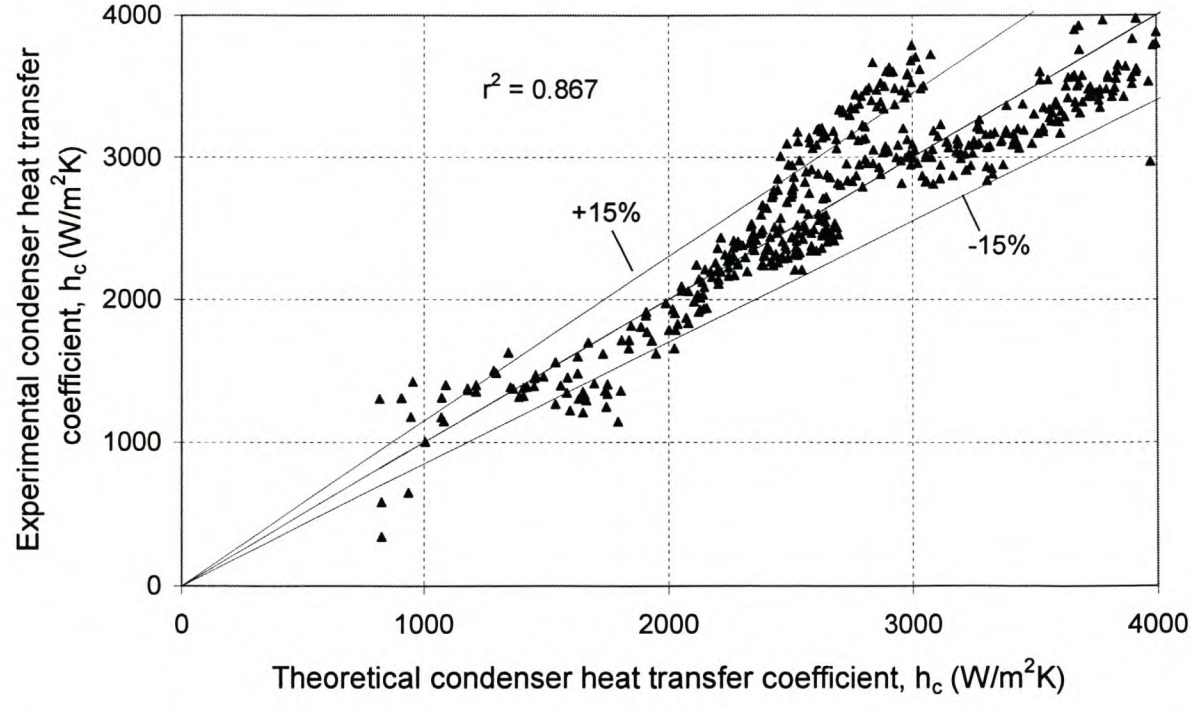

Figure 6.14 Comparison between experimental and theoretical (using equation 6.2) values for the condenser heat transfer coefficient. Vertical operation. The correlation coefficient is $r^2 = 0.867$

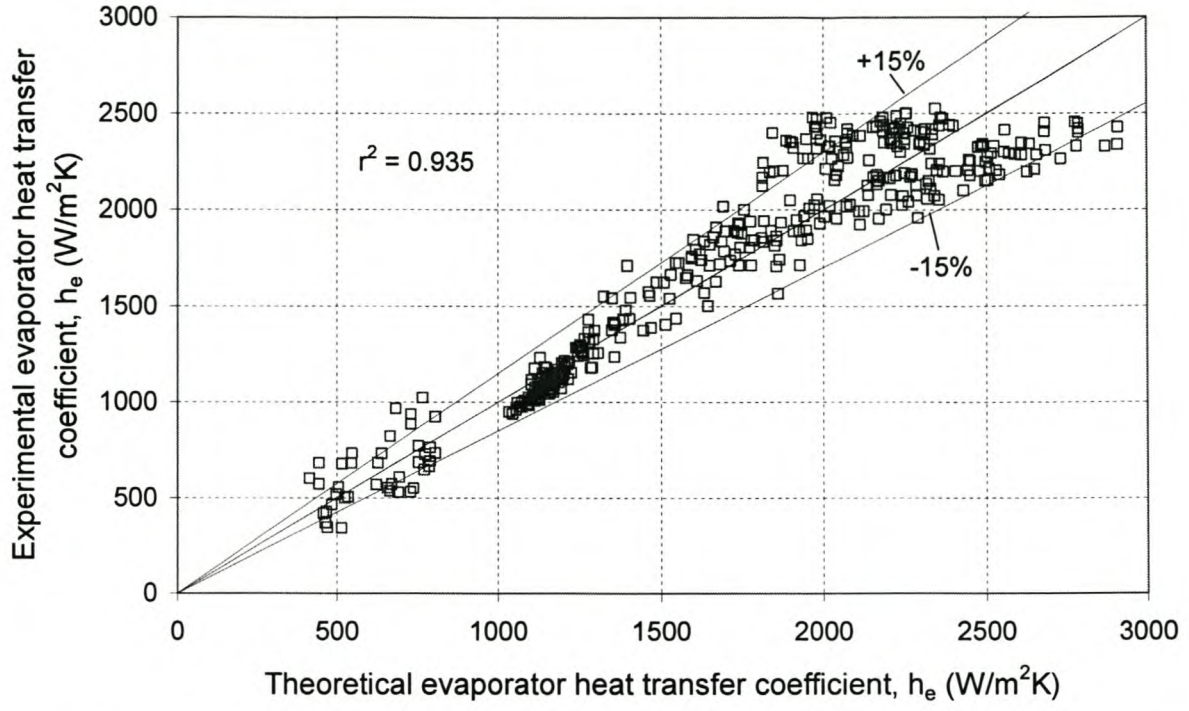

Figure 6.15 Comparison between experimental and theoretical (using equation 6.3) values for the evaporator heat transfer coefficient. Horizontal operation. The correlation coefficient is $r^2 = 0.935$

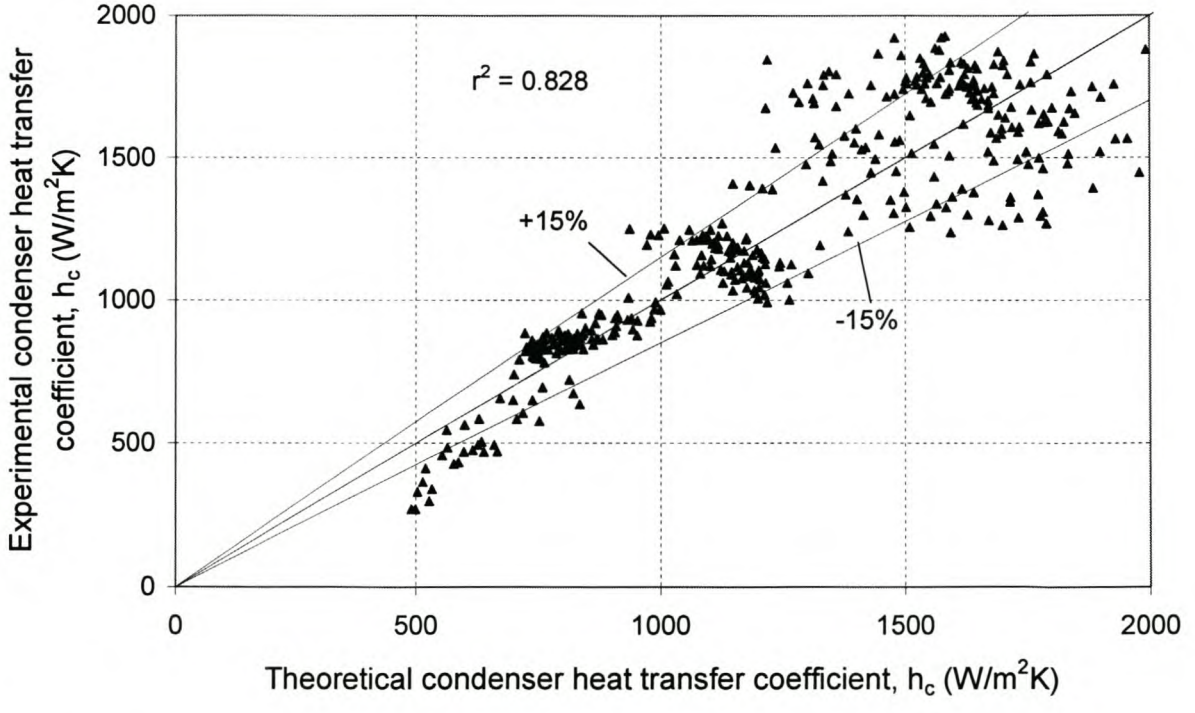

Figure 6.16 Comparison between experimental and theoretical (using equation 6.4) values for the condenser heat transfer coefficient. Horizontal operation. The correlation coefficient is $r^2 = 0.828$

6.2 FIN THERMAL CHARACTERISTICS

The thermal capacitance of the fins should be given with adequate accuracy by theory, since the geometry, mass, specific heat and conductivity of the fins are all well known. The convection coefficient for air flowing over the fins was investigated experimentally, to see how well it compares to the theoretical values.

The graphs in figures 6.17 to 6.27 show the experimentally determined (see section 4.2) heat transfer rates and forced convection coefficient between the cooling air and the fin surfaces (h_{fc}). The heat transfer coefficient is based on the heat transfer rate as measured through the rise in air temperature, $\dot{Q}_{air}$, since this is expected to be the most accurate measurement. The other two heat transfer rates shown on the graphs are evaporator heat transfer rate $\dot{Q}_e$ as determined using the radial temperature measurements in the heating block, as well as the difference between the evaporator heat transfer rate and the heat transfer rate absorbed by the fin mass to increase its temperature, $\dot{Q}_e - \dot{Q}_{fm}$ (refer to Appendix B, equation B.65). Ideally, the value of $\dot{Q}_e - \dot{Q}_{fm}$ should equal that of $\dot{Q}_{air}$. In figures 6.17 to 6.27 there are differences between these two heat transfer rates during the first 200– 400 seconds, when the temperature of the fin increases quickly and transient behaviour is experienced. During the latter stages of the graphs, steady state conditions are approached, and the heat transfer rates coincide quite well. It also seems as if the heat transfer coefficient is not only a function of the mass flow rate (which is constant for each graph), since the heat transfer coefficients increase with an increase in heat transfer rate. However, it could be that the steady state approach (over the 10 second data acquisition period) used result in errors during the time that transient heat transfer takes place. Therefore, only the heat transfer coefficients determined during steady state conditions (thus on average after about 500 seconds), were used further. Sample calculations to find the heat transfer rates and forced convection coefficient are given in Appendix B (B.2 and B.3). Figure 6.28 shows the comparison between the experimental and theoretical forced convection heat transfer coefficient, as a function of the Reynolds number of the cooling air.

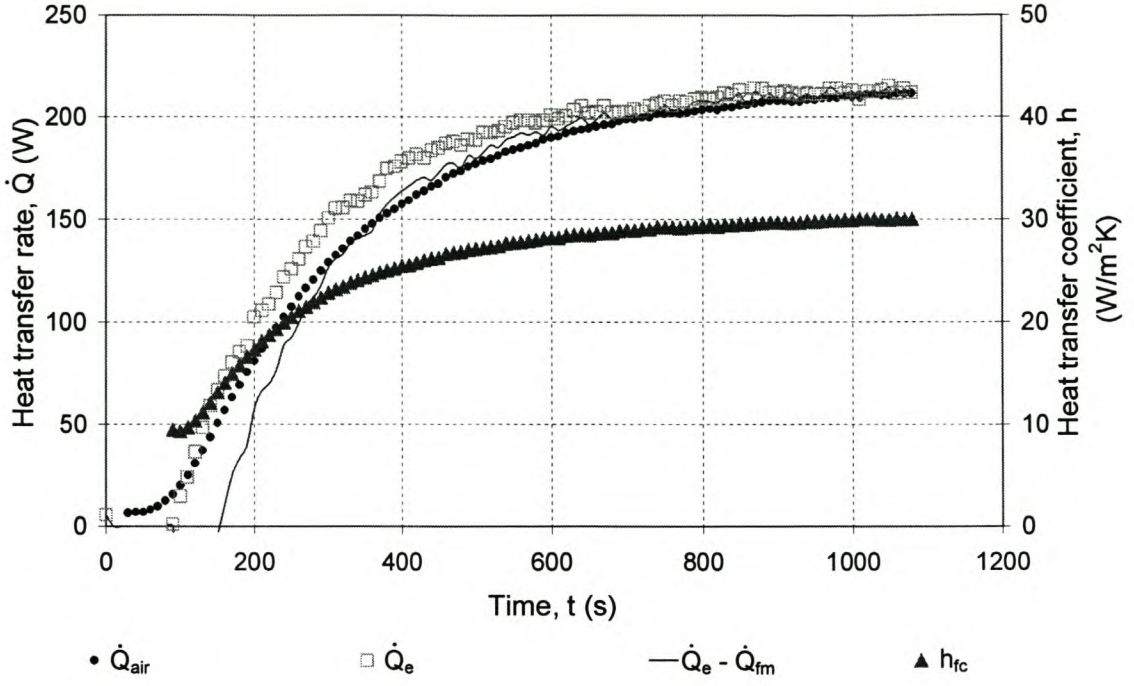

Figure 6.17 Heat transfer rates and forced convection heat transfer coefficient (between fin and air) versus time for experiment 2.1 ($\dot{m}_{air} = 12.5\ g/s$, $V_{rw} = 50$ V)

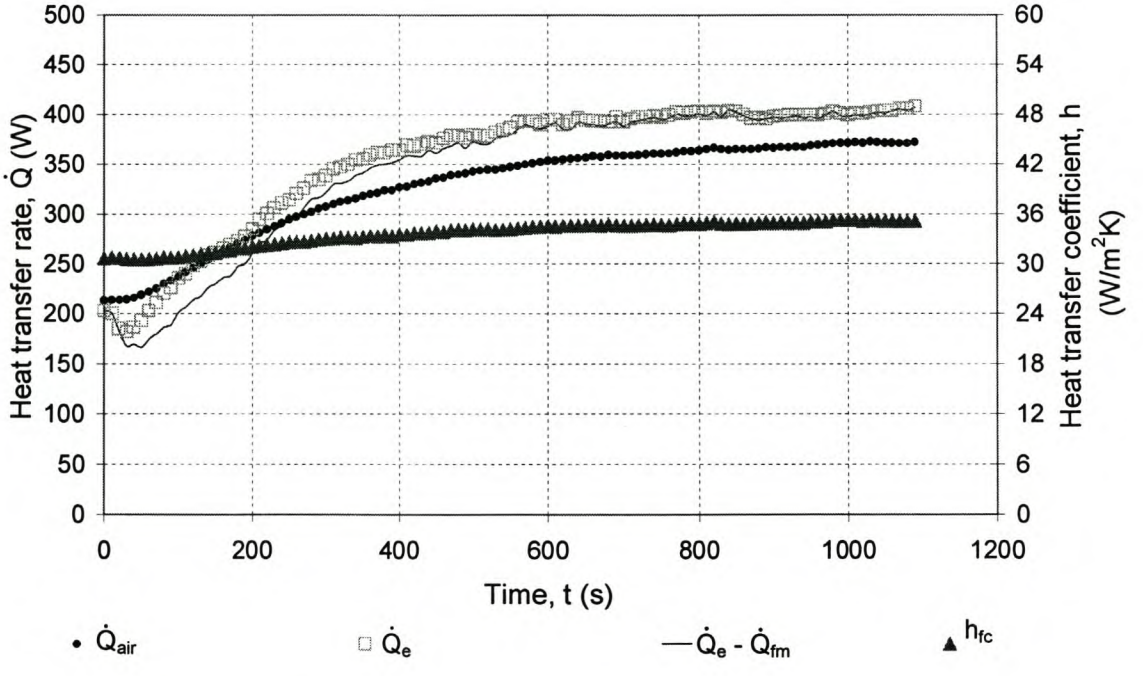

Figure 6.18 Heat transfer rates and forced convection heat transfer coefficient (between fin and air) versus time for experiment 2.2 ($\dot{m}_{air} = 12.5\ g/s$, $V_{rw} = 70$ V)

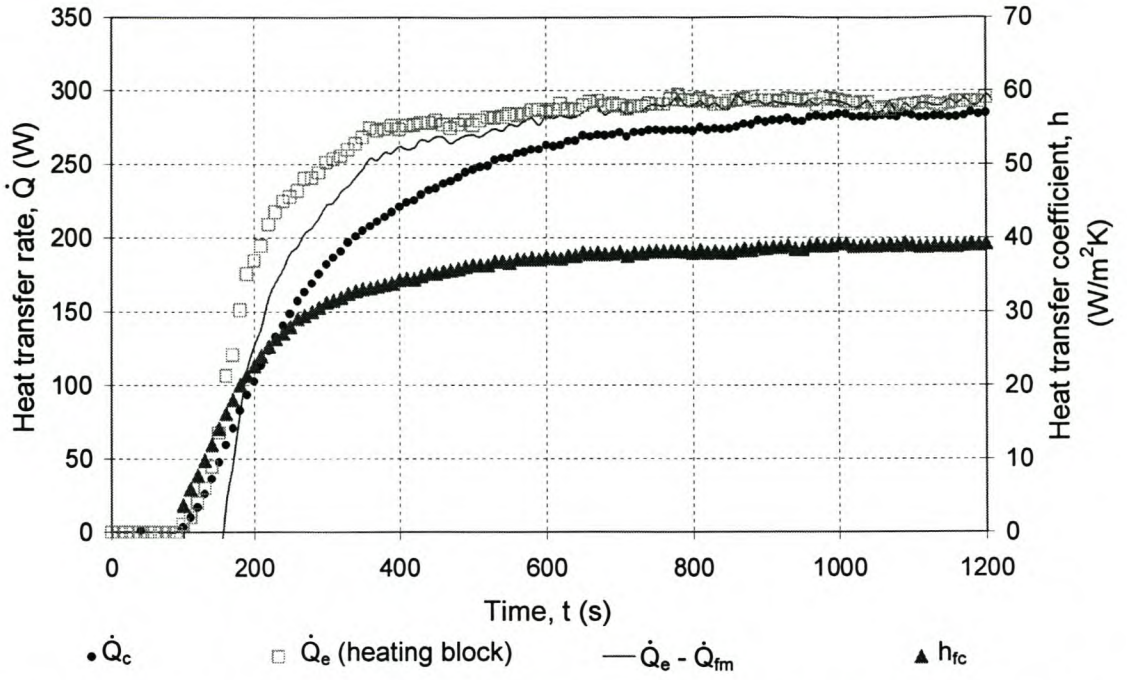

Figure 6.19 Heat transfer rates and forced convection heat transfer coefficient (between fin and air) versus time for experiment 2.3 ($\dot{m}_{air} = 21.5\ g/s$, $V_{rw} = 60$ V)

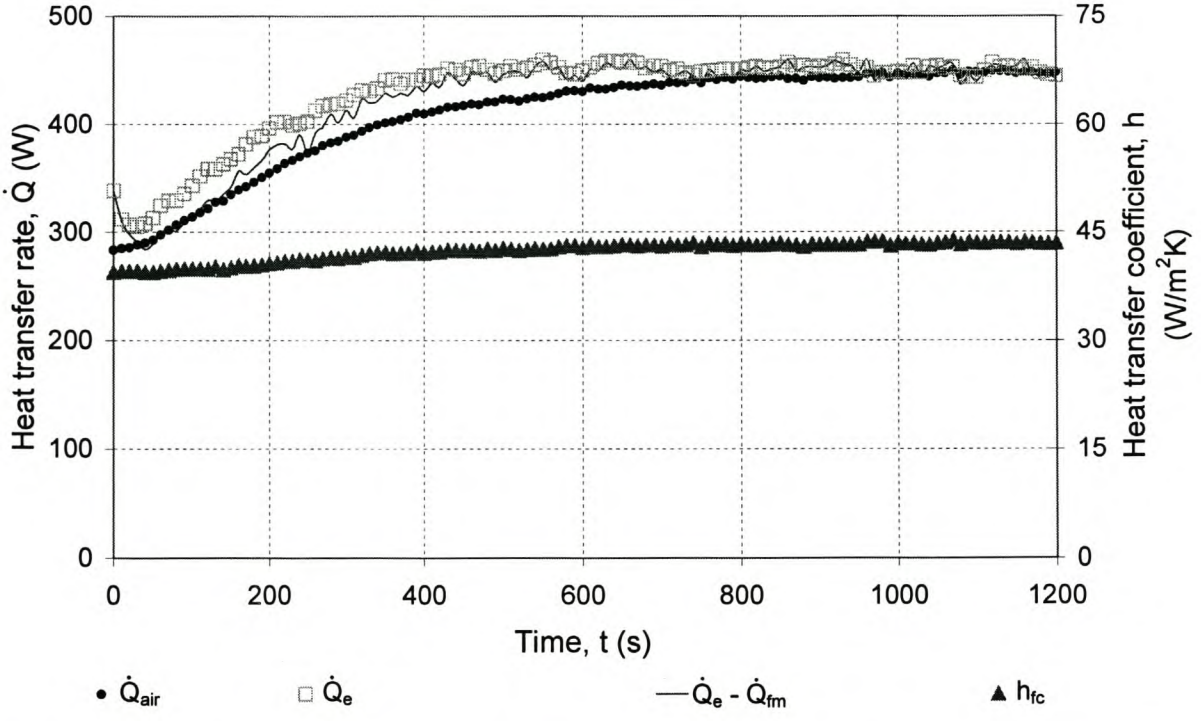

Figure 6.20 Heat transfer rates and forced convection heat transfer coefficient (between fin and air) versus time for experiment 2.4 ($\dot{m}_{air} = 21.5\ g/s$, $V_{rw} = 80$ V)

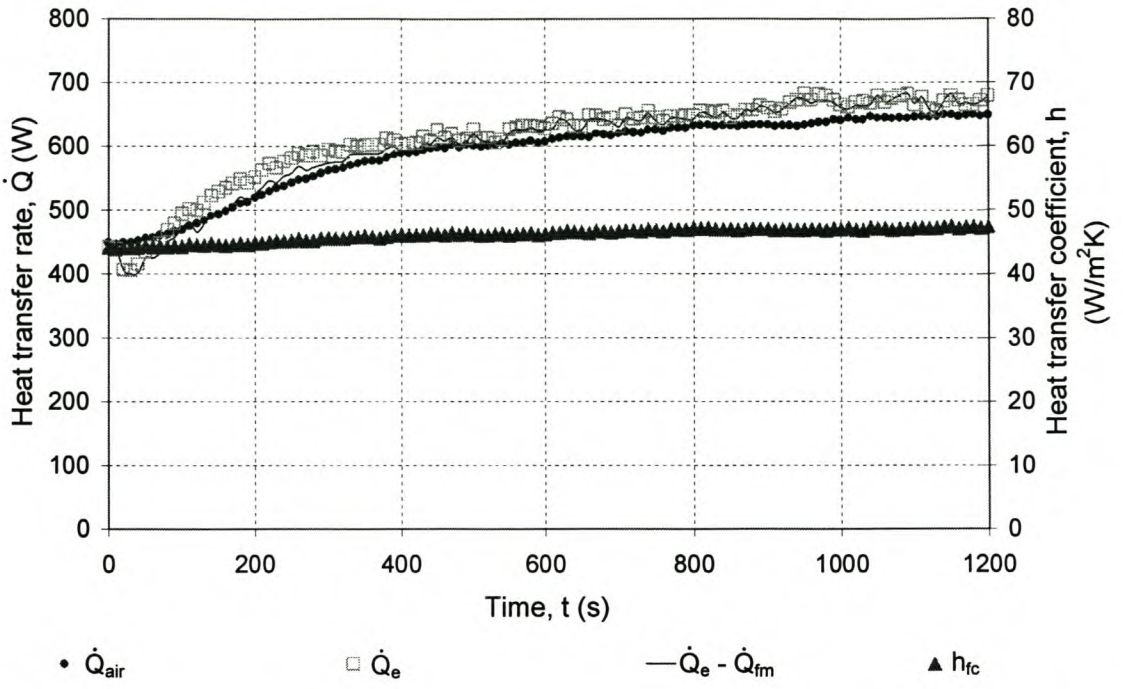

Figure 6.21 Heat transfer rates and forced convection heat transfer coefficient (between fin and air) versus time for experiment 2.5 ($\dot{m}_{air} = 21.5\ g/s$, $V_{rw} = 100$ V)

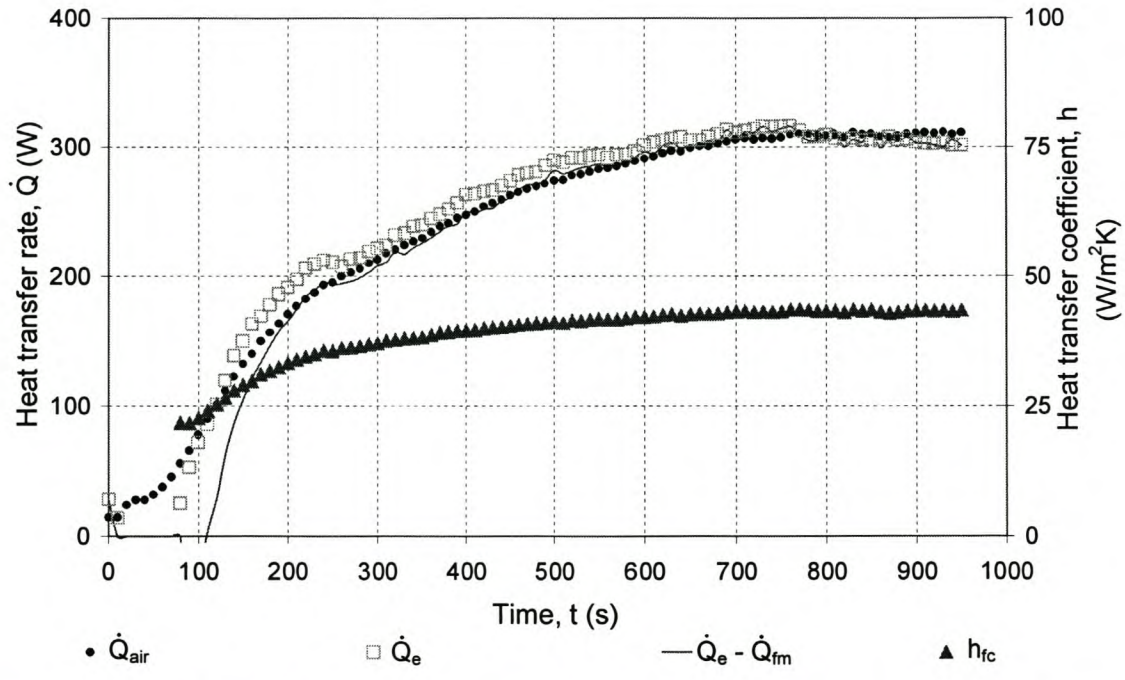

Figure 6.22 Heat transfer rates and forced convection heat transfer coefficient (between fin and air) versus time for experiment 2.6 ($\dot{m}_{air} = 23.9\ g/s$, $V_{rw} = 65$ V)

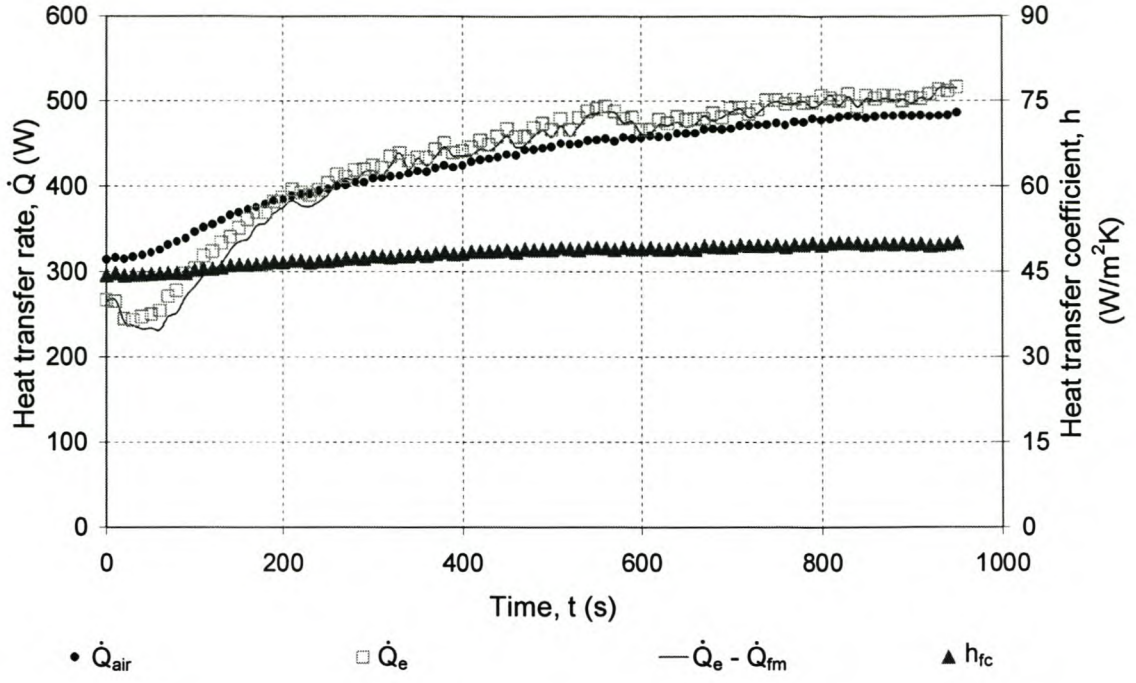

Figure 6.23 Heat transfer rates and forced convection heat transfer coefficient (between fin and air) versus time for experiment 2.7 ($\dot{m}_{air} = 24.1\ g/s$, $V_{rw} = 85$ V)

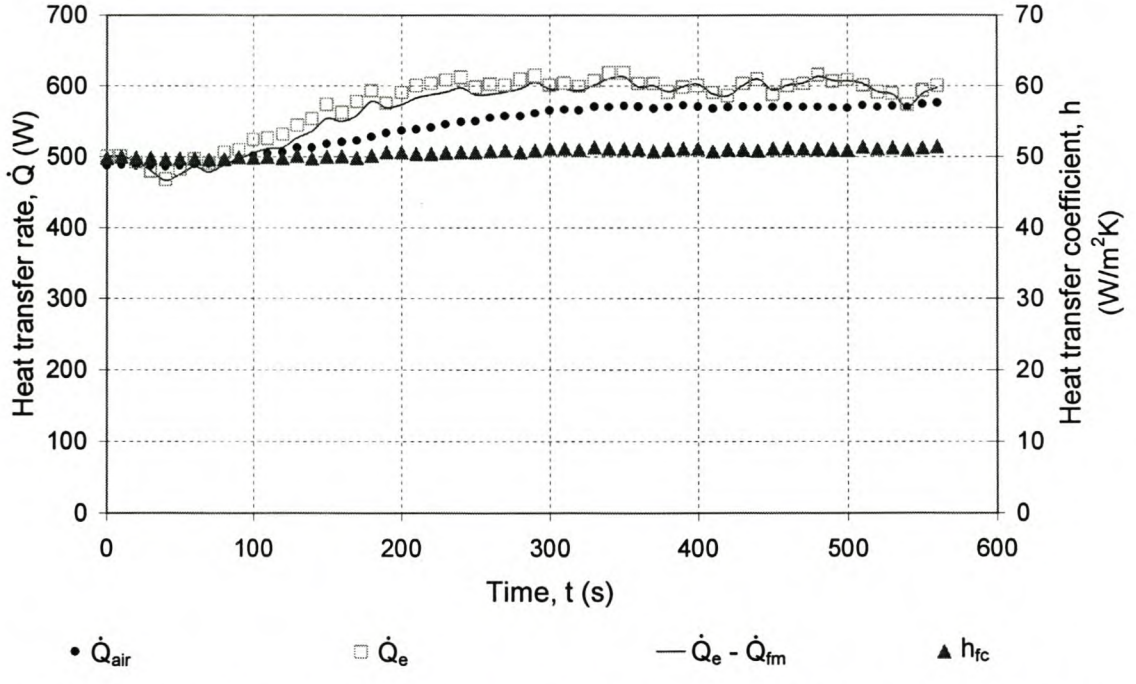

Figure 6.24 Heat transfer rates and forced convection heat transfer coefficient (between fin and air) versus time for experiment 2.8 ($\dot{m}_{air} = 24.0\ g/s$, $V_{rw} = 105$ V)

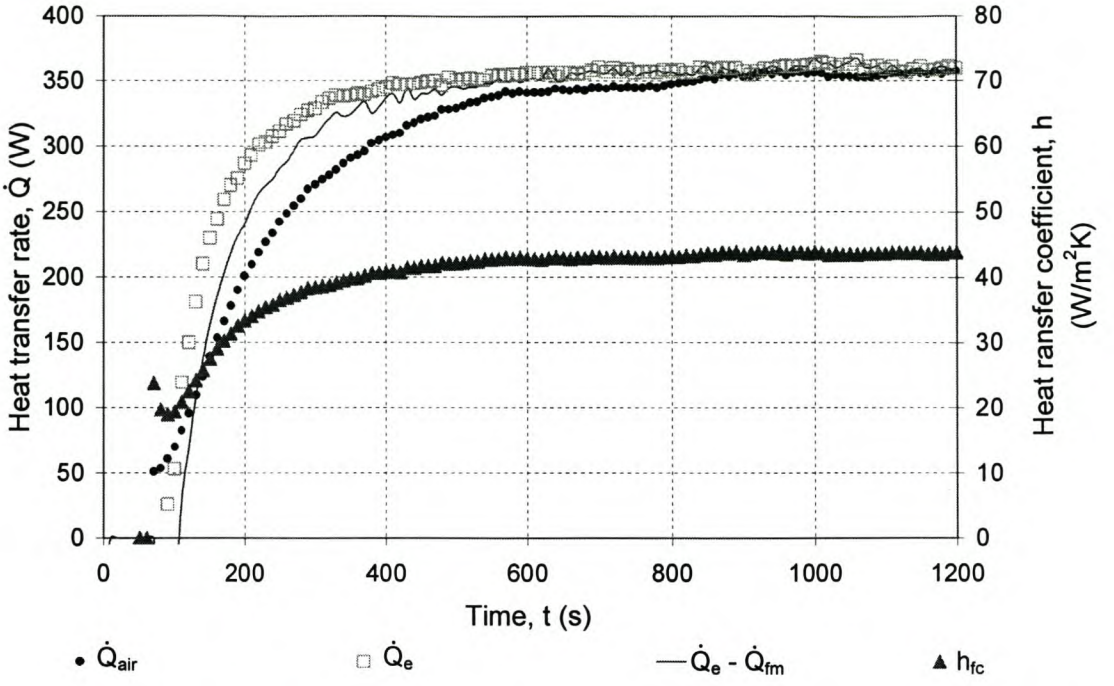

Figure 6.25 Heat transfer rates and forced convection heat transfer coefficient (between fin and air) versus time for experiment 2.9 ($\dot{m}_{air} = 30.5\ g/s$, $V_{rw} = 70$ V)

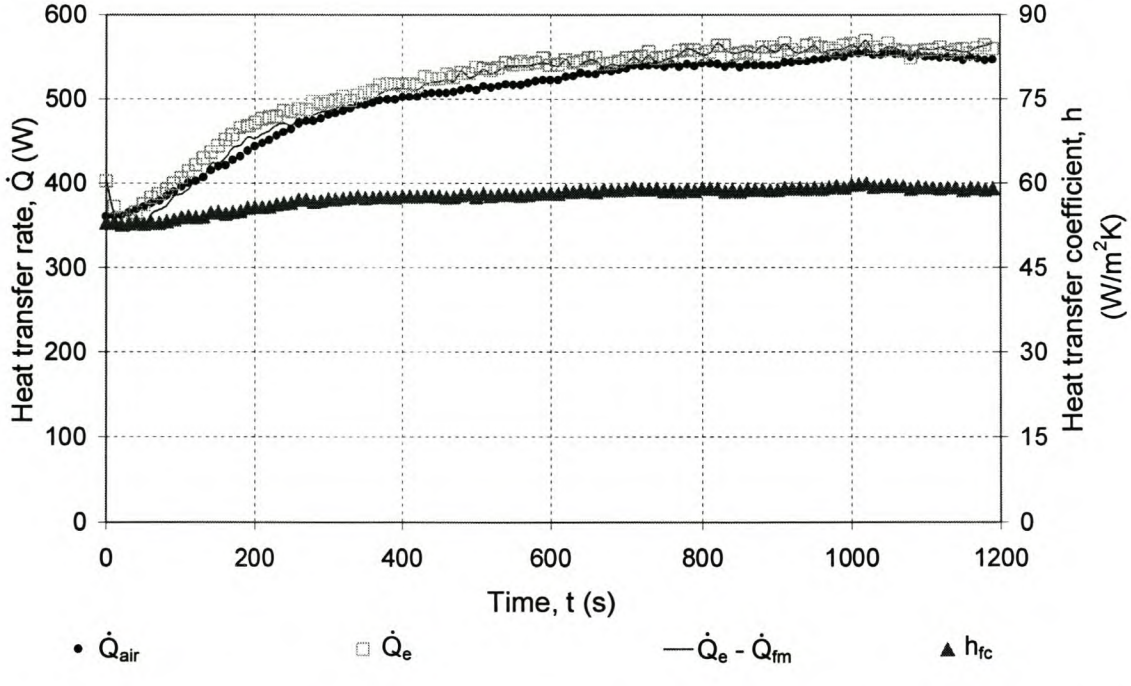

Figure 6.26 Heat transfer rates and forced convection heat transfer coefficient (between fin and air) versus time for experiment 2.10 ($\dot{m}_{air} = 30.5\ g/s$, $V_{rw} = 90$ V)

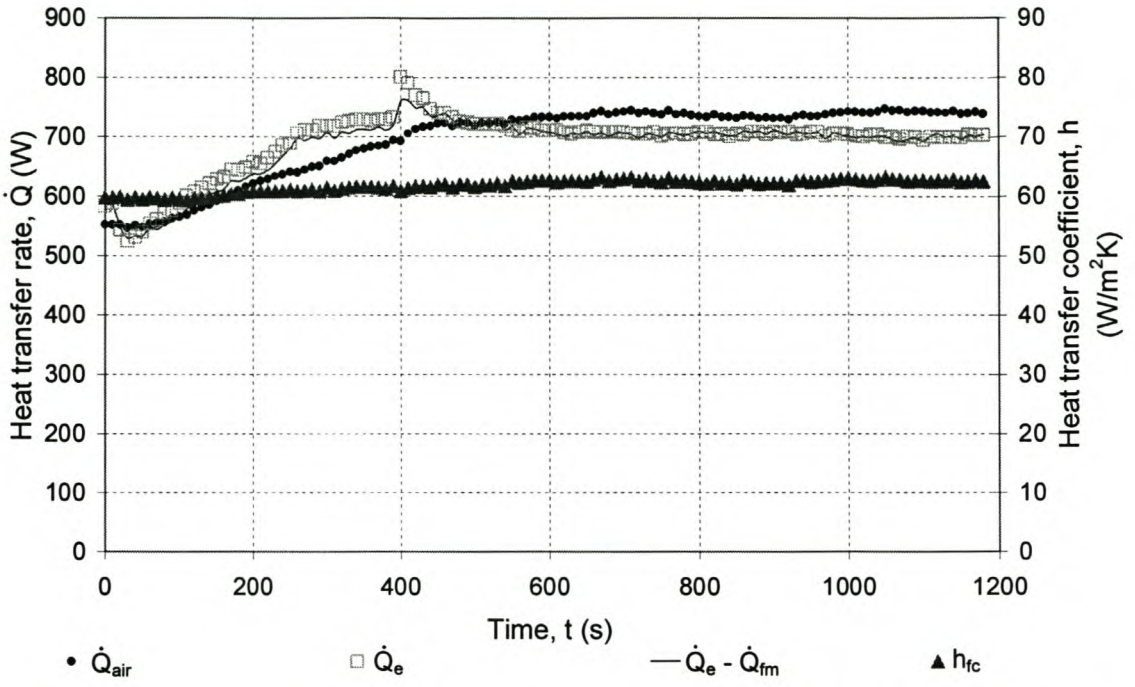

Figure 6.27 Heat transfer rates and forced convection heat transfer coefficient (between fin and air) versus time for experiment 2.11 ($\dot{m}_{air} = 30.5\ g/s$, $V_{rw} = 110$ V)

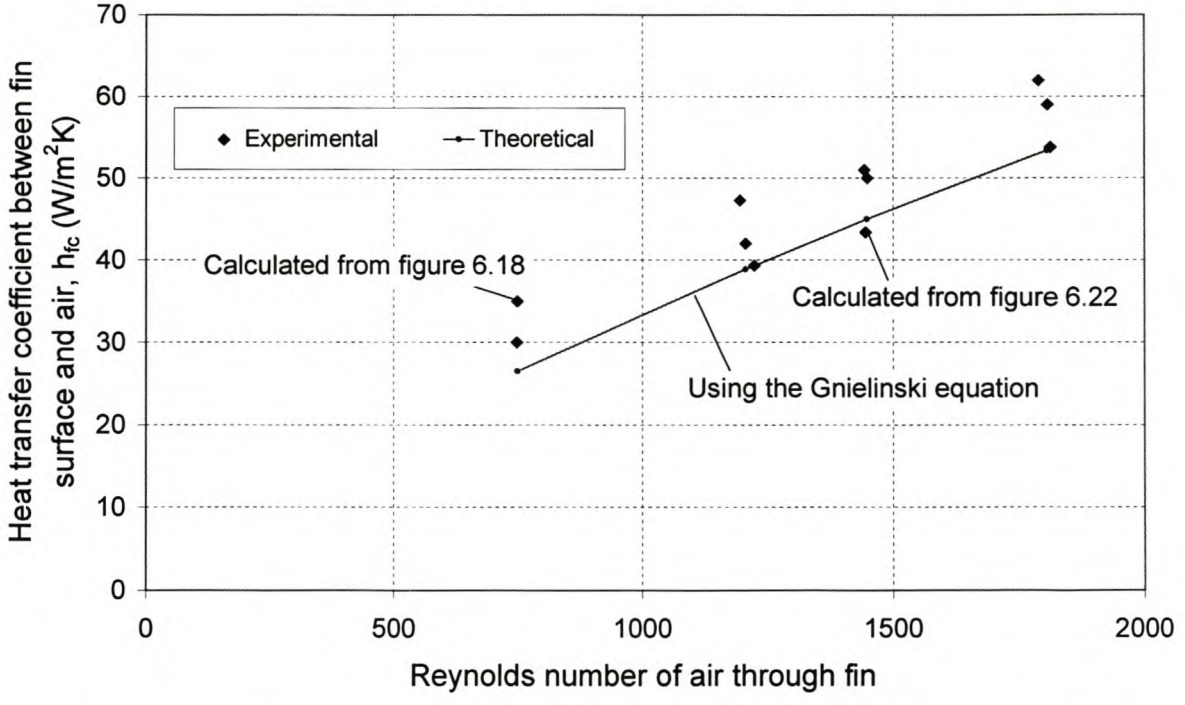

Figure 6.28 Theoretical and experimental forced convection heat transfer coefficients as a function of the Reynolds number

Figure 6.28 shows that the experimental and theoretical heat transfer coefficients are in reasonable agreement with one another. The values for the experimental points are determined by taking the average of the heat transfer coefficients for each of the graphs in figures 6.17 to 6.27, after steady state has more or less been reached. The theoretical line in figure 6.28 is found using the Gnielinski equation for the air flowing through the fin ducts, using the hydraulic diameter approach. It was found that the heat transfer coefficient increases with heat transfer rate, which explains the four "groupings" of different experimental values for the heat transfer coefficient at more or less the same Reynolds number (thus mass flow rate).

6.3 THE MOULD HEATING CASE

The physical description and experimental procedure for the mould heating case are given in section 4.3, and the thermal modelling thereof is described in section 5.3. It was decided to perform a sensitivity analysis on the material properties (of the steel, heating elements and heat pipes) as well as the boundary conditions (the natural convection coefficient and surface emissivity values) used in the FEM simulation. Experiment 3.1 in table 4.4 was performed in order to do such a sensitivity analysis on the above mentioned variables, with the exception of the heat pipe properties, since no heat pipes are used in experiment 3.1, only the heat source block is heated.

Figures 6.29 to 6.32 show experimental (obtained from experiment 3.1) and theoretical (using FEM, see section 5.3) temperatures as a function of time, where different groups of material properties and boundary conditions are used in the FEM simulation. The power input into the heating elements were measured to be 250 W, and the power was switched of after about 660 seconds (11 minutes) so that the block could be cooled by the atmosphere. The property groups are named FEMGroups, and are given in tables 6.1 and 6.2. The shaded properties were varied and the temperatures so determined compared in figures 6.29 to 6.32. The difference between tables 6.1 and 6.2 is that in table 6.1, the heating element is assumed to be a homogeneous material and in table 6.2 it is modelled as consisting of a

magnesium oxide core, surrounded by a nickel-chrome resistance wire layer and another magnesium oxide layer outside, as shown in figure 5.10.

The experimental temperature is taken as the average of temperatures T_1 and T_2 shown in figure 4.15.a, which have more or less identical values. The calculated theoretical temperatures on the corresponding positions are also exactly the same, because of symmetry. Therefore only one temperature (representing both T_1 and T_2) are shown on the graphs for the experimental and theoretical cases. The ambient temperature during experiment 3.1 was about 19°C. In figure 6.29, the influence of different properties for the heating element (using the homogeneous model for the heating elements) is analysed. It can be seen from the figures that the properties of FEMGroup 2 gives the most accurate results, although the FEM temperatures are not very sensitive regarding changes of the (homogeneous) heating element properties.

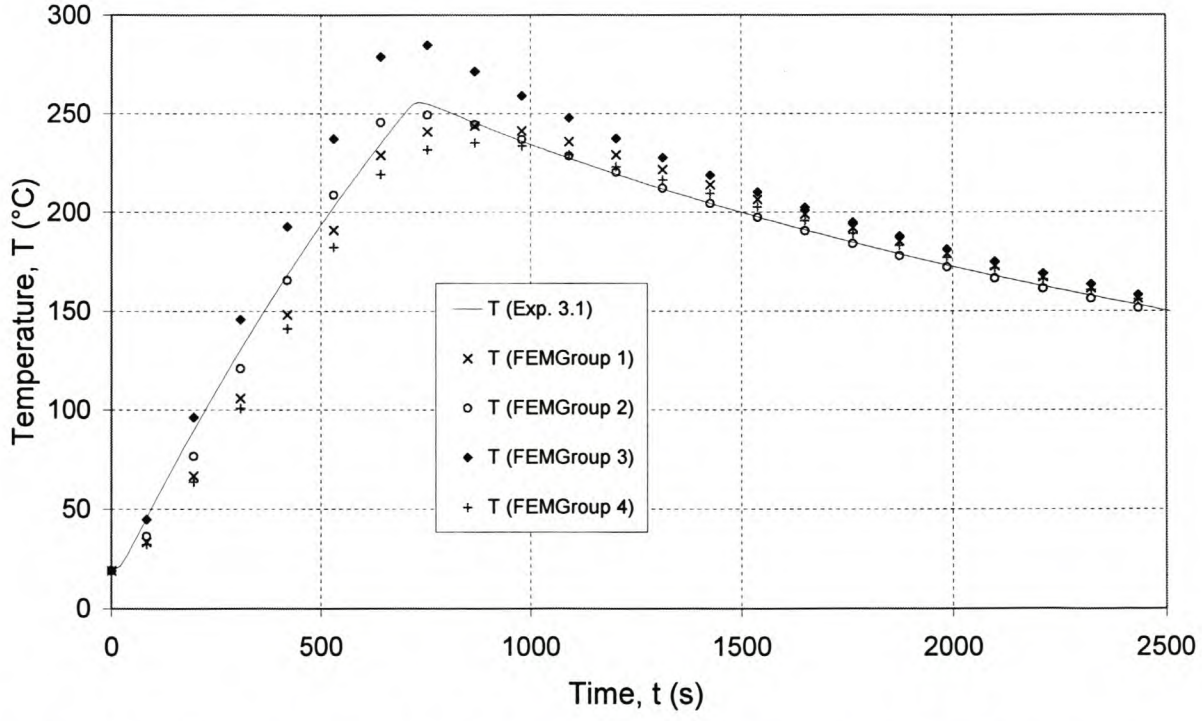

Figure 6.29 Experimental (exp. 3.1) and theoretical (using FEM) temperatures for the heat source block being heated on it's own, using different properties for the heating element (assuming homogeneous model)

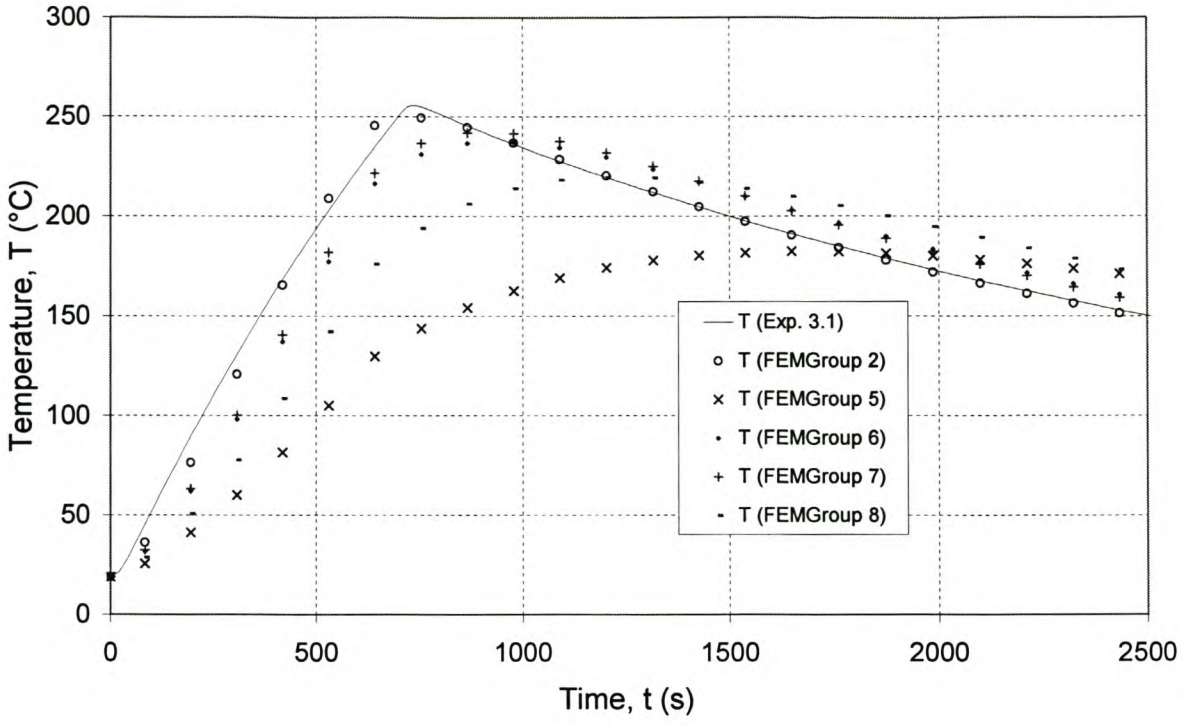

Figure 6.30 Experimental (exp. 3.1) and theoretical (using FEM) temperatures for the heat source block being heated on it's own, using different properties for the heating element (Including MgO_2 core and resistance wire)

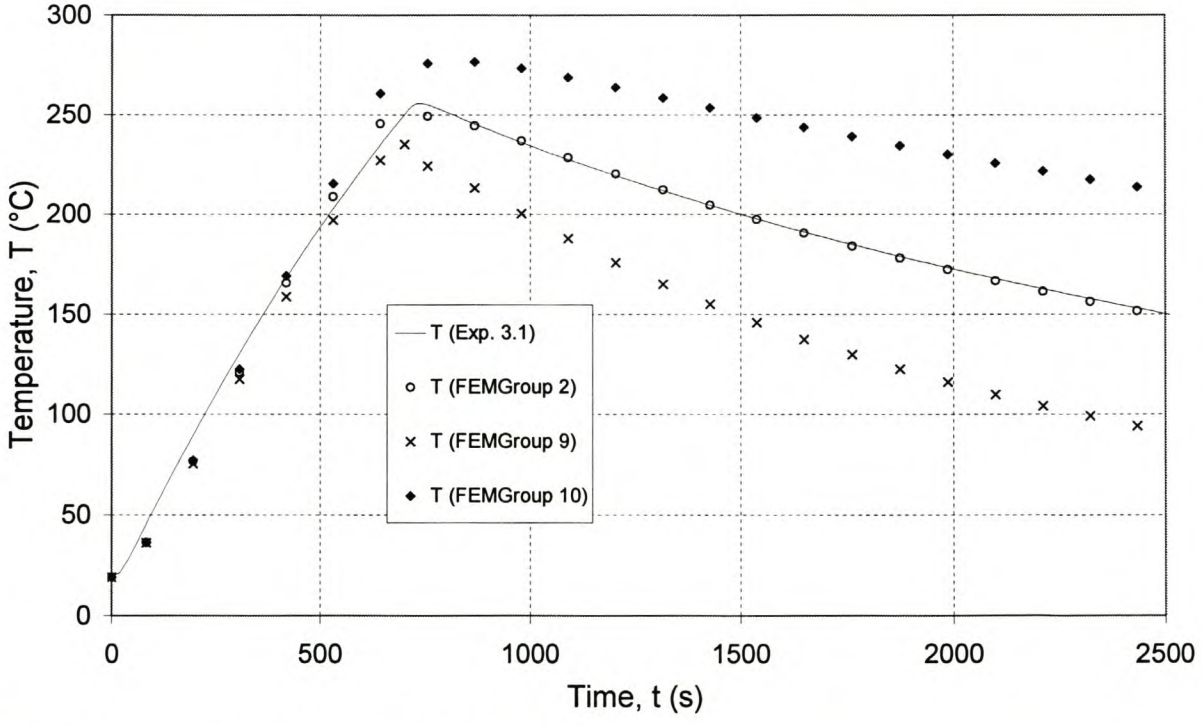

Figure 6.31 Experimental (exp. 3.1) and theoretical (using FEM) temperatures for the heat source block being heated on it's own, using different convection and radiation boundary conditions

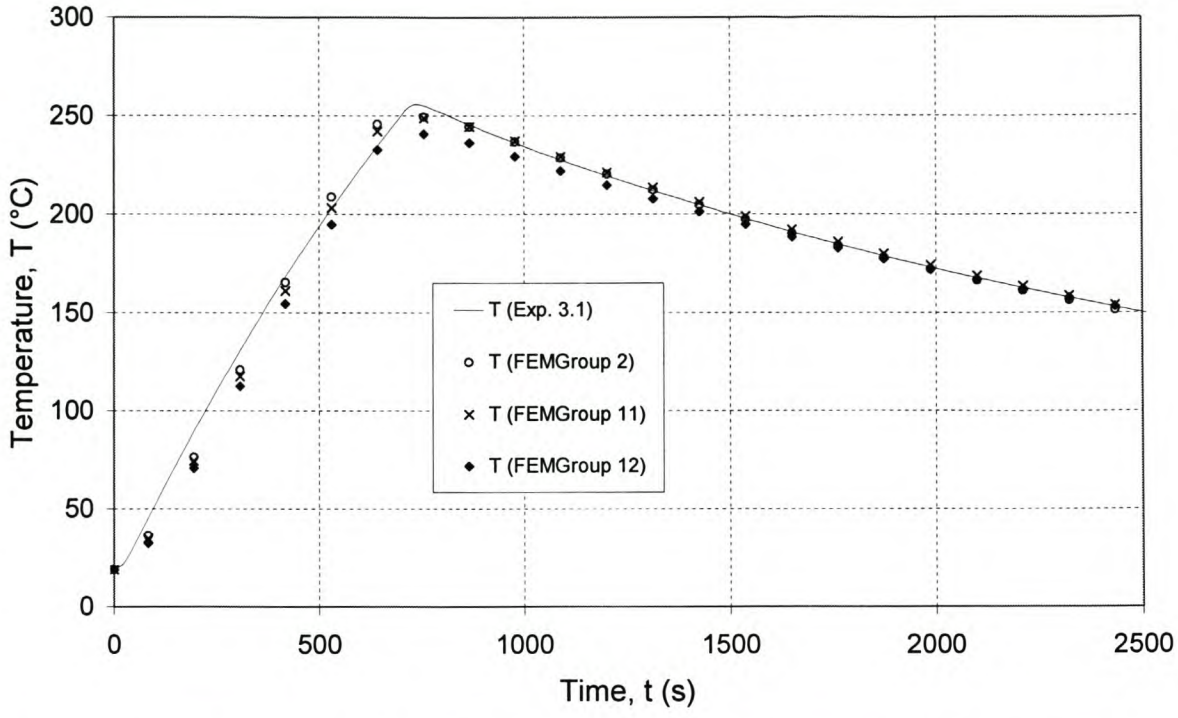

Figure 6.32 Experimental (exp. 3.1) and theoretical (using FEM) temperatures for the heat source block being heated on it's own, using different properties for the steel.

From figure 6.30 it can be seen that the results are more sensitive when the resistance wire model for the heating elements are used. FEMGroup 7 gives the best results for this type of model. Figure 6.31 shows that the choice of the natural convection coefficient and the surface emissivity is important. (The natural convection coefficients plotted as functions of temperature in chapter 5, was not used. The reason is that to be absolutely correct, the convection coefficient should also be a function of the position on the surface. Therefore, an average value was rather assumed and tested as in figure 6.31). It can be seen from figure 6.32 that the different properties assigned for the steel did not make much difference at all. By studying figures 6.29 to 6.32, it was decided that the properties of FEMGroup 7 are the most realistic. Although FEMGroup 2 gives slightly more accurate results than is the case with FEMGroup 7, the modelling of the heating elements are more realistic for FEMGroup 7.

Table 6.1 Material properties, natural convection coefficients and surface radiation properties used in the finite element model to establish accurate material properties. (Refer to figures 6.29, 6.31 and 6.32). The material of the heating element is assumed to be homogeneous. The properties that were varied are shaded

Property or coefficient	**FEMGroup Number**							
	1	**2**	**3**	**4**	**9**	**10**	**11**	**12**
$h_{convection}$ (W/m^{2}K)	5	5	5	5	10	3	5	5
$\varepsilon_{radiation}$	0.5	0.5	0.5	0.5	1	0.2	0.5	0.5
$\alpha_{radiation}$	0.5	0.5	0.5	0.5	1	0.2	0.5	0.5
ρ_{steel} (kg/m^3)	7840	7840	7840	7840	7840	7840	7840	7840
k_{steel} (W/mK)	50	50	50	50	50	50	64	40
$C_{p\,(steel)}$ (J/kgK)	450	450	450	450	450	450	432	480
$\rho_{heating\ element}$ (kg/m^3)	4000	7840	4000	7840	7840	7840	7840	7840
$k_{heating\ element}$ (W/mK)	50	200	200	100	200	200	200	200
$C_{p\,(heating\ element)}$ (J/kgK)	1000	1000	1000	1000	1000	1000	1000	1000

Table 6.2 Material properties, natural convection coefficients and surface radiation properties used in the finite element model to establish accurate material properties. (Refer to figure 6.30) The properties that were varied are shaded

Property or coefficient	FEMGroup Number			
	5	**6**	**7**	**8**
$h_{convection}$ (W/m^{2}K)	5	5	5	5
$\varepsilon_{radiation}$	0.5	0.5	0.5	0.5
$\alpha_{radiation}$	0.5	0.5	0.5	0.5
ρ_{steel} (kg/m^3)	7840	7840	7840	7840
k_{steel} (W/mK)	50	50	50	50
$C_{p\ (steel)}$ (J/kgK)	450	450	450	450
$\rho_{(filament)}$ (kg/m^3)	7840	7840	8000	10000
$k_{(filament)}$ (W/mK)	20	30	50	25
$C_{p\ (filament)}$ (J/kgK)	1000	400	600	500
$\rho_{(magnesium\ oxide)}$ (kg/m^3)	4000	4000	5000	2000
$k_{(magnesium\ oxide)}$ (W/mK)	4	10	15	50
$C_{p(magnesium\ oxide)}$ (J/kgK)	1000	700	1000	800

The sensitivity analysis regarding figures 6.29 to 6.32 and FEMGRoups 1 to 12, did not include the properties of the heat pipes. For experiment 3.2, in table 4.4, the heat sink block is connected to the heat source block with the heat pipes. The temperatures of the heat sink block, T_3 and T_4 are therefore also measured (refer to figure 4.15.a). Figure 6.33 shows the theoretical and experimental temperatures if the properties and boundary conditions given by FEMGroup 7 in table 6.2 are used, together with the heat pipe properties calculated in section 5.1.2. Once again the power input to each heating element was 250 W. The power was switched off after about 1020 seconds (17 minutes) and the blocks were left to cool. The thermal equalisation effect of the heat pipes can be seen after about 1500 seconds where all four experimental temperatures start to coincide.

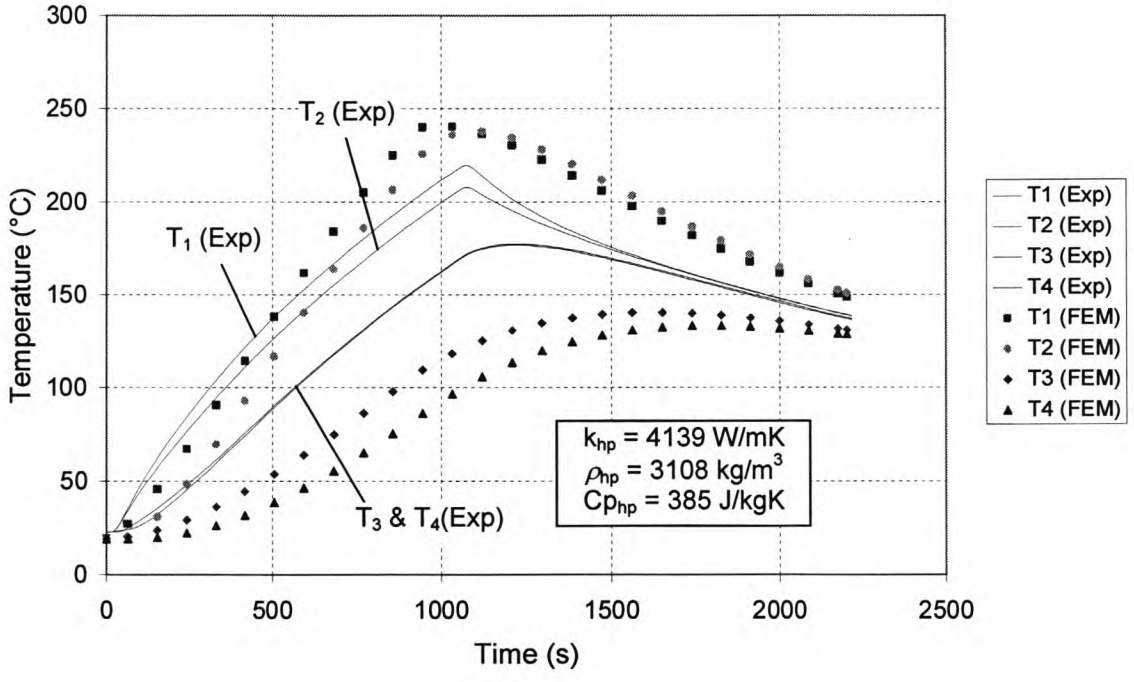

Figure 6.33 Experimental (exp. 3.2) and theoretical (using FEM) temperatures for the heat source block and the heat sink block (connected by heat pipes), using the properties of FEMGroup 7. The heat pipe properties are shown in the graph.

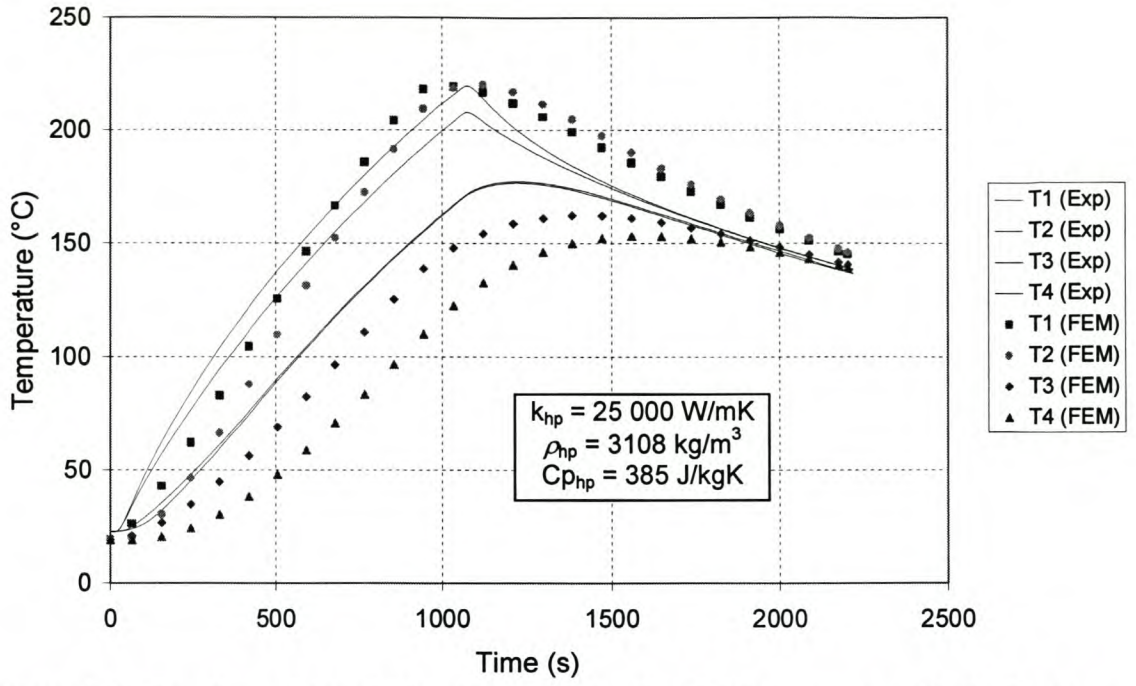

Figure 6.34 Experimental (exp. 3.2) and theoretical (using FEM) temperatures for the heat source block and the heat sink block (connected by heat pipes), using the properties of FEMGroup 7. The heat pipe properties are shown in the graph.

By comparing figures 6.33 and 6.34 it can be seen that a thermal conductivity of 25 000 W/mK instead of 4139 W/mK yields theoretical temperatures that are somewhat closer to the experimental temperatures. To asses the influence of the properties used for the heat pipe, the average error between the theoretical and experimental results is considered. The average error is defined as the average difference between the theoretical and experimental temperatures, so that:

$$E = \sum_{n=1}^{N}\sum_{i=1}^{4}\left|T^{n}_{i\,(experimental)} - T^{n}_{i\,(theoretical)}\right| \Big/ N \qquad (6.5)$$

where n is the number of the time step and N is the total number of time steps considered.

A total of 15 simulations similar to those shown in figures 6.33 and 6.34 were performed, using different values for the properties of the heat pipes. Equation 6.5 is used to evaluate the accuracy of the theoretical results compared to the experimental temperatures.

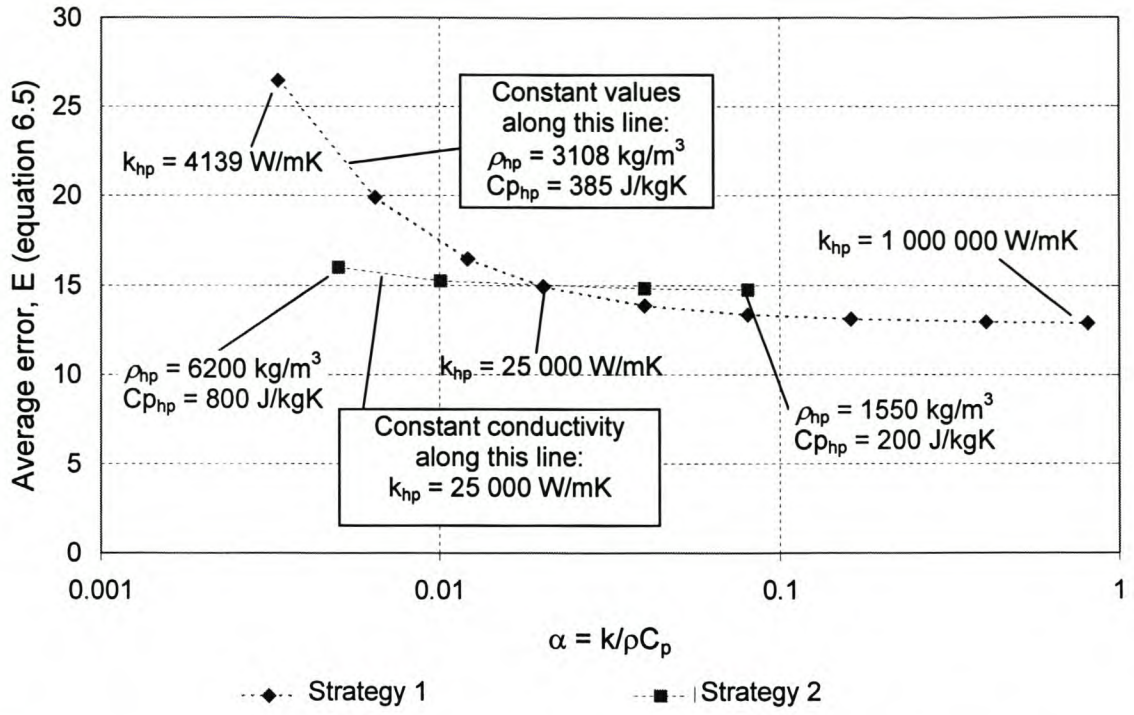

Figure 6.35 Average error (using equation 6.5) versus the thermal diffusivity for different properties of the heat pipe used in the FEM simulation (obtained for the simulation of experiment 3.2)

Two strategies were followed to obtain the results shown in figure 6.35. Strategy 1 is to keep the values for the specific heat capacity and density of the heat pipes constant, while changing the thermal conductivity, to obtain different thermal diffusivities. The values assigned were those calculated in section 5.1.2, namely $\rho_{hp} = 3108$ kg/m^3 and $C_{p(hp)} = 385$ J/kgK. From this line it can be seen that a higher conductivity results in a smaller average error, but convergence seems to take place, when $k_{hp} > 25\ 000$ W/mK. For strategy 2, the conductivity is kept constant at $k_{hp} = 25\ 000$ W/m^{2}K, while changing the specific heat capacity and density of the heat pipe, to obtain different thermal diffusivity values. By comparing the results of the strategies shown in figure 6.35, it can be seen that the effect the conductivity value is more significant than that of the thermal capacity. Based on figure 6.35, it was decided that reasonable properties for the heat pipe would be:

$k_{hp} = 25\ 000$ W/mK

$C_{p(hp)} = 385$ J/kgK

$\rho_{hp} = 3108$ kg/m^3

The results of using these heat pipe properties (as well as the properties of FEMGroup 7) to simulate experiment 3.2 are shown in figure 6.34. Figures 6.36 and 6.37 show the results of using these heat pipe properties and FEMGroup 7 for the simulation of experiments 3.3 and 3.4.

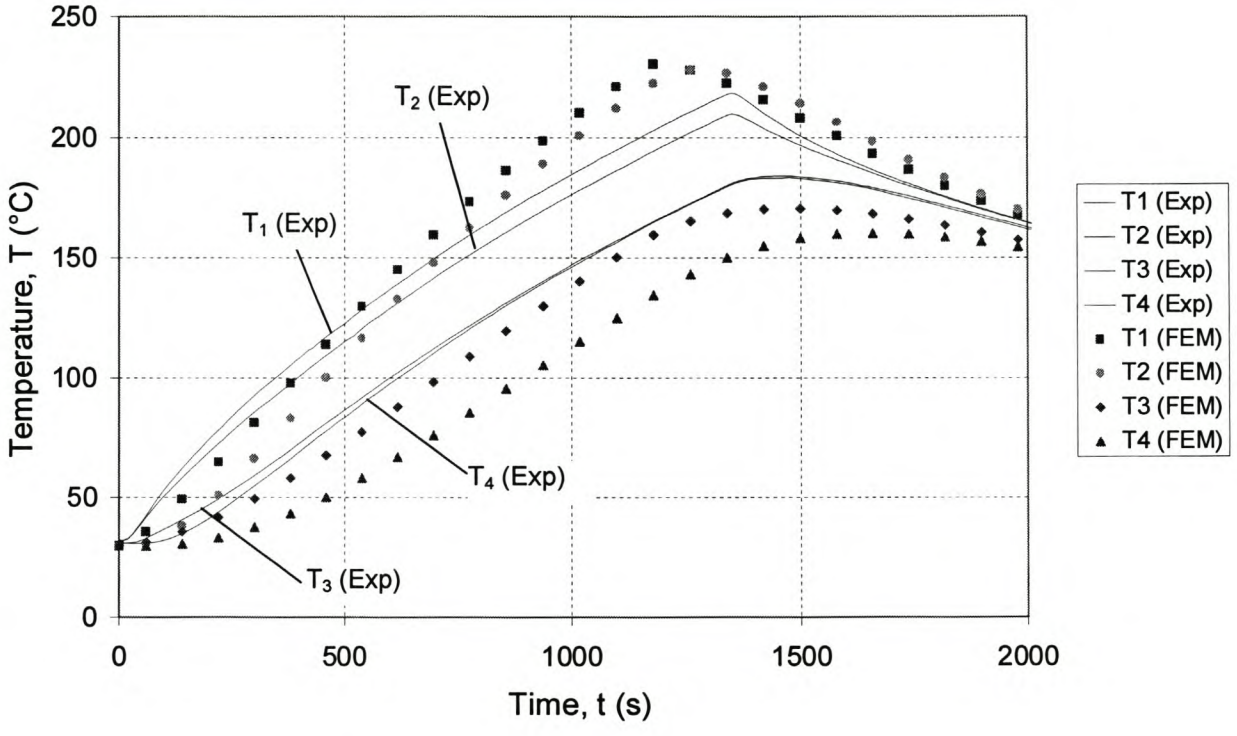

Figure 6.36 Experimental (exp. 3.3) and theoretical (using FEM) temperatures for the heat source block and the heat sink block (connected by heat pipes), using the properties of FEMGroup 7, and k_{hp} = 25 000 W/mK, ρ_{hp} = 3108 kg/m^3, $C_{p(hp)}$ = 385 J/kgK. Power input to heating elements = 200W

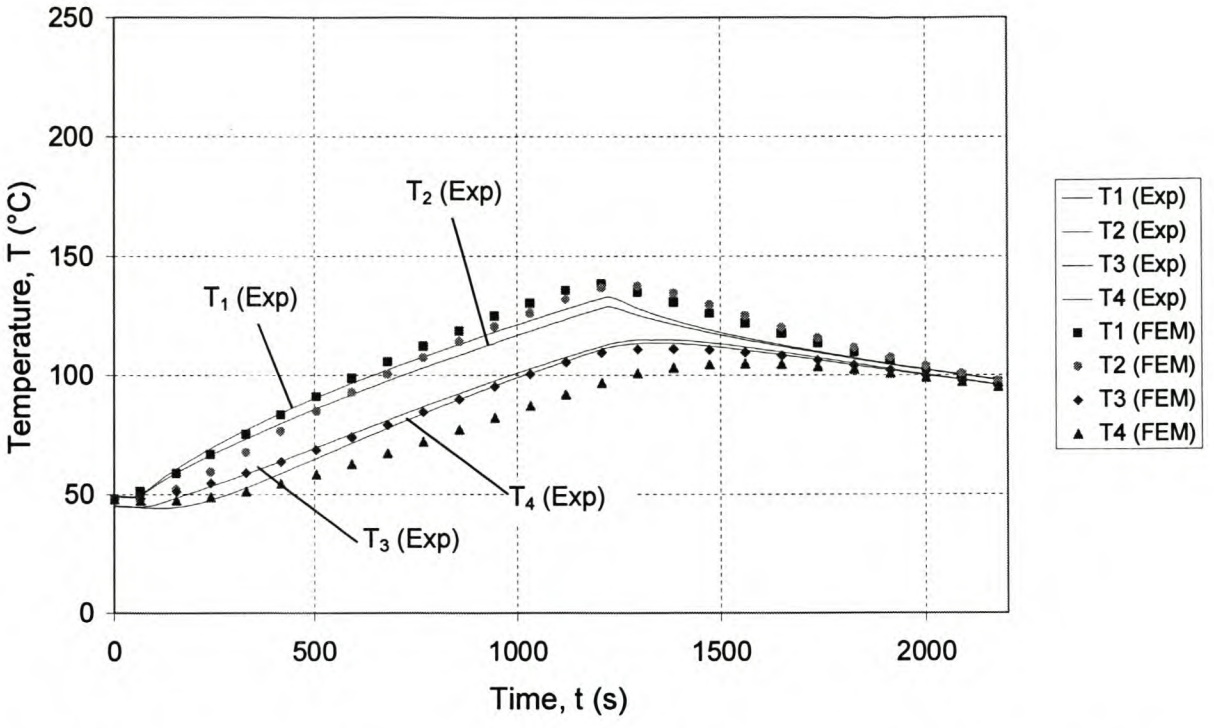

Figure 6.37 Experimental (exp. 3.4) and theoretical (using FEM) temperatures for the heat source block and the heat sink block (connected by heat pipes), using the properties of FEMGroup 7, and k_{hp} = 25 000 W/mK, ρ_{hp} = 3108 kg/m^3, $C_{p(hp)}$ = 385 J/kgK. Power input to heating elements = 100W

The heat pipe model described in section 5.1.3, the "outer shell and super conductive core model", was expected to work well. This model did not work at all in the finite element analysis. No heat is transferred through this heat pipe model, and only the temperature of the heat source increases, while the temperature of the heat sink stays constant. This model is therefore not discussed further in this chapter, but in chapter 8.

6.4 THE CORE COOLING CASE

The experimental set-up for the core cooling case is discussed in section 4.4 and the thermal modelling is discussed in section 5.4, as well as Appendix C. Three types of casting operations are performed for the core cooling case, as described in table 4.5. Four castings (experiments 4.1 to 4.4) were made without the heat pipe inserted into the core, and the casting and core were left inside the external mould to cool down. Another four castings (experiments 4.5 to 4.8) were also made without the heat pipe inserted, but were removed

from the mould to cool in the atmosphere. Five castings (experiments 4.9 to 4.13) were made with the heat pipe and fins connected to the core, with the fins being air-cooled. The castings were removed from out of the external mould after solidification. Referring to figure C.2 in appendix C, the contact resistance between the casting and the mould surfaces are not known. It is not in the scope of this thesis to determine this resistance exactly. The only estimate for the interfacial heat transfer coefficient h_{CR} (from $R_{CR} = \frac{1}{h_{CR}A}$) is experimentally determined values between tin and a graphite mould (Trovant and Argyropoulos, 2000). The value starts at about 1000 W/m^{2}K, then drops to about 400 W/m^{2}K over a period of about 200 seconds from where it stays relatively constant. These values were determined for a specific casting (with a diameter of 60mm and a height of 300mm) and will probably not be exactly the same for the castings of this thesis. The value for the contact thermal resistance is taken as a constant. To estimate a value for the contact resistance, three different values for the interfacial contact heat transfer coefficient were tested in the numerical simulation of experiment 4.1, so that the theoretical and experimental temperatures can be compared to each other. Figures 6.38 to 6.40 show the theoretical temperatures for the three contact heat transfer coefficients used. Figure 6.38 shows the temperatures of the core and the mould (with the core and casting left to cool inside the external mould for the whole time) when the contact resistance is ignored, in other words the heat transfer coefficient approaches infinity. It can be seen that the theoretical casting and core temperatures drop much quicker than the experimental temperatures do, since the low thermal resistance between the casting and the core or the external mould causes a too high theoretical heat transfer rate from the casting to the core and mould. Figure 6.39 shows the temperatures when the interfacial heat transfer coefficient is chosen as 350 W/m^{2}K. In this case the theoretical response of the core temperature is too slow, which indicates that the heat transfer rate between the casting and the core is too low, hence the contact resistance is too high. Figure 6.40 shows temperatures for $h_{CR} = 700\ W/m^2K$. This value gives the most accurate theoretical temperatures as compared to the experimental temperatures, and it was therefore used for the remainder of the core cooling simulations.

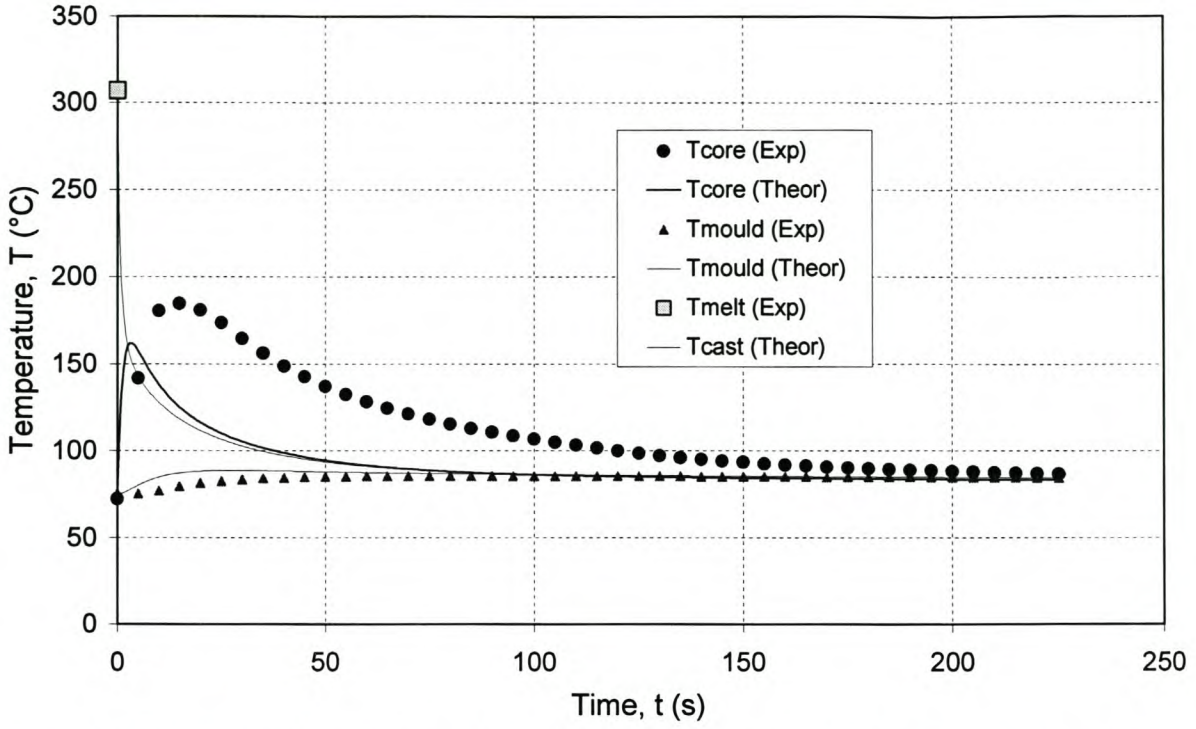

Figure 6.38 Experimental (exp. 4.1) and theoretical (using finite differences) temperatures for the core cooling case. The average ambient temperature is T_a = 17.5 °C. Temperature of melt at start of casting process is T_{melt} = 307 °C. The interfacial contact resistance is ignored.

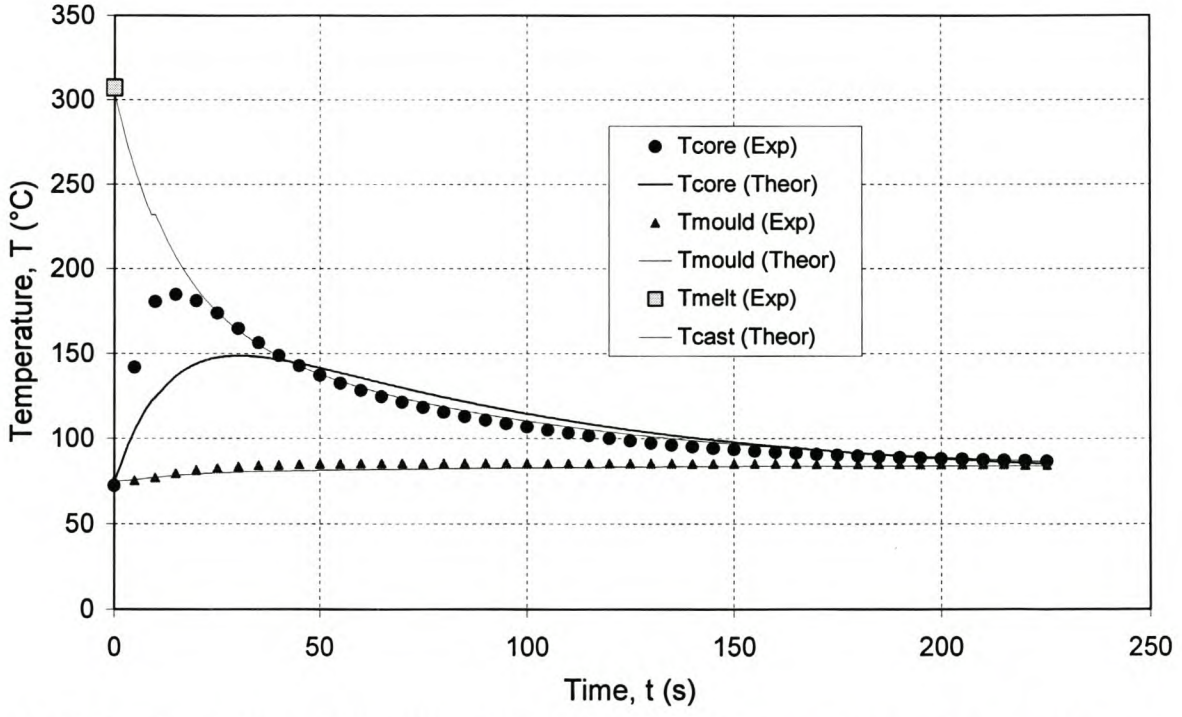

Figure 6.39 Experimental (exp. 4.1) and theoretical (using finite differences) temperatures for the core cooling case. The average ambient temperature is T_a = 17.5 °C. Temperature of melt at start of casting process is T_{melt} = 307 °C. The interfacial contact heat transfer coefficient is h_{CR} = 350 W/m^{2}K

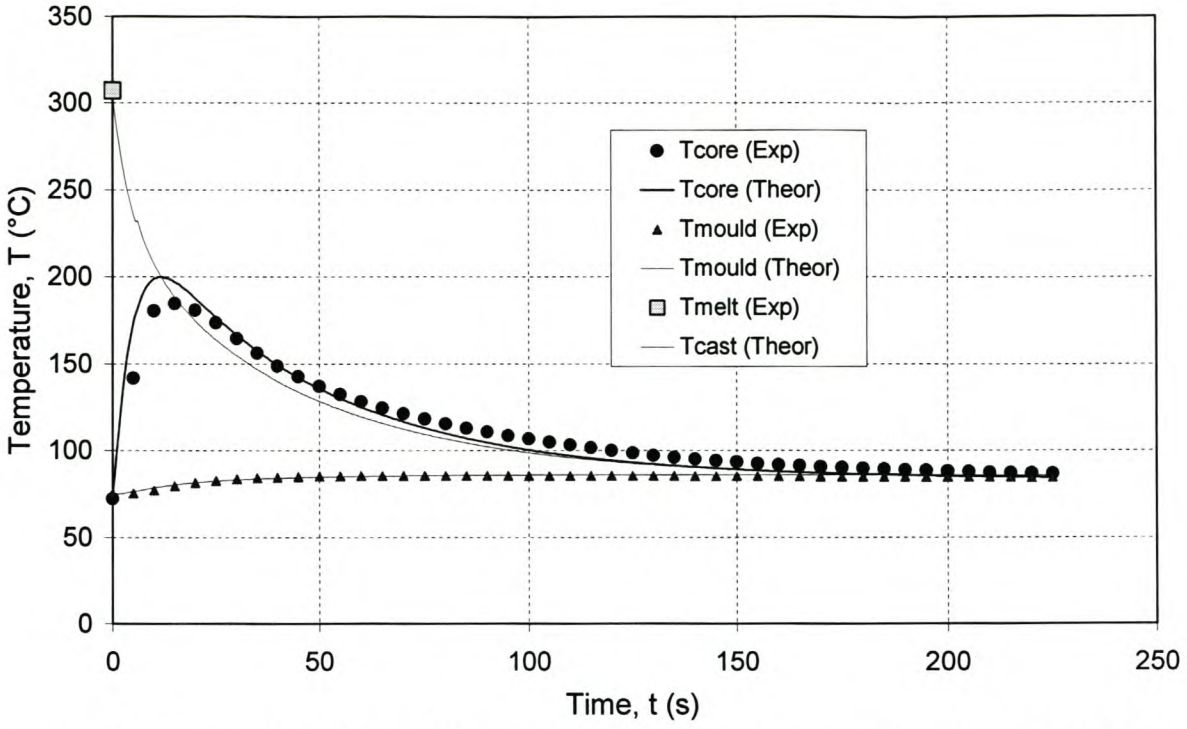

Figure 6.40 Experimental (exp. 4.1) and theoretical (using finite differences) temperatures for the core cooling case. The average ambient temperature is T_a = 17.5 °C. Temperature of melt at start of casting process is T_{melt} = 307 °C. The interfacial contact heat transfer coefficient is h_{CR} = 700 W/m^{2}K

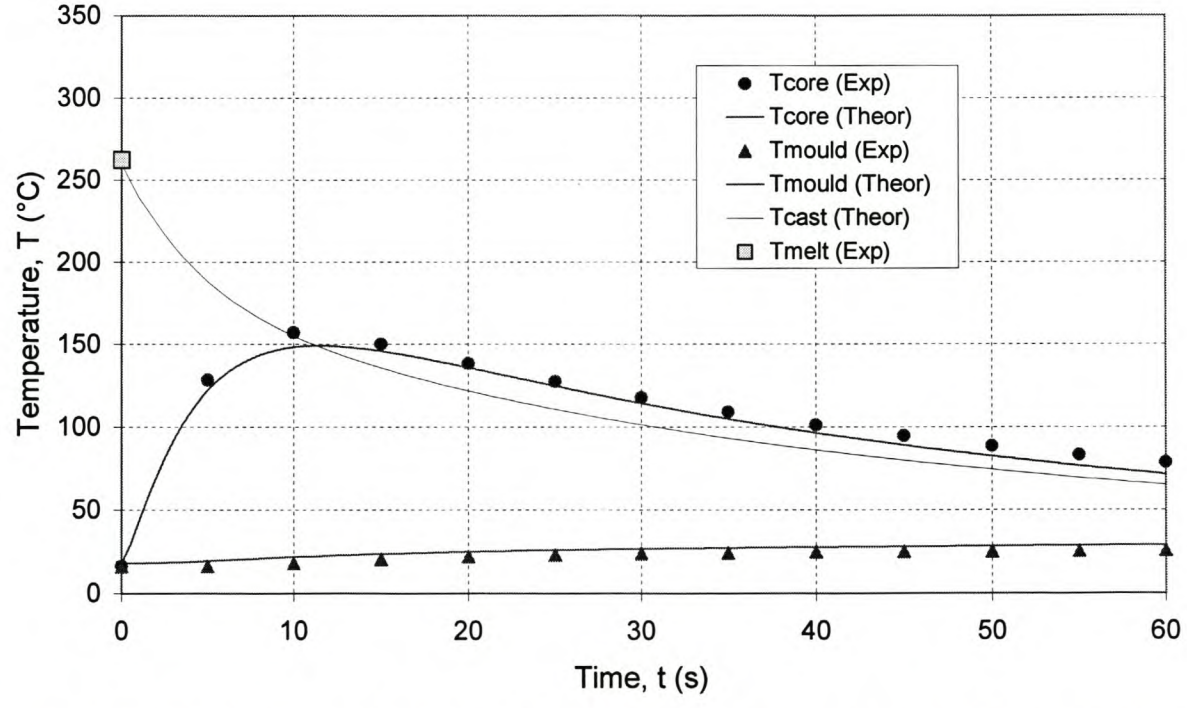

Figure 6.41 Experimental (exp. 4.2) and theoretical (using finite differences) temperatures for the core cooling case. The average ambient temperature is T_a = 16.5 °C. Temperature of melt at start of casting process is T_{melt} = 262 °C. The interfacial contact heat transfer coefficient is h_{CR} = 700 W/m^{2}K

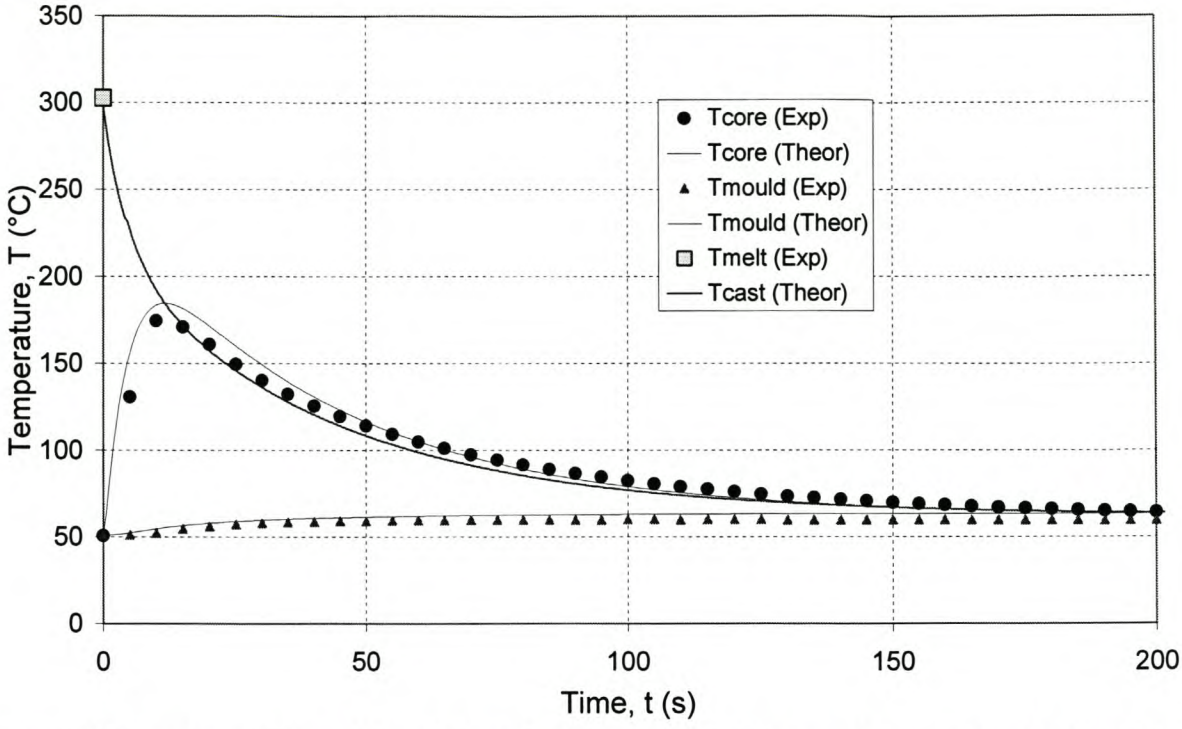

Figure 6.42 Experimental (exp. 4.3) and theoretical (using finite differences) temperatures for the core cooling case. The average ambient temperature is T_a = 16.5 °C. Temperature of melt at start of casting process is T_{melt} = 303 °C. The interfacial contact heat transfer coefficient is h_{CR} = 700 W/m^{2}K

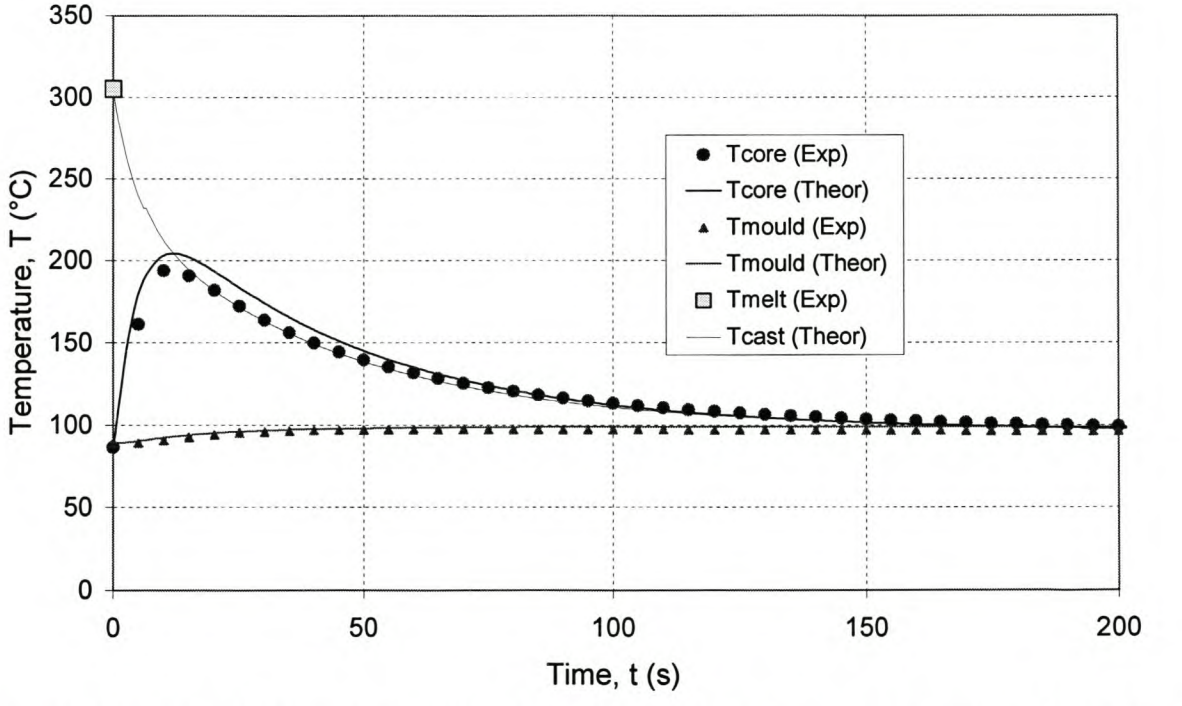

Figure 6.43 Experimental (exp. 4.4) and theoretical (using finite differences) temperatures for the core cooling case. The average ambient temperature is T_a = 18 °C. Temperature of melt at start of casting process is T_{melt} = 305 °C. The interfacial contact heat transfer coefficient is h_{CR} = 700 W/m^{2}K

In figures 6.38 to 6.43, the theoretical core temperature is the temperature of node # 73 (i = 13, j = 4) on grid B in figure C.4 (refer to appendix C). The theoretical mould temperature is the temperature of node # 56 (i = 11, j = 4) on grid A of figure C.3. Figures 6.41 to 6.43 show the theoretical and experimental temperatures for experiments 4.2, 4.3 and 4.4, where the interfacial heat transfer coefficient is taken as 700 W/m^{2}K. As can be seen, reasonable results are achieved. Figures 6.44 to 6.47 show the theoretical and experimental temperatures with respect to experiments 4.5 to 4.8 (where the heat pipe and fin are not used, but the casting and core are removed from the mould after solidification). For these cases, the theoretical mould temperatures are only plotted to the point where the casting is removed from out of the mould. Clear changes in the slopes of the temperatures are observed, since less heat is removed from the casting via natural convection and radiation, than is the case with direct conduction into the outer mould.

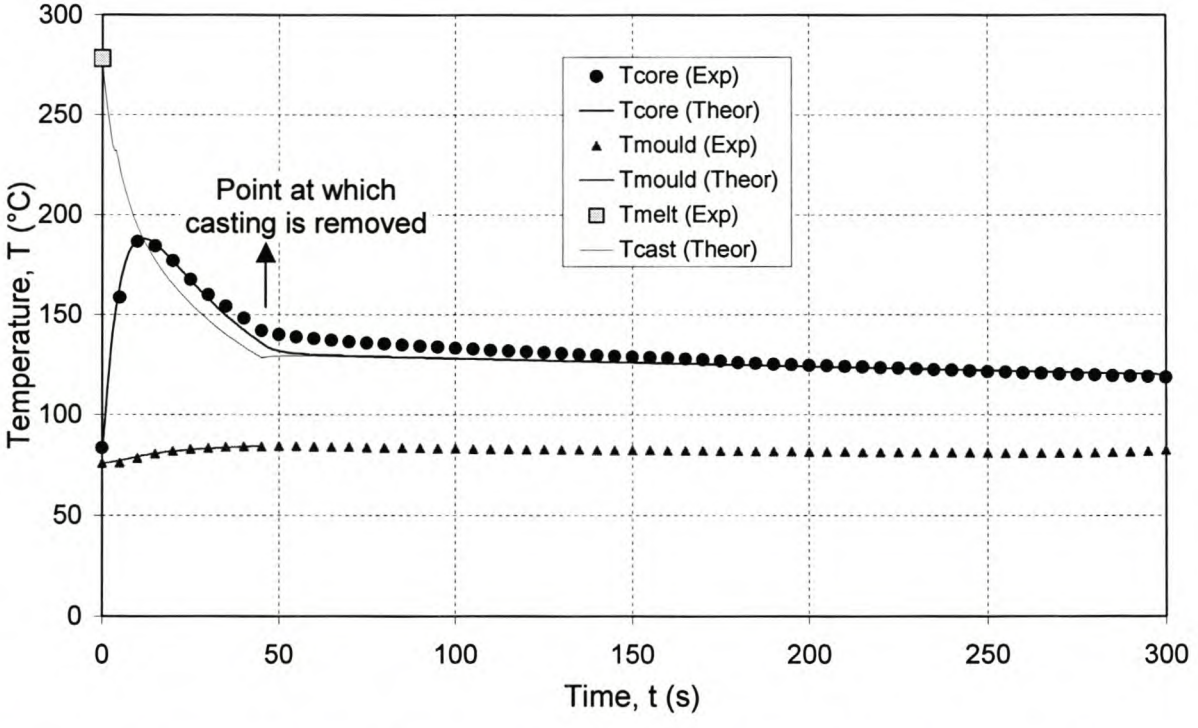

Figure 6.44 Experimental (exp. 4.5) and theoretical (using finite differences) temperatures for the core cooling case. The average ambient temperature is T_a = 17.9 °C. Temperature of melt at start of casting process is T_{melt} = 278 °C. The interfacial contact heat transfer coefficient is h_{CR} = 700 W/m^{2}K

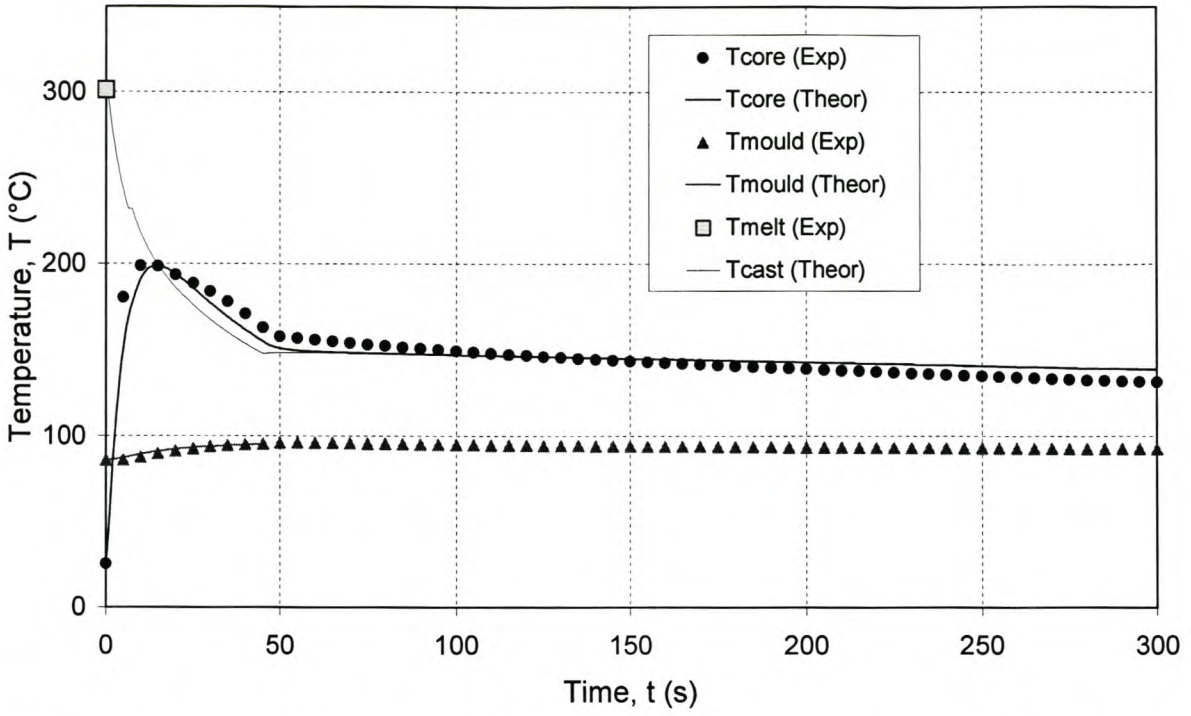

Figure 6.45 Experimental (exp. 4.6) and theoretical (using finite differences) temperatures for the core cooling case. The average ambient temperature is T_a = 18.1 °C. Temperature of melt at start of casting process is T_{melt} = 300 °C. The interfacial contact heat transfer coefficient is h_{CR} = 700 W/m^{2}K

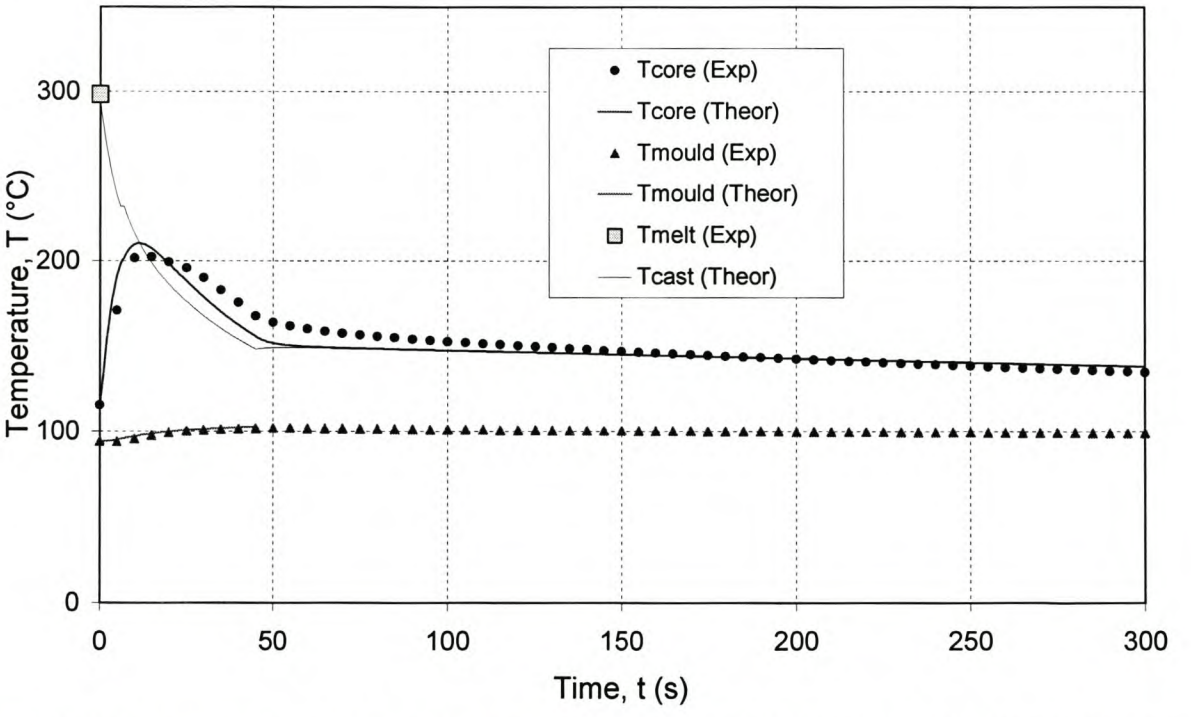

Figure 6.46 Experimental (exp. 4.7) and theoretical (using finite differences) temperatures for the core cooling case. The average ambient temperature is T_a = 18.3 °C. Temperature of melt at start of casting process is T_{melt} = 298 °C. The interfacial contact heat transfer coefficient is h_{CR} = 700 W/m^{2}K

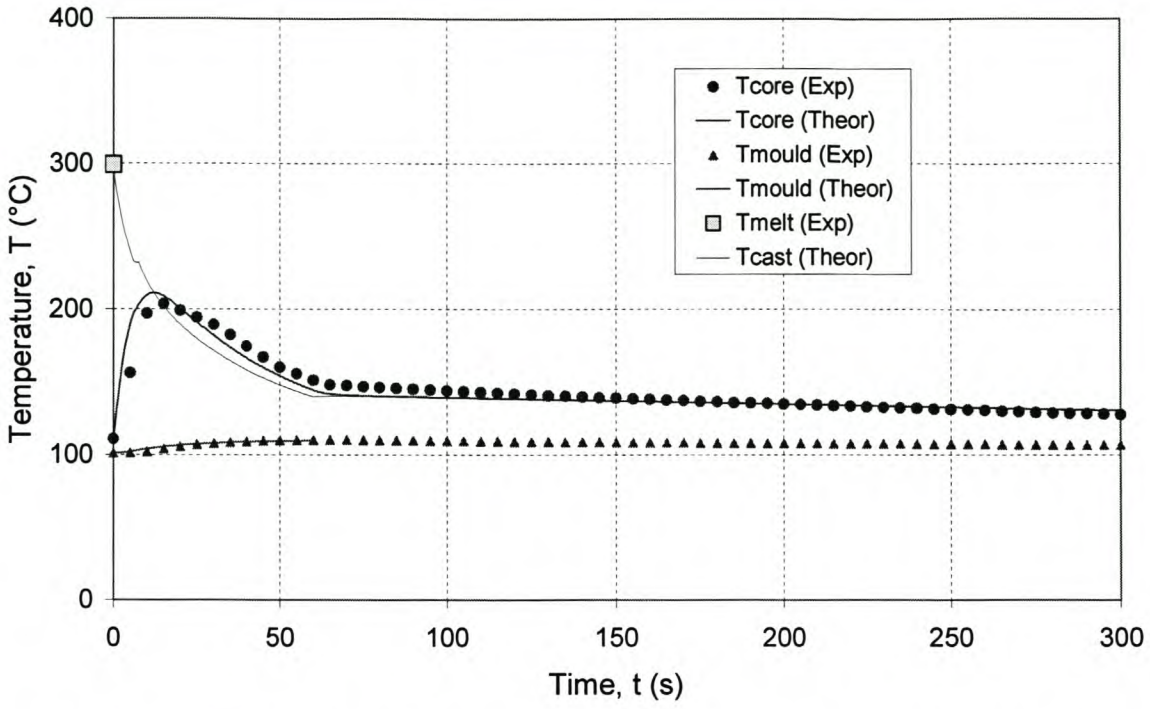

Figure 6.47 Experimental (exp. 4.8) and theoretical (using finite differences) temperatures for the core cooling case. The average ambient temperature is T_a = 18.3 °C. Temperature of melt at start of casting process is T_{melt} = 299 °C. The interfacial contact heat transfer coefficient is h_{CR} = 700 W/m^{2}K

Figures 6.40 to 6.47 show that the theoretical simulations give relatively accurate results when the convection heat transfer coefficient is h_{NC} = 8 W/m^{2}K, the heat transfer coefficient for the contact resistance over the casting-mould interface is taken as h_{cr} = 700 W/m^{2}K and the properties for the steel and tin are used as given in appendix A. The remaining experiments for the core cooling case, experiments 4.9 to 4.13, concern the use of the heat pipe and the air cooled fin that is inserted into the core. For these five experiments, the casting and core are removed from the mould after solidification, and the fins are cooled. The castings were made for different melt, mould, core and fin temperatures. For these experiments and simulations there are three new variables of concern which are the fin base temperature, the air outlet temperature and the heat transfer rate through the heat pipe, all as functions of the time. Figures 6.48 to 6.57 show these results. Once again the theoretical mould temperatures are plotted only to the point where the casting is removed.

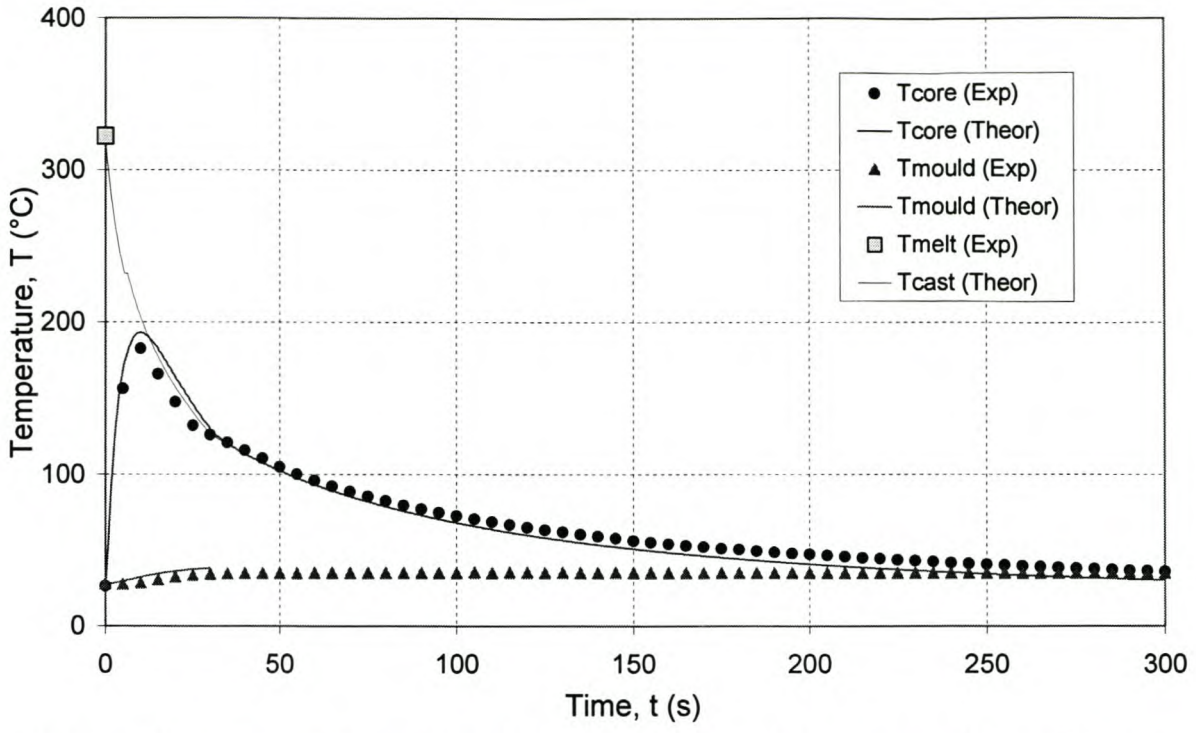

Figure 6.48 Experimental (exp. 4.9) and theoretical (using finite differences and figure 5.28) temperatures for the core cooling case. The mass flow rate of the cooling air is 14.05 g/s and the average ambient temperature is $T_a = 20$ °C. Temperature of melt at start of casting process is $T_{melt} = 320$ °C; $h_{CR} = 700$ W/m^{2}K

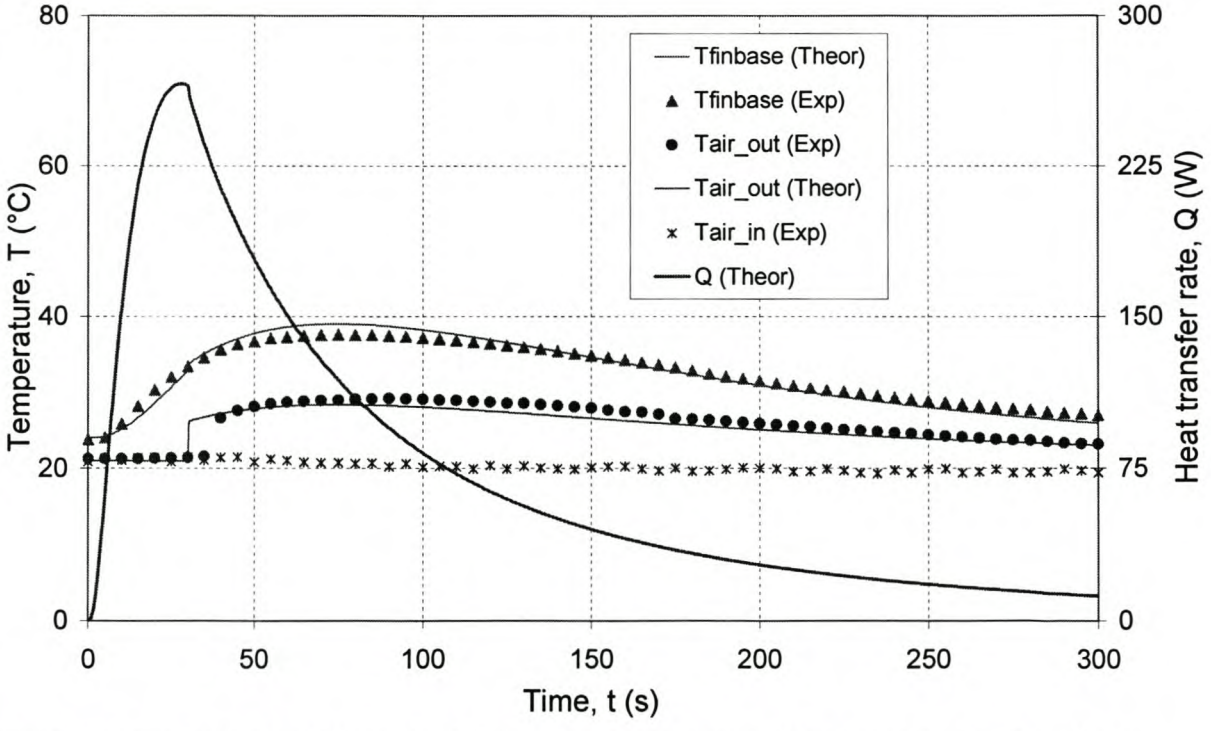

Figure 6.49 Experimental and theoretical air and fin temperatures and heat transfer rate through the heat pipe versus time. (For the same conditions described in figure 6.48)

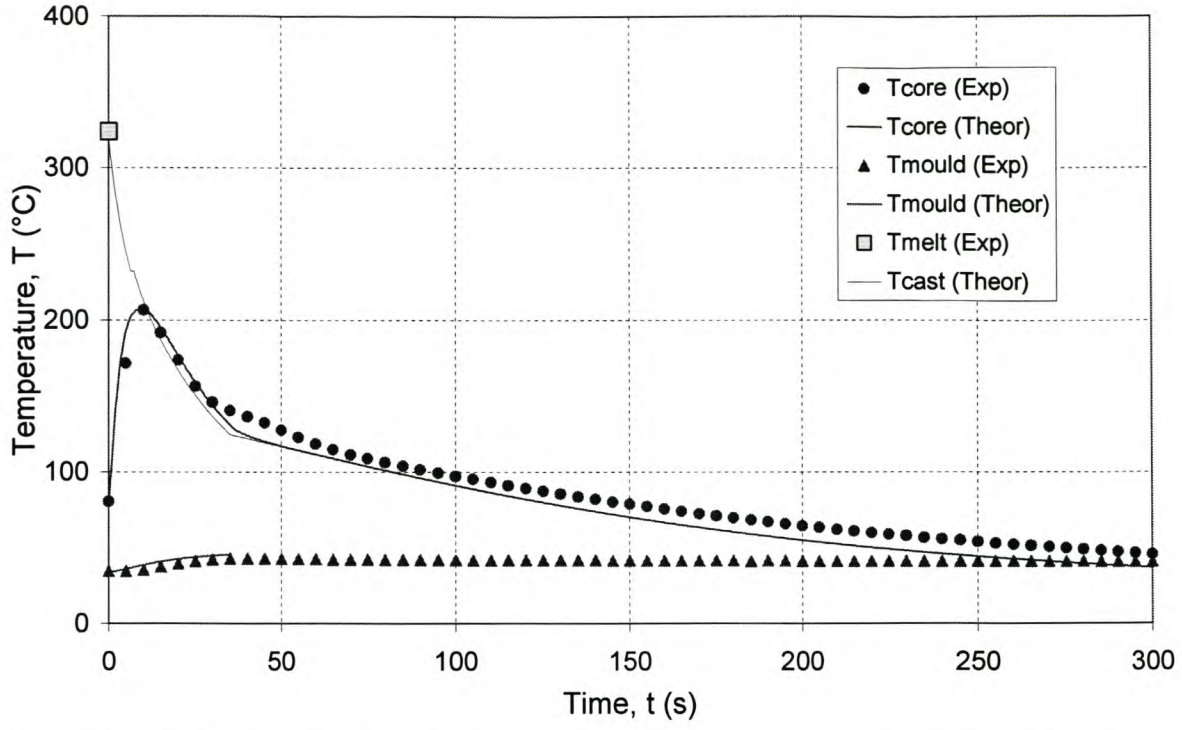

Figure 6.50 Experimental (exp. 4.10) and theoretical (using finite differences and figure 5.28) temperatures for the core cooling case. Mass flow rate of the cooling air is 16.03 g/s and the average ambient temperature is T_a = 19 °C. Temperature of melt at start of casting process is T_{melt} = 323 °C and h_{CR} = 700 W/m^{2}K

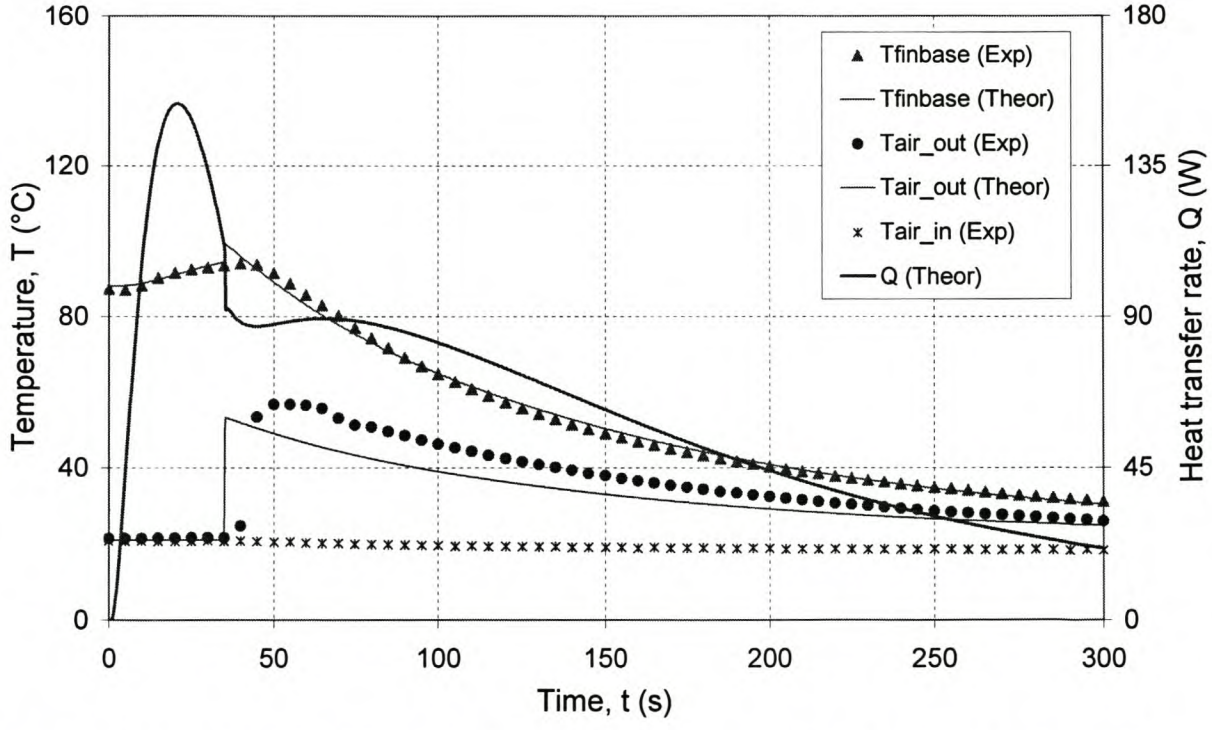

Figure 6.51 Experimental and theoretical air and fin temperatures and heat transfer rate through the heat pipe versus time. (For the same conditions described in figure 6.50)

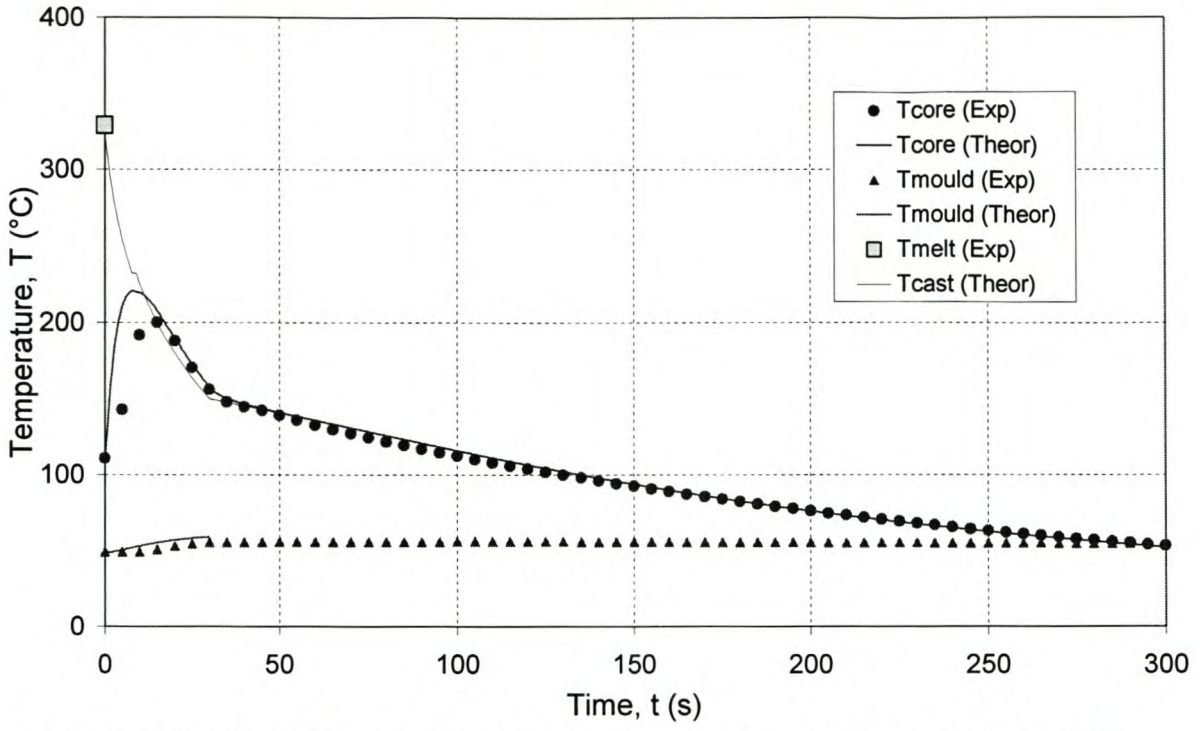

Figure 6.52 Experimental (exp. 4.11) and theoretical (using finite differences and figure 5.28) temperatures for the core cooling case. Mass flow rate of the cooling air is 10.44 g/s and the average ambient temperature is T_a = 19.5 °C. Temperature of melt at start of casting process is T_{melt} = 328 °C and h_{CR} = 700 W/m^{2}K

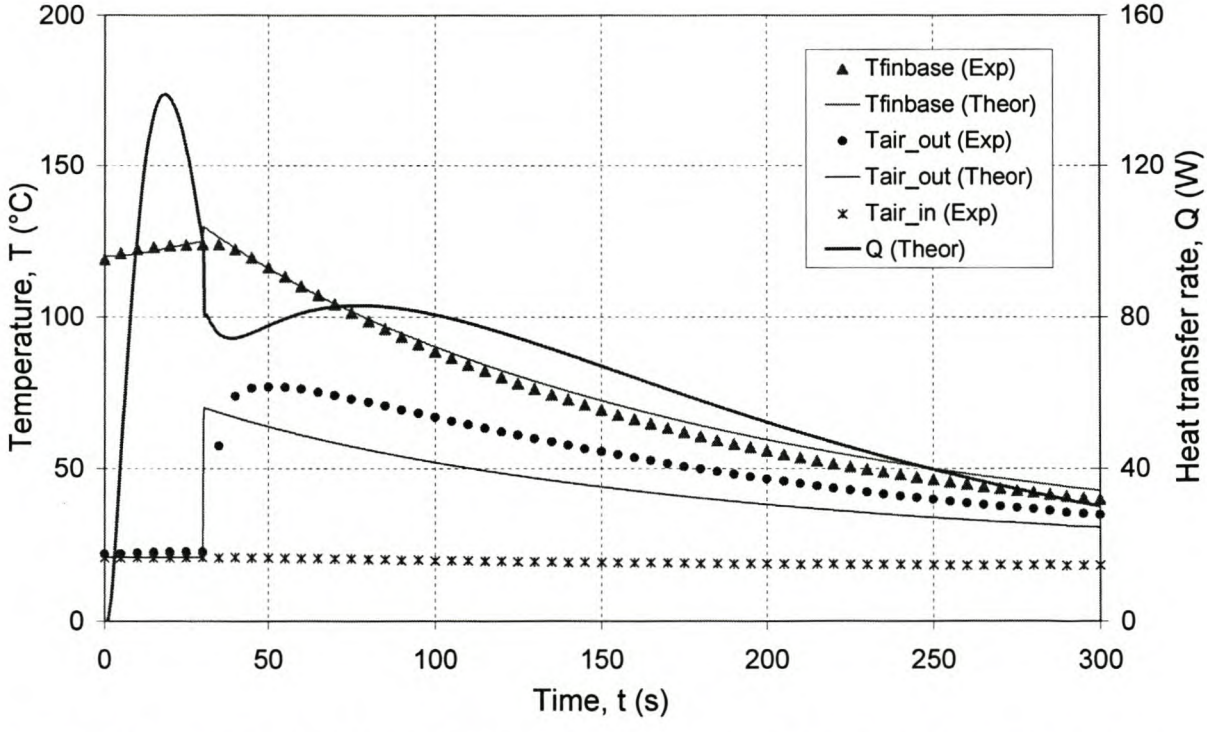

Figure 6.53 Experimental and theoretical air and fin temperatures and heat transfer rate through the heat pipe versus time. (For the same conditions described in figure 6.52)

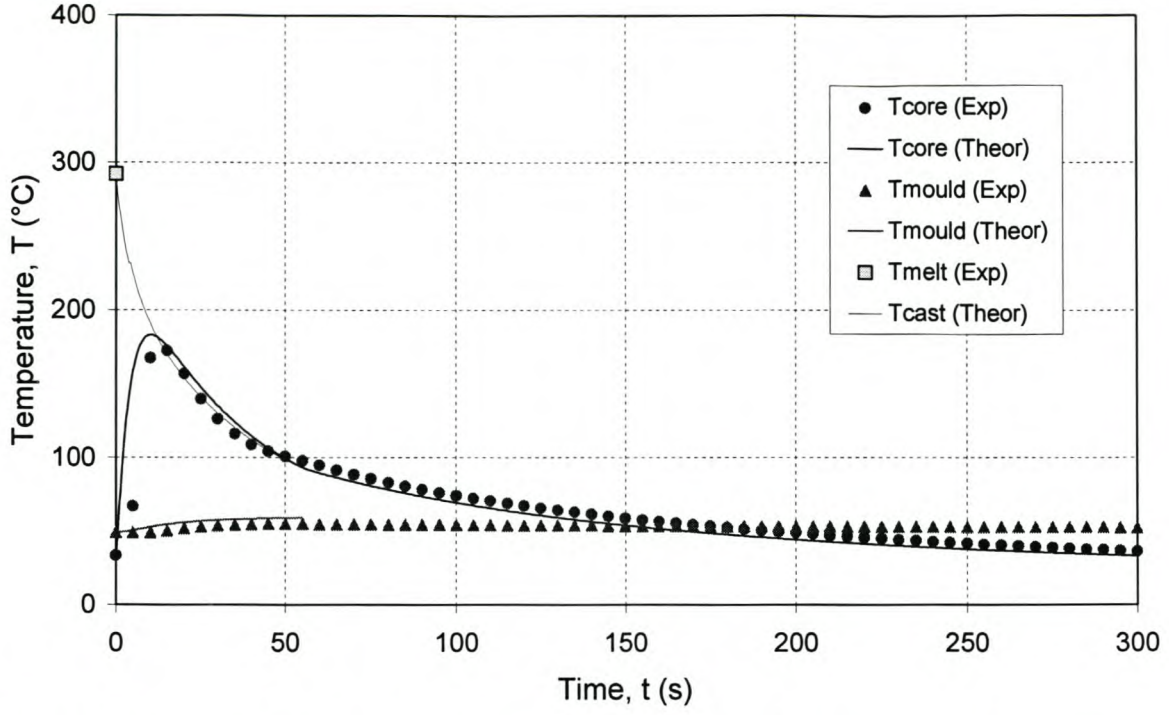

Figure 6.54 Experimental (exp. 4.12) and theoretical (using finite differences and figure 5.28) temperatures for the core cooling case. Mass flow rate of the cooling air is 12.61 g/s and the average ambient temperature is $T_a = 21$ °C. Temperature of melt at start of casting process is $T_{melt} = 292$ °C and $h_{CR} = 700$ W/m^{2}K

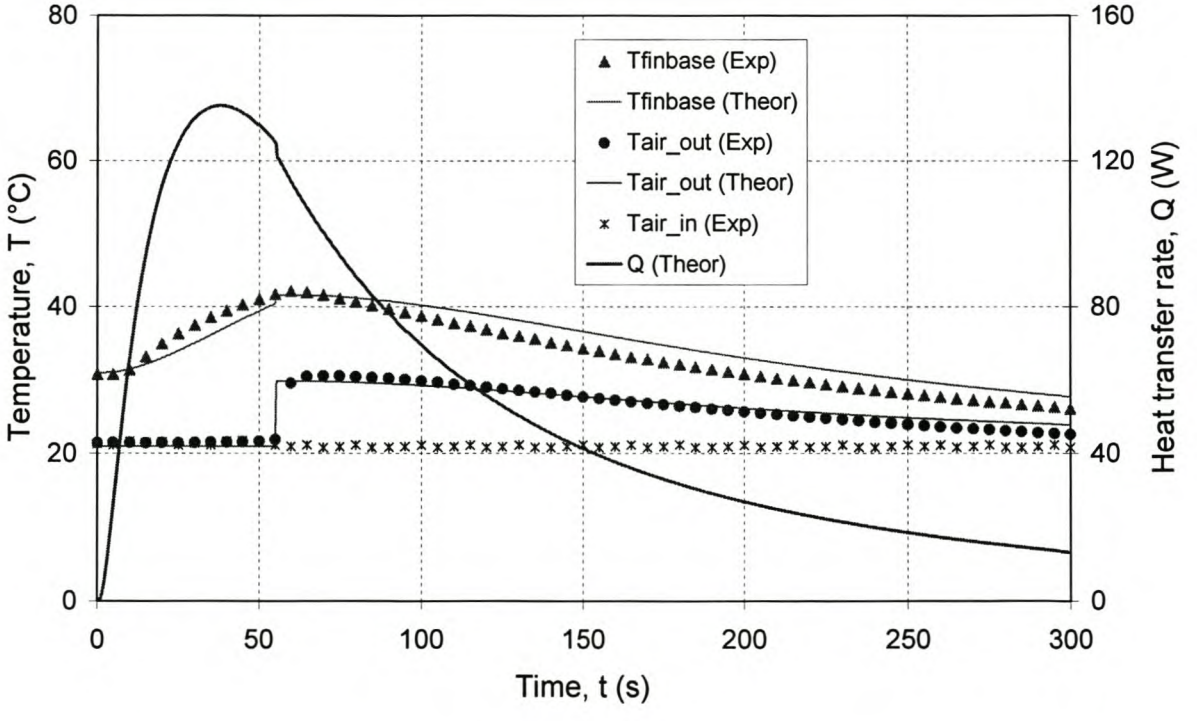

Figure 6.55 Experimental and theoretical air and fin temperatures and heat transfer rate through the heat pipe versus time. (For the same conditions described in figure 6.54)

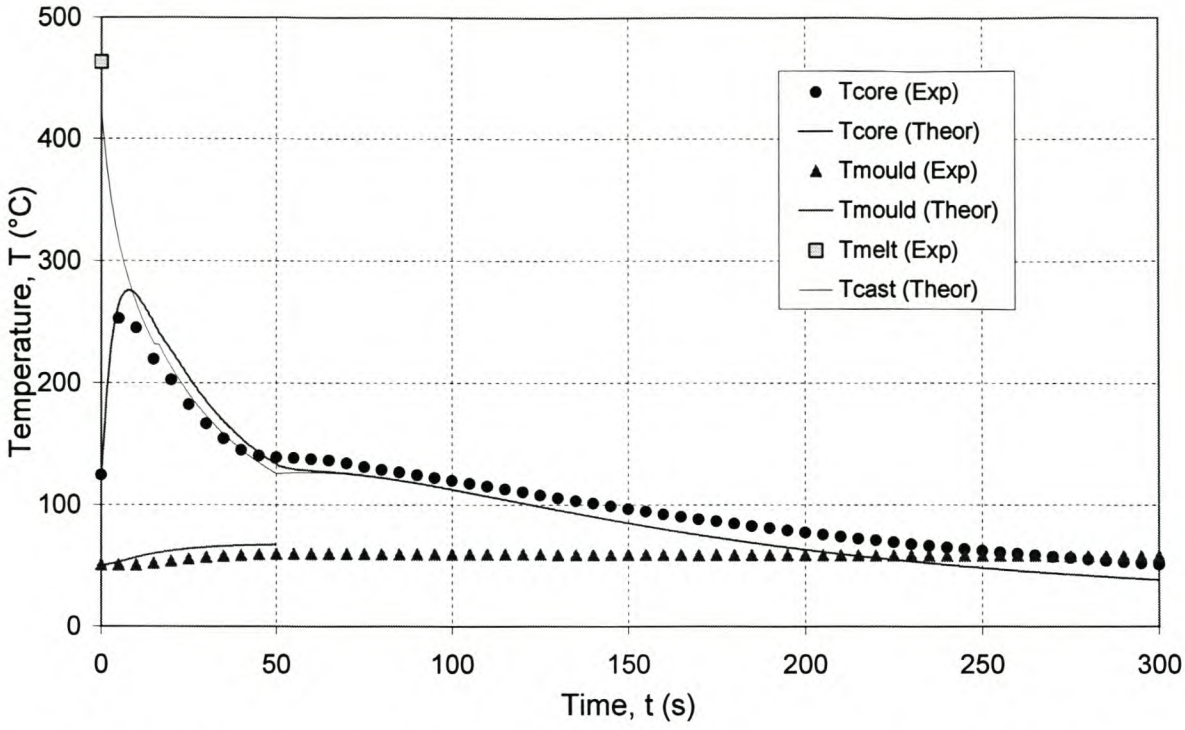

Figure 6.56 Experimental (exp. 4.13) and theoretical (using finite differences and figure 5.28) temperatures for the core cooling case. Mass flow rate of the cooling air is 20.0 g/s and the average ambient temperature is T_a = 18.5 °C. Temperature of melt at start of casting process is T_{melt} = 461 °C and h_{CR} = 700 W/m^{2}K

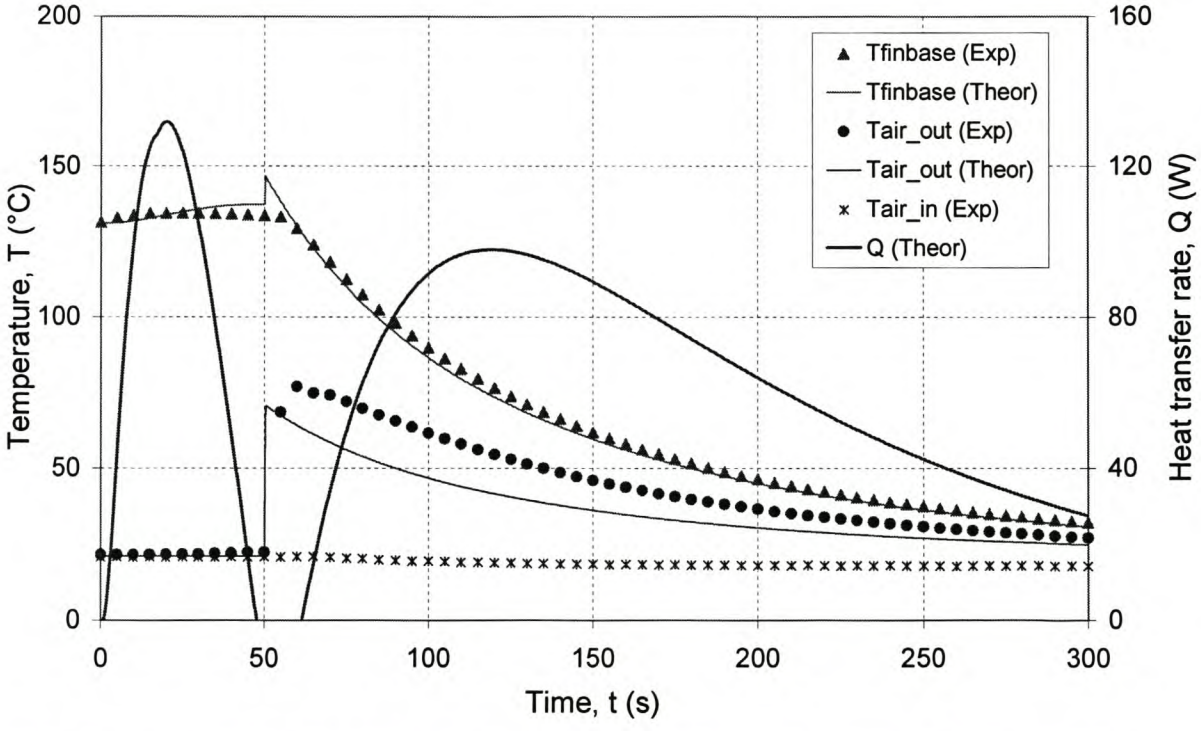

Figure 6.57 Experimental and theoretical air and fin temperatures and heat transfer rate through the heat pipe versus time. (For the same conditions described in figure 6.56)

The comparison between the theoretical and experimental results in figures 6.48 to 6.57 is reasonable. The heat transfer rate through the heat pipe is only calculated theoretically, since for these experiments it was not possible to measure the heat transfer rate directly. The heat transfer rate from the fins to the air could be measured, but it would exclude the effect of the thermal capacity of the fin which is substantial since transient heat transfer takes place. Instead, the theoretical and experimental temperatures of the fin base and the outlet air can be compared as to asses the accuracy of the model. The comparisons are reasonable, therefore the accuracy of the theoretically predicted heat transfer rate should be in the same order of accuracy. In figure 6.57, the theoretically predicted heat transfer rate is zero between about 48 and 62 seconds, since for this period of time the theoretical core and fin base temperatures are more or less the same.

6.5 THE MOULD COOLING CASE

The experimental set-up for the mould cooling case is discussed in section 4.5, and the thermal modelling is discussed in section 5.5. Four types of mould cooling experiments were performed namely experiments 5.1 to 5.4 which are discussed in table 4.6.

During experiment 5.1, tin is cast into the mould, without the heat pipes and heat sink connected. The castings are left inside the mould to cool After a casting is removed, new molten tin is cast into the mould. Figure 6.59 shows how the experimental mould temperature rises after a casting is made. A total of six castings are made. The temperature of the mould rises to above 200 °C after the 4^{th} casting, and stays there for the remaining castings. The theoretical mould temperature shown in figure 6.59, is calculated using the finite element model developed in section 5.5 (refer to figures 5.18 (a-e)). Figures 5.18 (d & e) show heat flux boundary conditions, entering the mould in the radial direction, as a result of the temperature difference between the casting and the mould. Figure 6.58 show these heat flux boundary conditions used in the FEM simulation to produce the theoretical mould temperatures of figure 6.59.

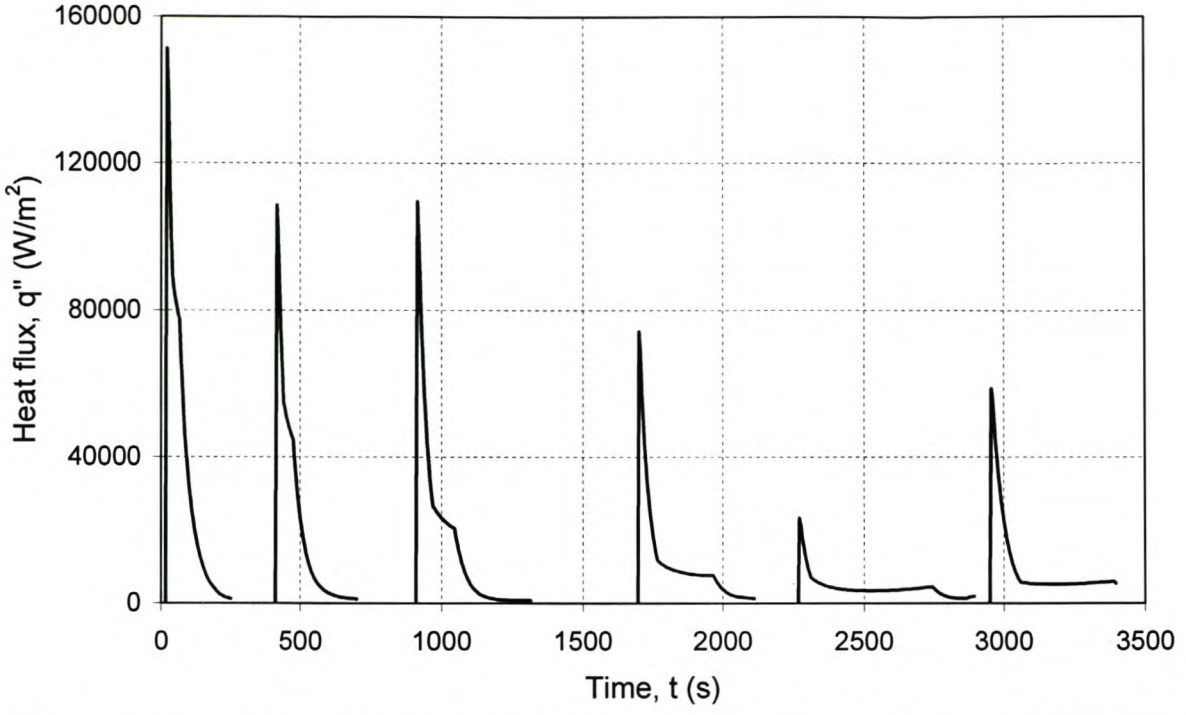

Figure 6.58 The radial heat flux boundary conditions between the casting and the mould, used as input to the FEM simulation of the core cooling case, as a function of time (for the modelling of experiment 5.1). The interfacial contact heat transfer coefficient is $h_{CR} = 500$ W/m^{2}K

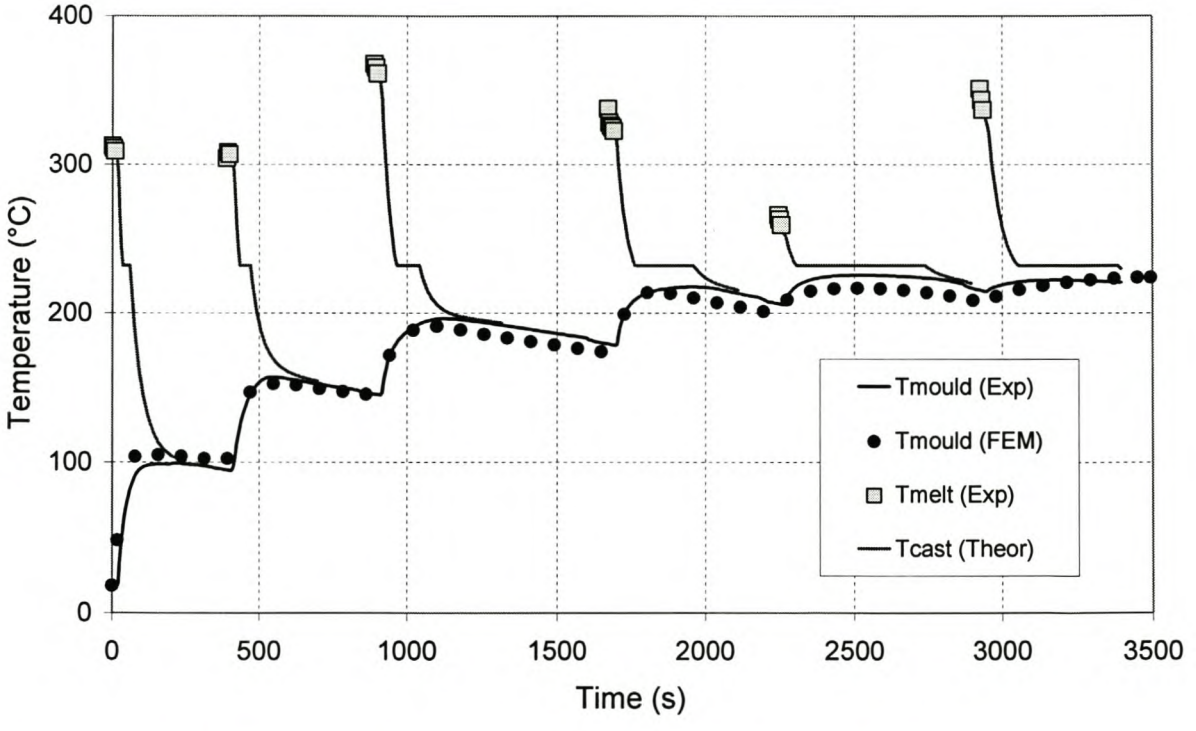

Figure 6.59 Experimental (exp. 5.1) and theoretical (using FEM) temperatures as a function of time. The ambient temperature is $T_a = 17$ °C

The heat fluxes of figure 6.58 are found through an iterative process. The casting is not included in the finite element model, therefore the only link between the casting (modelled as a one node control volume) and the finite element discretisation of the mould (and heat pipes and heat sink, where applicable), is the heat flux boundary condition described in figure 6.58. To find the heat flux boundary condition for the first time step considered, the temperature of the tin melt, as measured just before the casting is made, is assigned to T_{cast} and the experimental temperature of the mould (which is the average of T_1, T_2 and T_3 in figure 4.20) is assigned to T_{mould} (refer to figure 5.20). The value of the interfacial contact heat transfer coefficient used for the core cooling case, $h_{CR} = 700$ W/m^{2}K, can be used as a first estimate in order to calculate $R_{contact}$ (see equation 5.76) and thus to determine the heat transfer rate and heat flux for the time step. This can be used to calculate the amount of energy that flows out of the casting over the discretised time step and hence a new theoretical casting temperature can be calculated for the following time step, and the process can be repeated. In this way the theoretical casting temperature, as well as the heat flux boundary condition are created as functions of time. The heat flux boundary condition is then used as input to the FEM program, which produces the theoretical mould temperature versus time. By comparing the experimental and theoretical temperatures, the accuracy of the heat flux boundary condition can be evaluated. When the interfacial heat transfer coefficient is chosen as $h_{CR} = 700$ W/m^{2}K, the theoretical mould temperatures were higher than the experimental temperatures, suggesting that this coefficient should be lower. By using $h_{CR} = 500$ W/m^{2}K, the heat flux boundary conditions become lower and the theoretical temperatures are very close to the experimental temperatures. If a interfacial heat transfer coefficient of $h_{CR} = 300$ W/m^{2}K is used, the heat flux boundary conditions are lower than those shown in figure 6.58 and the theoretical temperatures are consequently also lower than the experimental temperatures. The iterations are omitted and only the final results (using $h_{CR} = 500$ W/m^{2}K) are shown in figure 6.59. Possible reasons for the difference between the interfacial contact heat transfer coefficient for the core cooling and mould cooling cases, are discussed in chapter 8.

Figures 6.60 to 6.71 show the experimental results for experiments 5.2 to 5.4. The same iterative procedure used to produce the results for experiment 5.1 are used. Experiment 5.2 differs from experiment 5.1 in the sense that the castings are removed from the moulds after a time. This can be seen in figure 6.61, where the casting is removed at the points where the theoretical casting temperatures stop and a change in slope of the experimental mould temperature is evident. The heat flux boundary conditions used to find the theoretical (FEM) temperatures shown in figure 6.61, are given in figure 6.60. Experiment 5.3 is similar to experiment 5.1 in the sense that a casting is left inside the mould to cool and is not removed until just before the next casting is made. The difference between experiment 5.1 and 5.3 is that for experiment 5.3 the heat sink is connected to the mould via heat pipes. Another difference is the way in which the experimental data is logged for experiment 5.3. For experiments 5.1, 5.2 and 5.4, the data is logged for sequential castings over a long period of time, so that the total temperature histories of the mould and heat sink are displayed. For experiment 5.3 though, the temperatures were recorded for each casting on its own in order to also investigate the effect of water cooling the heat sink a little closer. Figures 6.62 to 6.69 show the heat flux boundary conditions and temperatures of the casting, mould and heat sink for the four castings made, experiments 5.3(a-d). Figure 6.63 shows the temperatures for experiment 5.3.a. During this experiment the heat sink was not cooled. Figures 6.65 and 6.67 show the temperatures for experiments 5.3.b and 5.3.c respectively, where the heat sink is water cooled after 90 to 100 seconds. Figure 6.69 shows the temperatures for experiment 5.3.d, where the water cooling is started after 180 seconds and stopped after 320 seconds, with the resulting temperature response of the heat sink. Figures 6.70 and 6.71 show the heat flux boundary conditions and temperatures for experiment 5.4, where five castings are made and removed from the mould after some time. The heat sink is not cooled during the casting process, but after the final casting is removed, so that the accuracy of the modelling of the water cooling can also be evaluated.

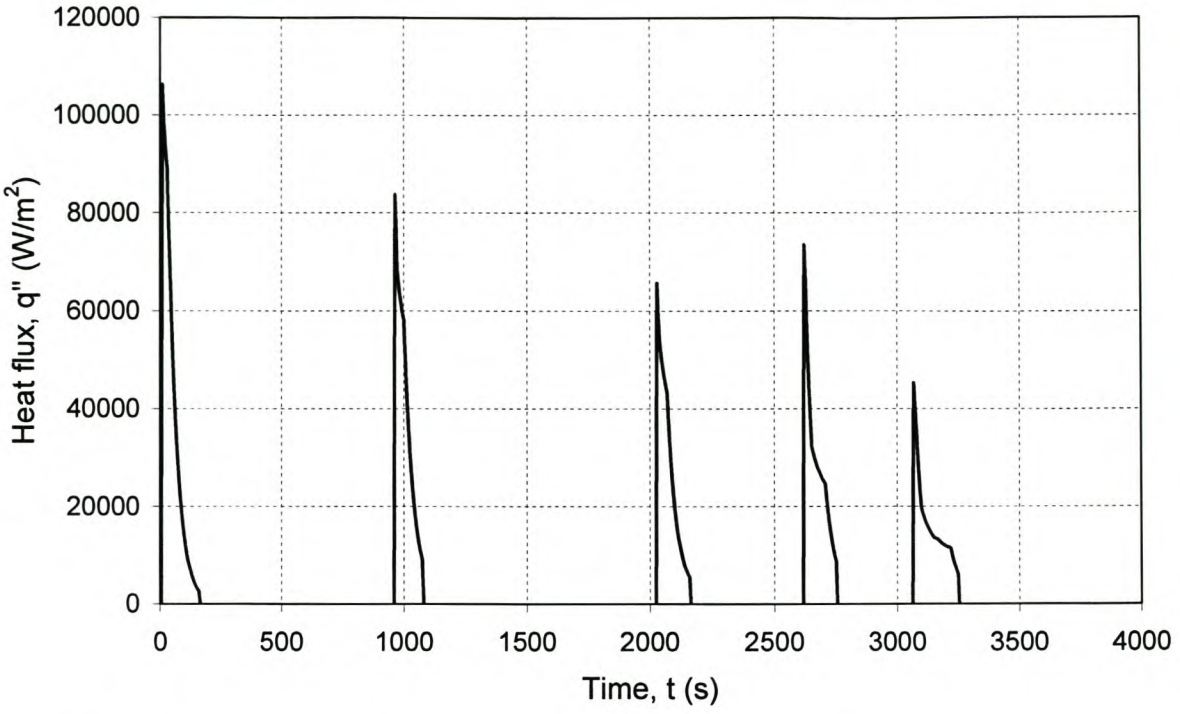

Figure 6.60 The radial heat flux boundary conditions between the casting and the mould, used as input to the FEM simulation of the core cooling case, as a function of time (for the modelling of experiment 5.2). The interfacial contact heat transfer coefficient is $h_{CR} = 500$ W/m^{2}K

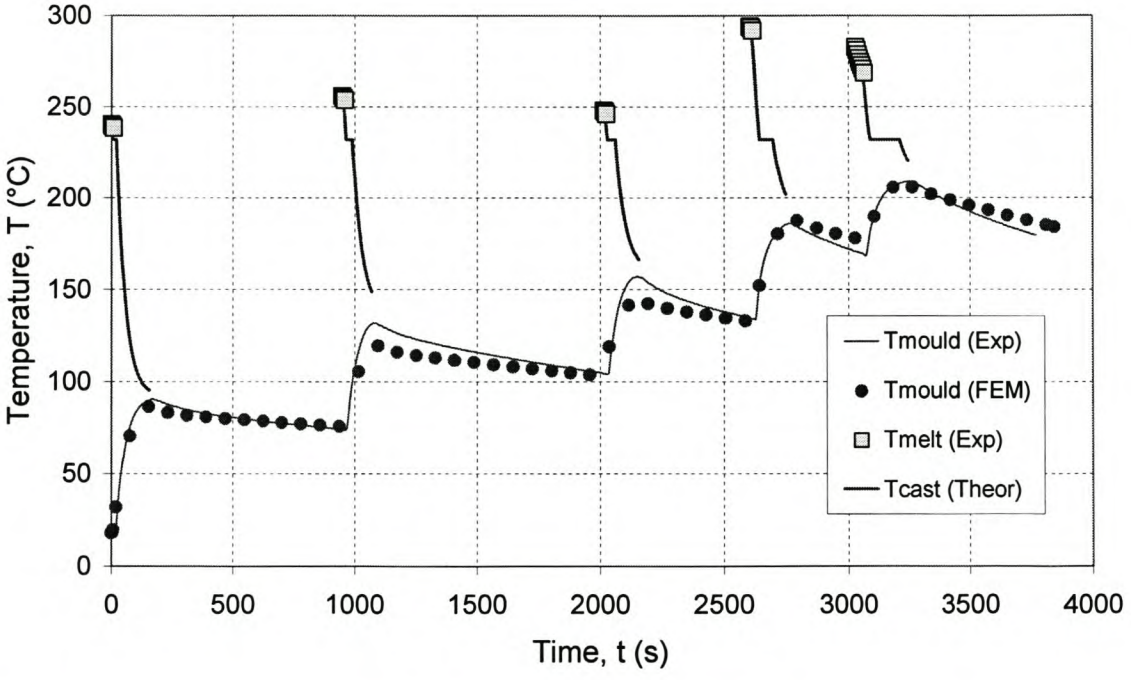

Figure 6.61 Experimental (exp. 5.2) and theoretical (using FEM) temperatures as a function of time. The ambient temperature is $T_a = 18$ °C

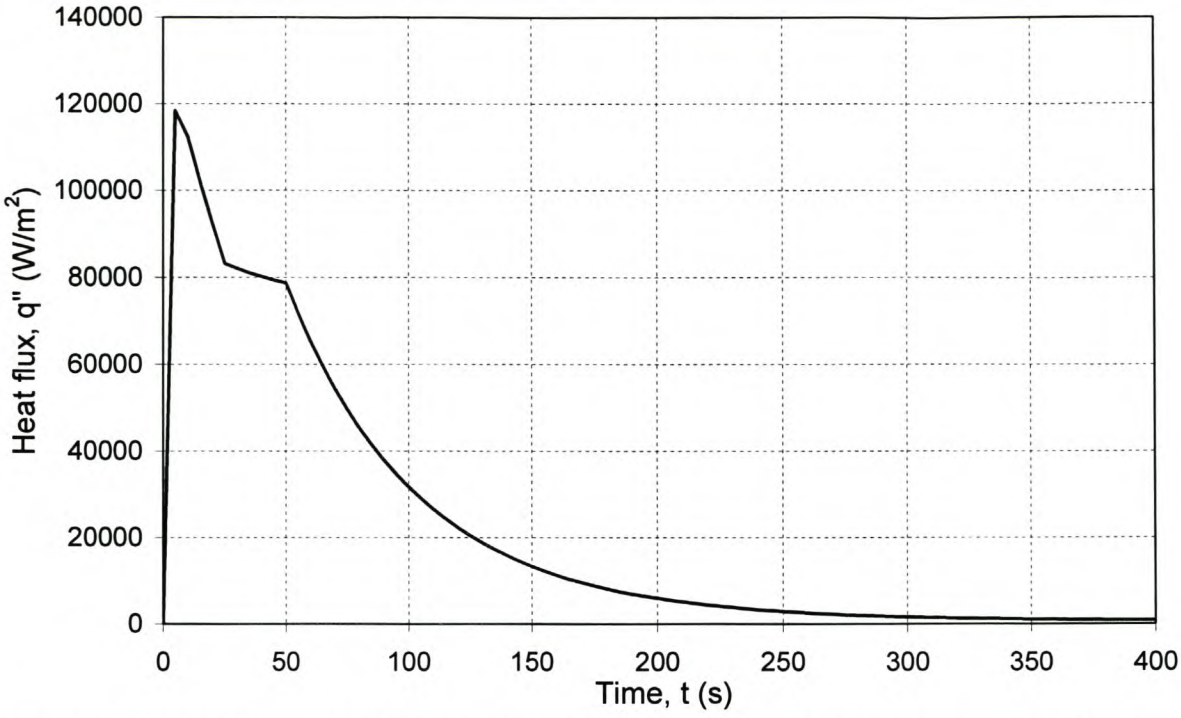

Figure 6.62 The radial heat flux boundary conditions between the casting and the mould, used as input to the FEM simulation of the core cooling case, as a function of time (for the modelling of experiment 5.3.a). The interfacial contact heat transfer coefficient is $h_{CR} = 500$ W/m^{2}K

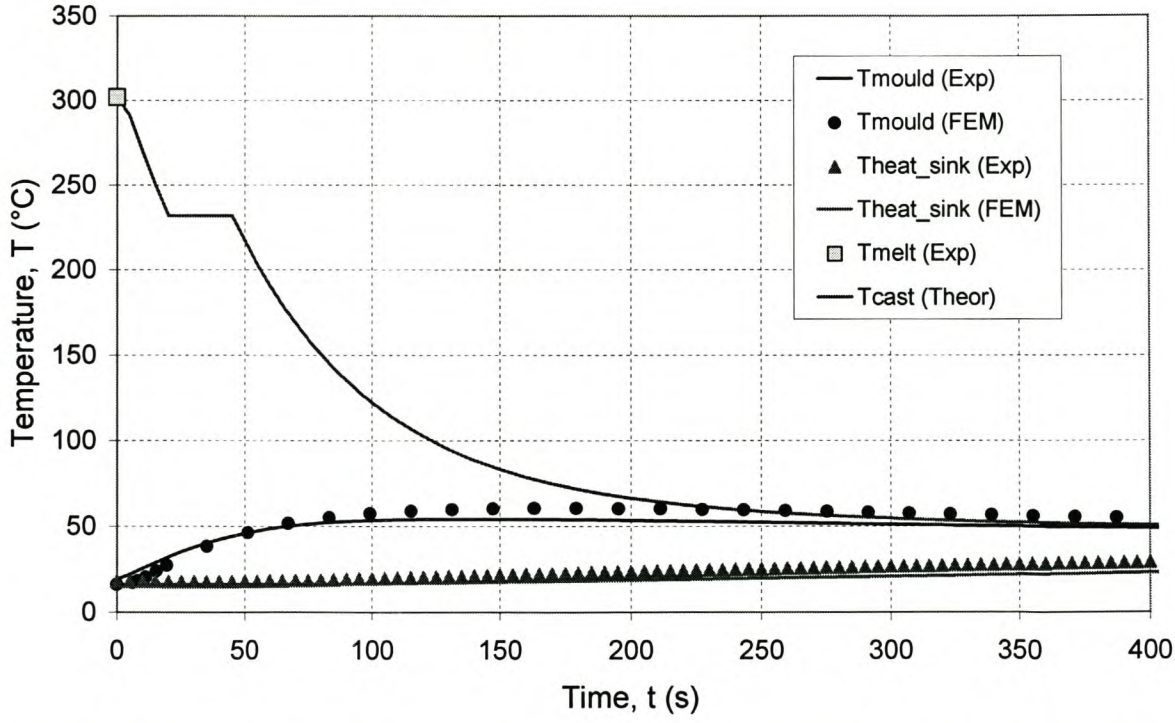

Figure 6.63 Experimental (exp. 5.3.a) and theoretical (using FEM) temperatures as a function of time. The ambient temperature is $T_a = 16.5$ °C

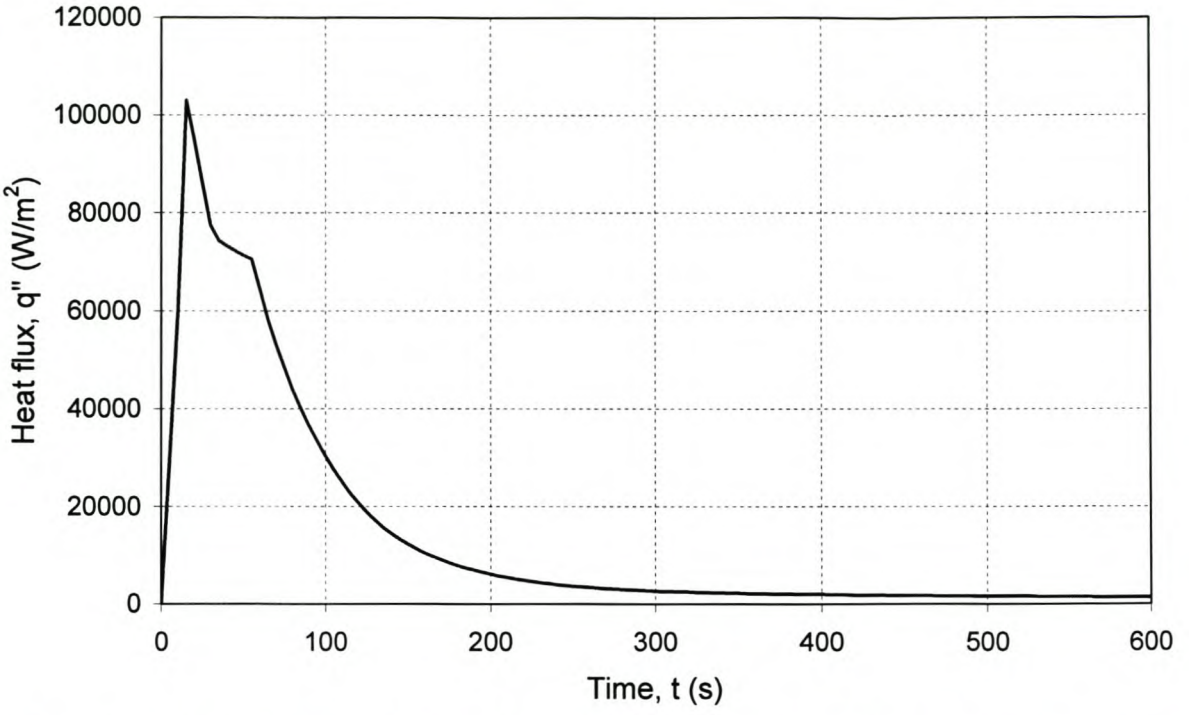

Figure 6.64 The radial heat flux boundary conditions between the casting and the mould, used as input to the FEM simulation of the core cooling case, as a function of time (for the modelling of experiment 5.3.b). The interfacial contact heat transfer coefficient is $h_{CR} = 500$ W/m^{2}K

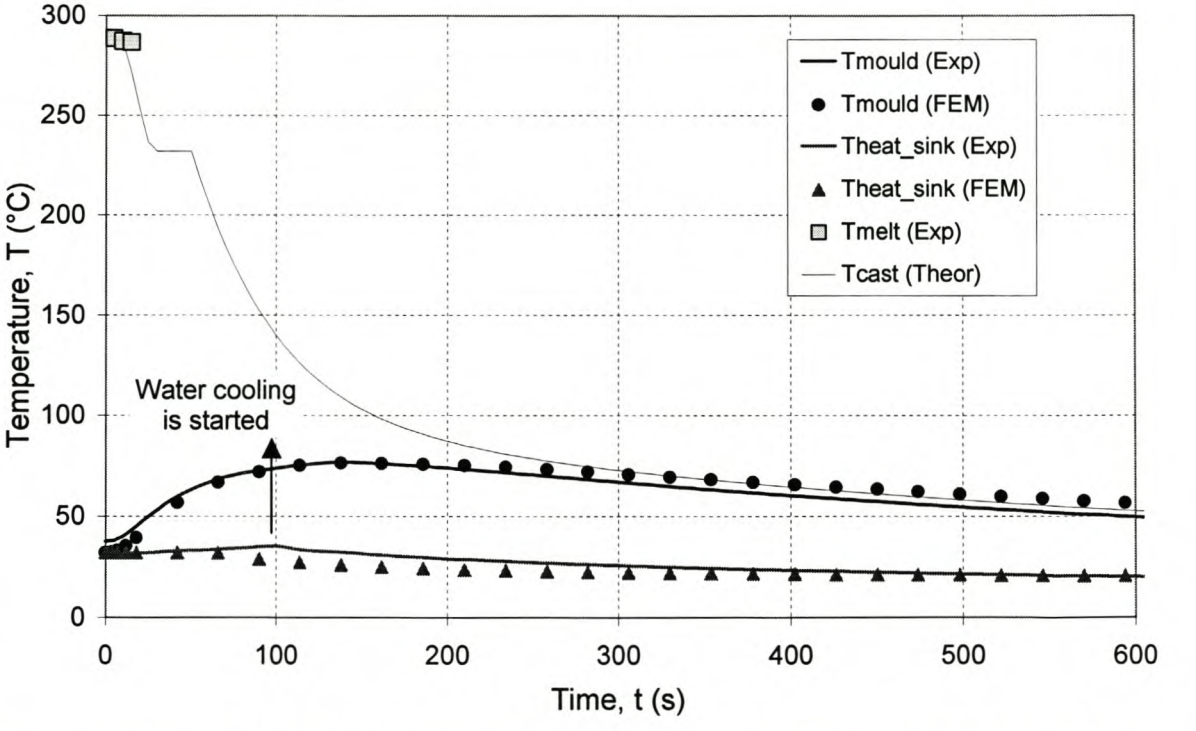

Figure 6.65 Experimental (exp. 5.3.b) and theoretical (using FEM) temperatures as a function of time. The ambient temperature is $T_a = 16.5$ °C

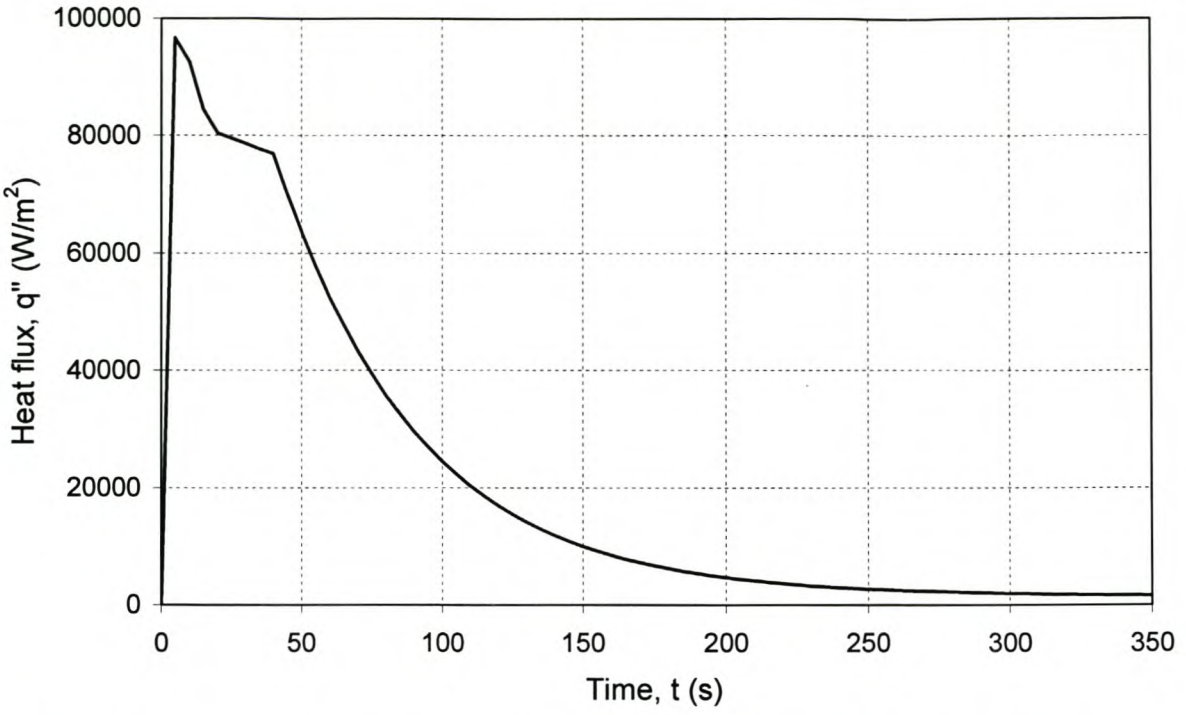

Figure 6.66 The radial heat flux boundary conditions between the casting and the mould, used as input to the FEM simulation of the core cooling case, as a function of time (for the modelling of experiment 5.3.c). The interfacial contact heat transfer coefficient is $h_{CR} = 500$ W/m^{2}K

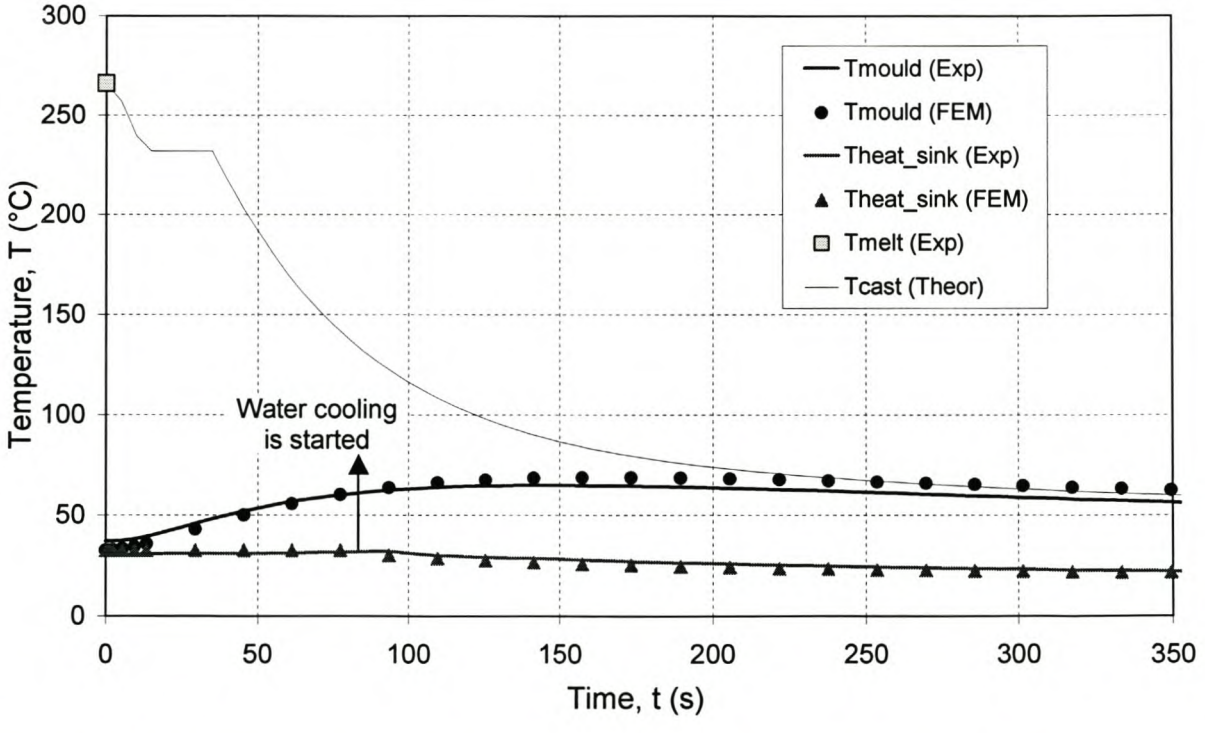

Figure 6.67 Experimental (exp. 5.3.c) and theoretical (using FEM) temperatures as a function of time. The ambient temperature is $T_a = 16$ °C

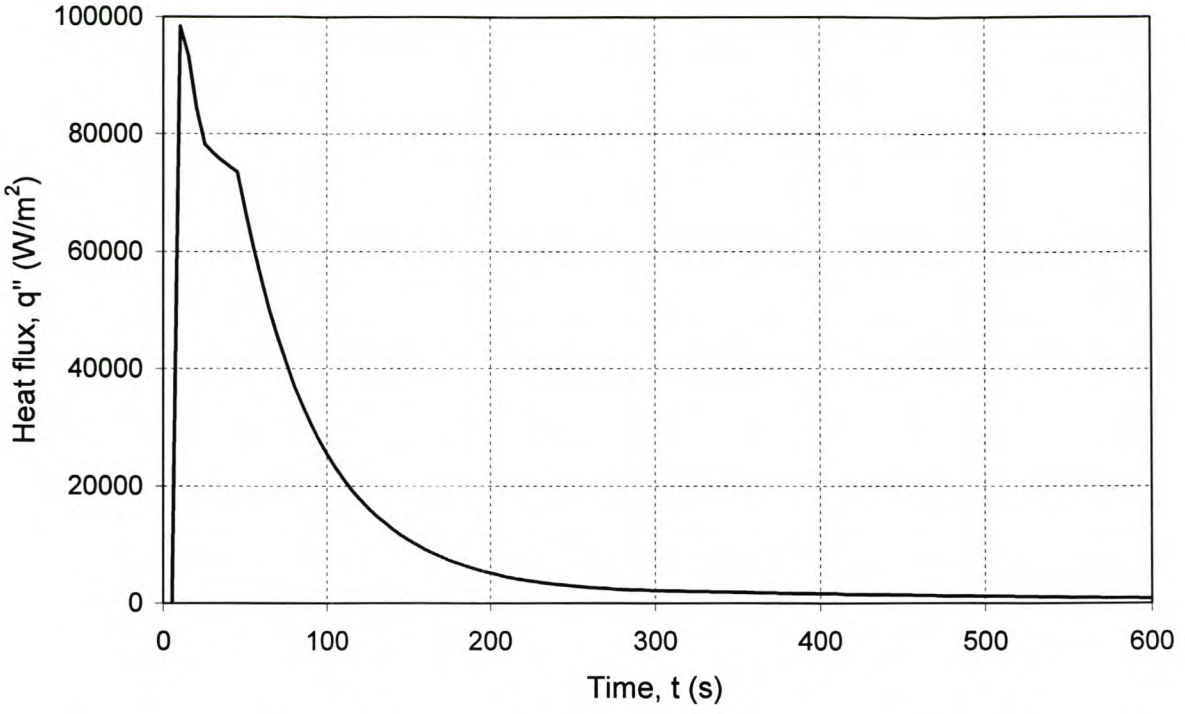

Figure 6.68 The radial heat flux boundary conditions between the casting and the mould, used as input to the FEM simulation of the core cooling case, as a function of time (for the modelling of experiment 5.3.d). The interfacial contact heat transfer coefficient is $h_{CR} = 500$ W/m^{2}K

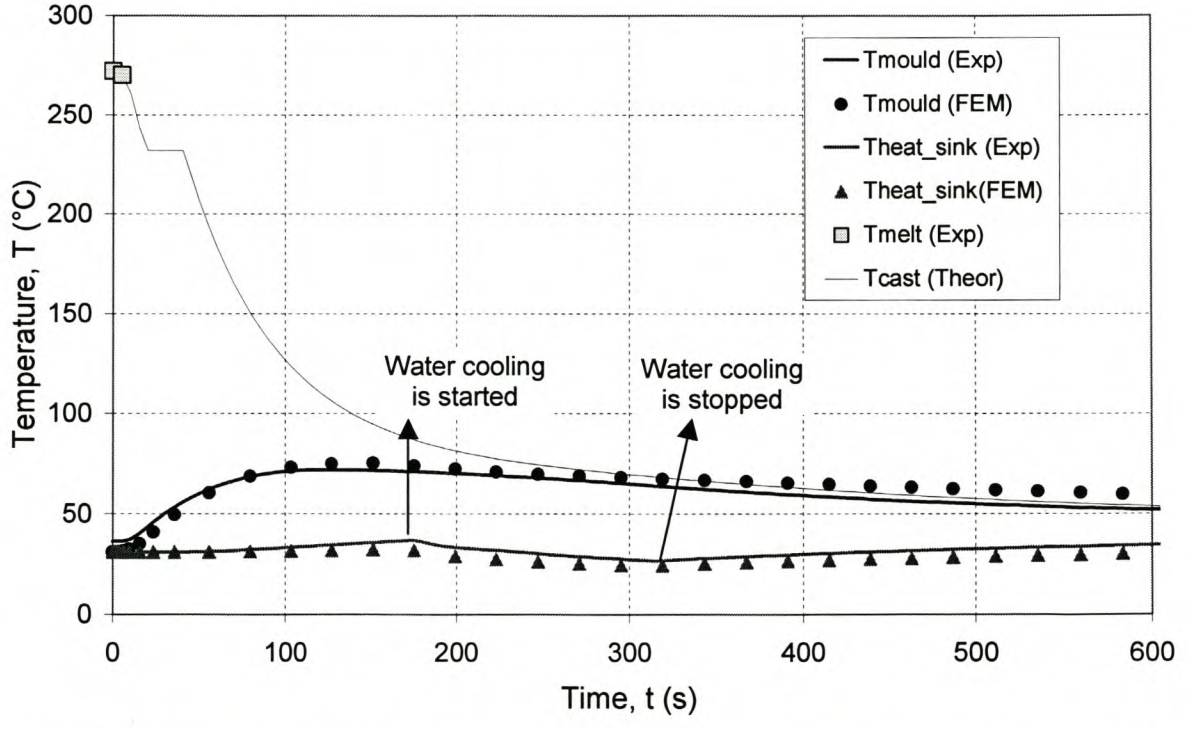

Figure 6.69 Experimental (exp. 5.3.d) and theoretical (using FEM) temperatures as a function of time. The ambient temperature is $T_a = 16$ °C

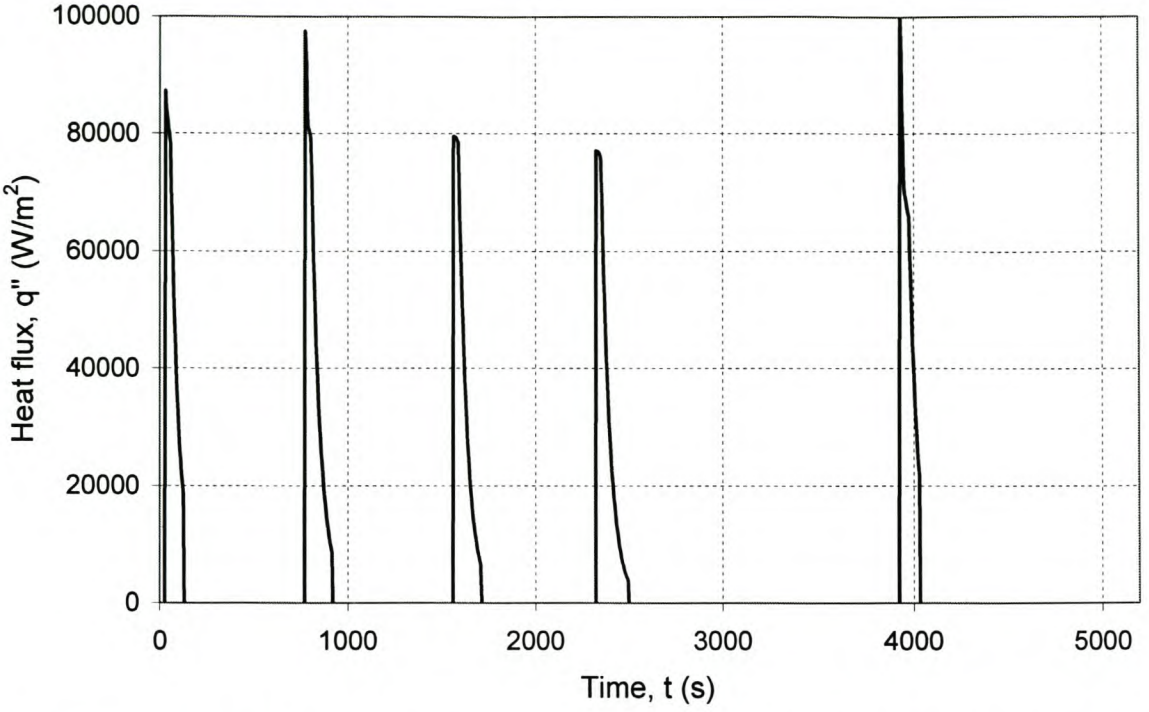

Figure 6.70 The radial heat flux boundary conditions between the casting and the mould, used as input to the FEM simulation of the core cooling case, as a function of time (for the modelling of experiment 5.4). The interfacial contact heat transfer coefficient is $h_{CR} = 500$ W/m^{2}K

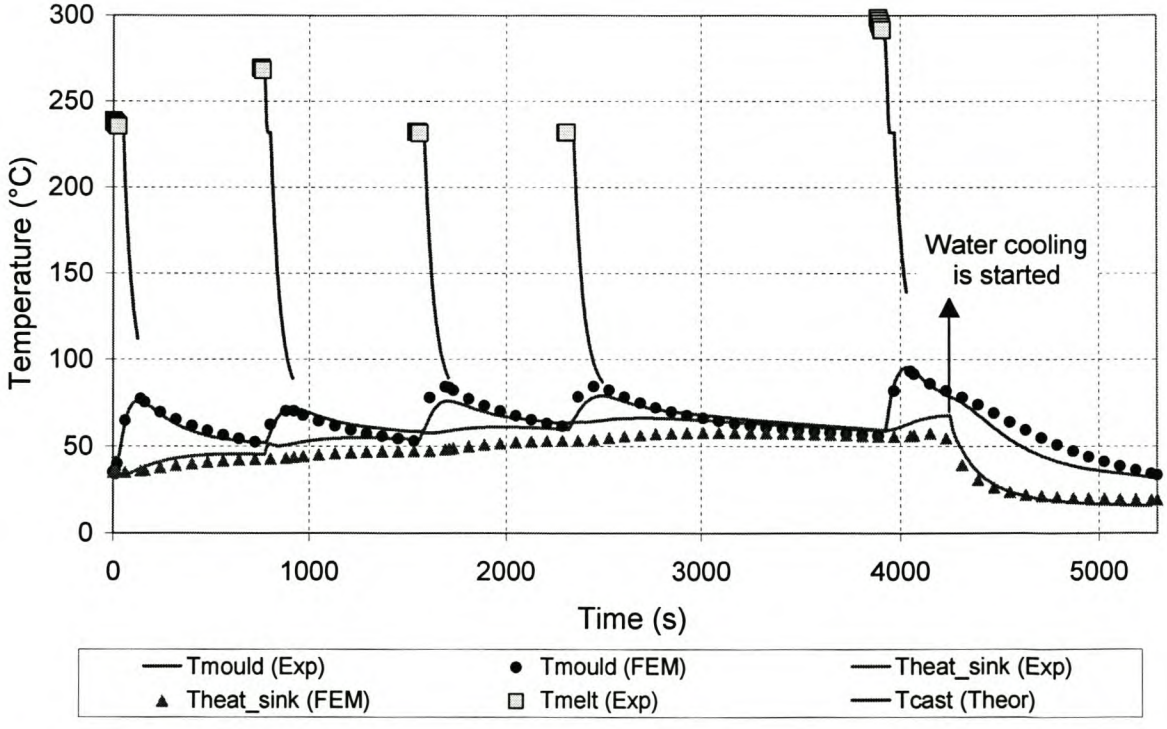

Figure 6.71 Experimental (exp. 5.4) and theoretical (using FEM) temperatures as a function of time. The ambient temperature is $T_a = 17$ °C. The cooling water is switched on at 4200 seconds

CHAPTER 7 - Simulation Case

In this chapter a simple example is presented to show how predicting the temperature of a specified position in a casting mould fitted with heat pipes, may be of use for the practical casting industry.

Consider the mould used for the mould cooling case, discussed in sections 4.5 and 5.5. Suppose that the tin castings are to be made in a production line, and the technical requirements for the casting process are the following:

Table 7.1 Casting specifications for the simulation case

Casting material →	Tin
Casting Temperature →	250 °C
Temperature at which casting must be removed from the mould →	200 °C
Maximum allowable mould temperature to make casting →	100 °C
Minimum time needed to remove a casting and prepare the mould for the following casting →	1 minute

Two cases will be considered. For the first case, the assumption is made that the tin is cast into the mould without any heat pipes being fitted. The only way in which cooling of the mould can take place is therefore through natural convection and radiation. The second case is where the heat pipes and heat sink are fitted to the mould, and the heat sink is constantly cooled by water flowing through the cooling channels.

The thermal model is the same as the one described in section 5.5, and the numerical simulation is performed using the standard finite element method computer program (NASTRAN). Figures 7.1 and 7.2 show the temperatures of the casting (T_{cast}) and the mould (T_{mould}) as well as the radial heat flux from the casting into the mould that is used as the boundary condition in the NASTRAN program for case 1 (thus without heat pipes). Figures 7.3 and 7.4 shows the results for case 2, where the heat pipes are assumed to be connected to the water cooled heat sink.

The iterative process to determine the heat flux boundary conditions and resulting theoretical temperatures will now be described:

1. Estimate the time that the casting would take to cool down from 250°C to 200°C and the associated temperature rise of the mould during the time
2. The values for $(T_{cast} - T_{mould})$ can now be calculated at the time where the casting is poured in and also at the time where it is removed. Interpolate linearly between these two points and determine the heat flux, assuming a interfacial contact heat transfer coefficient of $h_{CR} = 500\ \mathrm{W/m^2K}$
3. Use the values of the heat flux as a function of time (determined in step 2) as the boundary conditions for the FEM simulation
4. Find the theoretically determined temperature rise of the mould over the estimated time, and calculate the new time that the casting takes to reach 200°C
5. Update the cool-down time of the casting and the temperature rise of the mould during that time, and go back to step 1, until convergence is more or less reached

In figure 7.1 it can be seen that for the first three castings the maximum allowable mould temperature is not exceeded. A time of about 330 seconds must elapse before the fourth casting can be poured and by 1800 seconds the mould has not yet cooled down to 100°C. In figure 7.3 it is seen that because of the enhancing effect of the heat pipes the time for the mould to cool down is reduced and ten castings can be made in the 1800 seconds.

These simulations are relatively simple, and similar simulations done for industrial castings would probably be more involved. It does however give an idea of how one should think when analysing a casting operation, from a thermal point of view.

The requirement for a mould to be at a specific temperature when the casting is made is quite common in industry, for example where directional solidification needs to be achieved. Therefore, the steadier the mould's temperature can be kept, the better– from both a quality and production rate point of view.

The possible advantages of using heat pipes in casting moulds are therefore illustrated, at least conceptually, by these simulations.

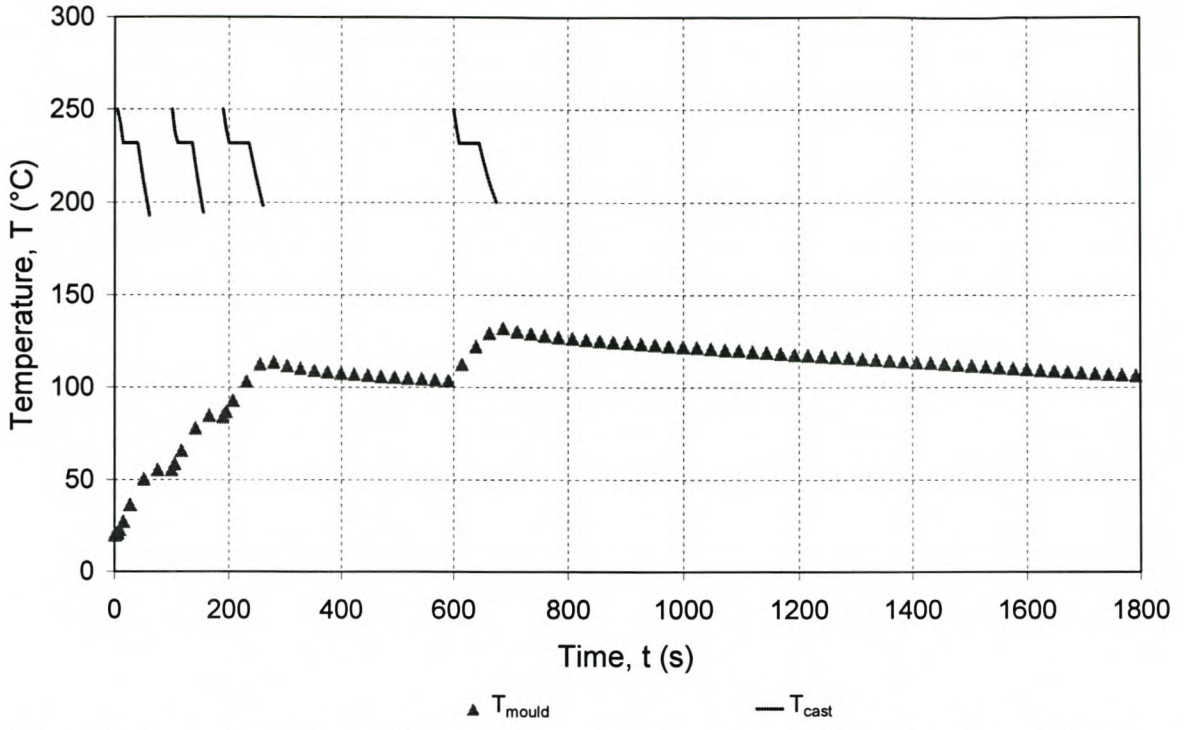

Figure 7.1 Theoretical (using FEM) temperatures of the tin casting and the external mould (similar as was used for the Mould Cooling Case) versus time, when no heat pipes are used for cooling

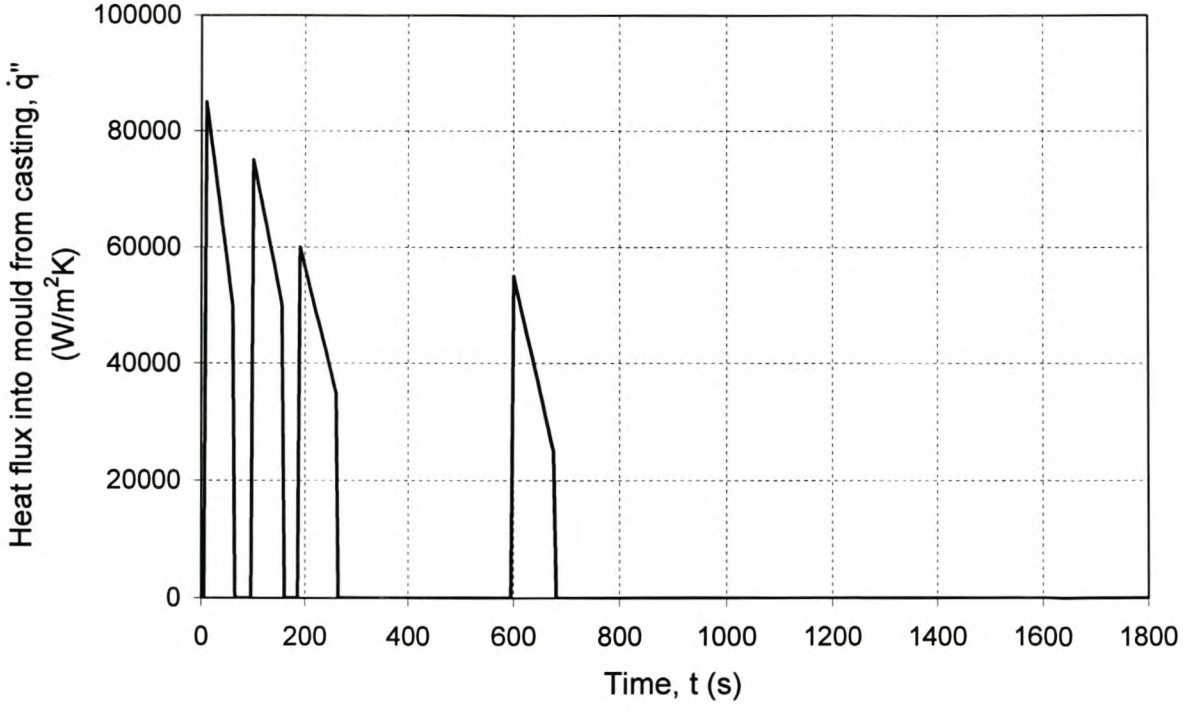

Figure 7.2 Radial heat flux entering the mould versus time, used as boundary conditions in the FEM simulation to produce the temperatures shown in figure 7.1

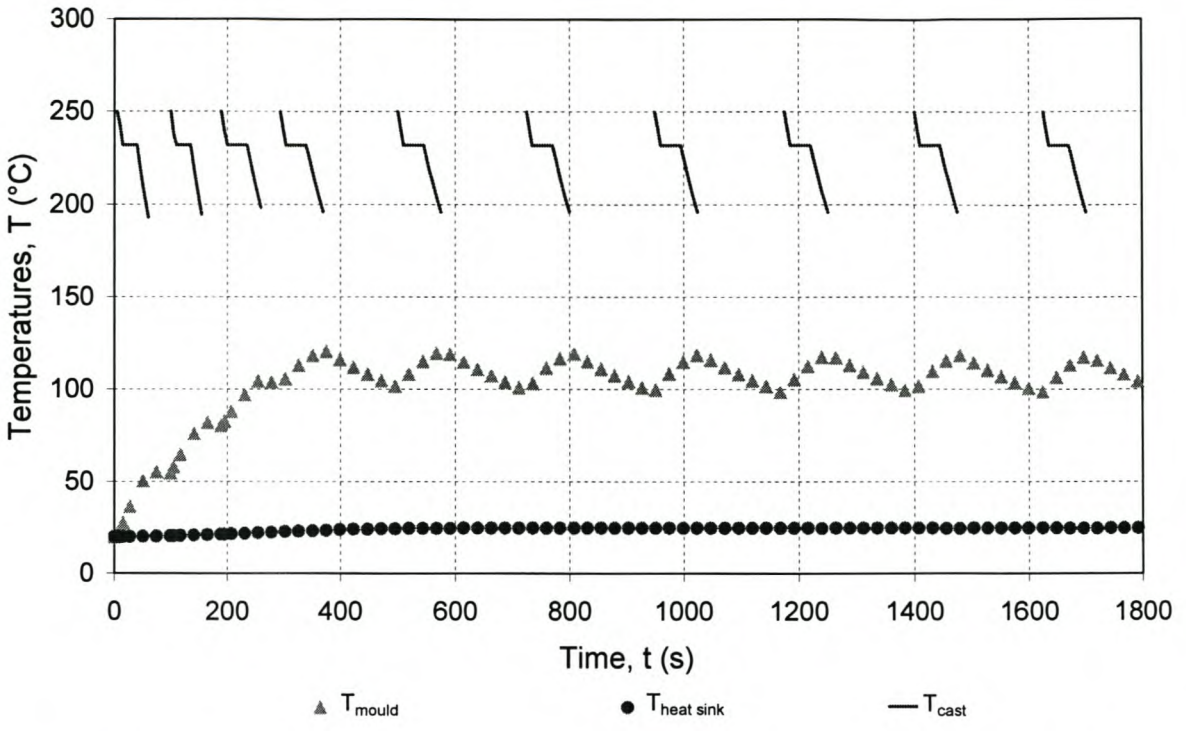

Figure 7.3 Theoretical (using FEM) temperatures of the tin casting, the external mould and the heat sink versus time when heat pipes, connected to the heat sink, are used for cooling

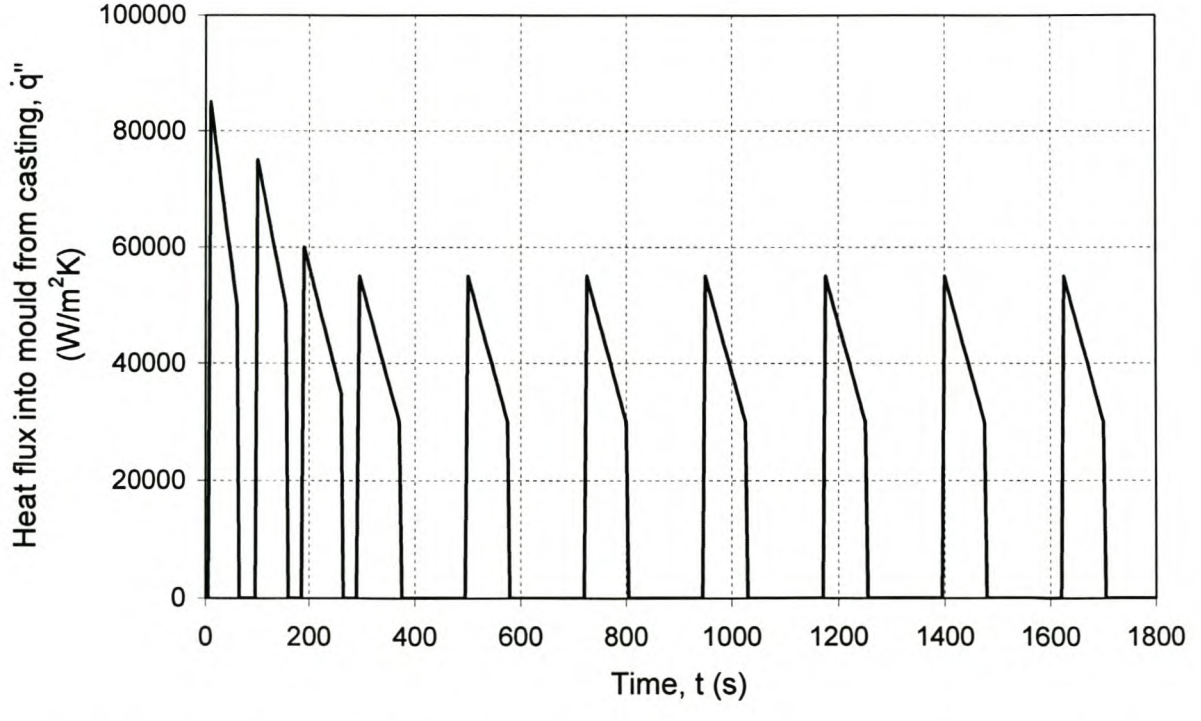

Figure 7.4 Radial heat flux entering the mould versus time, used as boundary conditions in the FEM simulation to produce the temperatures shown in figure 7.3

CHAPTER 8 - Discussion and Conclusions

The possibility of using heat pipes in casting moulds has been investigated in this thesis. The favourable heat transfer characteristics of heat pipes make them devices that can be used to perform thermal control of casting moulds. The temperature control of the moulds are one of the factors that will affect casting quality. The more constant, or controlled, the mould temperatures can be kept, the faster the production rate can be, and improvement of quality so that scrap rates can be less and energy is saved as well. It has been shown in chapter 7 that the production rate of castings can be improved when heat pipes are used, for certain casting geometries and temperature requirements. The case simulated in chapter 7 shows that a two and a half times (10:4) improvement in casing production rate is achieved when heat pipes are used. Figure 8.1 shows an improvement from 4 to 10 castings in 1800 s using heat pipes.

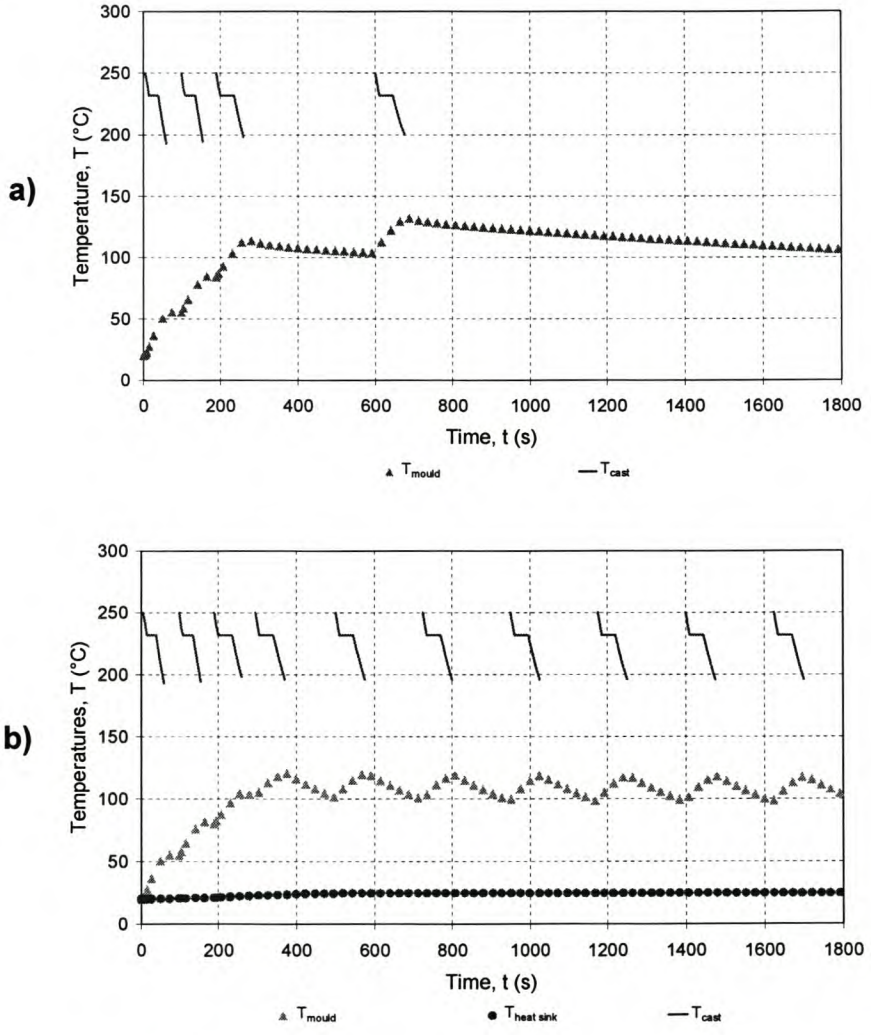

Figure 8.1 a) Four castings produced in half an hour in an un-cooled mould (copy of figure 7.1)
b) Ten castings produced over the same time using heat pipes (copy of figure 7.3)

The more rapid thermal response of the mould as seen in figure 8.1.b should be able to enhance casting processes. No particular industrial casting problem was solved in the thesis. Rather, simple casting situations were simulated (the core cooling case, the mould heating case and the mould cooling case), to evaluate the validity of the numerical programs. The results of the numerical simulations showed that although the results are generally acceptable for the prediction of trends, more refinement and improved modelling is required for improved accuracy.

An important issue that needs to be addressed in the improvement and building of the casting models, would be to determine more accurately the heat transfer between the casting and the mould. From the comparison of experimental and theoretical results it became clear that the contact resistance between the casting-mould interface plays a crucial role. During the planning of the thesis, the effect of this interfacial resistance was underestimated. More research, literature survey and experiments are needed in order to correctly model this resistance. For the purposes of the thesis, the interfacial thermal resistance was determined quasi-experimentally, and assumed to have a constant value. In reality, this resistance will be time dependant, since it is a function of the air gap between the casting and the mould. This air gap changes as the casting solidifies and also as the temperature of a solid casting changes. Research papers that have focussed on this issue show that the expected values will behave in the way that is suggested in figure 8.2.

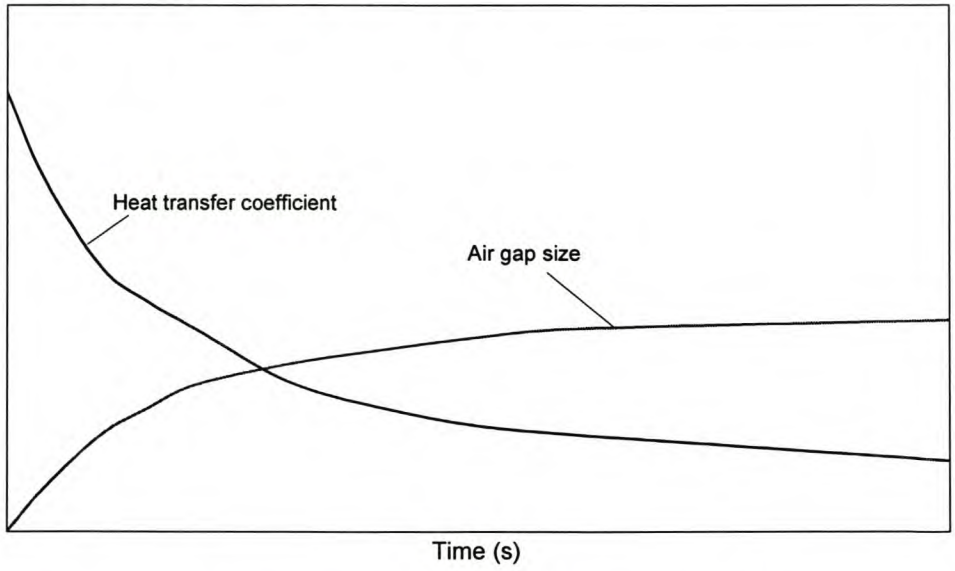

Figure 8.2 Typical trends of the interfacial heat transfer coefficient and size of the air gap versus time for certain castings

In this thesis the values used for the interfacial heat transfer coefficient was $h_{CR} = 700$ W/m^{2}K for the core cooling case and $h_{CR} = 500$ W/m^{2}K for the mould cooling case. The value of 700 W/m^{2}K was used for both the inside and outside surfaces of the casting involved. Since tin

has a higher coefficient of thermal expansion than steel, the casting would shrink more than the steel, thus clamping (quite tightly) onto the core but loosening from the (outer) mould. As time progress, the contact resistance of the casting-mould interface would become higher than the resistance of the casting-core interface. The value of 700 W/m^2K can therefore be seen as the average of the heat transfer coefficient over the casting-mould interface (probably closer to 500 W/m^2K) and the heat transfer coefficient over the casting-core interface (probably closer to 1000 W/m^2K). During the mould cooling case, the casting is made into an external mould, and would shrink faster than the mould and form an air gap (similar to the situation on the casting-mould interface of the core cooling case). This explains the lower coefficient used for the mould cooling case (500 W/m^2K). The fact that the contact resistance over the casting-mould interfaces were not known and could only be estimated, is seen as a limitation regarding the evaluation of the accuracy and relevancy of the theoretical models.

The castings were modelled as one node control volumes. Especially for the mould cooling case where a relatively large casting is used, a finer discretisation should be considered. The complexity and volume of work involved to do it by hand, and the lack of casting modelling software, restricted finer analysis though. The filling time of the mould with metal was also not included in the models. The castings were modelled as if they are cast instantaneously. The equipment used to fill the moulds can also be improved upon, to obtain more uniform filling rates and to have better control over the mass of metal poured into the moulds.

One of the potential problems of using heat pipes is that they are structurally fragile, especially for use in a relatively rough environment such as a casting factory. This became evident, especially during the core cooling case, where the core is connected to fins via a heat pipe. Two heat pipes were badly damaged during the core cooling case, where the core-and-casting is connected to the heavy fins only by means of the heat pipe. When considering using heat pipes in moulds, one should take steps to protect the heat pipes structurally.

Tin was used as the casting material, since it has a melting point of around 232°C, and one of the restrictions of the heat pipes is that its internal temperatures should not exceed 250°C. In retrospect, this was overly conservative and actually lead could have been used, and casting temperatures of up to 500°C would still have been acceptable. The casting temperatures used were in the regions of 300 to 350°C, which are about half of the 650-700°C used in casting aluminium alloys, for instance. Therefore, it is seen as a limitation of the research that casting temperatures were not higher, since aluminium alloys are important and popular casting materials.

The high conductivity, low thermal capacity solid finite element model used for the heat pipe, as described in section 5.1.2 led to the achievement of reasonable theoretically predicted temperatures. The heat transfer mechanism in an actual heat pipe differs from this model though, since the heat is only conducted through the wall and wick radially, whereafter the heat is absorbed and rejected through the latent heat of evaporation associated with the phase change of the working fluid inside the heat pipe. In order to obtain better results, the phase change of the fluid will have to be modelled for the finite element method. The model for the heat pipe consisting of an outer shell and super conductive core, discussed in section 5.1.3, seemed to be a very reasonable approximation for the heat pipe, as far as heat transfer is concerned. Surprisingly, this model did not work at all, since virtually no heat was transferred through such a heat pipe. The reason why it did not work, is not clear, and the objective of the thesis was not to investigate the finite element method in such close detail. The problem may lie in the way that the equations for the finite element method are derived. In the derivation, the internal energy of the elements is considered. The internal energies for a "super conductive core" and that for an actual working fluid are significantly different.

The NASTRAN program was able to model the casting moulds adequately, although it is not very user friendly in terms of downloading data to other programs. In general the numerical methods used (FEM and FDM) gave stable and accurate results.

One of the aspects of the thesis that proved to be very problematic to solve, was the actual fitting of the heat pipes into the relevant moulds and heat sinks. Special tools as well as experience in this area had to be developed. What made the soldering of the heat pipe into the fin difficult, was the fact that the fin is made from aluminium which is generally regarded as being difficult to solder. Also, a relatively long soldered length is necessary. Furthermore, the temperature of the solder had to be kept under the melting temperature of the lead seals at the ends of the heat pipe, therefore the temperature had to be kept below 250°C. The mould cooling case was also difficult - the heat pipes first needed to be inserted into the mould, then soldered in and then the top heat sink needed to be placed above and the heat pipes needed soldering. The successful fitting of the heat pipes into all the experimental set-ups is regarded as an achievement.

From material viewed on the internet (***www.thermacore.com ; www.norenproducts.com***), heat pipes are used in the production of plastic components (injection moulding) to cool cores, where production rates are very high and the cooling of dies is difficult. No references to the use of heat pipes in metal castings were found.

Regarding the experimental determination of the heat pipe heat transfer coefficients (with reference to sections 4.1, 5.1 and 6.1), there is some uncertainties about the accuracy of the estimation of the heat losses or gains from or to the water (refer to figure 4.10). Furthermore, the method used to calculate the heat transferred by the heat pipe to the cooling water, to find the condenser heat transfer rate $\dot{Q}_c$, causes fluctuations, as is seen in figure 8.3. This however does not invalidate the conservation of energy because the average of $\dot{Q}_c$ compares well with the average of $\dot{Q}_e$.

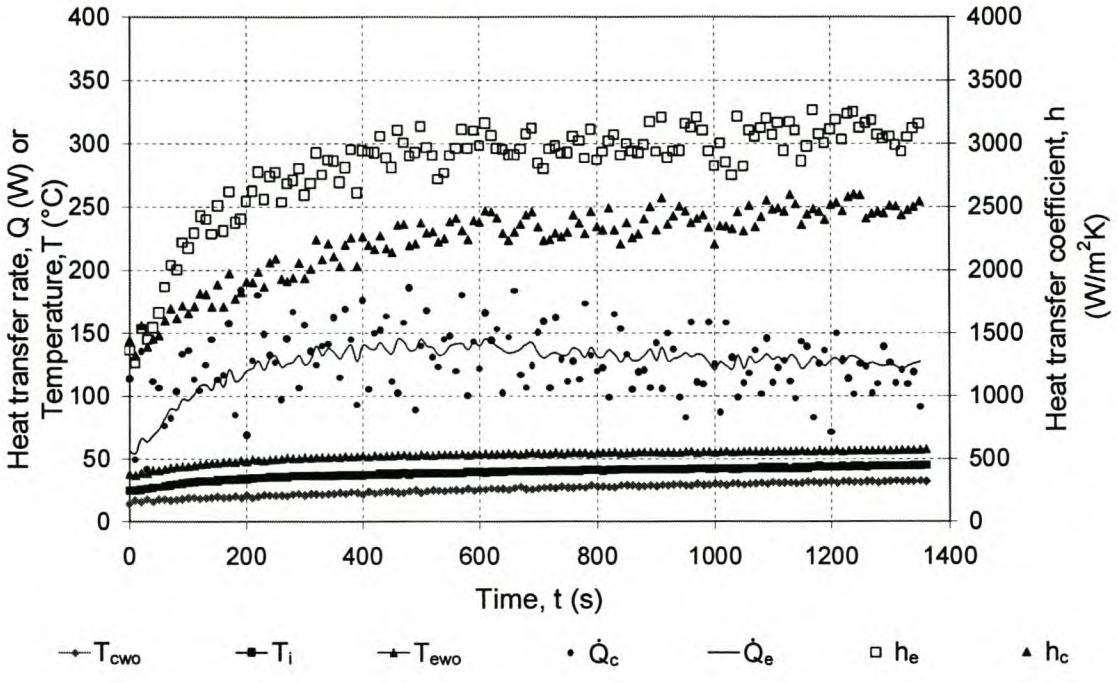

Figure 8.3 Temperatures, heat transfer rates and heat transfer coefficients for the special heat pipe versus time (copy of figure 6.1)

The modelling of the thermo-fluid processes inside thermosyphons / heat pipes are problematic. The two phase flow that occurs inside a thermosyphon complicates exact modelling to such an extent that researchers prefer to use experimentally determined correlations for heat transfer, rather than to theoretically model the processes. The modelling of the inclined thermosyphon in appendix D is such a theoretical approach, although it is known that the theoretical model would likely be limited. Instead of trying to statistically correlate the results, the difference between the theoretical and experimental results were analysed, to try and find out ***why*** the model is limited. The two phase flow effects splashing and/or geysering are assumed to be the components that cause the experimental results to deviate from the theoretical results. By processing these differences, information regarding the accuracy of the theoretical model can be obtained. This resulted in the definition of the

splashing factor, which is defined as $\frac{h_{ewi(\exp)}}{h_{ewi(theor)}}$. Only the evaporator end heat transfer coefficients were considered, since the splashing and geysering is assumed to affect mainly the heat transfer in the evaporator. For inclined operation, the splashing factor was described as a function of five variables, as shown in equation 8.1 (copied from equation D.53)

$$S = a_o(\dot{q}'')^{n_1}(L_p / L_e)^{n_2}(T_i)^{n_3}(T_{hw} - T_{cw})^{n_4}(\phi)^{n_5} \quad (8.1)$$

The difference between the theory and experiments is the most sensitive pertaining to the pool to evaporator length ratio L_e/L_p and the least sensitive pertaining to the angle of inclination ϕ, as is shown in figure 8.4.

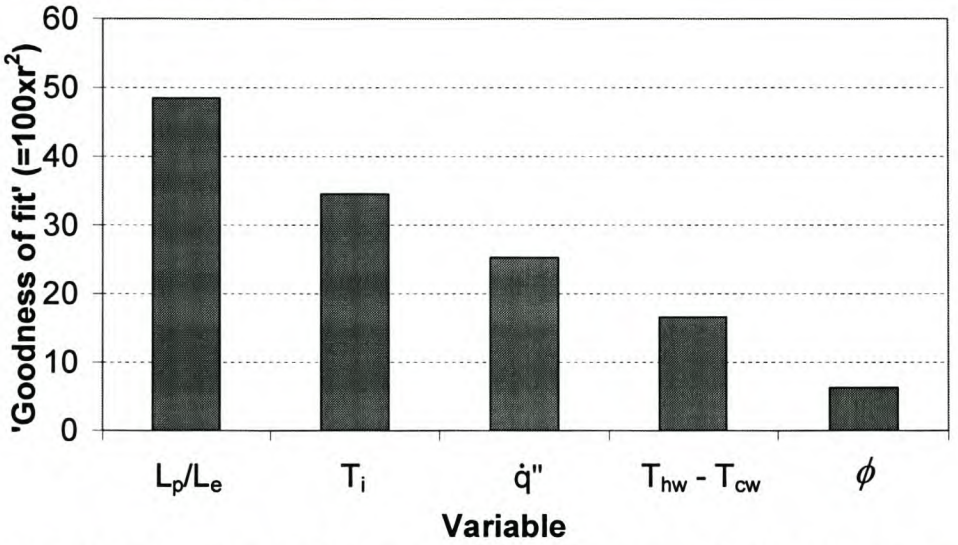

Figure 8.4 Relative importance of the variables used in equation A.1 in the determination of the splashing factor, for inclined thermosyphon operation (copy of figure D.25)

The splashing factor is regarded as being a significant contribution to the understanding of the behaviour of an inclined thermosyphon, as opposed to a vertical thermosyphon. In order to analyse the splashing factor further, different thermosyphon geometries and working fluids should be used, and a better theoretical modelling, capable of predicting the two phase flow in the thermosyphon, should be tried out.

A relatively wide variety of work was done in this thesis. From the results obtained and experienced gained, some of the points on which to focus in the future have been established.

CHAPTER 9 - Recommendations

The following recommendations are made:

1. The heat transfer coefficient over the casting-mould interface should be studied in a separate investigation, including different metals and mould materials.

2. A finite element, taking into account on the latent heat of evaporation of the working fluid inside a heat pipe, should be developed to replace the equivalent thermal conductivity model used in this thesis.

3. Thermosyphons, as opposed to heat pipes (with a wick) should be considered for use in casting moulds, as thermosyphons are easier to manufacture. Different types of working fluids should also be considered for high temperature use.

4. Instead of using fins and the solid steel heat sink used in the core cooling and mould cooling cases (which may be impractical in a casting operation) it would probably be better to use water cooling jackets (as described in section 4.1), since the maximum heat transfer rate of the heat pipe (more than 500 W) could be obtained using this method.

5. There are many correlations available that predict the heat transfer coefficient of a thermosyphon. A lack of the fundamental understanding and ability to predict the two-phase flow inside a thermosyphon seems evident in the literature. It is suggested that more fundamental theoretical approaches should be used. The deviations between theoretical and experimental results should not only be statistically correlated. Rather identifying parameters, such as the splashing factor, should be considered in future thermal studies pertaining to thermosyphons.

6. The effects of convection and radiation (especially the surface emissivity value) must be considered with more accuracy. For castings, this will be dependant on the mould geometry as well as the mould material.

7. Studies using higher melting point metals (such as aluminium and steel) and heat pipes capable of operating at higher temperatures (600°C +) should be undertaken in order to be more representative of industry's needs.

8. The experimental casting processes should be more controlled and uniform.

9. It would be beneficial if the internal temperature(s) of a casting can be measured during its solidification process.

10. Special tools and processes to fit the heat pipes into moulds should be developed – especially if industrial casting moulds are considered.

11. Shock and vibration tests might have to be performed on heat pipes that are considered to be used in certain casting processes where one die is "rammed" into another to close the mould.

LIST OF REFERENCES

Akyurt, M., Lamfon, N.J., Najjar, Y.S., Habeebullah, M.H. and Alp, T.Y., "*Modeling of waste heat recovery by looped water-in-steel heat pipes*", Int. J. Heat and Fluid Flow, Vol. 16, 1995, pp. 263-271

Ambrose, J.H. and Chow, L.C., "*Detailed model for transient liquid flow in heat pipe wicks*", J. Thermophysics, Vol. 5, No. 4, October-December, 1991, pp. 532-538

Bazzo, E., Heinen, L. and Nogoseke, M., "*Capillary pumps integrated to flat solar collectors*", 6th Int. Heat Pipe Symposium, Chiang Mai, Thailand, 5-9 November 2000

Bobco, R.P., "*Variable conductance heat pipe performance analysis: Zero-to-full load*", J. Thermophysics, Vol. 3, No. 1, January 1989, pp. 33-41

Bontemps, A., Goubier, C., Marquet, C., Solecki, J.C., *"Heat transfer performance of a toluene loaded two-phase thermosyphon"*, Heat Recovery Systems & CHP, Vol.9, No.4, 1989, pp. 285-297

Bullerschen, K.G. and Wilhelmi, H., "*Cooling of arc furnace electrodes with heat pipes*", Chem. Eng Technol. Vol. 14, 1991, pp. 45-53

Cao, Y. and Wang, Q., "*Thermal analysis of a piston cooling system with repciprocating heat pipes*", Heat Transfer Engineering, Vol. 16 no. 2, 1995, pp.50-57

Cao, Y. and Fagri, A., "*The thermal performance of heat pipes with localized heat input*", Int. J. Heat Mass Transfer, Vol. 32, No. 7, 1989, pp. 1279-1287

Carslaw, H.S., and Jaeger, J.C., *Conduction of heat in solids*, Oxford University Press, 1959

Cook, R.D., Malkus, D.S and Plesha, M.E., *Concepts and applications of finite element analysis*, John Wiley & Sons, 1989

Demidov, A.S. and Yatsenko, E.S., "*Investigation of heat and mass transfer in the evaporation zone of a heat pipe operating by the 'inverted meniscus' principle*", Int. J. Heat Mass Transfer, Vol. 37, No. 14, 1994, pp. 2155-2163

Dinh, K., "*Dehumidifier heat pipes for rice drying and storage*", 6th Int. Heat Pipe Symposium, Chiang Mai, Thailand, 5-9 November 2000

Dobson, R.T. and Kröger, D.G., *"Thermal characteristics of an ammonia charged two phase closed thermosyphon"*, 10th Int. Air Conditioning, Refrigeration & Ventilation Congress, Midrand, South Africa, 8-10 March 2000

Dube, V., Noie-Baghban, S.H., Awasthi, B. and Akbarzadeh, A., "*Waste heat recovery using a loop thermosiphon heat exchanger in a bakery*", 6th Int. Heat Pipe Symposium, Chiang Mai, Thailand, 5-9 November 2000

Dunn, P.D. and Reay, D.A., *Heat Pipes*, Pergamon Press, 1994

El-Genk, M.S. and Saber, H.H., *"Heat transfer correlations for liquid film in the evaporator of enclosed, gravity-assisted thermosyphons"*, ASME Journal of Heat Transfer, May 1998, Vol. 120, pp. 477-484

El-Genk, M.S. and Saber, H.H., *"Liquid pool heat transfer in small cylindrical enclosures with uniform wall heating"*, AIChE Symposium series, Heat Transfer – Baltimore 1997, pp. 131-137

El-Genk, M.S, Huang, L and Tournier, J.M., "*Transient experiments of an inclined copper-water heat pipe*", Journal of Thermophysics and Heat Transfer, Vol. 9, No. 1, January-March, 1995, pp. 109-116

Faghri, A. and Chen, M.M., "*A numerical analysis of the effects of conjugate heat transfer, vapor compressibility, and viscous dissipation in heat pipes*", Numerical Heat Transfer A, Vol. 16, 1989, pp. 389-405

Faghri, A., *Heat pipe science and technology*, Taylor & Francis Publishers, 1995

Griffiths, W.D., "*A model for the interfacial heat transfer coefficient during unidirectional solidification of an aluminum alloy*", Metallurgical and Materials Transactions B, Vol. 31B, April 2000, pp. 285-295

Groenewald, A., Basson, A.H. and Dobson, R.T., "*Theoretical modelling and numerical simulation of a two-phase closed thermosyphon considering splashing and geysering*", 6th Int. Heat Pipe Symposium, Chiang Mai, Thailand, 5-9 November 2000

Groll, M. and Rösler, S., "*Operation principles and performance of heat pipes and closed two-phase thermosyphons*", J. Non-Equilib. Thermodynamics, Vol.17, No.2, 1992, pp. 91-151

Gross, U., *"Reflux condensation heat transfer inside a closed thermosyphon"*, Int. J. Heat Mass Transfer, Vol. 35, No. 2, 1992, pp. 279-294

Gethin, D.T., Lewis, R.W. and Tadayon, M.R.,"*A finite element approach for modelling metal flow and pressurised solidification in the squeeze casting process*", Int. J. for Numerical Methods in Engineering, Vol. 35, 1992, pp. 939-950

Gunnerson, F.S. and Zuo, Z.J., "*Modeling of an inclined two-phase closed thermosyphon*", ASME/JSME Thermal Engineering Conference, Vol. 2, 1995, pp. 27-34

Hall, M.L., and Doster, J.M., "*A sensitivity study on the effects of evaporation/condensation accommodation coefficients on transient heat pipe modeling*", Int. J. Heat Mass Transfer, Vol. 33, No. 3, 1990, pp. 465-480

Hetu, J.F. and Florin Ilinca,"*A finite element method for casting simulations*", Numerical Heat Transfer A, Vol. 36, 1999, pp. 657-679

Issacci, F. and Catton, I., "*Use of spectral methods for heat pipe analysis*", AIChE Symposium Series, Vol. 87, No. 283, 1991, pp.198-206

Jialun, H., Ma Tongze and Zhenfang, Z., 1992, *"Investigation of boiling liquid pool height of a two-phase closed thermosyphon"*, Proc. 8th Int. Heat Pipe Conf., Beijing, China, pp. 317-322

Kang, M.G., *"Effect of tube inclination on pool boiling heat transfer"*, Transactions of the ASME, Vol. 122, February 2000, pp. 188-192

Kays, W.M. and Crawford, M.E., *Convective heat and mass transfer*, McGraw-Hill, 1993

Konev, S. V., Wang, J. L. and Tu, C.J., "*Characteristics of a heat exchanger based on a collector heat pipe*", Heat Recovery Systems & CHP, Vol. 15, No.5, 1995, pp. 493-502

Kröger, D.G., *Air-cooled heat exchangers and cooling towers*, Begell House, New York, 1998

Lally, B., Biegler, L. and Henein, H.,"*Finite difference heat transfer modeling for continuous casting*", Metallurgical Transactions B, Vol. 21B, August 1990, pp. 761-770

Loulou, T., Artyukhin, E.A. and Bardon, J.P., "*Estimation of thermal contact resistance during the first stages of metal solidification process: I – experiment principle and modelisation*", Int. J. Heat Mass Transfer, Vol. 42, 1999, pp. 2119-2127

Ma Tongze and Hou Zengqi, "*Heat pipe research and development in China*", Heat Recovery Systems & CHP, Vol. 9, No. 6, 1989, pp. 499-512

Mills, A.F., *Heat Transfer*, Irwin, 1992

Modest, M.F., *Radiative heat transfer*, McGraw-Hill, 1993

Nguyen-Chi, H., and Groll, M., *"Entrainment or flooding limit in a closed two phase thermosyphon"*, Proc. 4th Int. Heat Pipe Conf., Sept. 1981, pp. 147-161

Perry, J.H., *Chemical engineers' handbook*, McGraw-Hill, 1950

Peterson, G.P., *Heat pipes*, John Wiley & Sons, 1994

Pioro, L.S. and Pioro, I.L, *Industrial two-phase thermosyphons*, Begell House, New York, 1997

Poulikakos, D., *Conduction heat transfer*, Prentice Hall, 1994

Prescott, P.J and Incropera, F.P.,"*Convection heat and mass transfer in alloy solidification*", Advances in Heat Transfer, Vol. 28, 1996, pp. 231-338

Pruzan, D.A., Torrance, K.E and Avedisian, C. T., "*Two-phase flow and dryout in a screen wick saturated with a fluid mixture*", Int. J. Heat Mass Transfer, Vol. 33, No. 4, 1990, pp. 673-681

Rosenfeld, J.H.,"*Modeling of heat transfer into a heat pipe for localized heat input zone*", AIChE Symposium Series, Heat Tranfer - Pittsburgh 1987, pp. 71-76

Rosindale, I. and Davey, K.,"*Transient thermal model for the hot chamber injection system in the pressure die casting process*", Applied Mathematical Modelling, Vol. 23, 1999, pp. 255-277

Shiraishi, M., Kikuchi, K. and Yamanishi, T., *"Investigation of heat transfer characteristics of a two-phase closed thermosyphon"* , Heat Recovery Systems, Vol. 1, 1981, pp. 287-297

Shiraishi, M., Terdtoon, P., and Murakami, M., *"Visual study on flow behavior in an inclined two-phase closed thermosyphon",* Heat Transfer Engineering, Vol. 16, No. 1, 1995

Stasa, F.L., *Applied finite elements for engineers*, Holt, Rinehart and Winston, 1985

Stefanescu, D.M., Upadhya, G. and Bandyopadhyay, D.,"*Heat transfer solidification kinetics modeling of solidification of castings*", Metallurgical Transactions A, Volume 21A, April 1990, pp. 997-1005

Stephan, K. and Abdelsalam, *"Heat transfer correlations for natural convection boiling"*, Int J. Heat Mass Transfer, Vol. 23, pp73-87, 1980

Stephan, K., *Heat transfer in condensation and boiling*, Springer-Verlag, 1992

Stephan, P.C. and Busse, C.A., "*Analysis of the heat transfer coefficient of grooved heat pipe evaporator walls*", Int. J. Heat Mass Transfer, Vol. 35, No. 2, 1992, pp. 383-391

Swanepoel, G., Taylor, A.B. and Dobson, R.T., "*Theoretical modeling of pulsating heat pipes*", 6th Int. Heat Pipe Symposium, Chiang Mai, Thailand, 5-9 November 2000

Thomas, B.G and Najjar, F.M.,"*Finite element modelling of turbulent fluid flow and heat transfer in continuous casting*", Appl. Math. Modelling, Vol. 15, May 1991, pp. 226-243

Tournier, J.M and El-Genk, M.S.,"*A heat pipe transient analysis model*", Int. J. Heat Mass Transfer, Vol. 37, No. 5, 1994, pp. 753-762

Trovant, M. and Argyropoulos, S., "*Finding boundary conditions: A coupling strategy for the modeling of metal casting processes: Part I. Experimental study and correlation development*", Metallurgical and Materials Transactions B, Vol. 31B, February 2000, pp. 75-85

Usmani, A.S., Cross, J.T and Lewis, R.W.,"*A finite element model for the simulations of mould filling in metal casting and the associated heat transfer*", Int. J. for Numerical Methods in Engineering, Vol. 35, 1992, pp. 787-806

Vafai, K., Zhu, N. and Wang, W., "*Analysis of asymmetric disk-shaped and flat-plate heat pipes*", ASME Journal of Heat Transfer, Vol. 117, February 1995, pp. 209-218

Whalley, P.B., *Boiling, condensation and gas-liquid flow*, Clarendon Press, Oxford, 1987

Zuo, Z.J. and Gunnerson, F.S., *"Numerical modelling of the steady-state two-phase closed thermosyphon"*, Int. J Heat Mass Transfer, Vol. 37, No. 17, 1994, pp. 2715-2722

Zuo, Z.J. and Gunnerson, F.S.,"*Numerical study of the thermosyphon flooding limit*", ASME HTD, Vol. 278, 1994, pp.47-55

Zuo, Z.J. and Gunnerson, F.S.,"*Effect of the working fluid inventory on thermosyphon performance*", ASME HTD-Vol. 278, Fundamentals of Heat Pipes, 1994, pp.47-55

Zuo, Z.J. and Gunnerson, F.S., *"Heat Transfer analysis of an inclined two-phase closed thermosyphon"*, Journal of Heat Transfer, Vol. 117, November 1995, pp. 1073-1075

Zuo, Z.J. and Gunnerson, F.S., *"The effect of thermosyphon size reduction on heat transfer performance"*, ASME/JSME Thermal Engineering Conference, Vol. 2, 1995, pp. 51-59

APPENDIX A - Heat Pipe, Fluid and Material Properties

A.1 HEAT PIPE PROPERTIES AND DIMENSIONS

Three types of heat pipes are considered in this thesis. Their important properties and dimensions are shown in table A.1.

Table A.1: Heat pipe properties and dimensions

Name/ number	External dimensions	Container description	Wick description	Working fluid
IMC-E12008HT	8" long x 3/8" diameter	Pure copper tube, thickness t = 0.46 mm	Double layer of phosphor-bronze mesh (60% void fraction)	Water
IMC-E16012HT	12" long x ½" diameter	Pure copper tube, thickness t = 0.46 mm	Double layer of phosphor-bronze mesh (60% void fraction)	Water
'Special' heat pipe	12" long x ½" diameter	Pure copper tube, thickness t = 0.46 mm	Double layer of phosphor-bronze mesh (60% void fraction)	Water

Heat pipes IMC-E12008HT and IMC-16012HT are standard ("off the shelve") heat pipes. They are sealed off at both ends with a lead plug that melts at 296°C (and therefore acts as a 'fuse' to prevent too high an internal temperature). The special heat pipe is also sealed off at the ends with the same type of solder, but it has two axially positioned thermocouple wells that are used for the measurement of the internal temperature. The manufacturers specify that the internal temperature of the heat pipes should not exceed 250°C.

A.2 TEMPERATURE DEPENDANT PROPERTIES OF FLUIDS

The properties of ammonia, water and air are used in the thesis as functions of temperature. The following section give equations for the needed properties of the fluids as functions of the temperature T (Kröger, 1998).

SATURATED AMMONIA PROPERTIES (Temperatures in Kelvin)

$$\rho_l = 231.2 \times 0.2471^A \quad where \quad A = -(1 - T/405.5)^{0.2857} \qquad [kg/m^3]$$

$$\rho_g = -601.9 + 5.361T - 1.187 \times 10^{-2} T^2 - 1.161 \times 10^{-5} T^3 + 4.739 \times 10^{-8} T^4 \qquad [kg/m^3]$$

$$k_l = 1.068 - 1.577 \times 10^{-3} T - 1.229 \times 10^{-6} T^2 \qquad [W/mK]$$

$$k_g = -0.139 + 1.352 \times 10^{-3} T - 2.532 \times 10^{-6} T^2 - 4.884 \times 10^{-9} T^3 + 1.419 \times 10^{-11} T^4 \qquad [W/mK]$$

$$\mu_l = 10^B \quad where \quad B = -11.591 + \frac{876.4}{T} + 0.02681T - 3.612 \times 10^{-5} T^2 \qquad [kg/sm]$$

$$\mu_g = -2.748\times10^{-5} + 2.825\times10^{-7}T - 5.201\times10^{-10}T^2 - 6.062\times10^{-13}T^3 + 2.126\times10^{-15}T^4$$

$$C_{p(l)} = -2497.3 + 77.81T - 0.3006T^2 + 4.067\times10^{-4}T^3 \quad [\text{J/kgK}]$$

$$C_{p(g)} = -27761.1 + 339.1T - 1.306T^2 + 1.729\times10^{-3}T^3 \quad [\text{J/kgK}]$$

$$h_{fg} = 1.371\times10^{6}\left(\frac{405.55 - T}{165.83}\right)^{0.38} \quad [\text{J/kg}]$$

SATURATED WATER PROPERTIES (Liquid only)

$$\rho_l = \frac{1}{1.493\times10^{-3} - 3.716\times10^{-6}T + 7.098\times10^{-9}T^2 - 1.903\times10^{-20}T^6} \quad [\text{kg/m}^3]$$

$$k_l = -0.614 + 6.996\times10^{-3}T - 1.011\times10^{-5}T^2 + 4.747\times10^{-12}T^4 \quad [\text{W/mK}]$$

$$\mu_l = 2.414\times10^{-5}\times10^{(247.8/(T-140))} \quad [\text{kg/sm}]$$

$$C_{p(l)} = 8156.0 - 28.06T + 0.0511T^2 - 2.176\times10^{-13}T^6 \quad [\text{J/kgK}]$$

PROPERTIES OF DRY AIR

$$\rho_{air} = P_a/(287.08T) \quad [\text{kg/m}^3]$$

$$k_{air} = -4.938\times10^{-4} + 1.018\times10^{-4}T - 4.678\times10^{-8}T^2 + 1.251\times10^{-11}T^3 \quad [\text{W/mK}]$$

$$\mu_{air} = 2.288\times10^{-6} + 6.260\times10^{-8}T - 3.131\times10^{-11}T^2 + 8.150\times10^{-15}T^3 \quad [\text{kg/sm}]$$

$$C_{p(air)} = 1045.3 - 0.316T + 7.083\times10^{-4}T^2 - 2.705\times10^{-7}T^3 \quad [\text{J/kgK}]$$

A.3 CONSTANT MATERIAL PROPERTIES

The following are internal properties of selected materials, which are assumed to be constant for the purposes of the thesis (Mills, 1992):

Copper

$\rho_{cu} = 8950$ kg/m^3

$k_{cu} = 386$ W/mK

$C_{p(cu)} = 385$ J/kgK

Brass

$\rho_{brass} = 8530$ kg/m^3

$k_{brass} = 111$ W/mK

$C_{p(brass)} = 380$ J/kgK

Stainless steel

$\rho_{ss} = 8055$ kg/m^3

$k_{ss} = 15$ W/mK

$C_{p(ss)} = 480$ J/kgK

Mild steel

$\rho_{ms} = 7840$ kg/m^3
$k_{ms} = 50$ W/mK
$C_{p(ms)} = 460$ J/kgK

Tin

$\rho_{tin} = 7310$ kg/m^3
$k_{tin} = 66.6$ W/mK
$C_{p(tin)} = 227$ J/kgK
$\lambda_{tin} = 15.72$ kJ/kg (Latent energy of fusion, Perry, 1950)

Lead

$\rho_{Pb} = 11340$ kg/m^3
$k_{Pb} = 35.3$ W/mK
$C_{p(Pb)} = 129$ J/kgK

Aluminium (Type 6082)

$\rho_{AL} = 2770$ kg/m^3
$k_{AL} = 204$ W/mK
$C_{p(AL)} = 875$ J/kgK

The following values for surface emissivity are used (Modest, 1993):

Mild steel (mould surfaces)

$\varepsilon_{ps} = 0.07$ (for a polished steel surface)
$\varepsilon_{so} = 0.79$ (for a steel oxide surface)

Tin

$\varepsilon_{tin} = 0.06$ (for a bright tin surface)

Appendix B - Sample Calculations

B.1 CALCULATIONS REGARDING HEAT PIPE PROPERTIES

In order to determine the heat transfer coefficients for the heat pipe from the experimental data gathered (refer to sections 4.1 and 5.1.4), a set of calculations have to be performed, which will be described in this section. First, consider figure B.1:

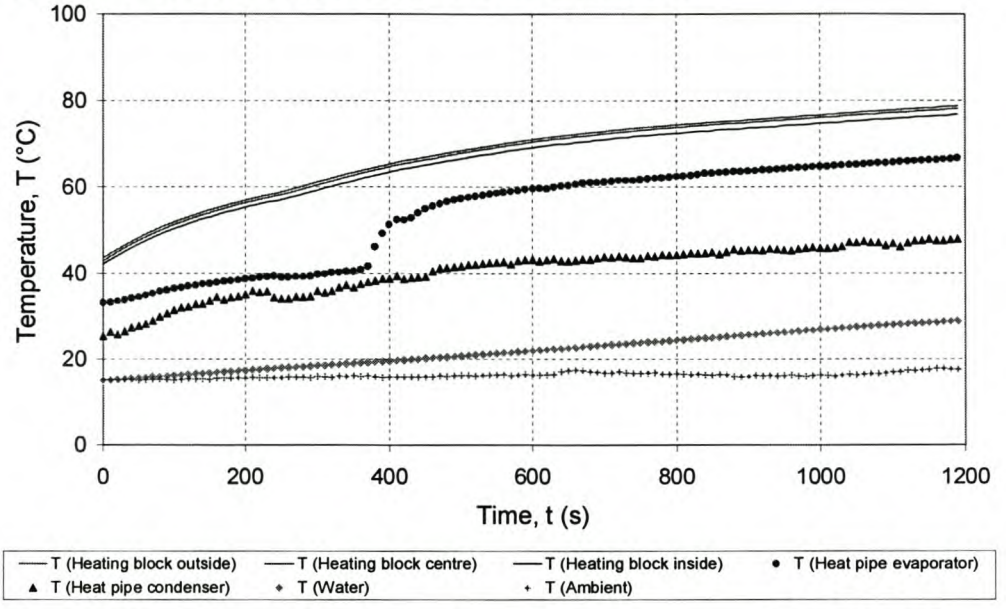

Figure B.1 Experimentally measured temperatures in order to calculate heat pipe thermal characteristics. Measurements taken for horizontal operation, with voltage over the resistance wire of the heating block = 40 V

This case has been selected to base the sample calculation on, since it can be observed that just before 400 seconds have elapsed, the evaporator temperature suddenly increases and breaks away from the condenser temperature, suggesting that some sort of a heat transfer limit has been reached. (From this point onwards, a relatively constant heat transfer rate is calculated). Consider figure B.1 at t = 600 s. The experimental data needed to perform the calculation is given in table B.1.

Table B.1 Experimental values to determine heat pipe properties at time t = 600s

Time (s)	T_{water} (°C)	$T_{heating\ block}$ (outside) (°C)	$T_{heating\ block}$ (centre) (°C)	$T_{heating\ block}$ (inside) (°C)	$T_{heat\ pipe}$ (condenser) (°C)	$T_{heat\ pipe}$ (evaporator) (°C)	$T_{ambient}$ (°C)
590	21.84	70.78	70.18	68.89	43.07	59.45	16.44
600	21.98	71.01	70.42	69.15	43.20	59.63	16.29

The properties of the water that are needed for the calculation, are taken at the average temperature of the water, therefore:

$$T_{water\,(av)} = \frac{21.84 + 21.98}{2} = 21.91\,°C = 295.02\,K \tag{B.1}$$

The properties of the water are therefore: (Kröger 1998, with temperatures in Kelvin)

$$C_{p\,(water)} = 8155.99 - 28.0627(T_{water}) + 0.0511283(T_{water})^2 - 2.17582\times10^{-13}(T_{water})^6$$
$$= 8155.99 - 28.0627(295.02) + 0.0511283(295.02)^2 - 2.17582\times10^{-13}(295.02)^6$$
$$= 4183.5\,J/kgK \tag{B.2}$$

$$\mu_{water} = 0.00002414\times10^{(247.8/(T_{water}-140))}$$
$$= 0.00002414\times10^{(247.8/(295.02-140))}$$
$$= 9.577\times10^{-4}\,kg/ms \tag{B.3}$$

$$k_{water} = -0.614255 + 0.0069962(T_{water}) - 1.01075\times10^{-5}(T_{water})^2 + 4.7473\times10^{-12}(T_{water})^4$$
$$= -0.614255 + 0.0069962(295.02) - 1.01075\times10^{-5}(295.02)^2 + 4.7473\times10^{-12}(295.02)^4$$
$$= 0.606\,W/mK \tag{B.4}$$

$$\mathrm{Pr}_{water} = \frac{\mu_{water}C_{p\,(water)}}{k_{water}} = \frac{(9.577\times10^{-4})(4183.5)}{0.606} = 6.611 \tag{B.5}$$

The mass flow rate of the water in the pump cycle can be calculated using the equation in figure 4.7, where the mass flow rate is given as a function of temperature (in °C):

$$\dot{m}_{water} = 1.3426\times10^{-5}T_w^2 - 6.4907\times10^{-4}T_w + 0.14808$$
$$= 1.3426\times10^{-5}(21.91)^2 - 6.4907\times10^{-4}(21.91) + 0.14808$$
$$= 0.1403\,kg/s \tag{B.6}$$

For water flowing through the cooling jacket with outer diameter d_o = 16 mm and inner diameter d_i = 12.7 mm, the Reynolds number based on the hydraulic diameter is therefore:

$$\mathrm{Re}_{Dh} = \frac{4\dot{m}_{water}}{\pi\mu_{water}(d_i + d_o)}$$
$$= \frac{4(0.1403)}{\pi(9.577\times10^{-4})(0.0127 + 0.016)} = 6499.1 \tag{B.7}$$

To find the Nusselt number based on the hydraulic diameter with the Gnielinski equation, the friction factor can be calculated as:

$$f = \left(0.97\ln\left(\mathrm{Re}_{Dh}\right) - 1.64\right)^{-2} = \left(0.97\ln\left(6499.1\right) - 1.64\right)^{-2} = 0.03566 \qquad \text{(B.8)}$$

Using the Gnielinski equation:

$$Nu_{Dh} = \frac{(f/8)(\mathrm{Re}_{Dh} - 1000)\,\mathrm{Pr}_{water}}{1 + 12.7(f/8)^{0.5}(\mathrm{Pr}_{water}^{2/3} - 1)}$$

$$= \frac{(0.03566/8)(6499.1 - 1000)(6.611)}{1 + 12.7(0.03566/8)^{0.5}(6.611^{0.6667} - 1)}$$

$$= 51.63 \qquad \text{(B.9)}$$

For an annulus the hydraulic diameter is $D_h = d_o - d_i$, so that the heat transfer coefficient between the cooling water and the outside wall of the heat pipe condenser is:

$$h_{cwo} = \frac{k_{water} Nu_{Dh}}{D_h} = \frac{(0.606)(51.63)}{(0.016 - 0.0127)} = 9481.9\ W/m^2K \qquad \text{(B.10)}$$

The cooling water flows over 110 mm of the heat pipe, and therefore the thermal resistance on the outside of the condenser wall is:

$$R_{cwo} = \frac{1}{h_{cwo} A_{cwo}} = \frac{1}{(9481.9)\pi(0.0127)(0.11)} = 0.02403\ K/W \qquad \text{(B.11)}$$

The internal temperature of the heat pipe is taken as the average of the internal condenser and evaporator temperatures measured, therefore:

$$T_i = \frac{1}{2}\left[\frac{43.07 + 43.2}{2} + \frac{59.45 + 59.63}{2}\right] = 51.34\ °C \qquad \text{(B.12)}$$

The net (and therefore uncorrected) heat transfer rate into the water can be found by using equation 5.38. The time step between which temperatures are logged, is 10 seconds. Therefore, if there were no heat losses to the environment or heat gain from the pump, the heat transferred to the water would be:

$$\dot{Q}_{uncorrected} = \frac{m_{water} C_{p(water)} \Delta T}{\Delta t} = \frac{2.5(4183.5)(21.98 - 21.84)}{10} = 146.4\ W \qquad \text{(B.13)}$$

The influence of heat losses and gains can be corrected with $\dot{Q}_{env} = m_{water} C_{p(water)} \dfrac{dT_w}{dt}$

where $\frac{dT_w}{dt}$ can be calculated as a function of the temperature difference between the water and ambient, using figure 4.10, so that:

$$\dot{Q}_{env} = m_{water} C_{p(water)} [-1.685 \times 10^{-7} (T_w - T_{ambient})^3 + 4.236 \times 10^{-6} (T_w - T_{ambient})^2 - 3.213 \times 10^{-4} (T_w - T_{ambient}) + 2.36 \times 10^{-3}]$$

$$= (2.5)(4183.5)[-1.685 \times 10^{-7} (21.91 - 16.37)^3 + 4.236 \times 10^{-6} (21.91 - 16.37)^2 - 3.213 \times 10^{-4} (21.91 - 16.37) + 2.36 \times 10^{-3}]$$

$$= 7.13\,W \qquad \text{(B.14)}$$

The positive value implies that the heat given by the pump to the water is more than the heat that is lost by the water to the environment, which implies that the net heat transfer rate absorbed by the water should be 7.13W more than the actual heat transfer rate through the heat pipe.

Therefore, the corrected heat transfer rate is:

$$\dot{Q}_c = 146.4 - 7.13 = 139.27\,W \qquad \text{(B.15)}$$

The thermal resistance of the heat pipe condenser can now be calculated:

$$\dot{Q}_c = \frac{T_i - T_w}{R_c + R_{cwo}} \qquad \text{(B.16)}$$

therefore,

$$R_c = \frac{T_i - T_{water}}{\dot{Q}_c} - R_{cwo} = \frac{51.34 - 21.91}{139.27} - 0.02403 = 0.18729\ K/W \qquad \text{(B.17)}$$

The heat transfer coefficient for the condenser section can now be calculated:

$$h_c = \frac{1}{R_c A_{cwo}} = \frac{1}{(0.18729)\pi(0.0127)(0.11)} = 1216.6\,W/m^2K \qquad \text{(B.18)}$$

Using equation 5.30, it follows that

$$T_{cwo} = \dot{Q}_c R_{cwo} + T_{water} = 139.27(0.02403) + 21.91 = 25.26\,°C \qquad \text{(B.19)}$$

To calculate the evaporator heat transfer coefficient, the heat transfer rate at the evaporator end is considered. Equation 5.43 can be used to find the uncorrected heat transfer rate through the aluminium shell, as:

$$\dot{Q}_{al} = 114.72(70.3 - 69.02) = 146.8\,W \qquad \text{(B.20)}$$

At time t = 590 s the average temperature of the shell with inside diameter 18mm and outside diameter 44mm is T = 69.54 °C and at time t = 600 s it is T = 69.79 °C. There is therefore an average temperature rise of 0.25°C of this mass over a period of 10 seconds. The heat flow needed to cause this temperature increase, is given by equation 5.44:

$$\dot{Q}_{cv} = 245.49\frac{\Delta T_{cv}}{\Delta t} = 245.49\left(\frac{0.25}{10}\right) = 6.14 = 6.14\,W \qquad \text{(B.21)}$$

The corrected heat transfer rate entering the evaporator is therefore:

$$\dot{Q}_e = 146.8 - 6.14 = 140.66\,W \qquad \text{(B.22)}$$

The heat transfer rate calculated at the condenser end is 139.27 W (equation B.15), and in this case (equation B.22) there is a very good agreement between the evaporator and condenser heat transfer rates.

The outside evaporator wall resistance is given by equation 5.32, as $R_{ewo} = 0.0054303\ K/W$. The heat transfer rate through the evaporator is:

$$\dot{Q}_e = \frac{T_{al(in)} - T_i}{R_e + R_{ewo}} \quad \text{, so that} \qquad \text{(B.23)}$$

$$R_e = \frac{T_{al(in)} - T_i}{\dot{Q}_e} - R_{ewo} = \frac{69.02 - 51.34}{140.66} - 0.0054303$$

$$= 0.12026\ K/W \qquad \text{(B.24)}$$

The evaporator heat transfer coefficient is therefore:

$$h_e = \frac{1}{R_e A_{ewo}} = \frac{1}{0.12026(\pi(0.0127)(0.08))} = 2605.2\,W/m^2K \qquad \text{(B.25)}$$

Using equation 5.29,

$$T_{ewo} = T_{al(in)} - \dot{Q}_e R_{ewo} = 69.02 - 140.66(0.0054303) = 68.26\,°C \qquad \text{(B.26)}$$

These values have been calculated for each of the time steps shown in figure B.1. The results were used to plot the graph in figure B.2. (Figure B.2 is the same graph as is figure 6.8 in section 6.1). The other graphs plotted in section 6.1 were obtained in the same fashion.

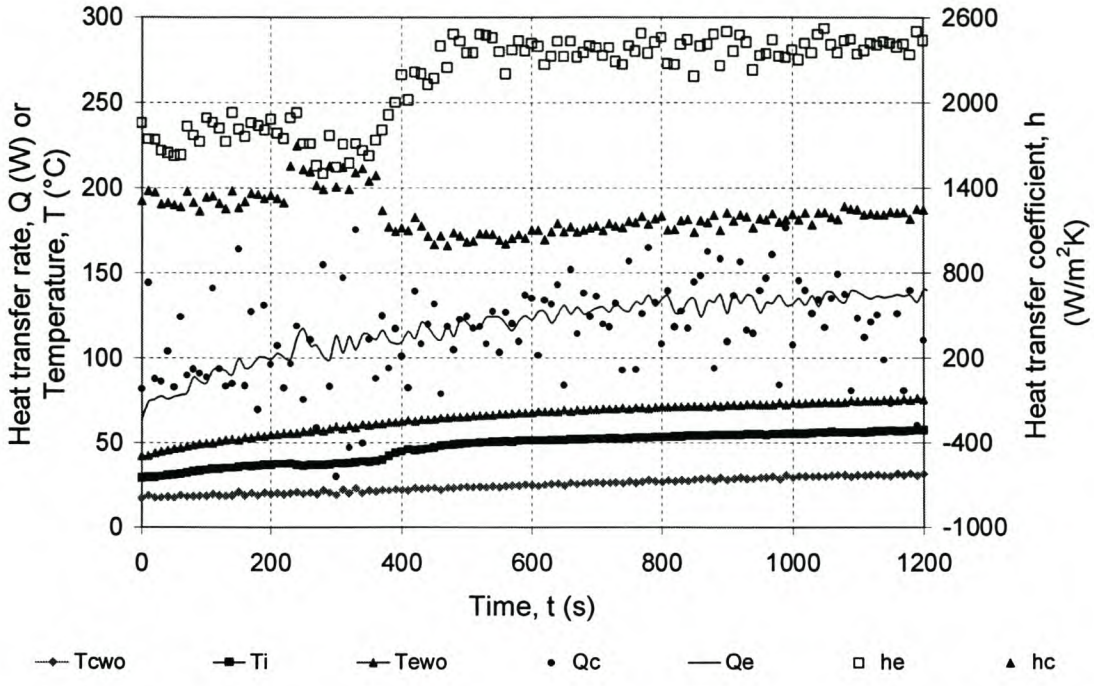

Figure B.2 Results for temperatures, heat transfer rates and heat transfer coefficients, making use of the experimental data shown in figure B.1

B.2: DETERMINATION OF MASS FLOW RATE OF COOLING AIR FOR FINS

These calculations are used in conjunction with sections 4.2 and 5.2, in order to determine the heat transfer characteristics of the cooling fin, as well as with sections 4.4 and 5.4, where the fin is used as the heat sink (connected to the core with a heat pipe).

The air flow rate is determined by measuring the pressure drop over the orifice plate inserted in a pipe leading to the settling chamber. The flow rate is determined in accordance with the British Standards 1042 section 1.1. An example showing how the mass flow rate may be determined follows:

Figure B.3 shows experimental pressure transducer data taken for an experiment. The average voltage over transducer 1 (i.e the pressure difference over the orifice plate) is V_1 = 3.114 V. Over transducer 2 (pressure difference between front of orifice plate and atmosphere), the average voltage is V_2 = 0.5964 V.

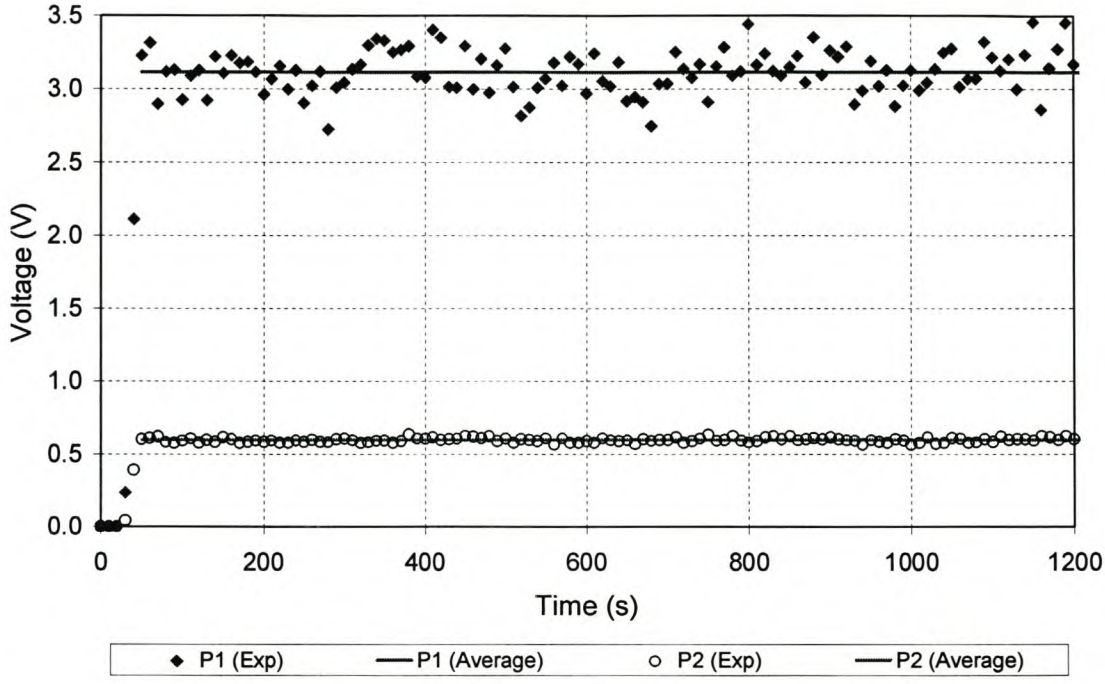

Figure B.3 Voltage measurements representing pressure drop over pressure transducers P_1 and P_2 (Refer to figure 4.11). Voltage over resistance wire of heating block = 60 V. Measured atmospheric pressure = 101.42 kPA

To determine the pressure differences, the equations from the calibration of the pressure transducers (section 4.7) can be used. For the pressure difference over the orifice, (at an average ambient temperature of 17.5 °C)

$$\Delta P_1 = 0.096063 \rho_{water} g V_1 = 0.096063(999)(9.81)(3.114) = 2931.6\ Pa \qquad \text{(B.27)}$$

The pressure difference between the orifice inlet and atmosphere is found by:

$$\Delta P_2 = 1.96231 \rho_{water} g V_2 = 1.96231(999)(9.81)(0.5964) = 11469.4\ Pa \qquad \text{(B.28)}$$

Equation B.33 can be used to determine the absolute pressure before the orifice plate:

$$P_{o\,(abs)} = P_a + \Delta P_2 = 101420 + 11469.4 = 112889.4\ Pa \qquad \text{(B.29)}$$

The average temperature of air flowing through the pipe is 21 °C. The pipe inner diameter is defined as $D = 0.029$ m and the orifice diameter as $d = 0.021$ m.

The mass flow rate can be calculated by (BS 1042) as:

$$\dot{m}_{air} = \frac{CE\varepsilon\pi d^2\sqrt{2\Delta P_1 \rho_{air}}}{4} \tag{B.30}$$

where:

$$C = 0.5959 + 0.0312\beta^{2.1} - 0.184\beta^8 + 0.0029\beta^{2.5}\left(\frac{10^6}{\mathrm{Re_D}}\right)^{0.75} + (0.09)\mathrm{L_1}(0.039)$$

$$- 0.033\mathrm{L'_2}\beta^3 \tag{B.31}$$

For this arrangement, $L_1 = 1$ and $L'_2 = 0.47$, and

$$\mathrm{Re}_D = \frac{4\dot{m}_{air}}{\pi D \mu_{air}} \tag{B.32}$$

and

$$\beta = d/D = 0.021/0.029 = 0.7241 \tag{B.33}$$

$$E = (1-\beta^4)^{-0.5} = (1-0.7241^4)^{-0.5} = 1.174416 \tag{B.34}$$

$$\varepsilon = 1 - (0.41 + 0.35\beta^4)\Delta P_1/(\gamma P_{o(abs)}) = 1 - (0.41 + 0.35(0.7241)^4)2931.6/(1.4(112889.4))$$

$$= 0.99061 \tag{B.35}$$

The density of the air can be calculated as:

$$\rho_{air} = \frac{P}{RT} = \frac{112889.4}{287.08(273+21)} = 1.3375\ kg/m^3 \tag{B.36}$$

The mass flow rate of the air can now be calculated using equation B.30, but since equation B.31 needs a Reynolds number which is a function of the mass flow rate, this needs to be found through iteration. By choosing $\dot{m}_{air} = 0.02167$ kg/s, equation B.32 becomes:

$$\mathrm{Re}_D = \frac{4\dot{m}_{air}}{\pi D \mu_{air}} = \frac{4(0.02167)}{\pi(0.029)(18.17\times10^{-6})} = 52362 \tag{B.37}$$

and substituting into equation B.31,

$$C = 0.5959 + 0.0312(0.7241)^{2.1} - 0.184(0.7241)^8 + 0.0029(0.7241)^{2.5}\left(\frac{10^6}{52362}\right)^{0.75}$$

$$+ (0.09)(1)(0.039) - 0.033(0.47)(0.7241)^3$$

$$= 0.60728 \tag{B.38}$$

Substituting into equation B.30,

$$\dot{m}_{air} = \frac{0.60728(1.174416)(0.99061)\pi(0.021)^2\sqrt{2(2931.6)(1.3375)}}{4}$$

$$= 0.02167\ kg/s \qquad \text{(B.39)}$$

which is the same as the chosen value and convergence is therefore implied.

B.3 DETERMINATION OF FIN HEAT TRANSFER COEFFICIENT

The calculations in section B.3 are used in connection with the experiments of section 4.2 and the thermal model of section 5.2, in order to find the experimental forced convection heat transfer coefficient for the cooling air as it flows over the fin surfaces in the duct.

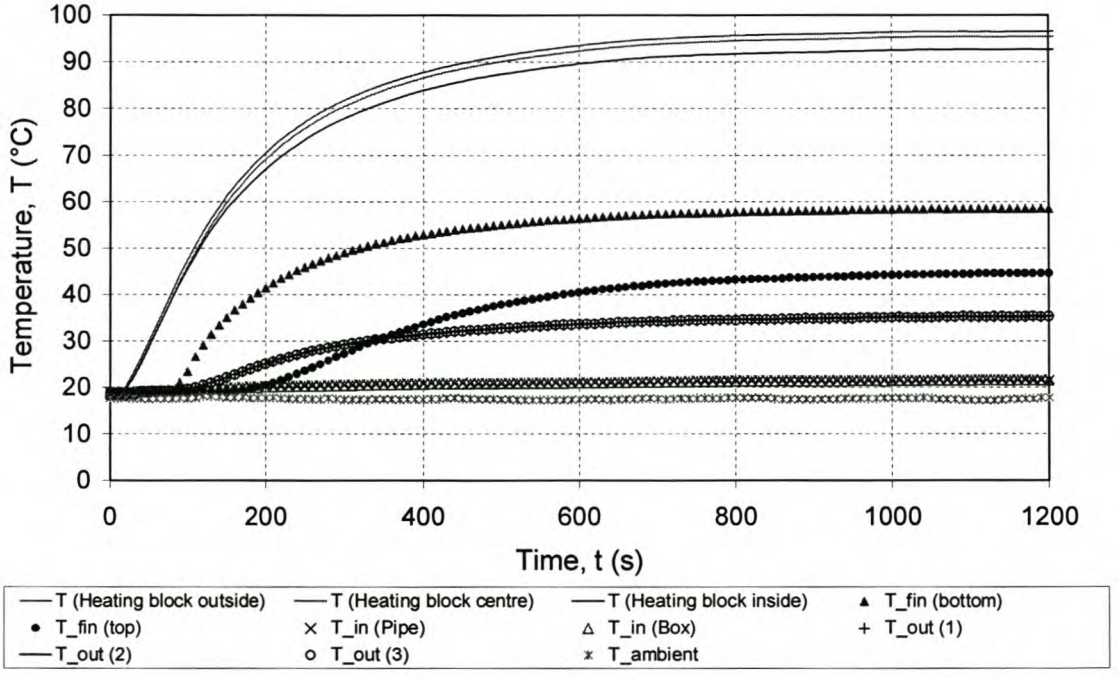

Figure B.4 Experimentally measured temperatures for experimental case 4.2. (Determination of forced convection heat transfer coefficient for air flowing over fins). Voltage over resistance wire of heating block = 60V. Mass flow rate of the air = 0.02167 kg/s

Using the same experiment (exp. 2.3, table 4.3) as in section B.2 where the mass flow rate of the cooling air is calculated, the other measurements are shown in figure B.4. It can be seen that the temperatures measured at the top and the bottom of the fin were not the same. Ideally these two temperatures would be the same. Through inspection, it seemed as if the top part of the fin (about the top 5 fins) did not heat up as much as the rest of the fins did. It was assumed that there is a problem at that part. Therefore, the top 8 fins (of the total of 41

total fins) were carefully covered with masking tape, so that heat were only transferred through the remaining 33 fins, of which the base temperature is taken as the temperature measured at the bottom of the fin. The experimental data for times of 490 and 500 seconds are given in table B.3.

Table B.2 Values needed to determine forced convection heat transfer coefficient at time t = 495 seconds

Time (s)	490	500
$T_{fin\ (top)}$ (°C)	37.48	37.80
$T_{heating\ block\ (outside)}$ (°C)	91.00	91.28
$T_{heating\ block\ (centre)}$ (°C)	89.61	89.88
$T_{heating\ block\ (inside)}$ (°C)	87.11	87.42
$T_{fin\ (bottom)}$ (°C)	54.86	54.98
$T_{air\ (in)}$ (°C)	20.89	20.91
$T_{air\ (in)}$ (°C)	20.83	20.86
$T_{air\ (out)}$ (°C)	32.63	32.74
$T_{air\ (out)}$ (°C)	32.79	32.91
$T_{air\ (out)}$ (°C)	32.64	32.71
$T_{ambient}$ (°C)	17.57	17.41

The average air inlet temperature is:

$$T_{air\,(in)} = \frac{20.89 + 20.83 + 20.91 + 20.86}{4} = 20.87\ °C \qquad \text{(B.40)}$$

and the average air outlet temperature is:

$$T_{air\,(out)} = \frac{32.63 + 32.79 + 32.64 + 32.74 + 32.91 + 32.71}{3} = 32.74\ °C \qquad \text{(B.41)}$$

The average temperature of the air used to determine the properties with, is therefore taken as:

$$T_{air} = \frac{T_{in} + T_{out}}{2} = \frac{20.87 + 32.74}{2} = 26.81\,°C = 299.92\,K \tag{B.42}$$

For air at P = 101.325 kPa and T = 300K, the properties needed are: (Kays & Crawford)

$$\mu_{air} = 18.53 \times 10^{-6}\ Pa.s \tag{B.43}$$

$$C_{p(air)}\ 1005\ J/kgK \tag{B.44}$$

$$\mathrm{Pr}_{air} = 0.711 \tag{B.45}$$

The mass flow rate of the air is given by equation B.39 as $\dot{m} = 0.02167\ kg/s$. The heat transfer rate absorbed by the air is therefore:

$$\dot{Q}_{air} = \dot{m}_{air} C_{p(air)} (T_{air(out)} - T_{air(in)}) = 0.02167(1005)(32.74 - 20.87) = 258.6\,W \tag{B.46}$$

Although the value given by equation B.46 is expected to be accurate and will be used to base the convection heat transfer coefficient on, the heat transfer rate through the evaporator and the effects of the fin mass are evaluated for an energy balance check.

Using equations B.21 and B.21, it follows that:

$$\dot{Q}_e = \frac{2\pi(204)(0.08)\left(\frac{89.88 + 89.61}{2} - \frac{87.42 + 87.11}{2}\right)}{\ln(0.044/0.018)}$$

$$- \frac{\frac{\pi}{4}(0.044^2 - 0.018^2)(0.08)(2770)(875)\left(\frac{89.88 + 87.42}{2} - \frac{89.61 + 87.11}{2}\right)}{10}$$

$$= 284.51 - 7.12 = 277.4\,W \tag{B.47}$$

It can be seen that the average temperature of the fin increased over the 10 seconds, by looking at the fin base temperatures at the top and bottom of the fin. To determine this, though, the convection heat transfer coefficient is needed. The heat transfer given off to the air from the fins is simply $\dot{Q} = \eta_f h_{fc} A \Delta T$ where the fin efficiency is given as (refer to section 5.2):

$$\eta_f = \frac{(2r_i/\beta)}{(r_o^2 - r_i^2)} \frac{K_1(\beta r_i) I_1(\beta r_o) - I_1(\beta r_i) K_1(\beta r_o)}{K_o(\beta r_i) I_1(\beta r_o) + I_o(\beta r_i) K_1(\beta r_o)} \tag{B.48}$$

and

$$\beta = \left(\frac{h_{fc}}{t_f k_{fin}}\right)^{1/2} \tag{B.49}$$

The convection heat transfer coefficient h_{fc} has to be found through iteration, though, since the fin efficiency is a function of β which is a function of h_{fc}.

Choosing $h_{fc} = 38.03\ \text{W/m}^2\text{K}$:

$$\beta = \left(\frac{38.03}{(0.00075)(204)}\right)^{1/2} = 15.77 \tag{B.50}$$

The fin efficiency is therefore:

$$\eta_f = \frac{(2(0.01)/15.77)}{(0.0375^2 - 0.01^2)} \frac{K_1(15.77\times0.01)I_1(15.77\times0.0375) - I_1(15.77\times0.01)K_1(15.77\times0.0375)}{K_o(15.77\times0.01)I_1(15.77\times0.0375) + I_o(15.77\times0.01)K_1(15.77\times0.0375)}$$

$$= 0.9709\frac{(6.1462)(0.3088) - (0.0791)(1.3286)}{(1.9814)(0.3088) + (1.0062)(1.3286)} = 0.8932 \tag{B.51}$$

The convection heat transfer coefficient can now be based on the heat transfer coefficient calculated using the rise in air temperature, as:

$$h_{fc} = \frac{\dot{Q}_{air}}{\eta_f A \Delta T} = \frac{258.6}{0.8932\left(33(2)\frac{\pi}{4}(0.075^2 - 0.02^2)\right)\left(\frac{54.86+54.98}{2} - 26.81\right)} = 38.03\ W/m^2K \tag{B.52}$$

This is the same as the value chosen for equation B.50, which implies convergence.

To incorporate the effect of the fin's thermal capacitance, refer to section 5.2 (figure 5.8 in particular). The fins are discretised into five concentric control volumes, each with temperature T_i. As an example, consider control volume number 3 (associated with temperature T_3 in figure 5.8). The radius at temperature T_3 is $r = 0.02375$ m. From equation 5.59, $F = I_0(z_b)K_1(z_o) + I_1(z_b)K_0(z_o)$, where $z = \beta r$ so that:

$$F = I_0(15.77\times0.01)K_1(15.77\times0.0375) + I_1(15.77\times0.01)K_0(15.77\times0.0375)$$

$$= 1.0026\times1.3286 + 0.0791\times0.7889 = 1.3945 \tag{B.53}$$

so that:

$$C_1 = \frac{K_1(z_o)}{F} = \frac{1.3286}{1.3945} = 0.9528 \tag{B.54}$$

$$C_2 = \frac{I_1(z_o)}{F} = \frac{0.3088}{1.3945} = 0.22144 \tag{B.55}$$

Since $\theta = C_1 I_o(z) + C_2 K_o(z)$, it follows that for $r = 0.02375$ m:

$$\theta = 0.9528 I_o(15.77 \times 0.02375) + 0.22144 K_o(15.77 \times 0.02375) = 0.9865 + 0.2596 = 1.2461 \quad \text{(B.56)}$$

and with $\theta = \dfrac{T(r) - T_a}{T_b - T_a}$, it follows that:

$$T_3 = \theta(T_b - T_a) + T_a = 1.2461(T_b - T_a) + T_a = 1.2461 T_b - 0.2461 T_a \quad \text{(B.57)}$$

After 490 seconds, this temperature is therefore:

$$T_3(t = 490s) = 1.2461 T_b - 0.2461 T_a = 1.2461(54.86) - 0.2461(26.77) = 61.77°C \quad \text{(B.58)}$$

and at 500 seconds, it is:

$$T_3(t = 500s) = 1.2461(54.98) - 0.2461(26.84) = 61.91°C \quad \text{(B.59)}$$

Therefore, the temperature rise of control volume 3 in the ten seconds is:

$$\Delta T_{cv(3)} = 61.99 - 61.77 = 0.22°C \quad \text{(B.60)}$$

The mass of control volume number 3 for one fin is (refer to equation 5.60):

$$m_{cv}(3) = 13.0533(r_3^2 - r_2^2) = 13.0533\left(0.0265^2 - 0.021^2\right) = 0.00341\ kg \quad \text{(B.61)}$$

For all 41 fins, the amount of energy absorbed is therefore:

$$E(3) = \left(m C_p \Delta T_{cv}\right)_3 = (41)(0.00341)(875)(0.22) = 26.91\ J \quad \text{(B.62)}$$

Since this energy has been absorbed in 10 seconds, the average heat transfer rate needed to do so is:

$$\dot{Q}_3 = \frac{26.91}{10} = 2.691\ W \quad \text{(B.63)}$$

The same can be done for the other four control volumes, and the total heat transfer rate absorbed by the fin mass is calculated as:

$$\dot{Q}_{fm} = 11.19\ W \quad \text{(B.64)}$$

If this is subtracted from the calculated evaporator heat transfer rate, the remaining part is:

$$\dot{Q}_e - \dot{Q}_{fm} = 277.4 - 11.19 = 266.2\ W \quad \text{(B.65)}$$

Ideally, the value given by equation B.65 must be the same as the heat transfer rate calculated using the temperature increase of the air, which is $\dot{Q}_{air} = 258.6\ W$. The difference

between the two heat transfer rates are about 3%. This is regarded as good enough to serve as an energy balance check. The heat transfer rate calculated in equation B.46 is regarded as the most accurate measurement. Since the heat transfer coefficient (equation B.52) was calculated using this value, it is therefore regarded as determined relatively accurately.

Figure B.5 shows the results for the rest of the time as well, calculated in the same fashion as above.

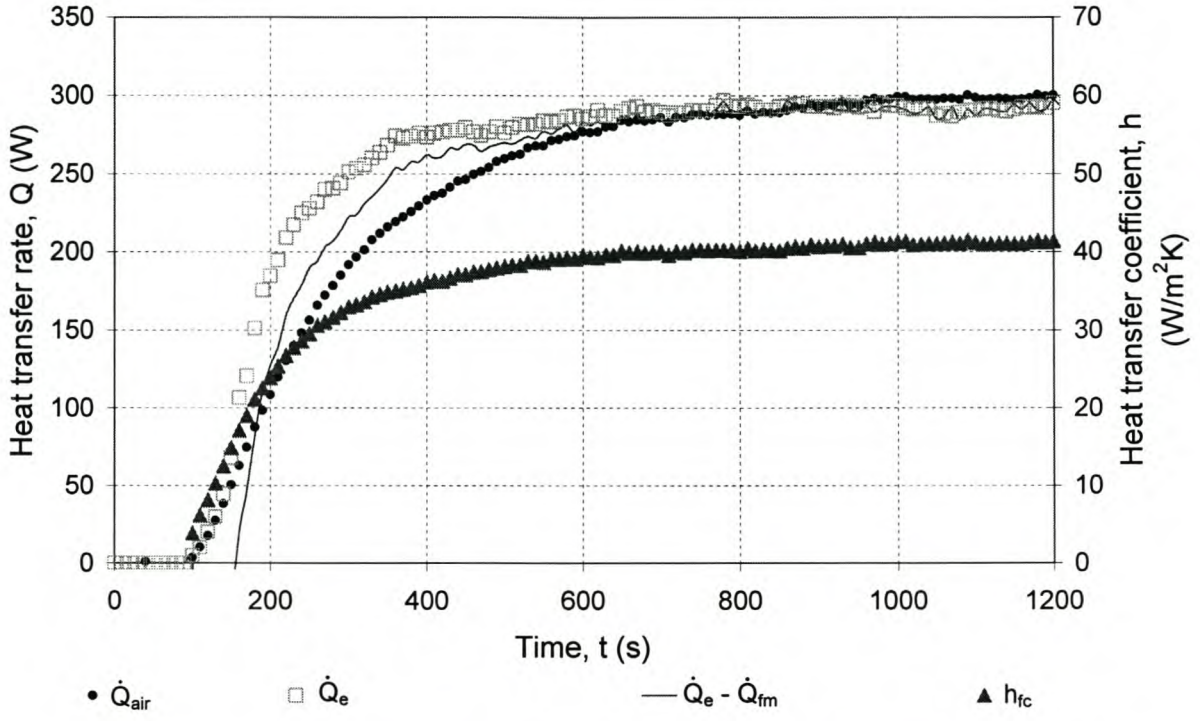

Figure B.5 Heat transfer rates and associated forced convection coefficient between air and fins, using the temperatures measured and shown in figure D.4. Mass flow rate = 0.02167 kg/s. (Corresponding to experiment number 2.3 in table 4.3)

It can be seen that the heat transfer coefficient changes from low to about 40 W/m^{2}K as time progress. The reason why this occurs is probably because of the quasi-steady state approach that is used to determine the heat transfer coefficient during the time intervals. For the first part, there is a significant transient heat transfer that takes place, and only later on this rate becomes more steady. An error should be expected if the heat transfer rate is not yet at steady state. Only after about 600 seconds does the heat transfer rate become steady and the heat transfer coefficient after this stage is expected to be much more accurately calculated.

Appendix C - Modelling of the Casting, Core and External Mould for the Core Cooling Case

The Core Cooling (casting) Case is described in sections 4.4 and 5.4 of the thesis. The theoretical modelling of this case differs from the mould heating and mould cooling cases in the sense that the standard FEM computer package is not used but instead the moulds are modelled using finite differences. The model also has to include the fact that the core is connected to a heat pipe and fin combination. A computer program was written for the modelling of this case. The core, mould and casting are modelled in this section. The other components (fin and heat pipe) are modelled in section 5.4, refer to figure 5.14.

The mould and core are modelled together, as shown in figure C.1, where three parts can be seen, parts A, B and C. Part A is the outside mould, part B is the core and part C is an in-between connecting piece.

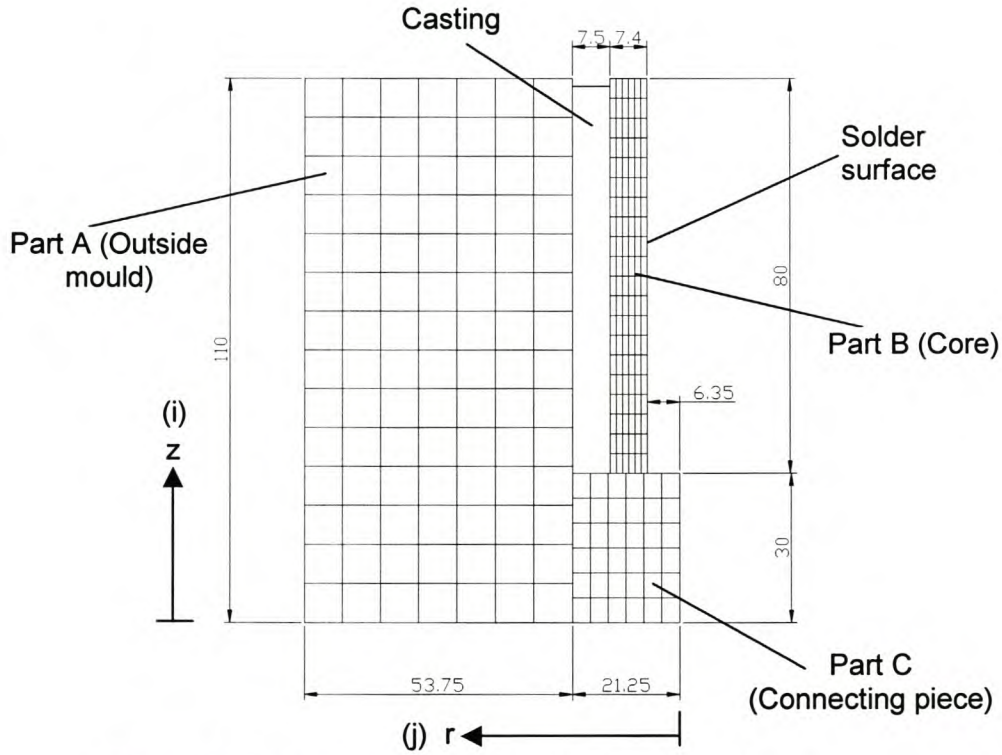

Figure C.1 Discretisation of moulds for the core cooling case

Since the moulds and heat pipe are symmetric around the z-axis it can be modelled as a two dimensional section in the r-z plane. The nodes are located at the intersections of the gridlines.

Let j and i be the counters (between 1 and J or 1 and I) with respect to a node's position in the radial direction (r) and axial direction (z), respectively. The radial grid spacing is denoted by Δr and the axial grid spacing by Δz. As can be seen from figure C.1, these values are different for parts A, B and C, with:

Δr_A = 7.679 mm	Δz_A = 7.857 mm	J_A = 7	I_A = 15
Δr_B = 1.233 mm	Δz_B = 4 mm	J_B = 6	I_B = 20
Δr_C = 3.542 mm	Δz_C = 5 mm	J_C = 7	I_C = 7

C.1 MODELLING OF THE CASTING

The casting fits in the space between the outside mould and the core.

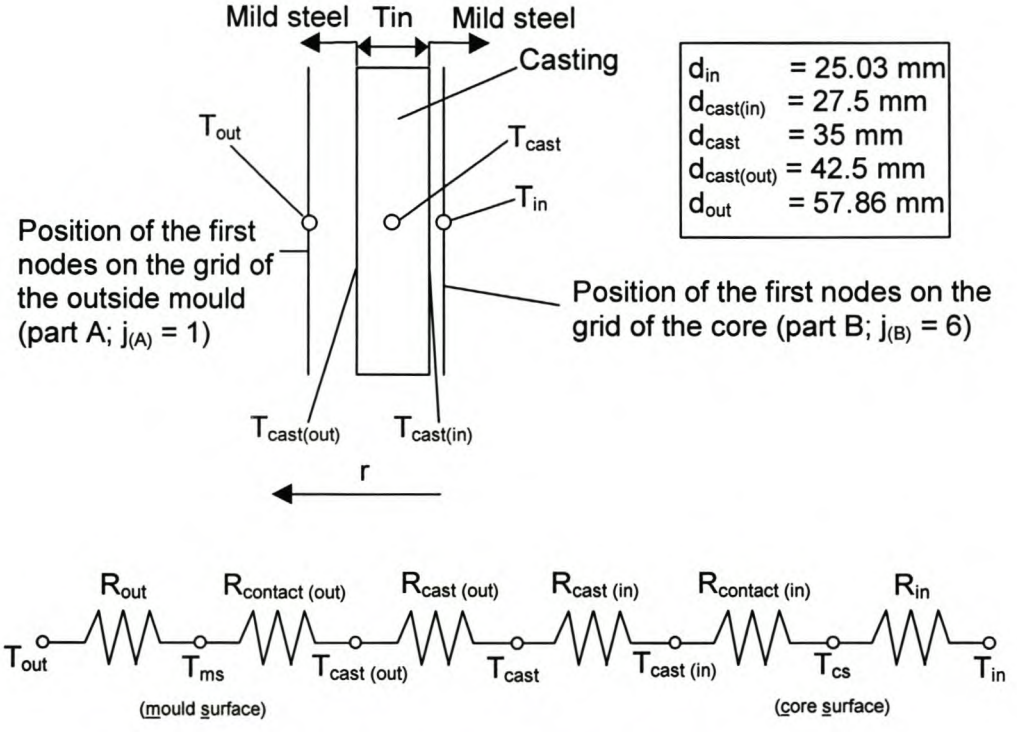

Figure C.2 Discretisation and thermal circuit of the casting

The casting is approximated as a single control volume with temperature T_{cast} (P), where P is the number of the discretised time step. To determine the casting's new temperature, the amount of heat transferred out of it needs to be calculated over the time step. The mass and properties (such as the specific heat capacity and the latent energy of fusion) of the casting is known and therefore the new temperature can be found if the amount of heat that left the casting is known. The heat transfer rate towards the core between the nodes at T_{cast} and T_{in} can be written as:

$$\dot{Q}_{in} = \frac{T_{cast} - T_{in}}{R_{cast(in)} + R_{in} + R_{contact(in)}} \qquad \text{(C.1)}$$

where $R_{cast(in)}$ is the thermal resistance between the centre of the casting and the casting-core interface and R_{in} is the resistance between the casting-core interface and the position of T_{in}. These two resistances are therefore expressed as:

$$R_{cast(in)} = \frac{\ln\left(\frac{d_{cast}}{d_{cast(in)}}\right)}{2\pi k_{cast} L_{cast}} \tag{C.2}$$

$$R_{in} = \frac{\ln\left(\frac{d_{cast(in)}}{d_{in}}\right)}{2\pi k_{core} L_{cast}} \tag{C.3}$$

The temperature on the core surface, T_{cs}, is given by:

$$T_{cs} = T_{cast} - \dot{Q}_{in}(R_{cast(in)} + R_{contact(in)}) = T_{in} + \dot{Q}_{in} R_{in} \tag{C.4}$$

The heat transfer rate towards the outside mould is given by:

$$\dot{Q}_{out} = \frac{T_{cast} - T_{out}}{R_{cast(out)} + R_{out} + R_{contact(out)}} \tag{C.5}$$

where

$$R_{cast(out)} = \frac{\ln\left(\frac{d_{cast(out)}}{d_{cast}}\right)}{2\pi k_{cast} L_{cast}} \tag{C.6}$$

$$R_{out} = \frac{\ln\left(\frac{d_{out}}{d_{cast(out)}}\right)}{2\pi k_{mould} L_{cast}} \tag{C.7}$$

The temperature on the mould surface, T_{ms}, is given by:

$$T_{ms} = T_{cast} - \dot{Q}_{out}(R_{cast(out)} + R_{contact(out)}) = T_{out} + \dot{Q}_{out} R_{out} \tag{C.8}$$

The contact resistances are not known but found empirically. The properties of the core and mould are those of mild steel and the properties of the casting is that of tin (see Appendix A). The heat transfer from the casting towards the bottom of the mould is ignored.

C.2 THE OUTSIDE MOULD (Part A)

The modelling of this part is based on figure C.3. (Note that it is rotated clockwise through 90° from figure C.1). The grid consists of 15x7 (*i*x*j*) nodes, thus 105 in total. The nodes are

numbered, starting with node 1 in the bottom left corner and continuing along the z direction, until node 15 is reached in the bottom right corner. Node 16 starts at the left side again, right above node 1, with node 30 then at the right hand side directly above node 15. Selected nodes are shown in figure C.3. The base temperatures, indicated by the black dots, are assumed to be known temperatures and is on the plane where part A (the outside mould) touches either part C (the connecting piece) or the outside surface of the casting (See figure C.1). The base temperatures underneath nodes 1 to 4 are temperatures on the outside of part C (for time step P) but the temperature assigned to the points underneath nodes 5 to 15 is that of the mould surface, T_{ms}.

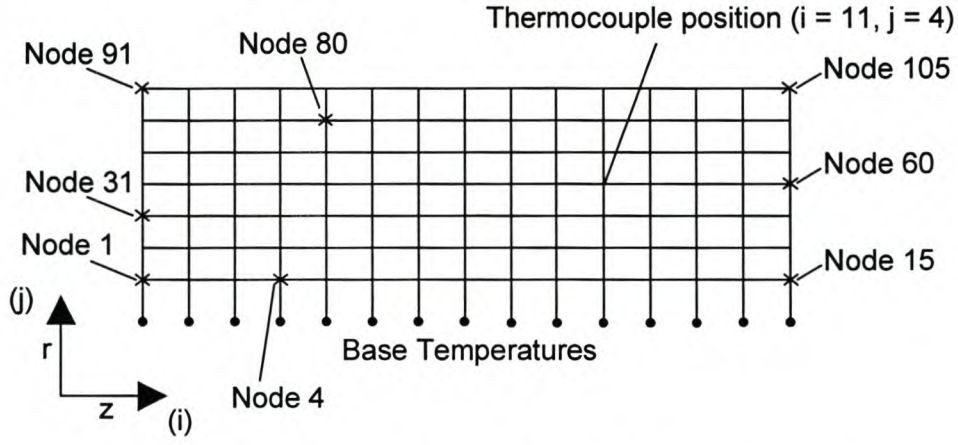

Figure C.3 Grid with node numbering of part A, the outside mould

The vertical surface on the left in figure C.3 is assumed to be insulated since that is the bottom of the mould that stands on the ground. The top and right surfaces are given radiation and convection boundary conditions, as it is open to the ambient atmosphere. The equation that is used to construct the 105 needed equations to solve the temperatures for each time step, is equation 3.76. The implicit method is used because of its good stability and therefore equation 3.76 becomes (where P denotes the time step):

$$\frac{\rho c}{\Delta t}T_{i,j}^{P} = \left[\frac{\rho c}{\Delta t} + \frac{k_r}{r\Delta r} + \frac{2k_r}{\Delta r^2} + \frac{2k_z}{\Delta z^2}\right]T_{i,j}^{P+1} - \left[\frac{k_r}{\Delta r^2}\right]T_{i,j-1}^{P+1} - \left[\frac{k_z}{\Delta z^2}\right]T_{i+1,j}^{P+1}$$
$$- \left[\frac{k_r}{r\Delta r} + \frac{k_r}{\Delta r^2}\right]T_{i,j+1}^{P+1} + \left[\frac{k_z}{\Delta z^2}\right]T_{i-1,j}^{P+1} \qquad \text{(C.9)}$$

Equation C.9 implies that the grid has to be divided into 9 areas, namely the bottom left corner, the bottom row, the bottom right corner, the left column, the inner grid, the right column, the top left corner, the top row and the top right corner.

The bottom left corner (Node 1 only)

For node 1, it can be seen that node i-1 falls (to the left) outside the grid, and does not exist. Secondly, node j-1 is below node 1 and therefore it falls on the first base temperature. This implies that the 2nd and 5th terms on the right hand side of equation C.9 need special consideration. To handle the second term is straight forward, but the fifth term needs more attention. Since the left wall is considered insulated, the heat flux in the z-direction over node 1 must be zero, therefore $\dot{q}''_z = -k_z \frac{dT}{dz} = 0$, which implies that $\frac{dT}{dz} = 0$. This can be approximated in the general form as $\frac{dT}{dz} \approx \frac{T(i+1) - T(i-1)}{2\Delta z} = 0$, and it therefore follows that $T^{P+1}_{i-1,j} = T^{P+1}_{i+1,j}$.

The second and fifth terms of equation C.9 therefore have to be updated with:

$$T^{P+1}_{i,j-1} = T_{BASE\,(1)} \tag{C.10}$$

$$T^{P+1}_{i-1,j} = T^{P+1}_{i+1,j} \tag{C.11}$$

Equation C.9 is now only a function of the unknown temperatures (at time step P+1) for the three existing nodes. (In this case, nodes 1, 2 and 16).

The bottom row (Nodes 2 to 14)

For this case the nodes below, at j-1, fall on the base temperatures. The second term on the right hand side of equation C.9 is therefore updated:

$$T^{P+1}_{i,j-1} = T_{BASE\,(i)} \tag{C.12}$$

The bottom right corner (Node 15)

In this case the positions of j-1 and i+1 need attention, which concerns the second and third terms in equation C.9. Convection and radiation boundary conditions are associated with the axial direction at node 15. If the combination of the heat flux due to convection and radiation is defined as $\dot{q}''_{env}$, the third term can be handled:

$$\dot{q}''_{env} = \dot{q}''_z = -k_z \frac{dT}{dz} \approx -k_z \frac{T(i+1) - T(i-1)}{2\Delta z} \tag{C.13}$$

Terms 2 and 3 of equation C.9 are therefore updated:

$$T^{P+1}_{i,j-1} = T_{BASE\,(15)} \tag{C.14}$$

$$T^{P+1}_{i+1,j} = T^{P+1}_{i-1,j} - \frac{2\Delta z \dot{q}''_{env}}{k_z} \tag{C.15}$$

The total heat flux to the environment is the sum of the convection and radiation heat fluxes. To find the radiation heat flux, consider equations 3.71 and 3.72. With the assumption that there is no external radiation, and that the size of the mould surface is very small compared to that of the atmosphere (which means that the view factor from ambient to the surface approach zero, but that from the mould to ambient is one), and denoting the mould outside as surface 1 and the atmosphere as surface 2, equation 3.71 reduces to:

$$\frac{q_1}{\varepsilon_1} = F_{1-2}(E_{b1} - E_{b2}) \tag{C.16}$$

Including equation 3.72, the heat flux leaving the boundary due to radiation is:

$$\dot{q}''_{rad} = \varepsilon_{ms}\sigma(T^4_{surface} - T^4_{amb}) \tag{C.17}$$

where $T_{surface}$ is the temperature of the node on the surface. (Thus, in effect $T_{surface} = T^P_{i,j}$)

The convective heat flux is simply $\dot{q}''_{conv} = h_{conv}(T_{surface} - T_{amb})$, so that:

$$\dot{q}''_{env} = \varepsilon_{ms}\sigma(T^4_{surface} - T^4_{amb}) + h_{conv}(T_{surface} - T_{amb}) \tag{C.18}$$

The left column (Nodes 16, 31, 46, 61 and 76)

These nodes have in common that the position i-1 falls outside the grid. This condition was already handled for node 1 and the same applies for these nodes. Therefore, the fifth term on the right hand side of equation C.9 is updated with:

$$T^{P+1}_{i-1,j} = T^{P+1}_{i+1,j} \tag{C.19}$$

The right column (Nodes 30, 45, 60, 75 and 90)

For these nodes the position i+1 falls outside the grid. It is once again subject to convection and radiation boundary conditions and is handled the same as node 15. Therefore,

$$T^{P+1}_{i+1,j} = T^{P+1}_{i-1,j} - \frac{2\Delta z\dot{q}''_{env}}{k_z} \tag{C.20}$$

can be used to update equation C.9.

The top left corner (Node 91)

The nodes to the left and above this node do not exist. At node 91, there are convection and radiation losses to the environment, in a radial direction. Therefore:

$$\dot{q}''_{env} = \dot{q}''_r = -k_r\frac{dT}{dr} \approx -k_r\frac{T(j+1) - T(j-1)}{2\Delta r} \tag{C.21}$$

Towards the left of node 91 there is an insulated boundary condition, so that the fourth and fifth terms on the right hand side of equation C.9 can be updated with:

$$T_{i,j+1}^{P+1} = T_{i,j-1}^{P+1} - \frac{2\Delta r \dot{q}''_{env}}{k_r} \quad \text{(C.22)}$$

$$T_{i-1,j}^{P+1} = T_{i+1,j}^{P+1} \quad \text{(C.23)}$$

where the heat flux to the environment is given by equation C.18.

The top row (Nodes 92 to 104)

For these nodes, the heat loss to environment in the radial direction needs to be considered and is handled the same as node 91, so that:

$$T_{i,j+1}^{P+1} = T_{i,j-1}^{P+1} - \frac{2\Delta r \dot{q}''_{env}}{k_r} \quad \text{(C.24)}$$

The top right corner (Node 105)

This node have a axial and radial heat flux to the environment, so that terms 3 and 4 of the right hand side of equation C.9 can be updated with:

$$T_{i+1,j}^{P+1} = T_{i-1,j}^{P+1} - \frac{2\Delta z \dot{q}''_{env}}{k_z} \quad \text{(C25)}$$

$$T_{i,j+1}^{P+1} = T_{i,j-1}^{P+1} - \frac{2\Delta r \dot{q}''_{env}}{k_r} \quad \text{(C26)}$$

The inner grid (All other nodes)

These are the majority of the nodes, the part that is located in-between the eight boundary positions discussed above. Its left bottom corner is at node 17, and its top right corner is at node 89. All these nodes are surrounded by four existing nodes in the unknown temperature field, and equation C.9 can be used without any modification. The 105 unknown temperatures can now be found by simultaneous solution of the 105 equations created, one for each node.

C.3 THE CORE (Part B)

Figure C.4 shows the discretisation of the core. The same approach that was taken for the outside mould is used again and equation C.9 is applicable, given that the special conditions at each surface are taken into consideration.

The bottom left corner (Node 1)

The nodes on the left and the bottom of node 1 (positions i-1 and j-1) are not on the grid of unknown temperatures. The temperature of the node on the left is taken as the temperature of part C at that position ($T_{C(1)}$) for the previous time step, P. Towards the bottom of node 1, there will be a radial heat flux into the heat pipe. If a constant heat flux radially into the heat

pipe over the total evaporator length is defined as $\dot{q}''_{HP}$, equation C.9 should be updated with (where if $\dot{q}''_{HP}$ is positive it means that heat is flowing *into the heat pipe*):

$$T_{i,j-1}^{P+1} = T_{i,j+1}^{P+1} - \frac{2\Delta r \dot{q}''_{HP}}{k_r} \tag{C.27}$$

$$T_{i-1,j}^{P+1} = T_{C(1)} \tag{C.28}$$

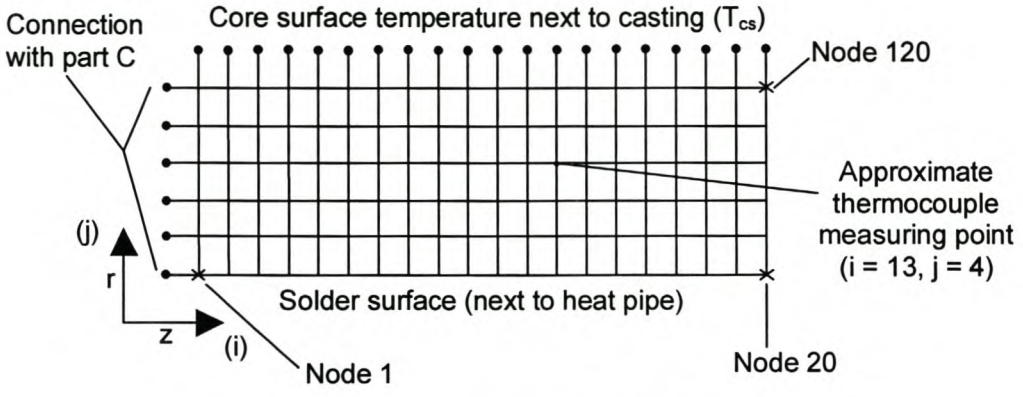

Figure C.4 Grid with node numbering of part B, the core

The bottom row (Nodes 2 to 19)

For these nodes, only the points below are of the grid, and therefore equation C.9 should be updated with:

$$T_{i,j-1}^{P+1} = T_{i,j+1}^{P+1} - \frac{2\Delta r \dot{q}''_{HP}}{k_r} \tag{C.29}$$

The bottom right corner (Node 20)

The nodes below and to the right of node 20 are off the grid. Towards the right of node 20, there is an axial heat flux (convection and radiation losses to environment) and therefore terms 2 and 3 of equation C.9 are updated with:

$$T_{i,j-1}^{P+1} = T_{i,j+1}^{P+1} - \frac{2\Delta r \dot{q}''_{HP}}{k_r} \tag{C.30}$$

$$T_{i+1,j}^{P+1} = T_{i-1,j}^{P+1} - \frac{2\Delta z \dot{q}''_{env}}{k_z} \tag{C.31}$$

where the heat flux to environment is given by equation C.18

The left column (Nodes 21, 41, 61 and 81)

Position i-1 is off the grid for these nodes. Equation C.9 is updated with:

$$T_{i-1,j}^{P+1} = T_{C(j)} \tag{C.32}$$

The right column (Nodes 40, 60, 80 and 100)

These nodes experience an axial heat flux, and the temperatures of the non existing nodes towards the right are updated as:

$$T_{i+1,j}^{P+1} = T_{i-1,j}^{P+1} - \frac{2\Delta z \dot{q}''_{env}}{k_z} \quad \text{(C.33)}$$

The top left corner (Node 101)

The temperature on the left is the temperature of part C at that point, and the temperature above it is the temperature of the inside of the core surface (T_{cs}). Equation C.9 is therefore updated with:

$$T_{i,j+1}^{P+1} = T_{cs} \quad \text{(C.34)}$$

$$T_{i-1,j}^{P+1} = T_{C(j)} \quad \text{(C.35)}$$

The top row (Nodes 102 to 119)

Only the above temperatures need to be updated with the core surface temperature so that:

$$T_{i,j+1}^{P+1} = T_{cs} \quad \text{(C.36)}$$

The top right corner (Node 120)

For this corner the casting temperature on top and the axial heat flux to the environment needs to be considered, so that:

$$T_{i,j+1}^{P+1} = T_{cs} \quad \text{(C.37)}$$

$$T_{i+1,j}^{P+1} = T_{i-1,j}^{P+1} - \frac{2\Delta z \dot{q}''_{env}}{k_z} \quad \text{(C.38)}$$

Once again equation C.9 can be used directly for the inner grid. A linear set of 120 equations with 120 unknowns are created and can be solved for each time step.

C.5 THE CONNECTING PIECE (Part C)

The discretisation of the connecting piece is shown in figure C.5.

The nodes are numbered in the same way as are parts A and B. Although part C has a 7x7 grid, three of the temperatures (in the top right area) are already known from the calculations regarding the casting. Therefore, only 46 temperatures need to be calculated for each time step. The shape of grid C implies that equation C.9 is not applicable everywhere (where $r = 0$). There are also eleven regions that need to be considered and not only nine as is the case with parts A and B. The first three regions namely the bottom left corner, the bottom row and

the bottom right corner, are located on $r = 0$. This means that equation 3.80 is applicable, which becomes, for the implicit scheme:

$$\frac{\rho c}{\Delta t}T_{i,j}^{P} = \left[\frac{\rho c}{\Delta t} + \frac{4k_r}{\Delta r^2} + \frac{2k_z}{\Delta z^2}\right]T_{i,j}^{P+1} - \left[\frac{k_z}{\Delta z^2}\right]T_{i+1,j}^{P+1} - \left[\frac{4k_r}{\Delta r^2}\right]T_{i,j+1}^{P+1} - \left[\frac{k_z}{\Delta z^2}\right]T_{i-1,j}^{P+1} \qquad \text{(C.39)}$$

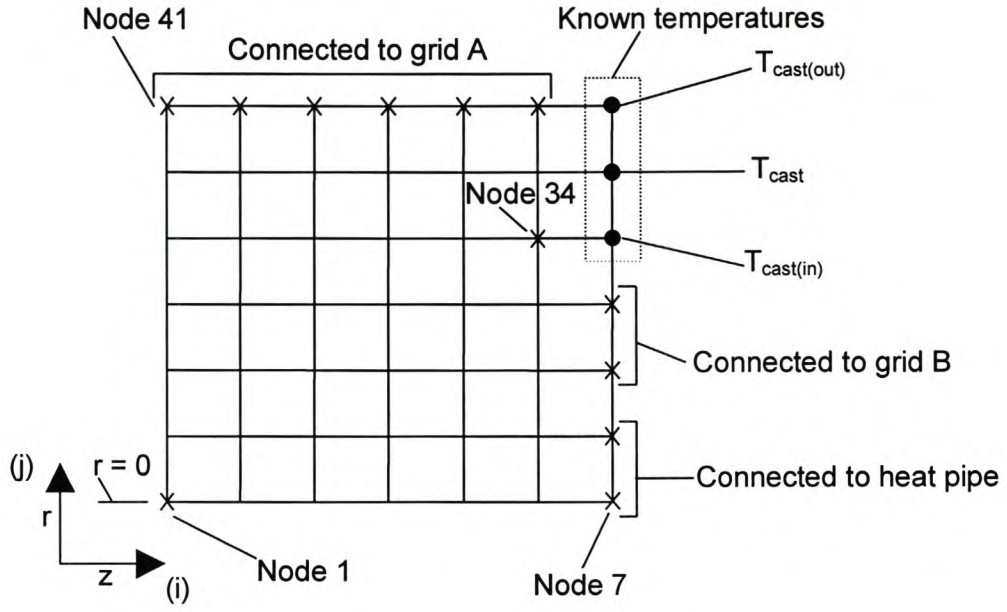

Figure C.5 Grid and node numbering of part C, the connecting piece

The bottom left corner (Node 1)

Node 1 is isolated towards its left which means that the axial heat flux is zero. Position i-1 is also outside of the grid. Therefore equation C.39 needs to be updated with:

$$T_{i-1,j}^{P+1} = T_{i+1,j}^{P+1} \qquad \text{(C.40)}$$

The bottom row (Nodes 2 to 6)

For these nodes, equation C.39 can be used without modification

The bottom right corner (Node 7)

At this node, position i+1 will fall outside the grid. The heat pipe is just to the right of node 7, but the assumption is made that no heat is transferred axially into the heat pipe through the end seals. An insulated condition is assumed, and equation C.39 can be updated with:

$$T_{i+1,j}^{P+1} = T_{i-1,j}^{P+1} \qquad \text{(C.41)}$$

For all the remaining regions, equation C.9 is again applicable:

The left column (Nodes 8, 15, 22, 29 and 35)

The insulated boundary towards the left implies that equation C.9 be updated with:

$$T_{i-1,j}^{P+1} = T_{i+1,j}^{P+1} \tag{C.42}$$

Node 14

This node is on the right hand wall, with the heat pipe towards its right. The insulation boundary condition means that equation C.9 be updated with:

$$T_{i+1,j}^{P+1} = T_{i-1,j}^{P+1} \tag{C.43}$$

Nodes 21 and 28

These nodes are just above node 14, but are connected to the grid of part B. A heat flux boundary condition therefore exists, with the flux determined by the temperature field calculated for part B. As an example, consider the axial heat flux entering node 21 from part B. Node 21 (on grid C) is approximately between radial position j=1 and j=2 (on grid B), just to the left of grid B. Since the temperatures of grid B have already been solved for time step P+1, the average heat flux into part C can be calculated using the average temperatures of part B for time steps P and P+1. So, for node 21, the axial heat flux can be calculated as:

$$\dot{q}_z'' = -k_z \frac{dT}{dz} \approx -k_z \frac{\Delta T_{(B\,to\,C)}}{\Delta z_B}$$

$$= -\frac{k_z}{\Delta z_B}\left(\left(\frac{T_{1,1}^{P} + T_{1,1}^{P+1} + T_{1,2}^{P} + T_{1,2}^{P+1}}{4}\right)_{(grid\ B)} - \left(T_{7,3}^{P}\right)_{(grid\ C)}\right) \tag{C.44}$$

The same can be done for node 28, where the position of the node is approximated to lie between radial positions j=4 and j=5 on grid B. Equation C.9 is therefore updated with:

$$T_{i+1,j}^{P+1} = T_{i-1,j}^{P+1} - \frac{2\Delta z \dot{q}_z''}{k_z} \tag{C.45}$$

Nodes 34 and 40

There are known temperatures to the right of these two temperatures. Equation C.9 is therefore updated with:

$$T_{i+1,j}^{P+1} = T_{cs}^{P} \qquad \text{(for node 34)} \tag{C.46}$$

$$T_{i+1,j}^{P+1} = \frac{T_{cs}^{P} + T_{ms}^{P+1}}{2} \qquad \text{(for node 40)} \tag{C.47}$$

The top left corner (Node 41)

This node is insulated towards its left and receives a radial heat flux from the temperature gradient that exists in grid A. The radial heat flux can be calculated as:

$$\dot{q}_r'' = -k_r \frac{dT}{dr} \approx -k_r \frac{\Delta T_{(A\,to\,C)}}{\Delta r_A}$$

$$= -\frac{k_r}{\Delta r_A}\left(\left(\frac{T_{1,1}^P + T_{1,1}^{P+1}}{2}\right)_{(grid\ A)} - \left(T_{1,7}^P\right)_{(grid\ C)}\right) \qquad \text{(C.48)}$$

since node 41 (position i=1, j=7) of grid C falls directly below node 1 (position i=1, j=1) of grid A. Therefore, equation C.9 is updated with:

$$T_{i-1,j}^{P+1} = T_{i+1,j}^{P+1} \qquad \text{(C.49)}$$

$$T_{i,j+1}^{P+1} = T_{i,j-1}^{P+1} - \frac{2\Delta r_C \dot{q}_r''}{k_r} \qquad \text{(C.50)}$$

The top row (Nodes 42 to 45)

These nodes receive radial heat fluxes from the temperature gradient in part A. These heat fluxes can be determined in the same way that equation C.48 is arrived, depending to the position of the node in grid C and the corresponding node above it in grid A. Therefore, update equation C.9 with:

$$T_{i,j+1}^{P+1} = T_{i,j-1}^{P+1} - \frac{2\Delta r_C \dot{q}_r''}{k_r} \qquad \text{(C.51)}$$

The top right corner (Node 46)

The radial heat flux from grid A is applicable, as well as the temperature just to the right of node 46. Equation C.9 is therefore updated with:

$$T_{i,j+1}^{P+1} = T_{i,j-1}^{P+1} - \frac{2\Delta r_C \dot{q}_r''}{k_r} \qquad \text{(C.52)}$$

$$T_{i+1,j}^{P+1} = T_{ms}^{P} \qquad \text{(C.53)}$$

For all the other internal nodes, equation C.9 can be used without modification. 46 equations are therefore created to find the 46 unknown temperatures for each time step.

When the casting-and-core is removed from the mould, only part B needs to be considered. The surface of the casting that is open to atmosphere is now given a convection and radiation boundary condition.

APPENDIX D - Modelling of an Inclined Ammonia Thermosyphon

The objective of this appendix is to theoretically model a thermosyphon that operates at different inclination angles and uses ammonia as the working fluid. Theoretical and experimental results are compared so as to asses the validity of the theoretical model and find possible reasons for differences between the experimental and theoretical results. The specific ammonia thermosyphon has been chosen since research has already been performed on it (Dobson, 2000).

D.1 EXPERIMENTAL SET-UP

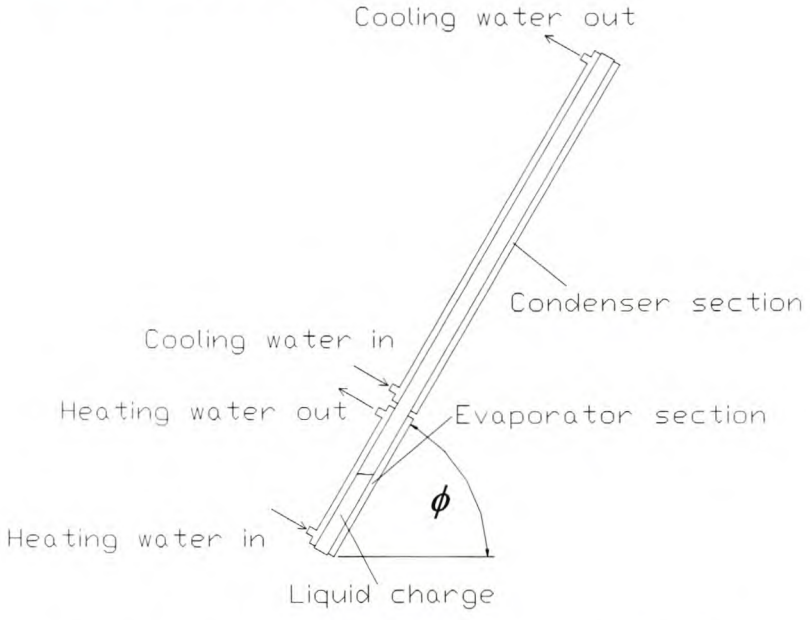

Figure D.1 Schematic of the thermosyphon experimental set-up

Figure D.1 shows a schematic of the thermosyphon experimental set-up. The thermosyphon is 6.2 m long, has an inside diameter of 31.9 mm and an outside diameter of 34.9 mm. The height of the pool formed by the liquid charge (L_p) is 0.4m. Adjustable length hot and cold water jackets (with inside diameter = 42.1 mm) are used at the evaporator and condenser ends respectively. The thermosyphon can be set up to operate at different angles of inclination ϕ. Experiments were performed at angles of ϕ = 30°, 45°, 60°, 75° and 90°. The evaporator lengths were set at L_e = 0.4m, 0.8m, 1.2m, 1.6m and 2m. The cooling water temperature (condenser end) was varied between 10°C and 20°C. The heating water temperature (evaporator end) was varied between 30°C and 80°C. Mass flow rates were varied between 0.2 and 1.5 kg/s (both evaporator- and condenser ends). A comprehensive set of experimental data was gathered and processed to find correlations for the heat

transfer characteristics of the thermosyphon. The heat transfer coefficient between the (heating or cooling) water and the outside surface of the thermosyphon was experimentally determined as (Dobson, 1998):

$$h_{ewo} = 4.553\,\mathrm{Re}_{hw}^{0.7333}\,\mathrm{Pr}_{hw}^{0.3626} \qquad \text{(D.1)}$$

$$h_{cwo} = 2.029\,\mathrm{Re}_{cw}^{0.8095}\,\mathrm{Pr}_{cw}^{0.3774} \qquad \text{(D.2)}$$

where the Reynolds numbers are based on the hydraulic diameter of the jackets.

D.2 THEORETICAL MODELLING

The thermosyphon's internal thermo-fluid processes are considered first. Figure D.2 shows the control volumes used to model the interior and also the heat transfer regions that forms.

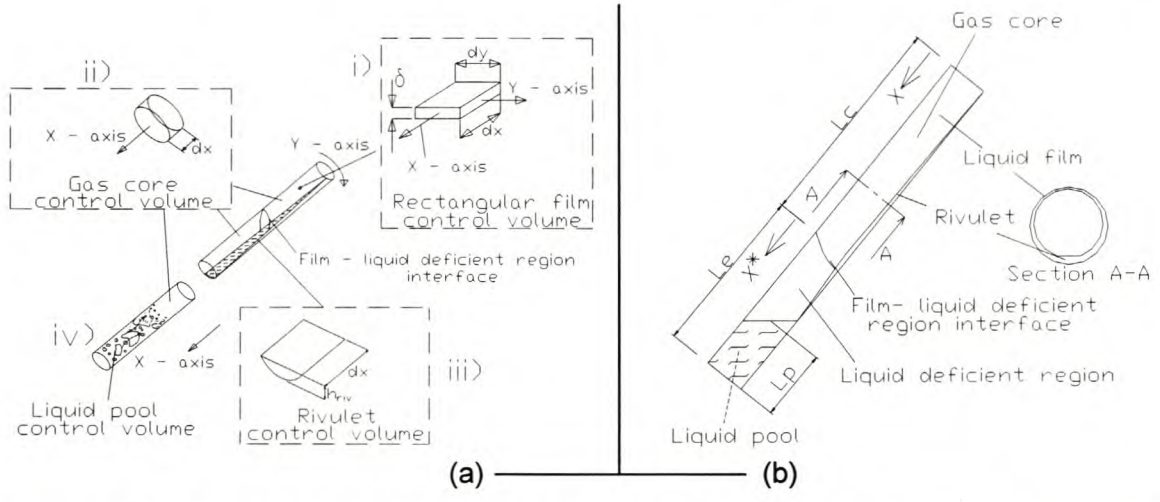

Figure D.2 (a) Control volume types to model the thermosyphon interior and (b) The heat transfer regions that form when theoretically modelling an inclined thermosyphon

The thermosyphon interior is modelled by using four types of control volumes. These control volumes are **i)** a two-dimensional array (x- and y directions) of relatively thin liquid *rectangular panel shaped control volumes*, where the liquid film is present; **ii)** a *gas-core control volume* (x-direction); **iii)** a *liquid rivulet control volume* (the rivulet is caused by liquid draining from the film into the bottom of the pipe section and is modelled in the x-direction only) and **iv)** a *liquid pool column* at the bottom, modelled as a single entity.

By solving the continuity, momentum and energy equations for the discretised control volumes, a numerical simulation can be performed. For inclined operation the solution yields four distinct heat transfer regions, as is shown in figure D.2(b). These regions will now be analysed in detail.

D.2.1 THE LIQUID FILM

Figure D.3 shows the relevant forces and mass flows over the liquid film control volume.

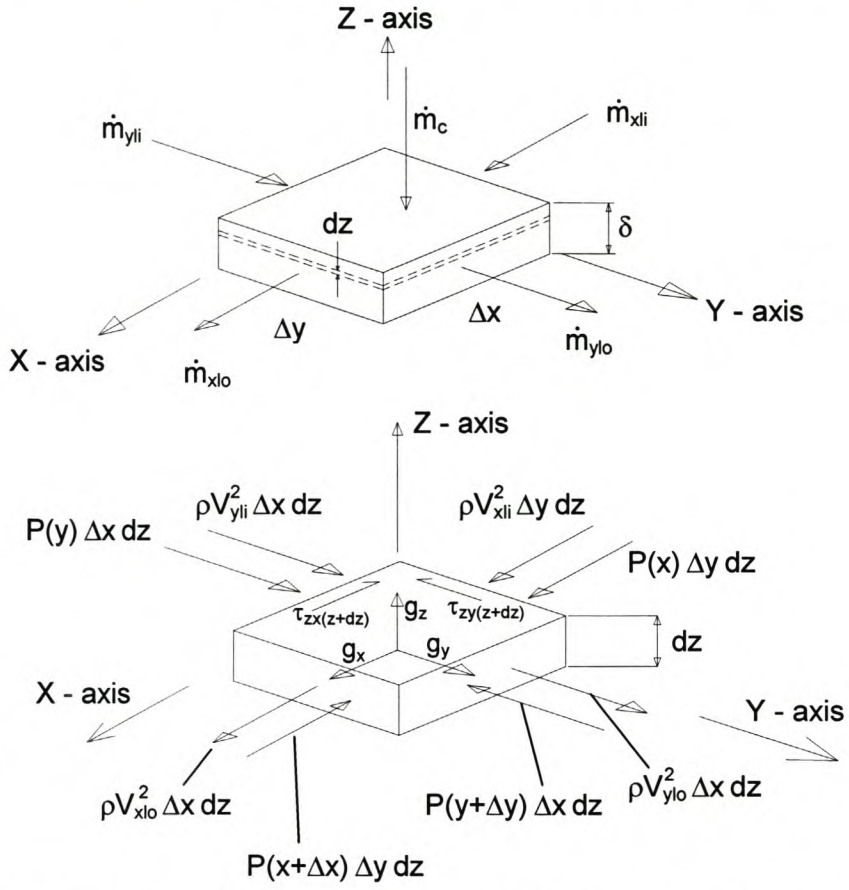

Figure D.3 Mass and momentum flow over the liquid film control volume

Conservation of mass in the control volume yields:

$$\dot{m}_{xli} + \dot{m}_{yli} + \dot{m}_c = \dot{m}_{xlo} + \dot{m}_{ylo} \qquad \text{(D.3)}$$

(Note that equation D.3 will hold for film condensation as well as evaporation. The film condensation mass flow rate $\dot{m}_c$ will be replaced by the evaporation mass flow rate $\dot{m}_e$)

For the momentum equation, the sum of the forces acting on the element are equal to the outflow of momentum – inflow of momentum + the "increase of storage" of momentum (Kays and Crawford, 1993). No chemical diffusion is expected in the film. For steady-state conditions $\frac{\partial}{\partial t}\rho v = 0$. Considering momentum in the x-direction, it follows that:

$$\rho_l V^2_{xlo}\Delta y dz - \rho_l V^2_{xli}\Delta y dz = P(x)\Delta y dz - P(x+\Delta x)\Delta y dz + g_x \rho_l \Delta y \Delta x dz$$
$$- \tau_{zx}(z)\Delta y \Delta x + \tau_{zx}(z+dz)\Delta y \Delta x \qquad \text{(D.4)}$$

Since the liquid mass flow rate is expected to be small, the difference in momentum (given by the left hand side of equation D.4) can be neglected. All normal stresses are neglected, and only the shear forces acting in the z-plane are considered. Using a truncated Taylor series approximation to describe properties at $(z + dz)$ and $(x + \Delta x)$, equation D.4 becomes:

$$0 = \left(P(x) - (P(x) + \frac{\partial P}{\partial x}\Delta x) \right) \Delta y dz + g_x \rho_l \Delta x \Delta y dz - \left(\tau_{zx}(z) - (\tau_{zx}(z) + \frac{\partial \tau_{zx}}{\partial z} dz) \right) \Delta x \Delta y \tag{D.5}$$

$P(x)$ and $\tau_{zx}(z)$ cancel out and dividing by $\Delta x \Delta y\, dz$, equation D.5 reduces to:

$$0 = -\frac{\partial p}{\partial x} - \frac{\partial \tau_{zx}}{\partial z} + \rho_l g_x \tag{D.6}$$

Following the same procedure in the y- and z-directions, the following equations results:

$$0 = -\frac{\partial p}{\partial y} - \frac{\partial \tau_{zy}}{\partial z} + \rho_l g_y \tag{D.7}$$

$$0 = -\frac{\partial p}{\partial z} + \rho_l g_z \tag{D.8}$$

It is assumed that pressure varies as a function of x only, thus:

$$\frac{\partial p}{\partial x} = \frac{dp}{dx}, \qquad \frac{\partial p}{\partial y} = 0 \qquad and \qquad \frac{\partial p}{\partial z} = 0 \tag{D.9}$$

The above assumption of $\frac{\partial p}{\partial z} = 0$, implies that $g_z = 0$ and therefore equation D.8 does not influence the fluid flow in any way.

For laminar, Newtonian fluid flow

$$\tau_{zx} = -\mu_l \left[\frac{\partial v_z}{\partial x} + \frac{\partial v_x}{\partial z} \right] \qquad and \qquad \tau_{zy} = -\mu_l \left[\frac{\partial v_y}{\partial z} + \frac{\partial v_z}{\partial y} \right] \tag{D.10}$$

but since $\frac{\partial v_z}{\partial x}$ and $\frac{\partial v_z}{\partial y}$ are viewed as negligible, substituting equations D.9 and D.10 into D.6 and D.7 leads to:

$$0 = -\frac{dp}{dx} + \mu_l \frac{\partial^2 v_x}{\partial z^2} + \rho_l g_x \tag{D.11}$$

and

$$0 = \mu_l \frac{\partial^2 v_y}{\partial z^2} + \rho_l g_y \tag{D.12}$$

The condensate film flow in the x-direction

Equation D.11 can now be integrated twice with respect to z which gives:

$$0 = -\frac{dp}{dx}\frac{z^2}{2} + \mu_l v_x + \rho_l g_x \frac{z^2}{2} + C_1 z + C_2 \qquad \text{(D.13)}$$

The applicable boundary conditions for equation D.13 are:

$$v_x = 0 \qquad if \qquad z = 0 \qquad \text{(D.14)}$$

$$\tau_{ix} = \tau_{zx} = \mu_l \frac{\partial v_x}{\partial z} \qquad \text{(interfacial shear stress between the liquid and the gas)} \qquad \text{(D.15)}$$

Substitution into equation D.13 (in its differentiated form for equation D.15) yields:

$$C_1 = \left(\frac{dp}{dx} - \rho_l g_x\right)\delta - \tau_{ix} \qquad and \qquad C_2 = 0 \qquad \text{(D.16)}$$

Substituting equation D.16 into equation D.13 and rearranging:

$$v_x = \frac{1}{\mu_l}\left[\left(\frac{z^2}{2} - \delta z\right)\left(\frac{dp}{dx} - \rho_l g_x\right) + \tau_{ix} z\right] \qquad \text{(D.17)}$$

The condensate film mass flow rate in the x-direction is

$$\dot{m}_x = \int_0^\delta \rho_l v_x \Delta y dz \qquad \text{(D.18)}$$

By substituting equation D.17 into D.18 and performing the integral:

$$\dot{m}_x = \frac{\rho_l \Delta y}{\mu_l}\left[\left(-\frac{dp}{dx} + \rho_l g_x\right)\frac{\delta^3}{3} + \frac{\tau_{ix}\delta^2}{2}\right] \qquad \text{(D.19)}$$

The condensate film flow in the y-direction

Integration of equation D.12 to z yields:

$$0 = \mu_l v_y + \rho_l g_y \frac{z^2}{2} + C_3 z + C_4 \qquad \text{(D.20)}$$

The boundary conditions are:

$$v_y = 0 \qquad if \qquad z = 0 \qquad \text{(D.21)}$$

$$\tau_{iy} = 0 \qquad if \qquad z = \delta \tag{D.22}$$

Substituting these into equation D.20, the constants are found as

$$C_3 = -\rho_l g_y \delta - \tau_{iy} \qquad and \qquad C_4 = 0 \tag{D.23}$$

Substituting equation D.23 into D.20 and rearranging:

$$v_y = \frac{1}{\mu_l}\left[\rho_l g_y \left(\frac{z^2}{2} - \delta z\right) + \tau_{iy} z\right] \tag{D.24}$$

The condensate film flow rate in the y-direction is

$$\dot{m}_y = \int_0^{\delta} \rho_l v_y \Delta x dz \tag{D.25}$$

Using v_y as given in equation D.24 and integrating equation D.25 gives

$$\dot{m}_y = \frac{\rho_l \Delta x}{\mu_l}\left[\frac{\rho_l g_y \delta^3}{3} + \frac{\tau_{iy}\delta^2}{2}\right] \tag{D.26}$$

The interfacial shear stress, τ_{iy}, is taken as zero since the vapour is assumed to be moving only in the x-direction. Therefore equation D.26 simplifies to

$$\dot{m}_y = \frac{\rho_l^2 g_y \Delta x \delta^3}{3\mu_l} \tag{D.27}$$

In order to determine the value of the gravity components in the x and y directions, consider figure D.4. The gravitational component in the x-direction is considered first. Since this is a straight axis which is independent of θ, the gravitational component is only dependant on the inclination angle ϕ. From geometry,

$$\frac{g_x}{g} = \sin\phi \qquad thus \qquad g_x = g\sin\phi \tag{D.28}$$

To determine g_y the gravitational component perpendicular to the x-axis first needs to be calculated. From figure D.4 it follows that:

$$\frac{g_{\perp x}}{g} = \cos\phi \qquad thus \qquad g_{\perp x} = g\cos\phi \tag{D.29}$$

When seen from view A→B, the control volume is under the influence of this gravitational component, $g_{\perp x}$. The component of this force in the y-direction is g_y and is dependant on θ, so that:

$$\frac{g_y}{g_{\perp x}} = \sin\theta \quad thus \quad g_y = g_{\perp x}\sin\theta \tag{D.30}$$

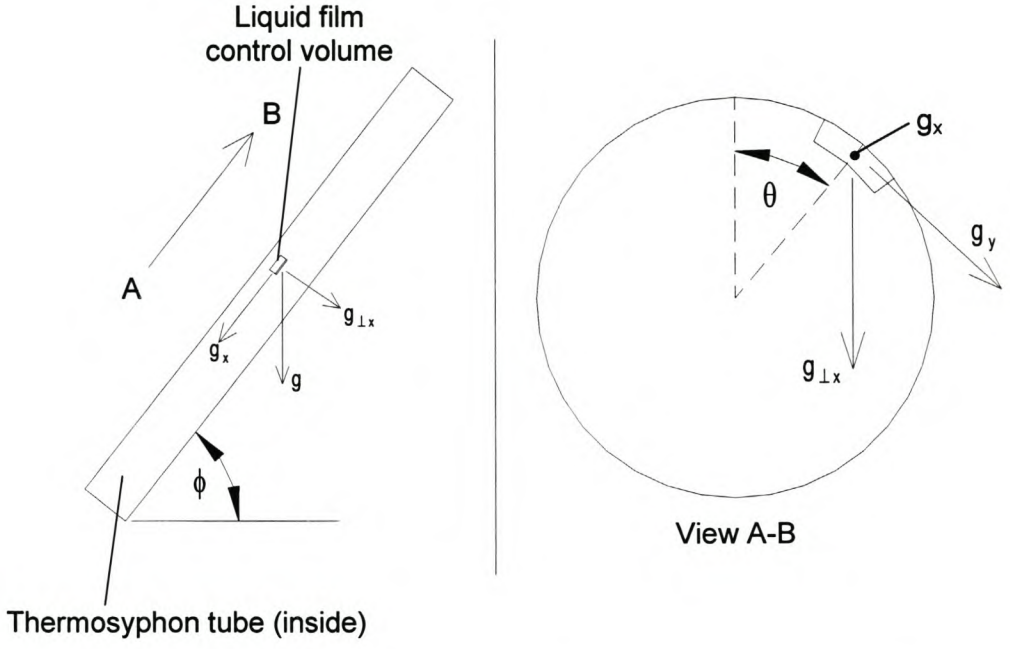

Figure D.4 Gravity components in the axial and circumferential directions

Substituting equation D.29 into D.30 yields

$$g_y = g\cos\phi\sin\theta \tag{D.31}$$

Heat transfer through liquid film

Only the radial heat transfer through the liquid film is considered. The applicable theory is discussed in chapter 3, and are given by equations 3.9, 3.10 and 3.11 for laminar, wavy-laminar and turbulent flow respectively.

D.2.2 THE GAS CORE

Two outputs are required from the gas flow analysis:

i) The pressure drop $\left(\frac{dp}{dx}\right)$

ii) The interfacial shear stress (τ_{ix}) on the gas-liquid interface

The gas flow is modelled with one dimensional control volumes, only in the x-direction. In the condenser section, the gas core loses some of its mass to the liquid film, and in the evaporator section gas is added to the core because of evaporation from the film. The conservation of mass and momentum equations can be derived with the help of figure D.5.

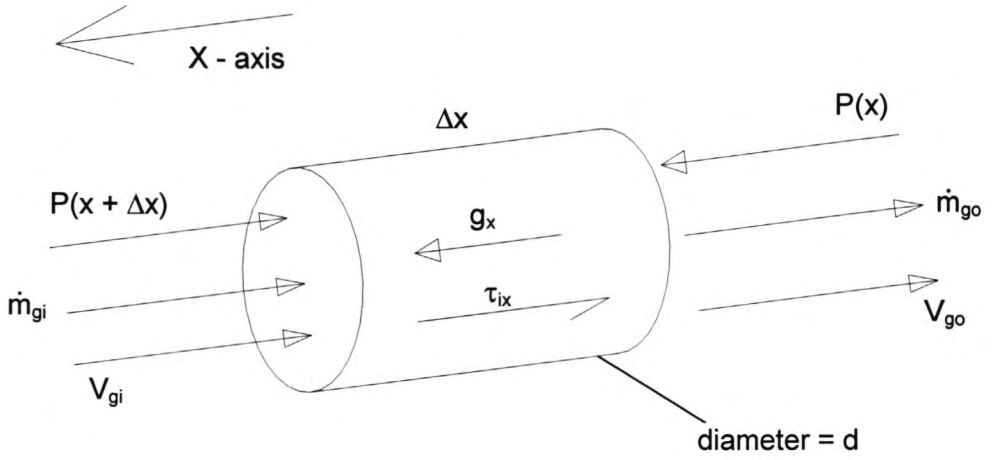

Figure D.5 Gas core control volume element

Conservation of mass for the gas core yields:

$$\dot{m}_{gi} = \dot{m}_c + \dot{m}_{go} \tag{D.32}$$

(where $\dot{m}_c = -\dot{m}_e$ in the evaporator section)

Applying the momentum equation:

$$\left(\dot{m}_{go} V_{go} - \dot{m}_{gi} V_{gi}\right) = -\tau_{ix}\pi d\Delta x + \left(P(x+\Delta x) - P(x)\right)\frac{\pi d^2}{4} - g_x \rho_g \Delta x \frac{\pi d^2}{4} \tag{D.33}$$

Introducing Taylor truncated terms, multiplying with $\dfrac{4}{\pi d^2 \Delta x}$ and rearranging:

$$\frac{dP}{dx} = \frac{4(\dot{m}_{gi} V_{gi} - \dot{m}_{go} V_{go})}{\pi d^2 \Delta x} - \frac{4\tau_{ix}}{d} - g_x \rho_g \tag{D.34}$$

To find the interfacial shear stress, the friction factor needs to be known. Often,

$$C_f = \frac{16}{\mathrm{Re}_g} \quad \textit{for laminar flow} \quad ; \quad C_f = 0.079\,\mathrm{Re}_g^{-0.25} \quad \textit{for turbulent flow} \tag{D.35}$$

but for this analysis, the effects of blowing and suction and waviness of the liquid film on the shear stress are included.

The effects of blowing and suction

When vapour condenses on a surface it is similar to gas flowing across a porous wall, called "suction". The opposite, evaporation, is called "blowing".

The net effect of blowing is to lower the interfacial shear stress, while suction will increase it. Thus the friction factor (given in equation D.35) needs to be adjusted with a factor β, so that (Stephan, 1992):

$$C_{f\_smooth} = \beta C_f \qquad and \qquad \beta = \frac{\varphi}{e^{\varphi - 1}} \tag{D.36}$$

where

$$\varphi = -25.32\,\mathrm{Re}_{cond}\,\mathrm{Re}_g^{-0.75}\ for\ condensation\ ;\ \varphi = 25.32\,\mathrm{Re}_{evap}\,\mathrm{Re}_g^{-0.75}\ for\ evaporation \tag{D.37}$$

Re_{cond} and Re_{evap} are the Reynolds numbers for the condensation and evaporation mass fluxes moving in a radial direction. For a gas core element with length Δx these Reynolds numbers can be written as:

$$\mathrm{Re}_{cond} = \frac{\dot{m}_{cond}}{\mu_g \pi \Delta x} \qquad and \qquad \mathrm{Re}_{evap} = \frac{\dot{m}_{evap}}{\mu_g \pi \Delta x} \tag{D.38}$$

The other Reynolds number, Re_g, is simply based on the axial gas velocity and cross sectional diameter.

The effects of waviness

For annular steam and water liquid flow a roughness correlation to take the waviness of the vapour-liquid interface into account is proposed as (Whalley, 1987):

$$C_{fi} = C_{f\_smooth}\left(1 + 360\frac{\delta}{d}\right) \tag{D.39}$$

where δ is the average film thickness and d is the diameter of the pipe.

According to Hewtt and Whalley, an equation that is better suited for general fluids, since it includes the liquid-over-gas density ratio, is (Whalley, 1987):

$$C_{fi} = C_{f\_smooth}\left(1 + 24\left(\frac{\rho_l}{\rho_g}\right)^{1/3}\frac{\delta}{d}\right) \tag{D.40}$$

Using equation D.40, the interfacial shear stress, updated with the effects of blowing, suction and waviness, can now be calculated as:

$$\tau_{ix} = \frac{1}{2} C_{fi} \rho_g V_g^2 \tag{D.41}$$

D.2.3 THE LIQUID RIVULET

If a thermosyphon is not operated vertically, but at an angle, the gravity component in the circumferential direction causes liquid in the film panels to flow towards the bottom of the container section where it accumulates into a rivulet. This liquid mass is also supplemented by direct condensation from the gas core onto the surface of the rivulet. In the evaporator section this liquid mass will decrease because of evaporation. Figure D.6 shows a rivulet control volume.

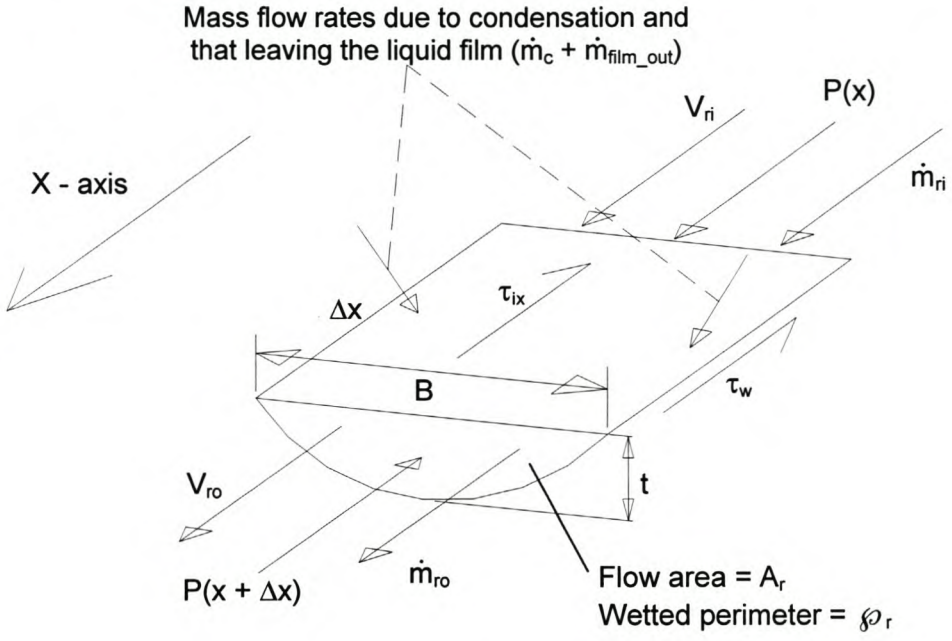

Figure D.6 Rivulet control volume

Considering the conservation of mass in figure D.6,

$$\dot{m}_{ri} + \dot{m}_c + \dot{m}_{film\_out} = \dot{m}_{ro} \tag{D.42}$$

The momentum equation can be written as:

$$\dot{m}_{ro} V_{ro} - \dot{m}_{ri} V_{ri} = \big(P(x) + P(x+\Delta x)\big) A_r - \tau_{ix} B \Delta x - \tau_w \wp_r \Delta x + g_x \rho_l A_r \Delta x \tag{D.43}$$

and reduces to

$$\frac{\dot{m}_{ro} V_{ro} - \dot{m}_{ri} V_{ri}}{\Delta x} = -\frac{dP}{dx} A_r - \tau_{ix} B - \tau_w \wp_r + g_x \rho_l A_r \tag{D.44}$$

The height of the rivulet, t, can be determined by balancing the left and right hand sides of equation D.44 (This needs to be done through iteration). Once the rivulet height is determined, the heat transfer coefficient associated with the control volume can be determined. Once again a laminar and turbulent case should be considered. For the laminar case, the rivulet is approximated as a thin rectangular flat panel, with the same width as the rivulet (thus B) but having an average thickness of δ_r. This implies that:

$$A_r \Delta x = B\delta_r \Delta x \quad and\ thus \quad \delta_r = \frac{A_r}{B} \quad so\ that \quad h_{r(laminar)} = \frac{k_l}{\delta_r} \tag{D.45}$$

For the turbulent case, the hydraulic diameter (where $D_{h(r)} = \frac{4A_r}{\wp_r}$) can be used to find the Reynolds number $\mathrm{Re}_r = \frac{\rho_l V_r D_{h(r)}}{\mu_l}$, and then $Nu_r = 0.023\,\mathrm{Re}_{Dh(r)}^{0.8}\,\mathrm{Pr}^{0.4}$.

Some of the dimensions of the rivulet needed for the analysis is portrayed in figure D.7 and are the following:

$$\gamma = \arccos\left(\frac{S}{R}\right) \quad where \quad S = R - t \quad and \quad thus \quad \gamma = \arccos\left(\frac{R-t}{R}\right) \tag{D.46}$$

$$_r = 2R\gamma \tag{D.47}$$

From figure D.7 it can be seen that $A_r = A_{sector} - A_\Delta$, and

$$A_{sector} = \gamma R^2 \quad and \quad A_\Delta = SB/2, \quad with \quad B = 2\sqrt{R^2 - S^2} \tag{D.48}$$

R is the fixed radius of the pipe, and if t is known, A_r can be expressed in terms of R and t as:

$$A_r = \arccos\left(\frac{R-t}{R}\right)R^2 - (R-t)\sqrt{R^2 - (R-t)^2} \tag{D.49}$$

As the rivulet forms and grow in height, it covers the panel/s at the bottom of the pipe section, either fully or partially. By knowing the rivulet height t, the amount of cover over the panels can be determined. Figure D.7 shows a situation where the j^{th} liquid film control volume is partially covered, and control volume number (j+1) is fully submerged.

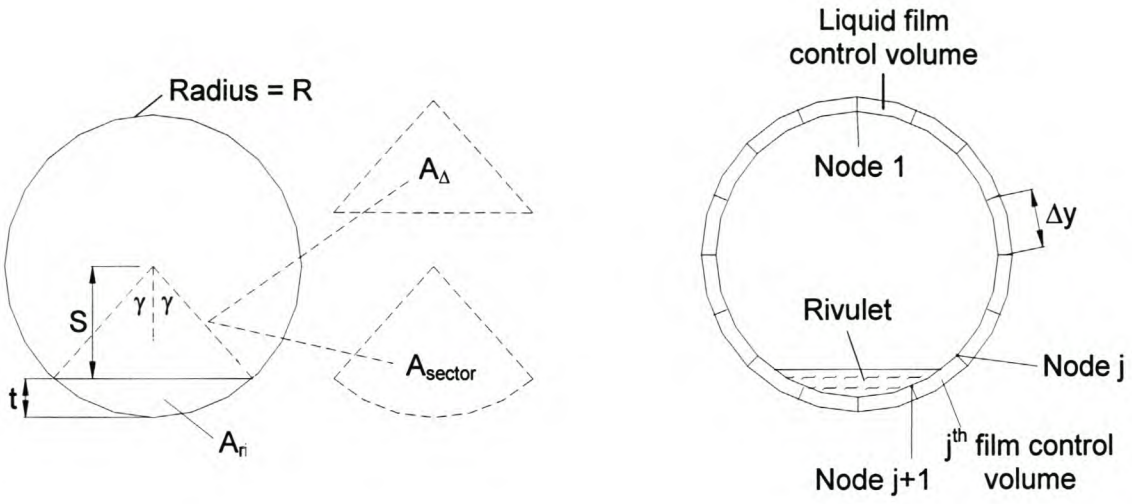

Figure D.7 Rivulet geometry and influence on liquid film control volumes

D.2.4 THE LIQUID POOL

It is assumed that the only way that mass can transfer from the pool is through the gas evaporating from it. The mass flow rate of the gas that leaves the pool (and therefore also returns in liquid form via the rivulet and evaporator film), is :

$$\dot{m}_p = \frac{\dot{Q}}{h_{fg}} \qquad \text{(D.50)}$$

Stephan and Abdelsalam (1980) have proposed a pool boiling heat transfer coefficient that can be used for ammonia as:

$$h_p = C_2(\dot{q}'')^{0.745} \qquad \text{with} \qquad C_2 = 0.3063 + 0.1214P_i - 0.002336P_i^2 \qquad \text{(D.51)}$$

Experimental work done on this specific thermosyphon (Dobson, 1998) has shown though that the actual heat transfer coefficient is on average 57% higher than suggested by equation D.51, and therefore the pool boiling heat transfer coefficient is taken as:

$$h_p = 1.57 \times C_2(\dot{q}'')^{0.745} \qquad \text{(D.52)}$$

D.2.5 THE TOTAL THERMAL RESISTANCE MODEL

The thermosyphon container is the stainless steel tube, and the heat source and sink are the water flowing through the hot and cold water jackets. Figure D.8 describes the physical set-up and corresponding thermal circuit. The values of the interior thermal resistances shown in figure D.8 can be calculated by using the heat transfer coefficients discussed in sections D.2.1 to D.2.4. The theoretical model of the thermosyphon is now complete, and a numerical simulation can be performed.

D.3 SPLASHING AND GEYSERING

One of the limits of the theoretical model is that it does not take into account the two-phase flow effects that ARE expected to occur. These two phase flow effects are flow patterns such as stratified flow, plug flow, slug flow, bubbly flow, wavy flow, annular flow and 'wispy' annular flow, and are described in text books on heat transfer and gas-liquid flow. It is not attempted to describe these flows or include them into the theoretical model because of the complexities involved. What can be said, though, is that these phenomena will cause liquid to be propelled ('splashed' or 'geysered') outside of the original free surface of the stationary pool. This will have an effect on the total behaviour of the fluid inside the thermosyphon. This will be addressed in the discussion of the results, section D.5.

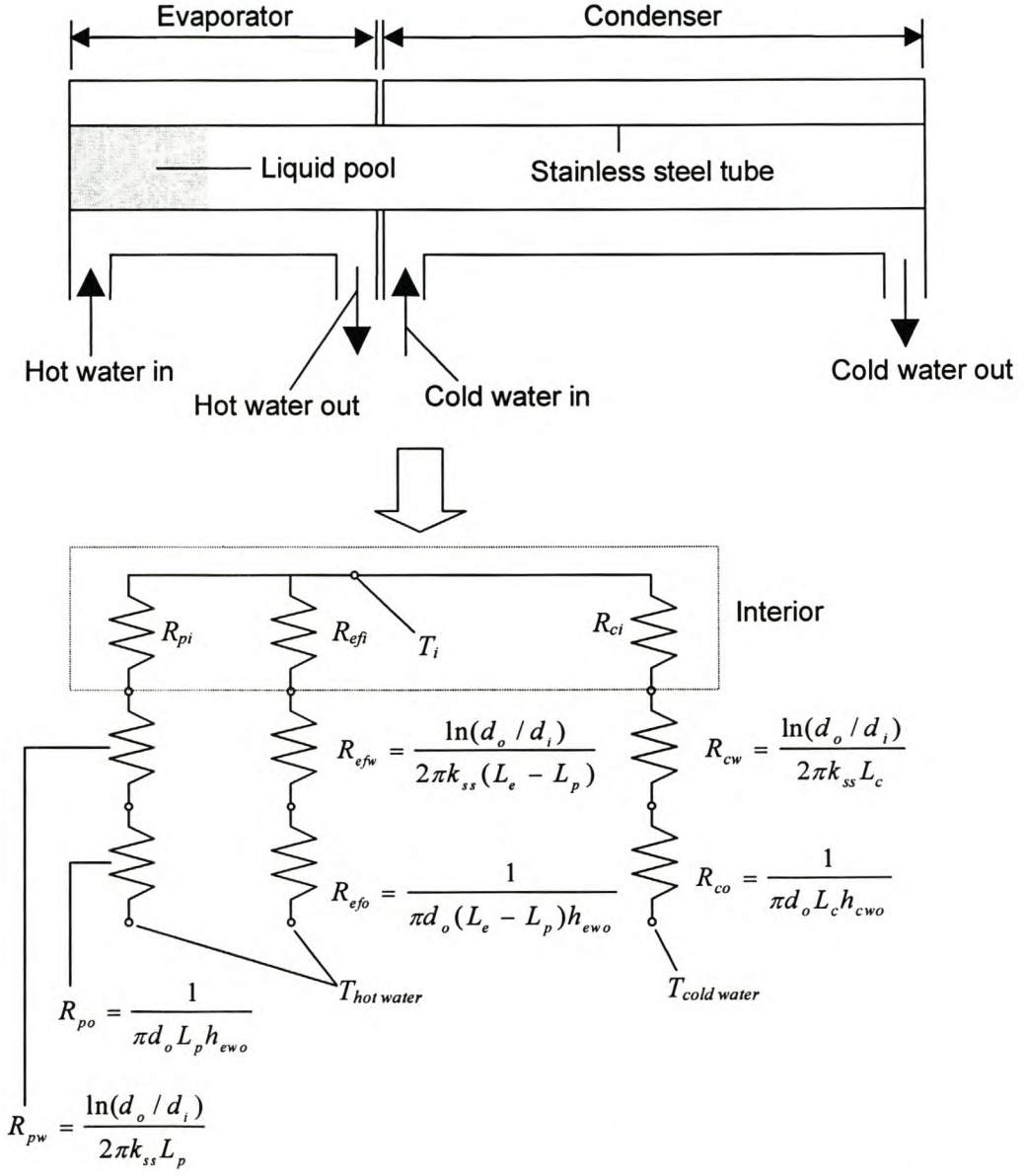

Figure D.8 Schematic set-up and corresponding thermal circuit of thermosyphon

D.4 NUMERICAL MODELLING

The flow diagram used to model the thermosyphon is shown in figure D.9. The steps involved will now be discussed:

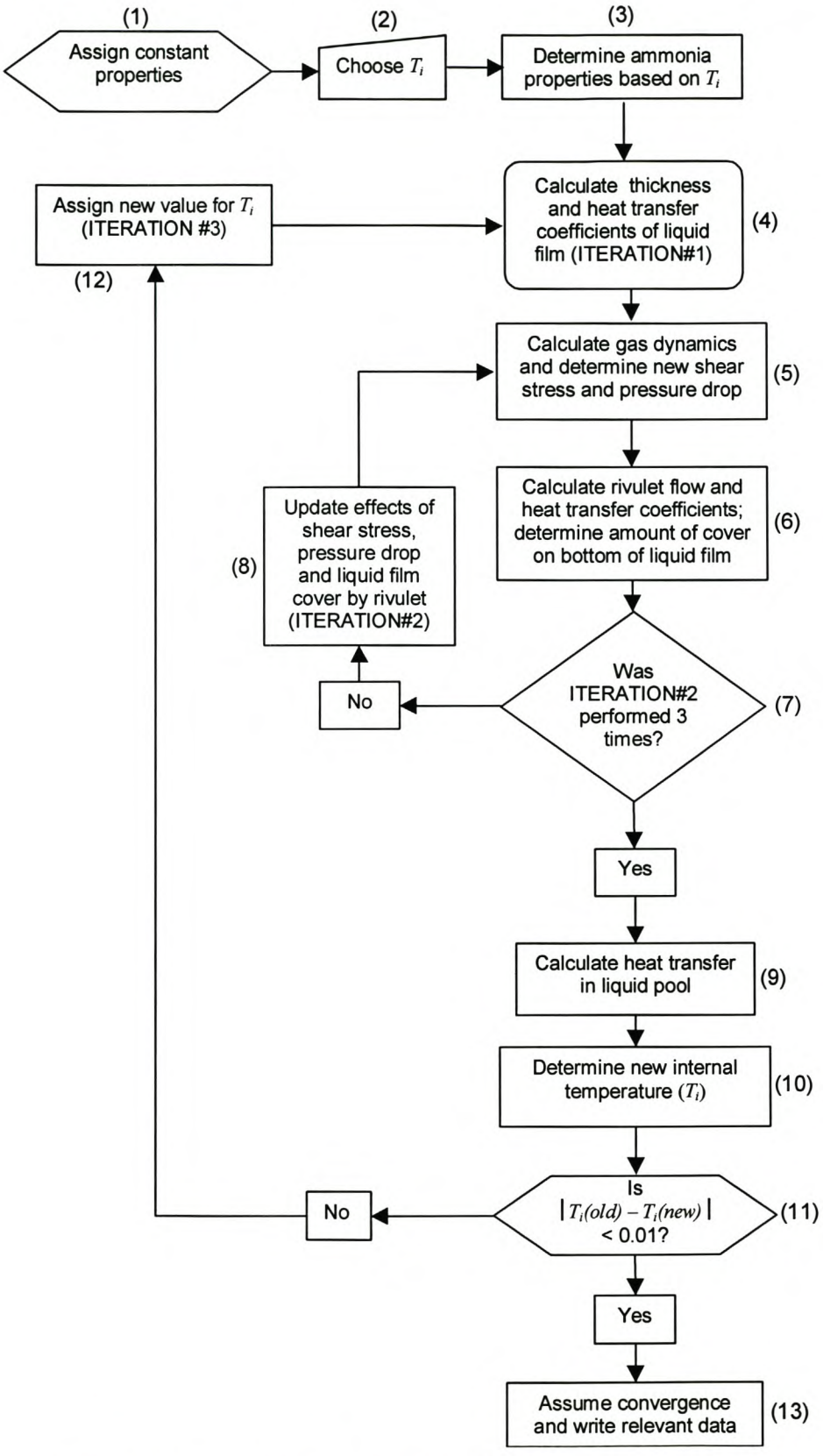

Figure D.9 Flow diagram of numerical simulation for the ammonia thermosyphon

STEP 1 (Assign constant properties)

During this step, all the constants needed are assigned to the program. This include values such as the mass flow rates and temperatures of the heating and cooling water, the evaporator length, the thermosyphon geometry, the properties of the heating and cooling water, the inclination angle, the discretised sizes for the numerical simulation and so on.

STEP 2 (Choose T_i)

The internal temperature has to be found iteratively, but the temperature is needed in the beginning to determine the ammonia properties and also to perform the iterative process needed to calculate the pool boiling heat transfer coefficient later on. Therefore a reasonable value for T_i needs to be assigned.

STEP 3 (Ammonia properties)

The internal temperature is assumed to be constant over the total length of the thermosyphon. It is known either through step 2 or through calculation after one or more iterations (ITERATION #3) have been performed (step 12). The thermo-physical properties of ammonia are known as a function of temperature (see appendix A) and can therefore be calculated.

STEP 4 (Calculate thickness and heat transfer coefficients of liquid film)

An iterative process is needed to determine the film thickness, δ, for each discretised liquid film control volume. If δ is known, the heat transfer coefficient can be calculated and also the heat transfer rate, so that the amount of condensation onto the control volume can be calculated. By changing δ until the momentum and continuity equations are balanced, the converged value for δ can be found for each control volume. In the evaporator section, film dry-out can of course be encountered (i.e. when δ = 0). When this happens, the velocity of the gas core can be used to determine a convective heat transfer coefficient.

STEP 5 (Calculate gas dynamics, shear stress and pressure drop)

The gas velocity, that is needed to calculate the interfacial shear stress and the pressure drop, can only be determined after the liquid film analysis (step 4) is finished. (Although, these effects are needed in step 4, so that for the first iteration (in step 4) the shear stress and pressure drop are taken as zero). The shear stress is also updated with the effects of blowing, suction and waviness.

STEP 6 (Calculate rivulet flow and it's effects)

One of the outputs of the film analysis (step 4) is the amount of liquid that leaves the film and flows towards the bottom section of the thermosyphon tube, due to the gravitational

component in the y-direction. The height of the rivulet, t, is determined iteratively by balancing the momentum and continuity equations. As the rivulet grows in height, it will partially or totally cover some of the liquid film control volumes at the bottom of the pipe section. The amount of cover is calculated and the x-y array of liquid film control volumes is updated. If a liquid film control volume is totally covered by the rivulet, it has to be cut out of the analysis and if it is partially covered, only the open part should be considered.

STEP 7 (Was ITERATION # 2 performed 3 times?)

ITERATION # 2 involves the re-calculation of the thicknesses and heat transfer coefficients for the liquid film control volumes. The changes are updated in step 8. This criteria does not imply 'full convergence', but it has been found through observation that basically no outputs from the program change any more after 3 iterations. This is shown and discussed in the results of section D.5. (See figures D.12 to D.17)

STEP 8

This is where the effects of pressure drop, shear stress and the amount of cover from the rivulet over the liquid film control volumes are updated, before the liquid film is re-analysed.

STEP 9 (Calculate heat transfer through liquid pool)

Once the analysis on the liquid film (and dried out region in the evaporator section, for inclined cases) has been done 3 times, convergence of the region above the liquid pool is assumed. The heat transfer coefficient for the pool region inside the thermosyphon, h_{pi}, is a function of the heat transfer rate, so it has to be found through iteration, using the (old) internal temperature T_i.

Step 10 (Determine new internal temperature)

After step 9 is performed, the whole thermosyphon is considered. All the thermal resistances shown in figure D.8 are now known. A new internal temperature, T_i, can therefore be calculated.

Step 11 (Final convergence criteria)

If the internal temperature that was chosen in step 2 (or calculated in step 10 after one or more iterations) is closer than 0.01°C to the new calculated internal temperature, convergence is assumed.

Steps 12 and 13 are straight forward.

D.5 RESULTS

The results are grouped into two sections. Section D.5.1 is a simulation of a hypothetical thermosyphon, with which the necessary convergence criteria for the computer program can be established. In section D.5.2 the heat transfer results for the correlated (see chapter 3), experimental and theoretical (using the computer program discussed in section D.4) are presented and discussed.

D.5.1 SIMULATION OF THE HYPOTHETICAL THERMOSYPHON

A theoretical simulation is performed of a 'cut-out' section of a thermosyphon, as shown in figure D.10. The container is a stainless steel tube with the same diameters as the actual one (see figure D.1), but the total length is only 0.6 m and not 6.2 m. The condenser and evaporator ends are assumed to be water cooled in the same way as the actual thermosyphon and therefore equations D.1 and D.2 are still applicable to determine the external heat transfer coefficients. The reason why this test section is considered, is so that important internal physical results (such as the liquid film thickness, rivulet flow and gas flow) can be considered and convergence criteria can be assessed. The liquid film thickness, the interfacial shear stress, the pressure drop across the section, the average gas velocity, the height of the rivulet and the total heat transfer rate are considered. This is only a hypothetical case, with an 'open' bottom (assuming a pool region to below), and the heat transfer rate into the part of the evaporator considered will not equal the heat transfer rate out of the condenser.

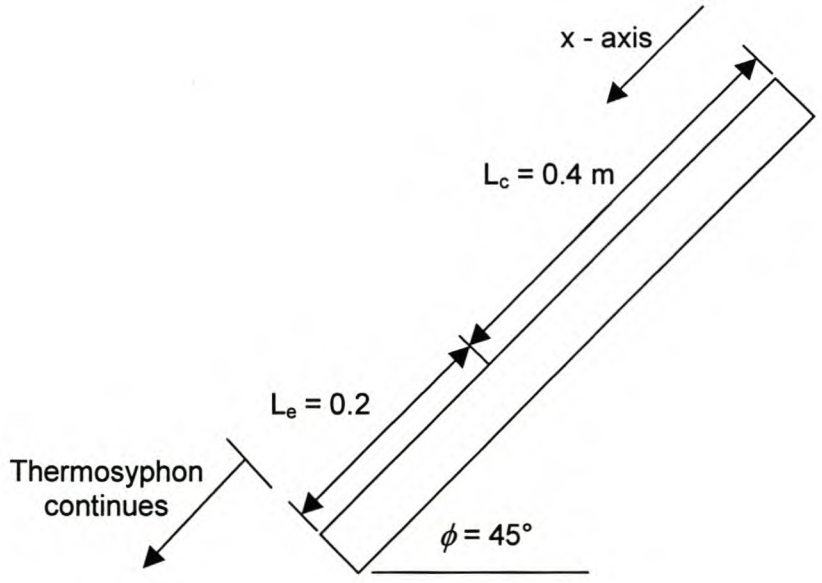

Figure D.10 'Open ended' thermosyphon test section with no pool region. The hot water temperature is taken as 80°C, the cold water temperature is 10°C and the internal temperature is taken as 45°C.

The results of this analysis are now presented.

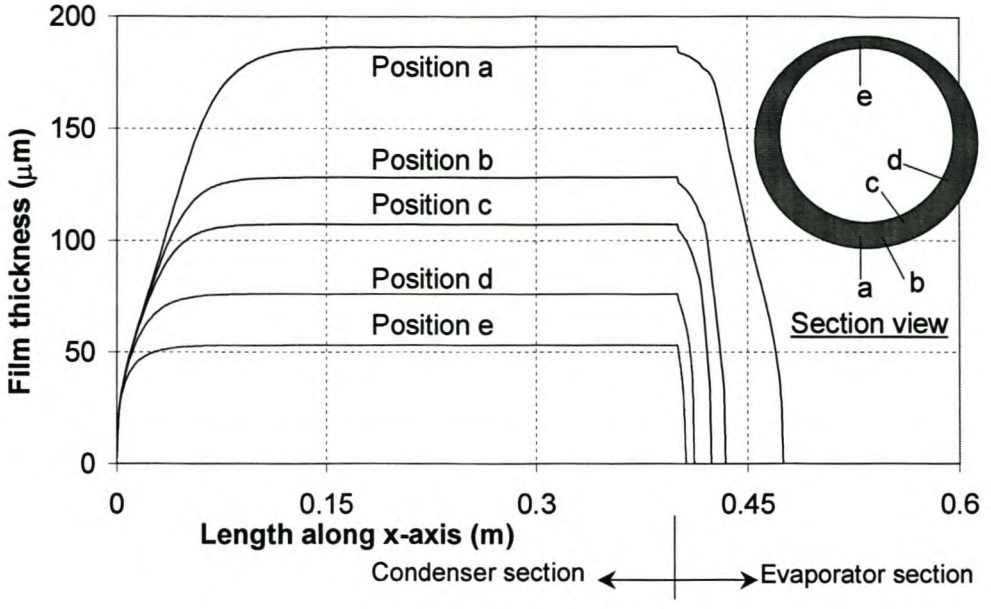

Figure D.11 Film thickness as a function of the axial position as well as the circumferential position

Figure D.11 shows that the films starts to grow until a steady value is reached. The film is the thinnest on top and the thickest at the bottom of the pipe section. Once the film enters the evaporator, it runs dry quite soon, because of depletion due to the circumferential gravity component. This implies that a large part of the evaporator inside wall is dry and there is no liquid that can evaporate.

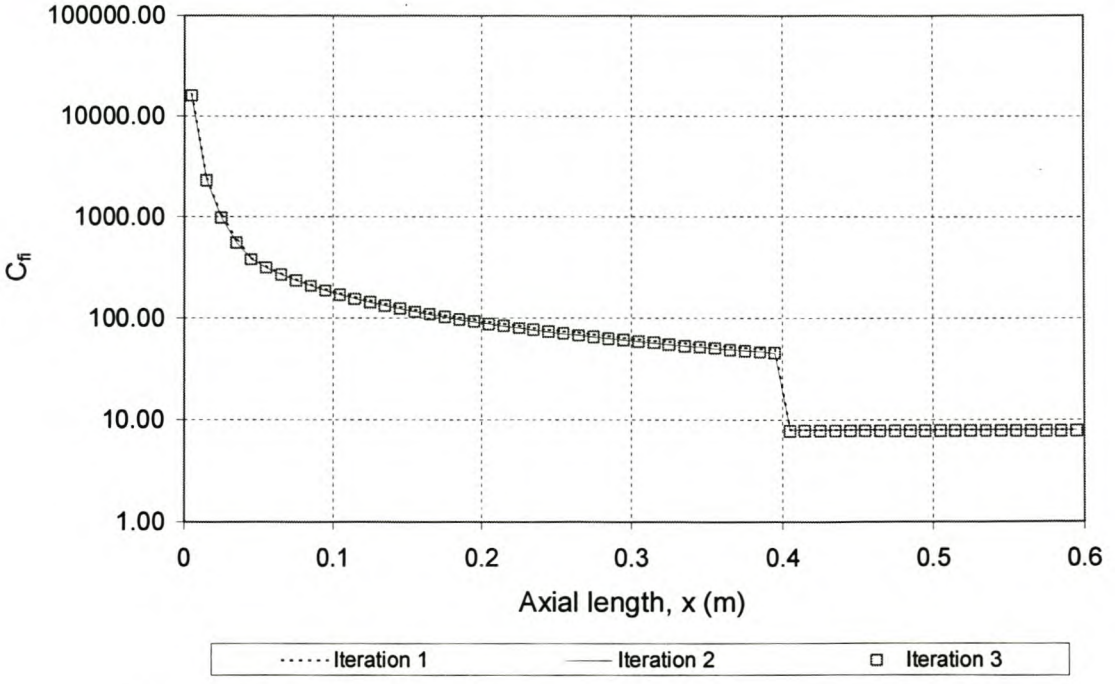

Figure D.12 Friction factor as a function of x for three consecutive iterations

As was explained in section D.4, ITERATION # 2 is stopped after 3 iterations. Figure D.12 shows the interfacial friction coefficient along the x-axis, for three iterations. As can be seen, there is basically no difference between the values produced with the three iterations. The sudden drop in the value, just when the evaporator section is reached, is because the suction effect in the condenser (higher friction coefficient) suddenly changes to blowing in the evaporator (lower friction coefficient).

Figure D.13 shows the interfacial shear stress as a function of x, for the three consecutive iterations. In this case there is a slight difference between the first and second iteration results, but virtually no difference between the second and third iterations.

The pressure difference, as shown in figure D.15, stays basically unchanged for all three simulations. The rivulet height shown in figure D.16 also converges after the second iteration. The sudden drop in rivulet height is because of the lower shear stress that is encountered in the evaporator section. (See figure D.13)

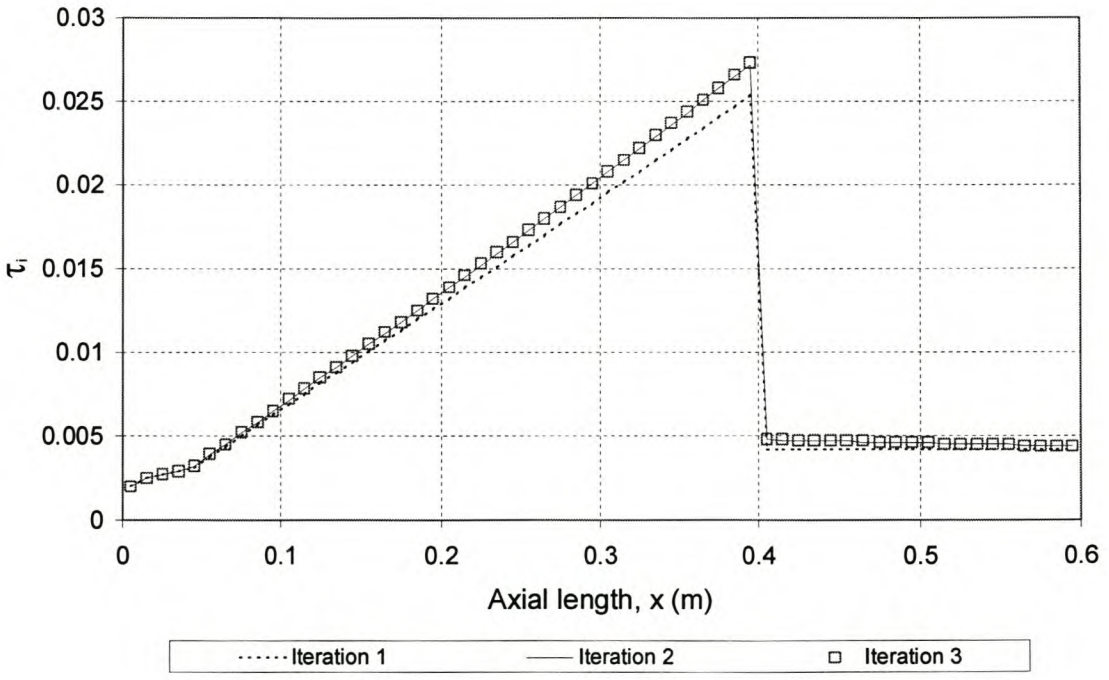

Figure D.13 Shear stress as a function of x for three consecutive iterations

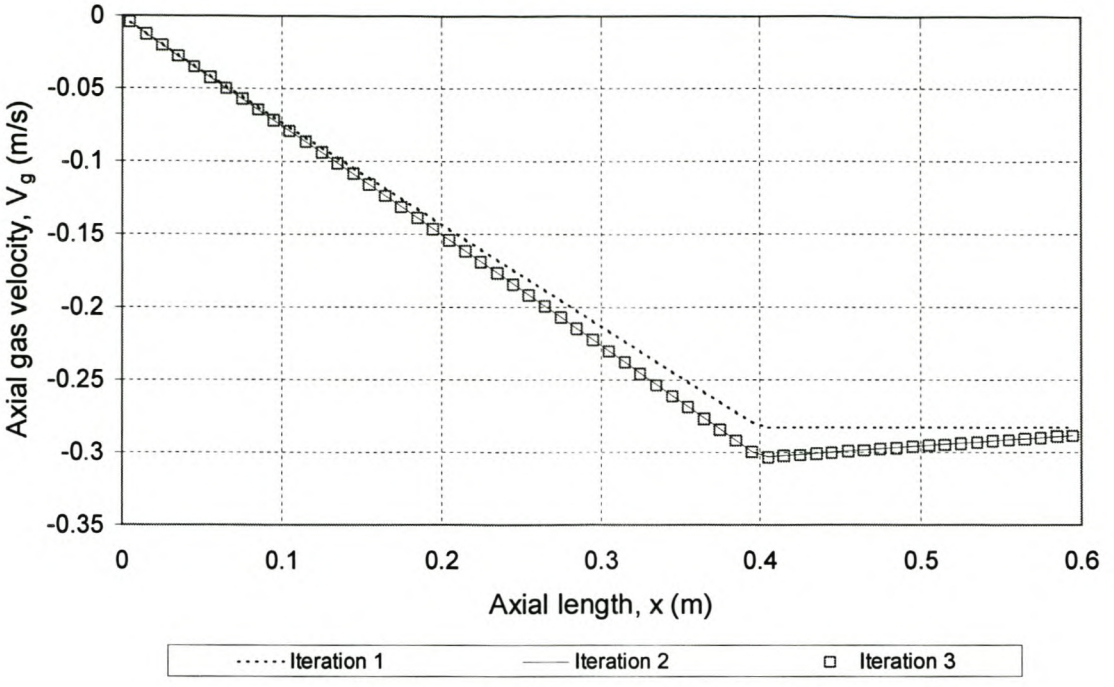

Figure D.14 Gas velocity as a function of x for three consecutive iterations

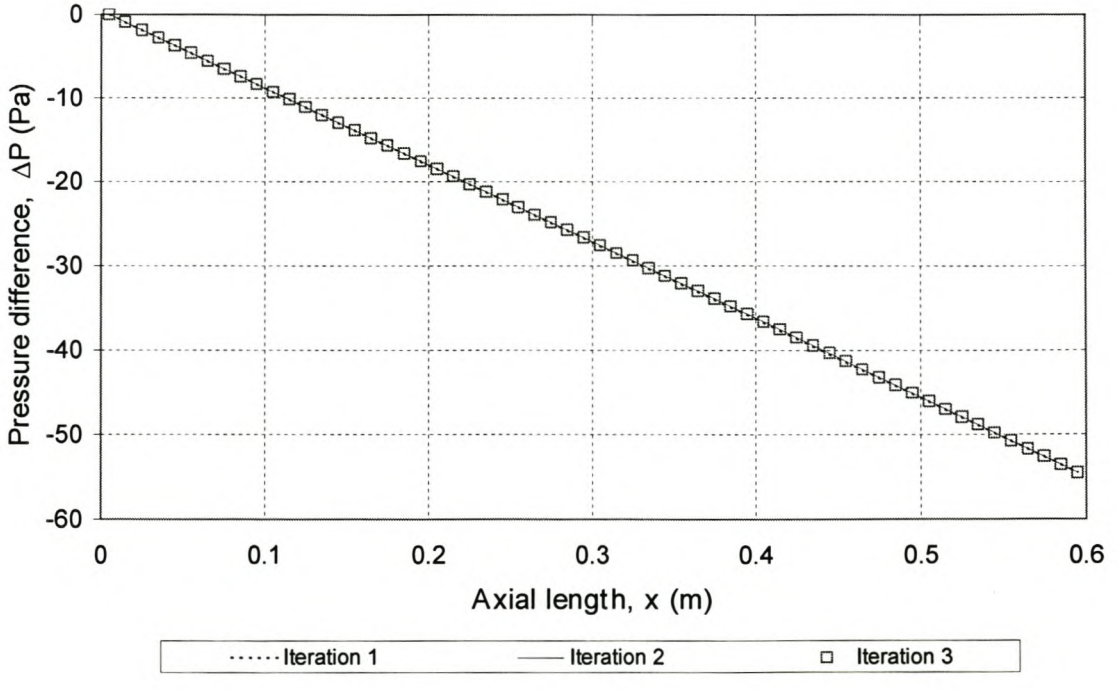

Figure D.15 Pressure loss as a function of *x* for three consecutive iterations

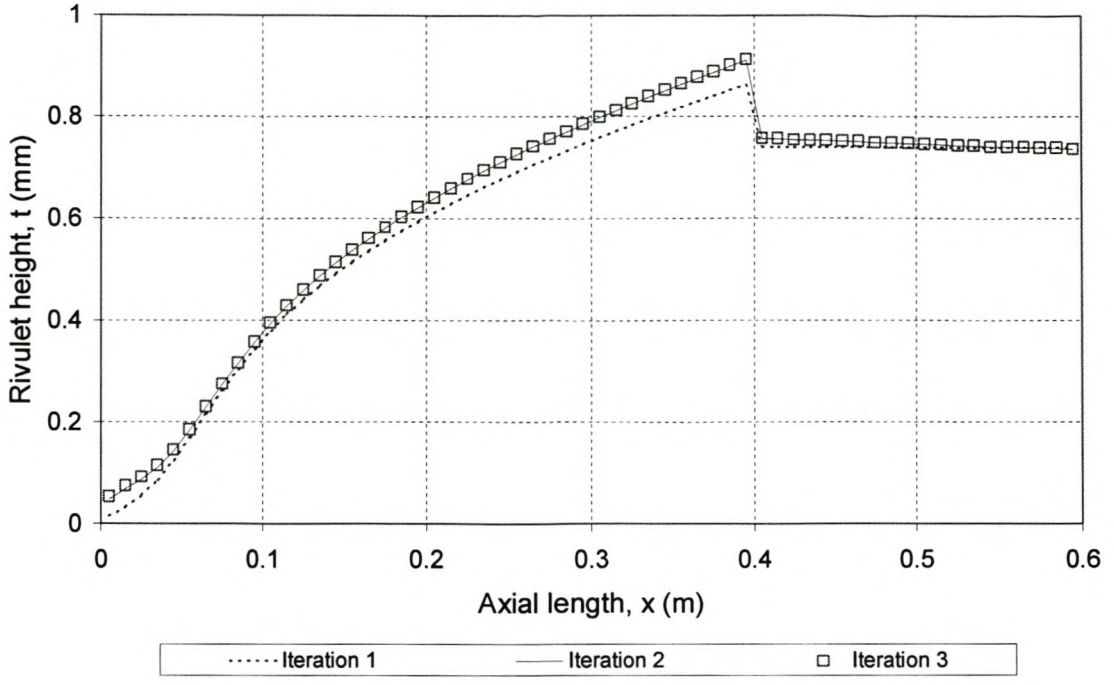

Figure D.16 Height of the rivulet as a function of x for three consecutive iterations

The final graph to be inspected is of the total power transferred through the condenser section.

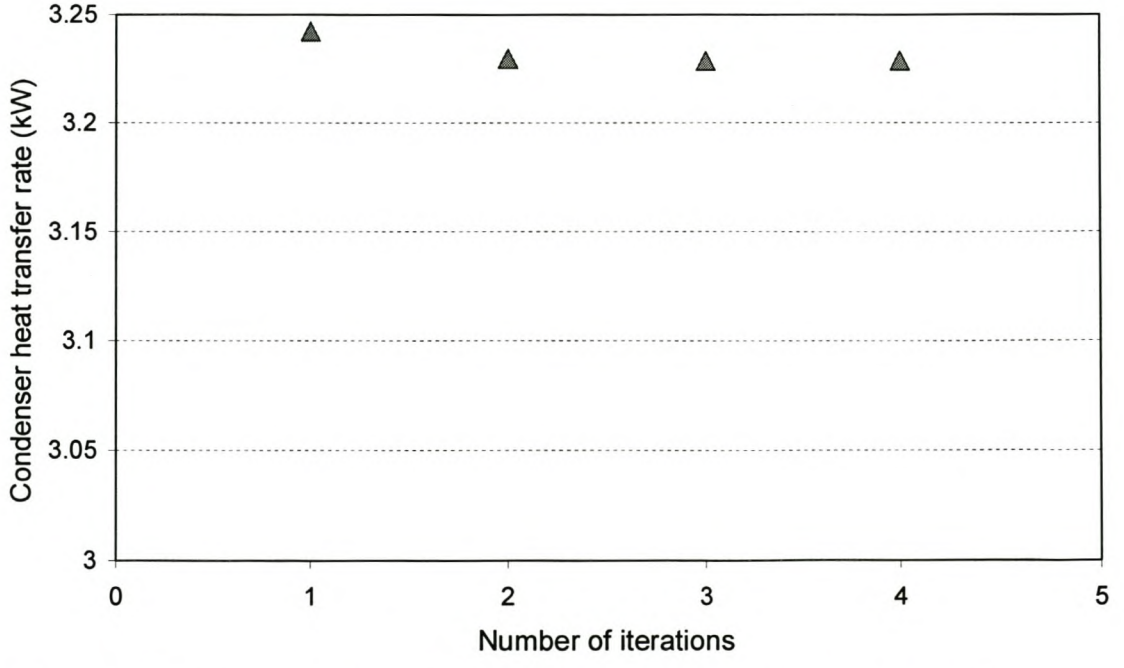

Figure D.17 Total heat transfer rate through the test section for four consecutive iterations

Figure D.17 clearly shows that there is virtually no difference between the heat transfer rate found by the third and fourth iterations. Based on these type of observations, it was thus decided that by performing ITERATION # 2 three times, convergence should be established for a specific internal temperature.

D.5.2 ANALYSIS OF THE ACTUAL THERMOSYPHON

An analysis on the thermosyphon described in section D.1 is performed. The constants are the following:

Pool length: $L_p = 0.396\ m$

Water mass flow rates: $\dot{m}_{hw} = \dot{m}_{cw} = 0.5\ kg/s$

Cold water temperature: $T_{cw} = 10\ °C$

The variables are

Evaporator lengths: $L_e = [0.4, 0.8, 1.2, 1.6, 2]\ m$

Inclination angles: $\phi = [30, 45, 60, 75, 90]\ °$

Hot water temperatures: $T_{hw} = [35, 50, 65, 80]\ °C$

Experimental and theoretical results will now be presented. In order to 'benchmark' these results, they are compared to results achieved by using the correlations of El-Genk (evaporator end) and Gross (condenser end), as discussed in chapter 3. From figure D.18 it can be seen that for the vertical case, relatively good agreement is found between the experimental and numerical results as well as those found using the correlations.

Before moving on to the results for the inclined cases, a very important difference between the theoretical results regarding vertical operation and inclined operation has to be noted. Figure D.11 shows what happens when the liquid film reach the evaporator section for a general inclined case - the liquid film dries out quite soon. For vertical operation though, there is no circumferential component of the gravitational force, so that liquid is not depleted to a rivulet in the bottom of the pipe section. The only way that the falling film can now be reduced and become thinner is therefore through evaporation.

Figure D.19 shows what happens to the liquid film around the circumference of the pipe for a vertical simulation case. It can be seen that the film in the evaporator region lasts until the pool is reached, which is drastically different than the very rapid film dry-out predicted for the inclined cases.

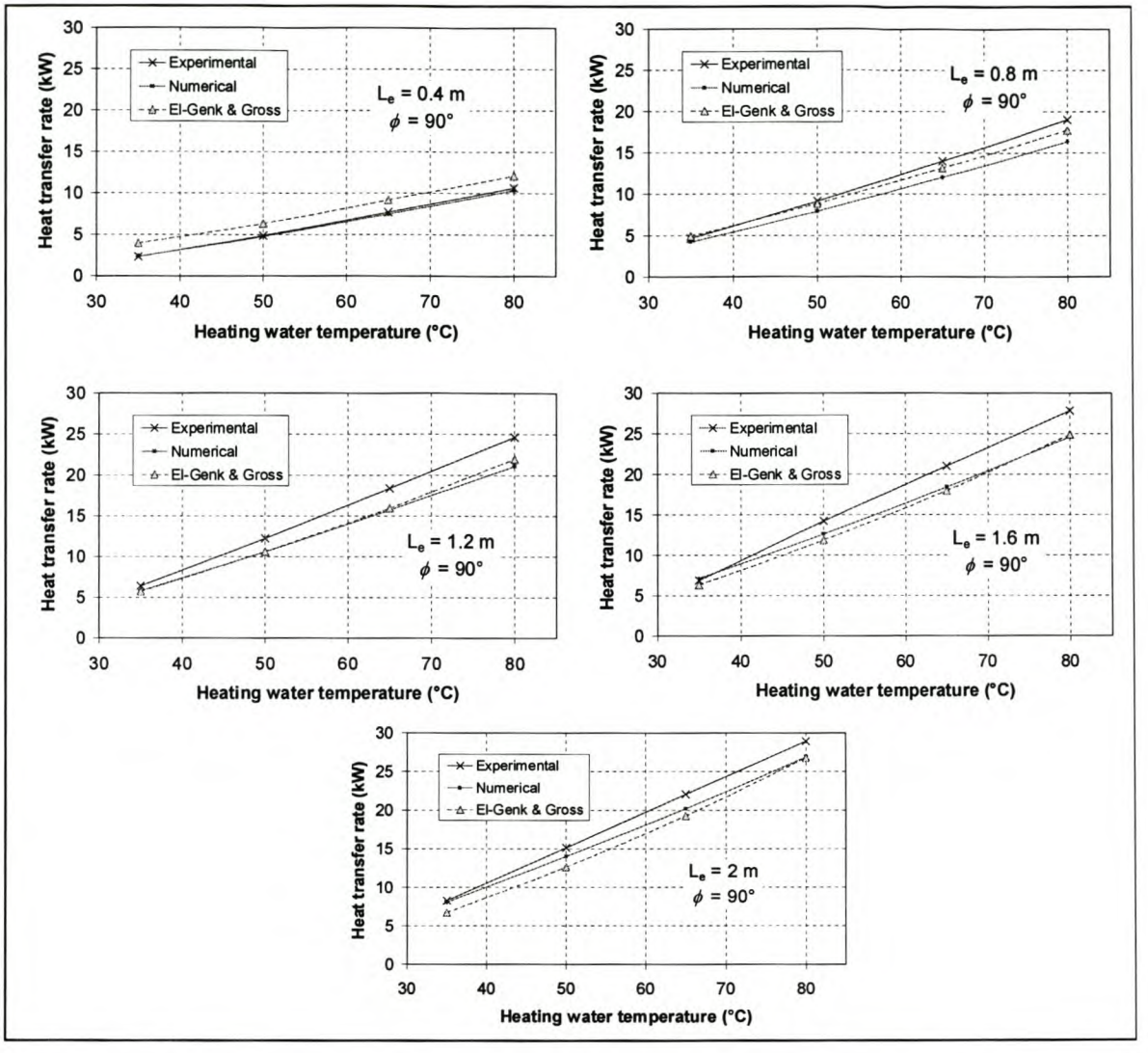

Figure D.18 Heat transfer rates for vertical thermosyphon operation and different evaporator lengths

The liquid film that is present throughout the total height of the evaporator above the pool region, is in effect a source of liquid from which evaporation can take place, mainly through nucleate film boiling. For the inclined cases though, the theoretically predicted dry walls in the part of the evaporator above the pool, can only transfer heat to the working fluid via convection due to the motion of the gas flowing towards the condenser end. This convection heat transfer coefficient is orders of magnitude smaller than the film nucleate boiling heat transfer coefficient and may be neglected. It can therefore be expected that the theoretically predicted heat transfer rate for the vertical case will be much higher than for the inclined cases.

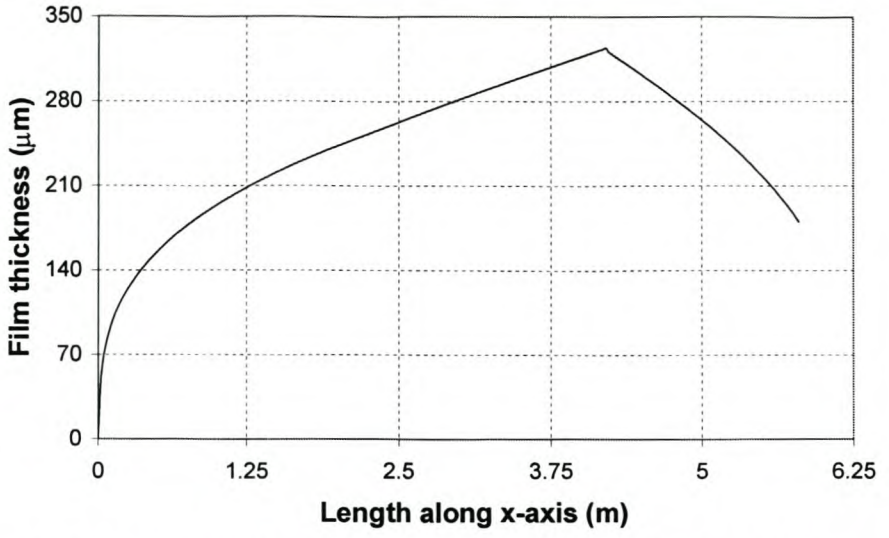

Figure D.19 The numerically predicted liquid film thickness in the vertical thermosyphon. (Total length = 6.2m, L_c = 4.2m, L_e = 2m, L_p = 0.4m, T_{hw} = 80°C, T_{cw} = 10°C, T_i = 45°C)

Figure D.20 portrays quite a different picture than figure D.18. For $\phi = 75°$ and $L_e = 0.4\ m$, there is good agreement between the numerical, experimental and correlated results. However, as the evaporator length becomes longer, the numerical heat transfer rate under-predicts the experimentally measured heat transfer rate. For evaporator lengths of 1.2, 1.6 and 2m, this under-prediction is significant. The reason for this difference is believed to be the fact that the theoretical model predicts quick dry-out of the liquid film in the evaporator region, whereas in reality the walls are wetted somehow by splashing and geysering, as discussed in section D.3. Notably, the correlations of El-Genk and Gross predicts the heat transfer rate very well for this case.

For the inclination angle of 45° shown in figure D.21, it can be seen that the correlations of El-Genk and Gross also under-predict the experimental heat transfer rates, although not as significantly as the numerical prediction does. Once again results are good for the case where the evaporator length is exactly equal to the pool length, for this is the case where there is no liquid film region in the evaporator section, but only a pool.

For the other inclined cases, the same trend as is seen in figures D.20 and D.21 prevail.

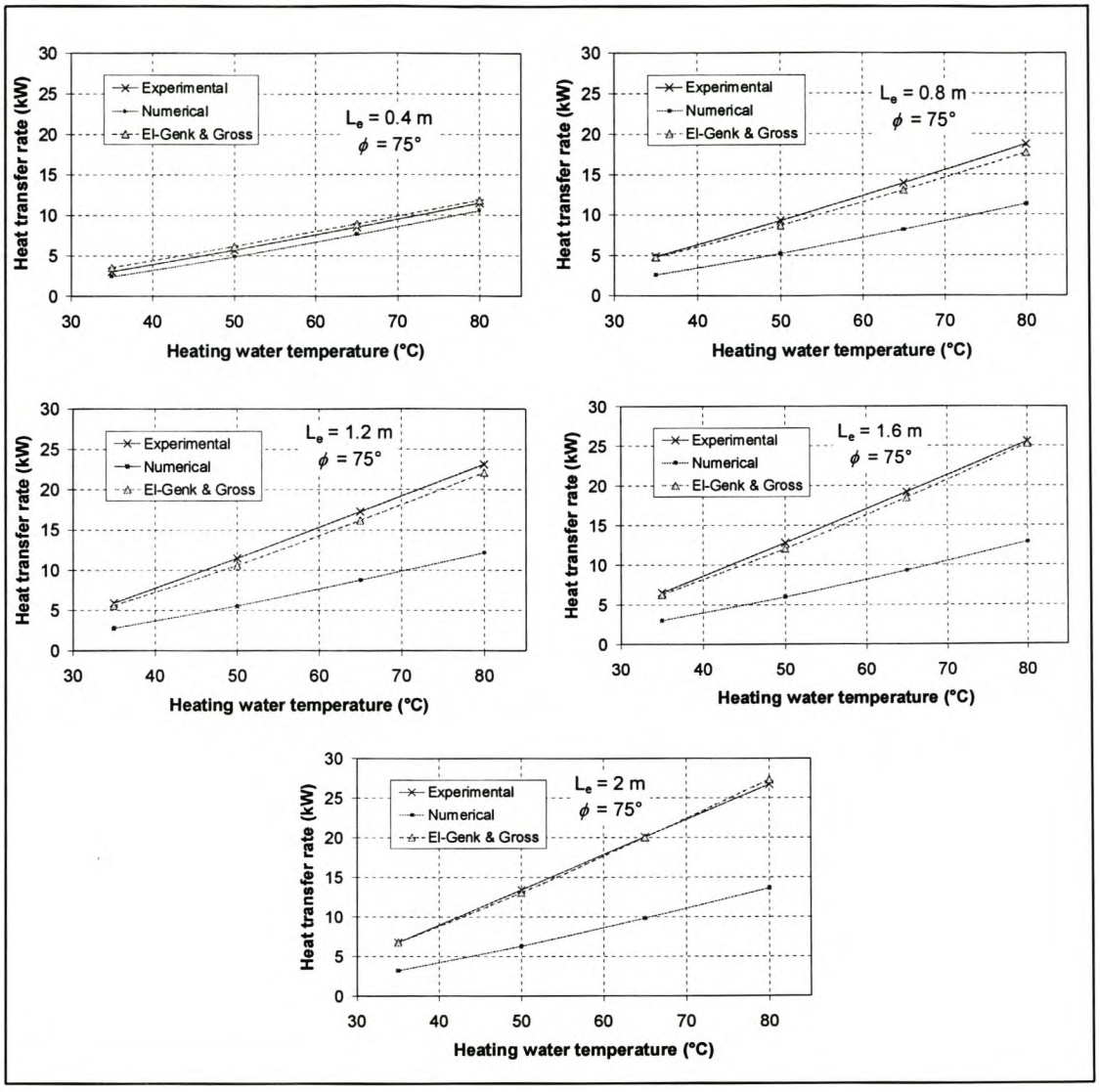

Figure D.20 Heat transfer rates for thermosyphon (operating at 75° above the horizontal) and different evaporator lengths

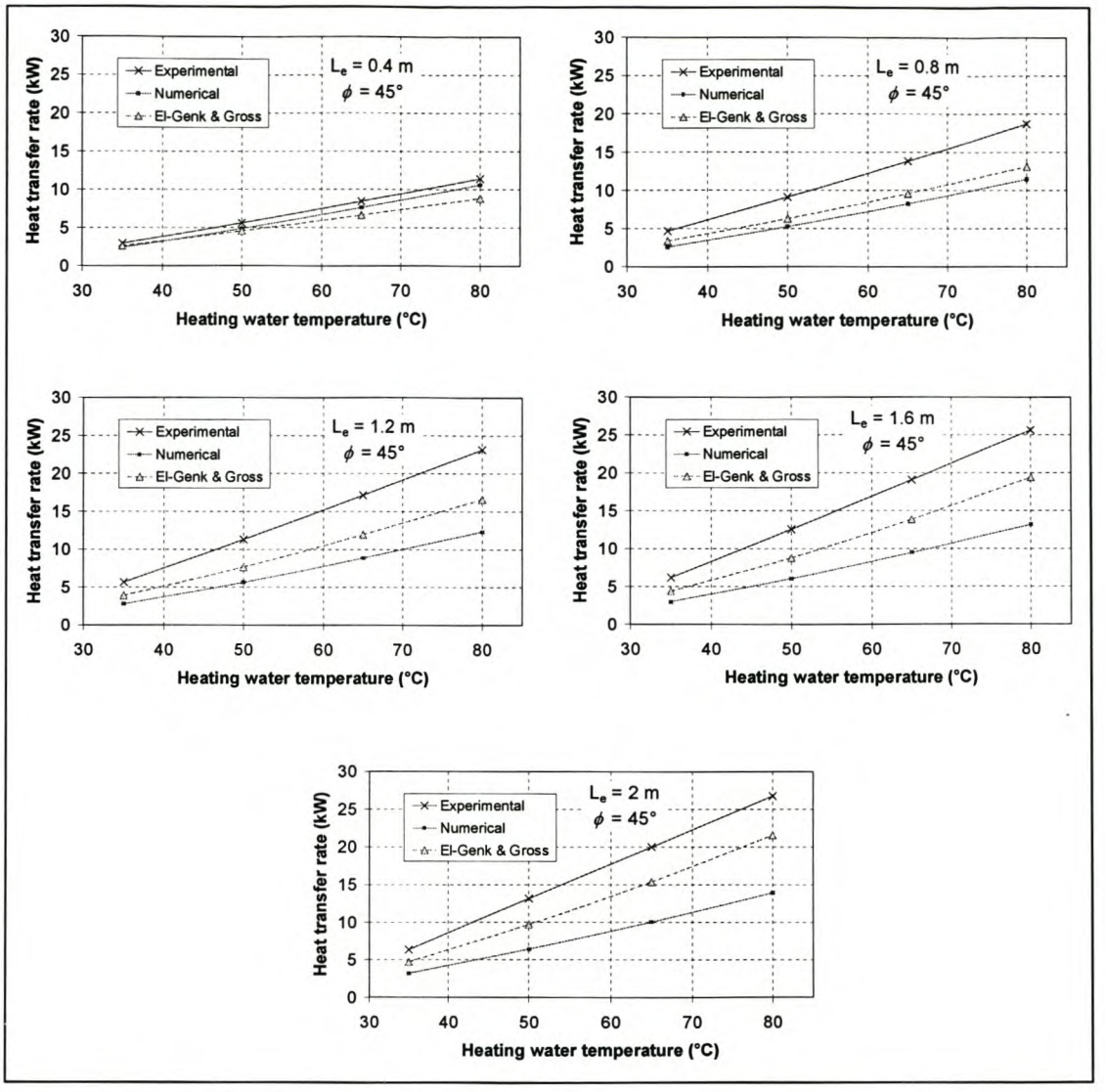

Figure D.21 Heat transfer rates for thermosyphon (operating at 45° above the horizontal) and different evaporator lengths

D.6 THE SPLASHING FACTOR

In an effort to accommodate the effects of splashing and geysering which are expected to be the main reason for the deviation between the experimental and theoretical results, a special correlating factor, the *splashing factor*, is defined as:

$$S = \frac{h_{ewi}(exp)}{h_{ewi}(theor)} \qquad (D.52)$$

Only the internal heat transfer coefficient in the evaporator region is used in the definition, because that is the part that is expected to be influenced the most by the effects of splashing and geysering.

Furthermore, it is assumed that the splashing and geysering are dependant on the heat transfer rate per evaporator wall area, the pool to evaporator length ratio, the internal temperature, the difference between the hot and cold water temperatures and the angle of inclination. The splashing factor is expected to be a function of these variables, and therefore:

$$S = a_o(\dot{q}'')^{n_1}(L_p / L_e)^{n_2}(T_i)^{n_3}(T_{hw} - T_{cw})^{n_4}(\phi)^{n_5} \quad \text{(D.53)}$$

where theoretical values are used in equation D.53.

Equation D.53 can be manipulated as follows:

$$\ln(S) = \ln(a_o) + n_1 \ln(\dot{q}'') + n_2 \ln(L_p / L_e) + n_3 \ln(T_i) + n_4 \ln(T_{hw} - T_{cw}) + n_5 \ln(\phi) \quad \text{(D.54)}$$

which is of the form $Y = A + BX_1 + CX_2 + DX_3 + EX_4 + FX_5$, thus a multi-linear equation.

For each of the 100 theoretical simulations, the theoretical evaporator internal heat transfer coefficient $h_{ewi}(theor)$ can be calculated, and the experimental heat transfer coefficient $h_{ewi}(exp)$ is known, so that the splashing factor can be calculated for each simulation, using equation D.52. For each of these simulations, the five variables mentioned in equation D.53 would also be known. With the values of S and the five variables known for each simulation, a multi-linear regression can be performed to determine the values of the coefficients in equation D.54.

Since there is such a significant difference between the vertical and inclined cases (due to the behaviour of the liquid film in the evaporator region), the data is split into two groups, namely vertical and inclined. There are 80 data points in the inclined group (4 inclination angles, 4 hot water temperatures and 5 evaporator lengths) and the remaining 20 data points are in the vertical group.

Inclined operation

By performing the multi-linear regression on equation D.54, the values of the coefficients are determined as:

$$\ln(a_o) = 74.67; \quad n_1 = -7.4018; \quad n_2 = -1.9807; \quad n_3 = -1.8942; \quad n_4 = 11.9436; \quad n_5 = 0.25504$$

The values for the splashing factor using equation D.53 can now be plotted against the values for the splashing factor obtained using the definition, equation D.52, to asses the accuracy of the above coefficients. Figure D.22 shows such a plot.

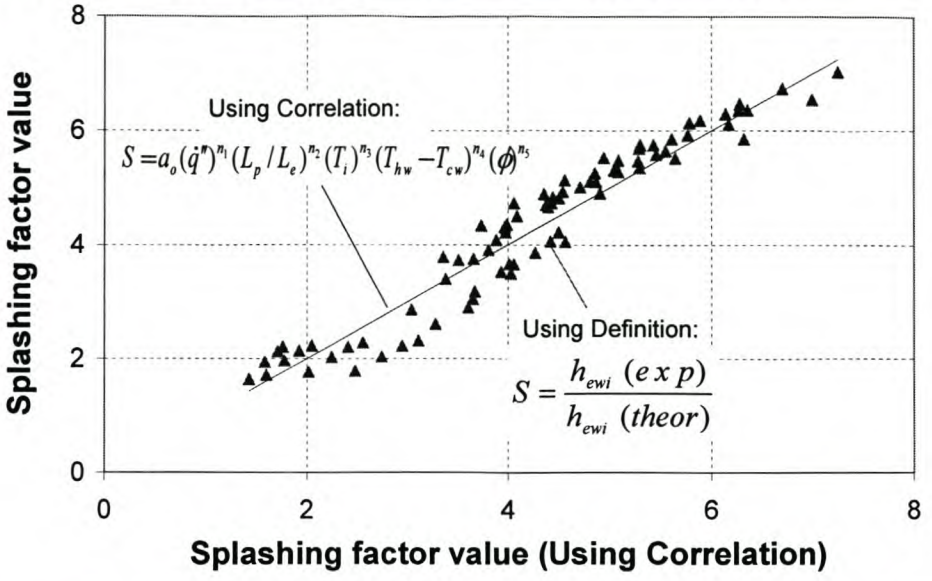

Figure D.22 Values for the splashing factor using the definition (equation D.52) and for the correlation (equation D.53), plotted versus the values for the splashing factor using equation D.53 (Inclined operation)

The straight line in figure D.22 is obtained by plotting equation D.53 against itself. The triangles are the result of plotting equation D.52 against equation D.53. The deviation or scatter of these triangles around the straight line therefore gives a visual indication of how well the correlation (equation D.53) describes the real splashing factor values obtained by using the definition (equation D.52). The correlation coefficient, which is a measure of the goodness of fit of a graph through data points, is $r^2 = 0.92$ for figure D.22, which indicates a reasonably good fit. This means that the splashing factor may be used with a certain degree of confidence to update the theoretically predicted evaporator internal heat transfer coefficient for this specific thermosyphon. To asses the influence or importance of each of the five variables used in equation D.53, another strategy is followed regarding the splashing factor. Instead of determining one correlation for the splashing factor using the mentioned five variables, five correlations are determined – one for each variable used on its own.

If the splashing factor is assumed to be a function of only the aspect ratio L_p/L_e, it is determined using linear regression as:

$$S = 2.502(L_p / L_e)^{-0.4916} \qquad \text{(D.55)}$$

Figures D.23 and D.22 are graphs of a similar type. Once again the results for the splashing factor using equation D.55 and equation D.52 are plotted on the same graph.

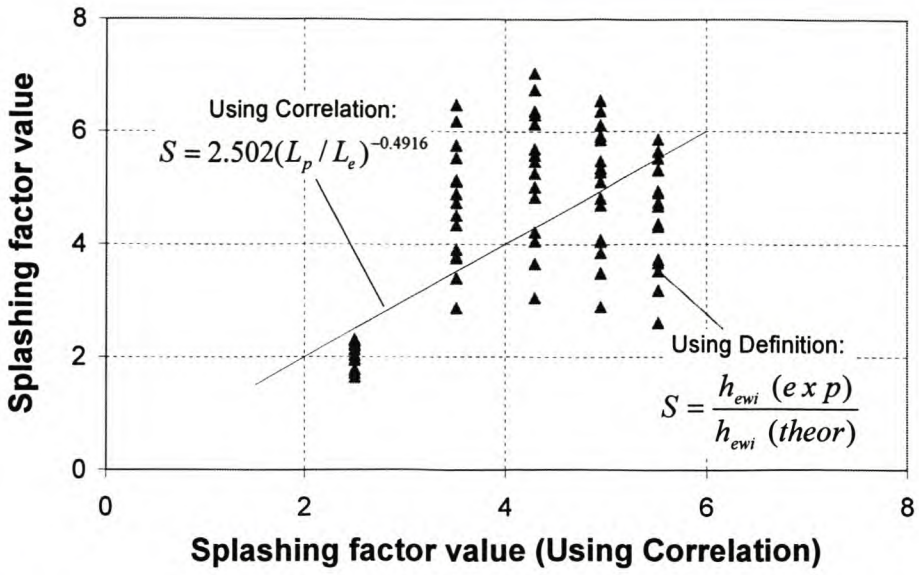

Figure D.23 Values for the splashing factor using the definition (equation D.52) and for the correlation (equation D.55), plotted versus the values for the splashing factor using equation D.55

It is clear from figure D.23 that there is a larger deviation of the real splashing factor values around those achieved by using equation D.55. The correlation coefficient for this case is also significantly lower, with $r^2 = 0.485$. This is therefore not a very good fit. However, when the angle of inclination is taken as the only variable to base the splashing factor is based upon, the goodness of fit becomes even worse. For the inclination angle as the variable, the correlation for the splashing factor becomes:

$$S = 1.273(\phi)^{0.2936} \qquad \text{(D.56)}$$

Figure D.24 shows these splashing factor values and the values obtained by using the definition plotted on the same graph. It can be seen that for this case the deviation of the defined values around the correlated values is quite significant. The correlation coefficient for this case is then also only $r^2 = 0.06$. The same analysis was performed for the other three variables as well (the heat flux, internal temperature and the temperature difference between the hot and cold water), and correlation coefficients were determined for each variable.

By multiplying the correlation coefficients by 100 (which will mean that a correlation coefficient of 1 will have a value of 100, which implies a '100% good fit') these values can be plotted along one another on a bar chart, as shown in figure D.25. The closer the value is to one hundred, the better is the approximation of the splashing factor using only that particular variable, and consequently the higher is the importance of the variable in the determination of the splashing factor.

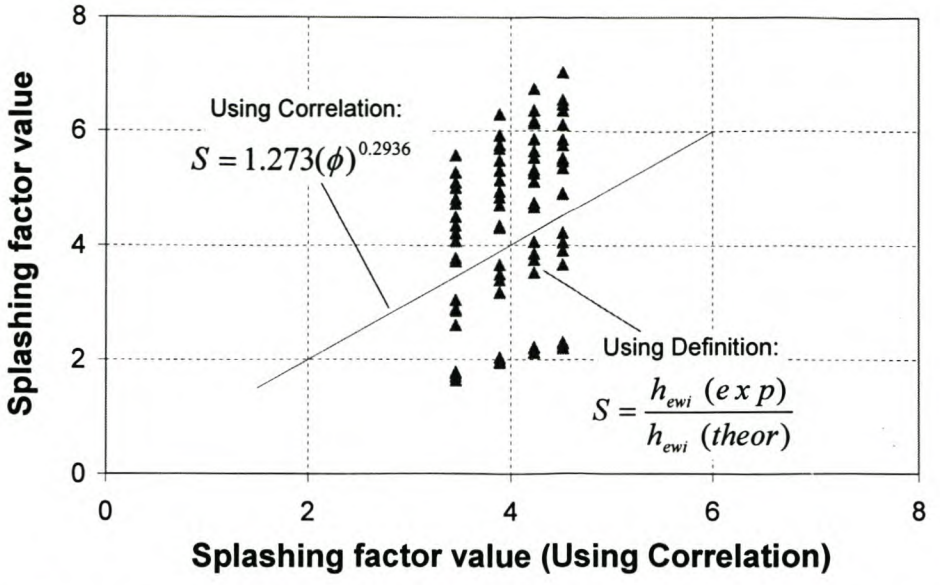

Figure D.24 Values for the splashing factor using the definition (equation D.52) and for the correlation (equation D.56), plotted versus the values for the splashing factor using equation D.56

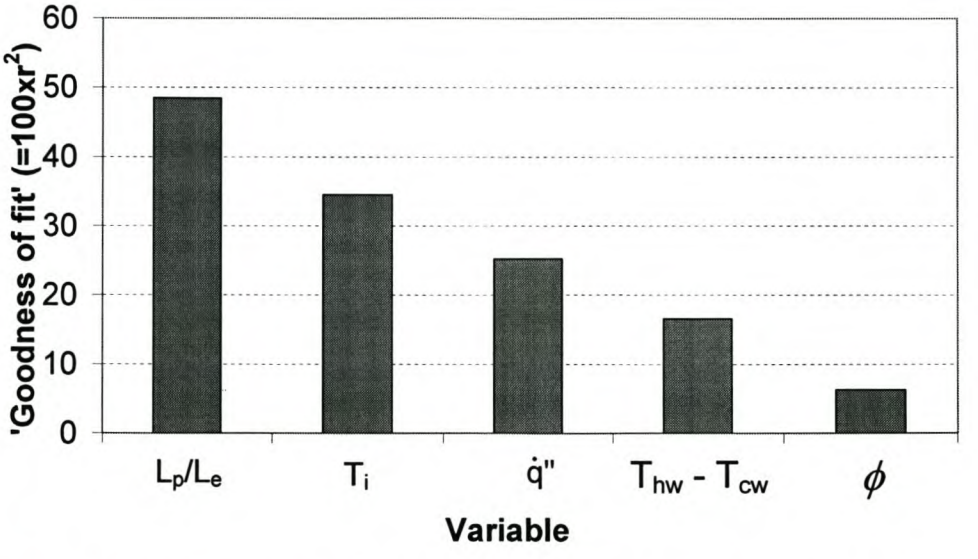

Figure D.25 Relative importance of the variables used in equation D.53 in the determination of the splashing factor, for inclined thermosyphon operation

From figure D.25 it can be seen that the ratio L_p/L_e carries the most weight in the determination of the splashing factor while the angle of inclination ϕ is the least significant, with the other variables in between. This means that the difference between the theoretical and experimental results are the most sensitive to a change in L_p/L_e and the least sensitive to a change in the angle of inclination, ϕ.

Vertical operation

The same type of analysis that was done for inclined operation is also performed for vertical operation. The only difference is that the angle of inclination is now a constant, so that equation D.53 now only has to be a function of four variables, so that:

$$S = a_o(\dot{q}'')^{n_1}(L_p / L_e)^{n_2}(T_i)^{n_3}(T_{hw} - T_{cw})^{n_4} \qquad \text{(D.57)}$$

By performing a multi-linear regression on the 20 available data points, the coefficients in equation D.57 are determined as:

$$\ln(a_o) = -6.074; \quad n_1 = 0.2498; \quad n_2 = 1.2338; \quad n_3 = -0.1922; \quad n_4 = 0.1968$$

The comparison between the splashing factor values using the definition (equation D.52) and the correlation (equation D.57) is shown in figure D.26.

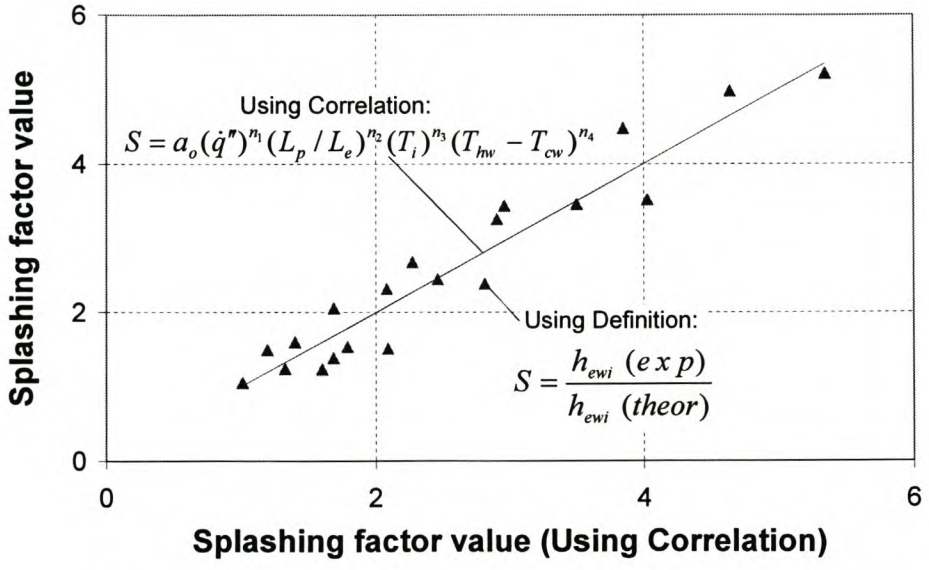

Figure D.26 Values for the splashing factor using the definition (equation D.52) and for the correlation (equation D.57), plotted versus the values for the splashing factor using equation D.57 (Vertical operation)

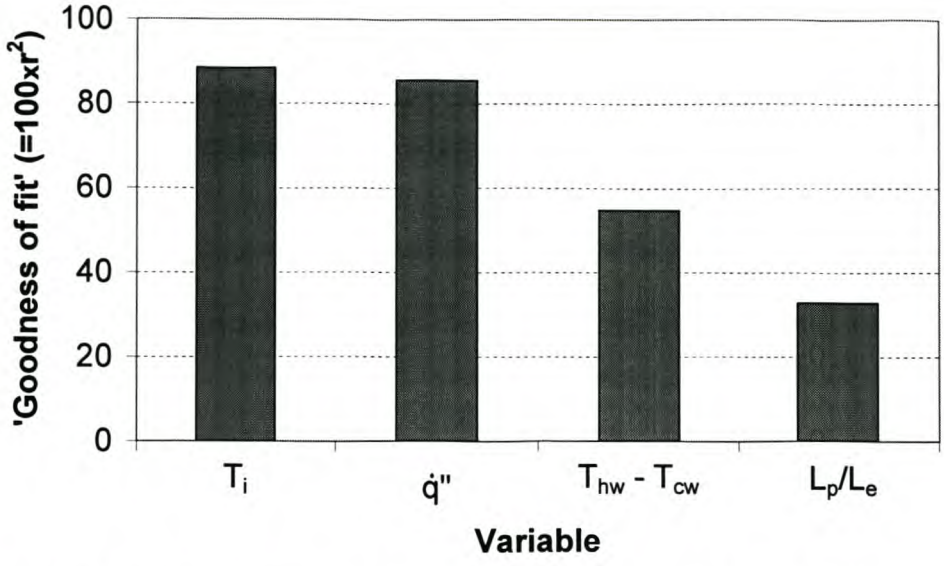

Figure D.27 Relative importance of the variables used in equation D.57 in the determination of the splashing factor, for vertical thermosyphon operation

D.7 DISCUSSION

A numerical simulation was performed on an ammonia thermosyphon, for inclined and vertical operation cases. It is clear from this analysis that making use of the simple control volume types used in this analysis can result in errors, especially when simulating operation at an inclination. The reason is accepted to be that a gas-fluid mix develops in the pool region and two-phase flow phenomena starts to take place, typically including slug flow and churn waves. This type of flow behaviour can effectively lengthen the pool boiling area and also causes liquid to splash against parts of the evaporator wall that is predicted to be dry by the model. Limiting effects, for instance the dry-out, burn out and flooding limit, was not considered, as this analysis is only concerned with the working range of the thermosyphon under these limits. The results for the splashing factor can be used as a design correction factor, but will only work in a limited range for this specific ammonia thermosyphon. The value of L_p/L_e is the most important independent variable that influences splashing and geysering for the inclined cases, and the angle of inclination, ϕ, is the least significant. For the vertical case though, the factor L_p/L_e is the least significant. This supports the idea that the dry area (predicted by the model for inclined cases), has to be wetted somehow (through splashing and geysering), so that enhanced heat transfer may take place. The internal temperature, heat flux and difference between the hot and cold water temperature keeps the same order of importance for both vertical and inclined cases. In order to expand this type of analysis and make it more generally applicable, the effects of thermosyphon geometry as well as the thermo-physical properties of the working fluid needs to be considered. The use of more (significant) dimensionless variables is also suggested.